Improving the Performance of Gas Sensor Systems with Advanced Data Evaluation, Operation, and Calibration Methods

Dissertation
zur Erlangung des Grades
des Doktors der Ingenieurswissenschaften
der Naturwissenschaftlich-Technischen Fakultät
der Universität des Saarlandes

von
Manuel Bastuck

Saarbrücken
2019

Tag des Kolloquiums: 20. September 2019

Dekan: Prof. Dr. Guido Kickelbick

Berichterstatter: Prof. Dr. Andreas Schütze

Dr. Mike Andersson

Prof. Dr. Maximilian Fleischer

Vorsitz: Prof. Dr.-Ing. Michael Möller

Akad. Mitarbeiter: Prof. Dr. Daniel Filippini

Dr.-Ing. Christoph Pauly

This thesis is the result of a joint PhD project between the

Lab for Measurement Technology,
Faculty of Natural Sciences and Technology,
Saarland University, 66123 Saarbrücken, Germany,

and the group of

Applied Sensor Science,
Division of Sensor and Actuator Systems,
Department of Physics, Chemistry, and Biology,
Linköping University, 58183 Linköping, Sweden.

Manuel Bastuck was enrolled in

The Joint European Doctoral Programme
in Materials Science and Engineering – DocMASE.

To my family.

In loving memory of my grandfather,
Richard Hessedenz.

It’s hard to make predictions,
especially about the future.

---

attributed to *Niels Bohr*

Abstract

In order to facilitate the widespread use of gas sensors, some challenges must still be overcome. Many of those are related to the reliable quantification of ultra-low concentrations of specific compounds in a background of other gases. This thesis focuses on three important items in the measurement chain: sensor material and operating modes, evaluation of the resulting data, and test gas generation for efficient sensor calibration.

New operating modes and materials for gas-sensitive field-effect transistors have been investigated. Tungsten trioxide as gate oxide can improve the selectivity to hazardous volatile organic compounds like naphthalene even in a strong and variable ethanol background. The influence of gate bias and ultraviolet light has been studied with respect to the transport of oxygen anions on the sensor surface and was used to improve classification and quantification of different gases.

DAV^{3}E, an internationally recognized MATLAB-based toolbox for the evaluation of cyclic sensor data, has been developed and published as *open-source*. It provides a user-friendly graphical interface and specially tailored algorithms from multivariate statistics.

The laboratory tests conducted during this project have been extended with an interlaboratory study and a field test, both yielding valuable insights for future, more complex sensor calibration. A novel, efficient calibration approach has been proposed and evaluated with ten different gas sensor systems.

Zusammenfassung

Vor der weitverbreiteten Nutzung von Gassensoren stehen noch einige Herausforderungen, insbesondere die zuverlässige Messung ultrakleiner Konzentrationen bestimmter Substanzen vor einem Hintergrund anderer Gase. Diese Arbeit konzentriert sich auf drei wichtige Glieder der erforderlichen Messkette: Material und Betriebsweise von Sensoren, Auswertung der anfallenden Daten sowie Generierung von Testgasen zur effizienten Kalibrierung.

Neue Betriebsmodi und Materialien für gassensitive Feldeffekttransistoren wurden getestet. Wolframtrioxid kann als Gateoxid die Selektivität für flüchtige organische Verbindungen wie Naphthalin in einem variierenden Ethanolhintergrund verbessern. Der Einfluss von Gate-Bias und ultravioletter Strahlung auf die Bewegung von Sauerstoffionen auf der Oberfläche wurde untersucht und genutzt, um die Klassifizierung und Quantifizierung von Gasen zu verbessern.

Eine international anerkannte MATLAB-Toolbox zur Auswertung zyklischer Sensordaten, DAV^{3}E, wurde entwickelt und als *open source* veröffentlicht. Sie stellt eine nutzerfreundliche Oberfläche und speziell angepasste Algorithmen der multivariaten Statistik zur Verfügung.

Die Laborexperimente wurden ergänzt durch vergleichende Messungen in zwei unabhängigen Laboren und einen Feldtest, womit wertvolle Erkenntnisse für die künftig notwendige, komplexe Kalibrierung von Sensoren gewonnen wurden. Ein neuartiger, effizienter Kalibrieransatz wurde vorgestellt und mit zehn unterschiedlichen Sensorsystemen evaluiert.

Sammanfattning

Innan gassensorer kan nå en bredare acceptans och användning i vardagen återstår en del utmaningar att övervinna. Många av dessa hänger ihop med att tillförlitligt kunna mäta ultra-små koncentrationer av specifika ämnen i en bakgrund av andra gaser. Den här avhandlingen fokuserar på tre viktiga delar i mätsystemet: sensorns design och arbetssätt, utvärderingen av sensordata, samt framställning av gasblandningar för effektiv sensor-kalibrering.

Nya driftlägen och material för gas-känsliga fälteffekt-sensorer har studerats. Volframtrioxid som gate-oxid kan förbättra selektiviteten gentemot flyktiga organiska föreningar som naftalen även i närvaro av höga och varierande halter av t.ex. etanol. Inverkan av gate-bias och ultraviolett strålning på transporten av syre-joner på sensorytan har undersökts och applicerats för att förbättra identifikationen och kvantifieringen av olika gaser.

En internationellt erkänd MATLAB-toolbox för utvärdering av cykliska sensordata, DAV^{3}E, har utvecklats och gjorts allmänt tillgänglig (*open source*). Den erbjuder ett användarvänligt grafiskt gränssnitt och speciellt anpassade algoritmer av multivariat statistik.

Genom att utvidga laboratoriemätningarna till att också omfatta jämförande mätningar vid två oberoende laboratorier samt fälttest har viktiga insikter nåtts avseende den komplexa sensorkalibrering som kommer att krävas i framtiden. En möjlig strategi för effektiv kalibrering har därvid tagits fram och utvärderats med tio olika gassensorsystem.

Populärvetenskaplig sammanfattning

Förbättring av prestandan hos gas-sensor-system genom utveckling av avancerade användnings-, datautvärderings-, och kalibrerings-metoder

För att möjliggöra en mer utbredd användning av enkla, kostnads-effektiva sensorer och sensor-system i vardagen, exempelvis för att övervaka kvaliteten på den luft vi andas, återstår en del hinder som behöver övervinnas. Några av de största stötestenarna är förknippade med att kunna mäta riktigt låga halter av hälsovådliga gasformiga ämnen i en miljö där det oftast förekommer ett stort antal andra ämnen, en del i betydligt högre koncentrationer än det/ de ämnen som önskas mätas. Arbetet i denna avhandling har därvid fokuserat på olika åtgärder/ metoder för att förbättra prestandan hos tre olika delar i sensor-systemets mätkedja; 1) Sensorernas design och användningssätt, 2) Utvärderingen av sensor-data, och 3) Kalibrering och utvärdering av sensor-systemens övergripande prestanda.

Under doktorand-arbetets gång har bl.a. nya gas-känsliga material för Fält-Effekt-Transistor (FET)-baserade gassensorer och nya sätt att styra hur dessa sensorer arbetar studerats för att avsevärt förbättra möjligheterna att noggrant kunna mäta halten av olika ämnen. Bl.a. har det kunnat visas att inkluderingen av WO_3 (Volfram-trioxid) som del av det gas-känsliga materialet i FET-baserade sensorer ger bättre möjlighet att urskilja flyktiga organiska föreningar (VOCs — Volatile Organic Compounds), exempelvis naftalen, från andra ämnen som kan förekomma i luften omkring oss. Utifrån experimentella studier har också en modell för de underliggande mekanismerna i ämnenas påverkan på sensor-signalen, baserad på hur syre-joner (från luftens syre-molekyler) kan förflytta sig över sensor-ytan under olika förhållanden, tagits fram, validerats och tillämpats för bättre styrning av sensorerna och därmed bättre noggrannhet i gas-mätningarna.

Som en del av doktorand-projektet har också en MATLAB-baserad toolbox – DAV^{3}E – utvecklats för utvärdering av data från olika typer av sensorer/sensor-system, som alla har det gemensamt att sensor-signalen/erna ej resulterar från en passiv, statisk utan aktiv och dynamisk styrning av sensorerna, exempelvis genom cyklisk förändring av sensorernas arbetstemperatur. DAV^{3}E har utvecklats för att bl.a tillhandahålla ett användar-vänligt gränssnitt och, av än större vikt, statistiska data-utvärderings-metoder som specifikt anpassats till sensor-tillämpningar. Publikt tillgänglig (publicerad som *open source*) har DAV^{3}E också snabbt fått både internationellt erkännande och spridning i såväl den akademiska som civila världen.

För att ytterligare utvärdera och validera de modeller/metoder för sensor-styrning och data-utvärdering som tagits fram har både en jämförande undersökning av modellernas/metodernas prestanda av två oberoende laboratorier och fält-mätningar i en av de tilltänkta tillämpningarna genomförts. Bl.a. baserat på resultaten och insikterna från dessa övningar har ett helt nytt angreppssätt avseende robust och effektiv kalibrering och kvalitets-utvärdering av sensor-system utvecklats och utvärderats för tio olika sensor-system.

Contents

V. Appendix 263

Preface

This dissertation is the result of my binational doctorate supervised by Prof. Andreas Schütze at Saarland University, Germany, as well as Dr. Mike Andersson and Dr. Donatella Puglisi at Linköping University, Sweden. It was completed during the time from February 2014 to July 2019 within the framework of *The Joint European Doctoral Programme in Materials Science and Engineering* (DocMASE) of *The European School of Materials* (EUSMAT).

Many—but not all—of the results discussed in this monograph have already been published in peer-reviewed scientific journals or presented at international conferences. These publications are acknowledged as references, but also re-evaluated and re-interpreted according to the latest insights.

This thesis is divided into four parts, preceded by an introduction in chapter 1 about sensors in general and chemical sensors and their applications in particular. The first part presents important concepts of multivariate data analysis in chapter 2 and then, in chapter 3, focuses on the MATLAB-based toolbox DAV^{3}E which has been developed during my studies.

Part two is concerned with the optimization of gas-sensitive field-effect transistors which are introduced in chapter 4, followed by the measurement setup used throughout this work in chapter 5. The influences of sensitive materials, gate bias, and UV light are discussed in chapters 6 through 8.

The third part takes up many previous concepts with a focus on the actual application of gas sensor systems. It outlines the issues with calibration in chapter 9 and proceeds to explain, in chapter 10, the hard- and software which have been developed, partly within my work, to make efficient and precise calibration possible. Three separate studies concerning interlaboratory testing, field testing, and a novel calibration scheme are discussed in chapters 11 through 13.

The thesis finishes with a conclusion and an outlook summarizing all chapters, followed by the list of references, a list of my own publications and contributions, as well as lists of acronyms, figures, tables, and code listings.

Friends, colleagues, family, and all other people who have contributed to the success of this work are acknowledged in a separate chapter.

Manuel Bastuck
Saarbrücken, July 2019

1. Introduction

1.1. Sensors

Sensors are an essential part of modern society. They are “the eyes and ears” of any machine that needs to perceive its environment. A good example are today’s smartphones which have an abundance of sensors built-in to record temperature, pressure, acceleration, earth’s magnetic field[1], lighting intensity, and more. Also the camera, replicating human sight, and the microphones, replicating human hearing[2], are sensors as they convert a non-electrical signal, like light or sound, to an electrical signal [1], [2]. Sensors must be discriminated from actuators, like speakers or motors, which convert electrical signals into non-electrical signals or actions. Both sensors and actuators are transducers, converting any signal (mechanical, thermal, magnetic, electric, chemical and radiation) into a different kind of signal [3]. The special status of electric signals arises from the prevalence of electric and electronic data processing.

All sensors mentioned in the above list are sensors for physical but not chemical quantities. They are, for the most part, based on well-understood physical relations and phenomena. A simple temperature sensor, for example, is made by measuring a metal’s resistivity which increases with temperature. A prominent example is the Pt-100 temperature sensor which, between 0 °C and 850 °C follows the relation [4]:

$$R(T) = R_0(1 + AT + BT^2) \tag{1.1}$$

A and B are known material parameters so that a simple one-point calibration, $R_0(0\,^\circ\mathrm{C}) = 100\,\Omega$ for a Pt-100, results in an accurate and precise sensor. Equation 1.1 is easily solved for T, so that a simple resistance measurement can give a quite exact temperature reading:

$$T = -\frac{A - \sqrt{\frac{A^2R_0 - 4BR_0 + 4BR(T)}{R(T)}}}{2B} \tag{1.2}$$

---

[1] Showing that sensors can also augment human perception.

[2] These are just two examples for replication of human senses through sensors, the list goes on and beyond the classic five human senses.

To avoid changes over time, i. e., drift, of the sensor through environmental influences other than temperature, it is usually encapsulated in a protective casing made from, e. g., ceramics.

Many types of physical sensors are based on similarly simple relations, like acceleration sensors on Newton's Second Law, or magnetic field sensors on the anisotropic magneto-resistive effect. This is not to say that physical sensors do not face future challenges and improvements; however, chemical sensors, due to the complex measurand and the plethora of different, competing influences, are still facing more fundamental challenges today which will be discussed in the following section.

1.2. Chemical sensors

In this thesis, the term chemical sensor refers to a sensor able to detect a chemical quantity, in particular the concentration of a gas. The leveraged sensor effect can be physical, chemical, or biological in nature [5]. The following sections will give a short overview of common sensing principles and the associated sensor technologies for gas sensors.

1.2.1. The nose as biological role model

Currently, sensors are, quite literally, "the eyes and ears" of devices, but not the nose or taste buds. Compared to sight and hearing, smell and taste are very complex sensations. As recently as 2004, Axel and Buck were awarded the Nobel Prize in Physiology or Medicine for their discoveries of "odorant receptors and the organization of the olfactory system" [6], [7]. Humans have around 350 odorant receptors [8] but can, according to a recent estimate, discriminate over one trillion olfactory stimuli [9]. As each odorant receptor reacts to only one specific molecule (and close variants of it) [7], the brain must play a significant part in the interpretation of the nervous signal pattern arising from different smells. In fact, it was even found that some substances can enter the brain directly from the nose [10], showing the strong connection of this specific sense to the brain. Hence, to replicate the sense of smell similarly to what already exists for sight and hearing, an adequate mechanical replication is necessary but not sufficient, and must be complemented by data post-processing. Moreover, the direct connection to the outside world has a strong impact on the olfactory receptors and requires them being constantly renewed for the sense to stay functional [11].

1.2.2. Sensor parameters

In order to understand the merits of the sensor technologies presented in the following section, it is important to understand the challenges of chemical sensing first, as well as the sensor parameters associated with them. While most of them are also used to characterize physical sensors, their weightings differ for chemical sensors. For example, stability issues play a greater role because gas sensors cannot be encapsulated from the environment. Stability, sensitivity, and selectivity are, arguably, the most important parameters of chemical sensors, also referred to as “the 3S” [12]. Additional parameters are, e. g., speed[3], resolution, and limit of detection. All these and more parameters are thoroughly discussed in any textbook dealing with the basics of (gas) sensors [2], [13], [14].

Sensitivity and response

The *sensitivity* S is, for any sensor, defined as the change of the output signal s_out due to a change in the input signal s_in at a specific working point $\boldsymbol{p}$ [2], [14]. Contrary to the definitions in these references, *working point* will, here, always refer to all parameters affecting the output signal but the stimulus s_in [5]:

$$S(s_\mathrm{in}, \boldsymbol{p}) = \left.\frac{\partial s_\mathrm{out}(s_\mathrm{in}, \boldsymbol{p})}{\partial s_\mathrm{in}}\right|_{s_\mathrm{in}, \boldsymbol{p}} \tag{1.3}$$

For linear transfer functions, the right side of this equation becomes a simple fraction, resulting in a constant sensitivity (in respect to the input signal) and the simple relation

$$s_\mathrm{out}(s_\mathrm{in}, \boldsymbol{p}) = s_0(\boldsymbol{p}) + S(\boldsymbol{p}) \cdot s_\mathrm{in} \tag{1.4}$$

for the output signal where s_0 is the baseline, i. e., the output signal without any stimulus ($s_\mathrm{in} = 0$). Even if there is no linear relationship, determining the sensitivity is usually simple as long as there is a reasonably precise model. Consider, for example, the Pt-100, for which the sensitivity is simply calculated by deriving Equation 1.1 with respect to the temperature T. Chemical sensors, on the other hand, usually exhibit a strongly non-linear response [15]–[17] due to a complex interplay of adsorption, desorption, and chemical reaction pathways. This leads to a non-constant sensitivity so that the sensor

---

[3] Dr. Steve Semancik, NIST, USA, considers speed to be the “fourth S” of gas sensors (*personal communication*).

response must be computed more generally as

$$s_{\text{out}}(s_{\text{in}},\boldsymbol{p}) = s_0(\boldsymbol{p}) + \int_0^{s_{\text{in}}} S(s,\boldsymbol{p})\,\mathrm{d}s. \tag{1.5}$$

From this it becomes clear that a chemical sensor's sensitivity can be a very complex, multi-dimensional function which is both hard to measure and to communicate, e. g., in data sheets or publications. Therefore, different measures for such a sensor's performance have been established in the scientific community [5], including, but not limited to:

response $$r = s_{\text{out}} - s_0(\boldsymbol{p}) \tag{1.6}$$

normalized signal $$s_{\text{norm}} = \frac{s_{\text{out}}}{s_0(\boldsymbol{p})} \tag{1.7}$$

normalized response $$r_{\text{norm}} = \frac{r}{s_0(\boldsymbol{p})} \tag{1.8}$$

All of these figures are obviously still dependent on the working point and the input signal[4], e. g., the analyte concentration, but they are often "good enough" to compare different sensor variations. The general goal in sensor design is a high and ideally constant sensitivity so that a small change in the input signal produces a large, proportional change in the output signal. It is important to distinguish sensitivity from other characteristics like selectivity, limit of detection, and resolution.

Selectivity

Selectivity is a term taken from analytical chemistry and is a measure of how strongly a sensor is influenced by non-target analytes in a mixture [18], [19]. The use of the term *specificity*, sometimes used to express perfect selectivity to one component, is discouraged [18], [19]. A simple expression to quantify the selectivity to a substance i with respect to another substance j, both measured at the same concentration, is given in [5]:

$$\mathrm{Sel}_{i,j} = 1 - \frac{r_j}{r_i} \tag{1.9}$$

However, the actual determination of these values becomes very time-consuming very quickly, especially when, according to the definition, mixtures are used

---

[4] For shorter notation, these dependencies will not be given explicitly from here on as long as the parameters are clear from the context.

instead of each substance alone [19]. Moreover, there is practically an infinite amount of possible substances, so that a value for the sensitivity, be it quantitative or qualitative, must always be given with a description of the tested substances and concentrations. Hence, selectivity can usually only be reported for specific applications.

Stability and reversibility

Stability is a sensor's ability to maintain an identical response to identical stimuli as well as a stable baseline over time. Changes in baseline are caused by additive drift whereas changes in the response are the result of multiplicative drift [13]. Drift is usually caused by aging of the involved materials, i. e., restructuring, oxidation or reduction, or unintentional deposition of additional layers, e. g., diffusion barriers. The latter is also commonly referred to as *poisoning* of a sensor [13] and typical substances are organic silica, e. g., *hexamethyldisiloxane* (HMDSO) which deposit a layer of SiO_2, i. e., glass, on the sensitive layer [20].

A related parameter is *reversibility*, which determines if and how quickly the sensor reaches its baseline again once the stimulus is removed [13]. In the most extreme case, molecules, once adsorbed on the surface, cannot leave it anymore so that the sensor integrates the gas concentration over time. This is often the case for biochemical principles which offer excellent selectivity at the expense of not only reversibility, but also stability since biological receptors typically deteriorate over time.

Speed

Speed (of response) refers to the speed with which a sensor's output reacts to a change in stimuli. It is influenced by many properties like temperature, porosity, process limitations (reaction- or diffusion-limited). Usually, the speed is measured as a time constant τ_x, i. e., the time it takes for the sensor after a sudden step in analyte concentration to reach x % of its new signal.

Resolution and limit of detection

The *resolution* of a non-digital measurement is defined by its noise level [5]. In order to distinguish a response from noise, the response amplitude must be clearly larger than the noise amplitude, commonly used factors range from 3 to 6 [5]. The resolution of a sensor (system) is, thus, the noise level divided by the sensitivity and is, therefore, also dependent on the working point. The *limit of detection* is the quantity of analyte which produces a response just above the chosen multiple of the noise level.

1.2.3. Detection principles and sensor technologies

Detection principles in gas sensing are manifold and can be divided into physical, chemical, and biochemical principles, the latter of which are out of scope of this work. Most sensor technologies rely on surface adsorption of gas molecules. One distinguishes physisorption, a weak binding through van-der-Waals forces, and the stronger chemisorption, usually in the form of ionic binding. Some sensing principles can detect physisorption directly; most, however, require physisorption followed by chemisorption to influence the transducer's physical properties [21]. The following list of principles is based on the books by Fraden [2] and Tränkler and Reindl [14] and does not claim completeness. For a more detailed discussion of the mentioned and other principles [21], the reader is referred to these or other books about gas sensor basics [22].

It should be noted that the definitions of *sensor* and *instrument* are fluent and not in all cases mutually exclusive. Tränkler and Reindl define a gas sensor as a component for continuous detection of substances in the gas phase, comprised of a sensitive layer whose properties are changed by the gas and a transducer which translates these changes into electric signals [14]. An instrument or analytical system, on the other hand, is considerably larger in dimension, transports and pre-conditions the analyte which is then detected by a, possibly unspecific, sensor. Similar definitions are used in other sources [21].

Purely physical sensing principles are, for example, based on thermal conductivity, ionizability, gravimetry, or absorption measurements. While each gas has a specific thermal conductivity which can be determined through the temperature change of a heated wire, this sensing principle alone is not selective, i. e., it reacts to all gases in a mixture. The same is true for flame ionization and photoionization detectors, both of which ionize the gas thermally or optically and measure the resulting current of electrons. Therefore, these sensors are rarely used alone, but mostly as a detector after a gas chromatograph which has already separated the gases.

The gravimetric principle measures the mass of physisorbed molecules. This is usually achieved through a *quartz crystal microbalance* (QCM) changing its resonance frequency with the adsorption of molecules. Selectivity can be achieved through functionalization of the surface which, however, often has a negative impact on reversibility. Absorption principles like *non-dispersive infrared* (NDIR) spectroscopy, on the other hand, can be very selective (and reversible) by measuring the absorption of light from a source emitting at a gas-specific wavelength, but have limited sensitivity and cannot be miniaturized.

Similar to thermal conductivity sensors, pellistors [23], [24] measure the caloric heat of a gas mixture by burning it on a catalytic surface. Due to their inherent selectivity to combustible gases, they are particularly well-suited for early warning systems against explosive atmospheres.

Optical sensors change their optical properties, like color or refraction index, upon gas ad- or absorption. Hence, strictly spoken, they are no sensors on their own since they require another sensor converting their optical output to an electric signal. The optical output, however, allows true wireless transfer of the signal, e. g., from the inside of a vacuum chamber through a window to the outside. Systems are available with optical waveguides detecting changes in refraction index through evanescent waves just outside a fiber, as well as colorimetric sensors, e. g., for hydrogen (reversible) [25], [26] and formaldehyde (irreversible) [27]. The latter, based on a chemical reaction, currently reaches the best selectivity available on the market.

Electrochemical cells belong to the most common types of gas sensors currently in use. They contain a liquid or solid electrolyte between two electrodes made from a porous catalyst. Gas molecules dissociate and are ionized on the catalyst which either leads to a potential difference (potentiometric principle) or an electric current at a constant voltage (amperometric principle). Amperometric sensors usually contain a membrane limiting gas diffusion to the catalyst, resulting in a linear response. Due to the sensing principle, selectivity is difficult to achieve. A prominent exception is the Lambda probe using an oxygen-selective solid electrolyte. Liquid-electrolyte cells are efficient as they can operate at room temperature, but have to be replaced regularly due to the electrolyte being depleted.

Resistive-type sensors change their conductivity upon gas exposure. They are based on grainy, semiconducting materials, classically tin dioxide (SnO_2). Oxygen adsorption increases the resistance close to the grain surface by binding formerly free electrons to the oxygen anions. Oxidizing or reducing gases change the amount of oxygen on the surface which is measured as a change in conductivity. It suffers, like many of the previous principles, from poor selectivity, but shows excellent sensitivity down to the *parts per billion* (ppb_v) range. This sensor type is of major importance and more in-depth discussions can be found in [22], [28], [29]. Instead of semiconducting materials, dielectrics are also used for gas detection, e. g., TiO_2 for humidity, by measuring their impedance.

Field-effect sensors rely on the change in charge carriers in a doped semiconductor through a change in electric field which is, in turn, caused by ionized or polarized gas molecules adsorbing on the gate insulator. With exception of the catalyst, commonly used as gate contact material, they can be made in a standard *complementary metal-oxide-semiconductor* (CMOS) process and can be tuned for either selectivity to hydrogen or broadband sensing. However, compared to many other principles, the required sensor structure is relatively complex which increases the potential for failure. A more detailed discussion of this sensor type can be found in chapter 4.

1.2.4. Approaches to selectivity enhancement

Materials and functionalization

The materials used in a sensor influence the adsorption processes and chemical reactions taking place and, hence, the sensor response [30]. Most gas sensors contain a catalyst, like platinum or other metals from the platinum group, to catalyze the reactions on the sensor surface[5]. Different catalysts promote different reactions, so that selectivity to a certain gas can be improved by choosing the right catalyst. Some sensor technologies, like field-effect sensors, also contain an insulator in contact with the gas atmosphere and the catalyst, creating three-phase boundaries as special reaction sites so that the choice of insulator also may influence the sensor response [31]. The lambda sensor employs the selective oxygen ion transport of its *yttria-stabilized zirconia* (YSZ) electrolyte to achieve oxygen selectivity [32]. Not only the material itself, but also its structure and topology has an influence on sensor performance. Gas-sensitive materials with, e. g., a higher degree of porosity increase the surface area and may change the distribution of molecules on the surface [33]. The sensitivity and selectivity of a *metal-oxide semiconductor* (MOS) sensor can be tuned by altering the grain size [34], [35], and nanostructured sensitive layers, e. g., graphene, nanowires, etc., are showing many interesting effects [29]. Formally, the materials may thus be considered parameters of the sensor's working point $\boldsymbol{p}$ in Equation 1.5.

A slightly different approach is used with biosensors [36] where the surface commonly is *functionalized* through molecular receptors with a high selectivity to a certain molecule, very similar to the olfactory receptors in the mammalian nose (section 1.2.1). This leads to a significant gain in selectivity, but can have a negative impact on stability and speed, going so far that the analyte cannot be removed anymore once bound to the surface.

Filters and preconcentrators

Instead of optimizing the sensor for selectivity, another option is to use a sensitive broadband sensor behind a selective filter, similar to a gas chromatograph. Several principles exist: dense layers deposited on top of the

---

[5] Semiconductors can also act as catalysts themselves [28].

sensitive layer like Pd [37] or SiO_2 [38] act as molecular sieves letting only small particles like hydrogen atoms or protons pass. The opposite effect, i. e., removing hydrogen and most hydrogen-containing gases, can be achieved with catalytic combustion upstream of the sensor [39], [40]. The selectivity can, again, be tuned by choice of materials and temperature [41], [42].

Instead of removing or converting undesired compounds, a specific adsorbent, like black carbon or certain *metal-organic frameworks* (MOFs), can be used to preconcentrate target compounds. This has the advantage that the target substances are mostly removed from the gas stream during the adsorption phase, providing a reference atmosphere, and are present at increased concentrations during desorption, e. g., through a heat pulse [43], [44].

Sensor arrays

Sensor arrays imitate the human nose by measuring with several sensors at once and then interpreting the resulting signal patterns [45]. In order for this approach to work, all of the sensors must have different responses to different compounds. “Perfect” selectivity like in the biological counterpart is, however, not necessary. It has even been argued that an array of broadband sensors can be more capable than an array of specialized sensors for general tasks. Sensor arrays can be comprised of different sensor types and technologies to combine their individual benefits. They have been widely used to detect, for example, fires [46], [47], odors [16], [48], and *volatile organic compounds* (VOCs) [49], [50].

Sensor arrays with subsequent pattern recognition are also referred to as *electronic nose* (or *electronic tongue* for liquids), a term first coined by Gardner in 1987 [51]. They trade selectivity for stability since the larger number of sensors increases the potential for failure. Replacing a defective sensor can, due to large manufacturing tolerances, change the pattern trained during calibration and render the system unusable [52]. The pattern can also change over time through different drift processes of the individual sensors. These issues can be mitigated through redundancies and/or drift and error-tolerant data processing [53]–[55].

Cycled operation

Cycled operation uses only one physical sensor to simulate a sensor array and is, therefore, also referred to as the *virtual multisensor* approach [56]. Compared to a real sensor array, this approach lowers the potential for failure, assuming the sensors are the element most likely to fail. In addition, differences in the pattern over time due to drift between multiple physical sensors becomes less severe as all signals come from the same sensor element.

It can be seen from Equation 1.3 that a sensor's sensitivity is influenced by its working point. The parameters defining this working point depend on the sensor technology. The working point for MOS gas sensors, for example, is mainly defined by their temperature of operation, i. e., $\boldsymbol{p} = (T)$. Amperometric sensors have the sensing voltage as an additional parameter, so that $\boldsymbol{p} = (T, V_{\text{sens}})$, and *gas-sensitive field-effect transistors* (GasFETs) have, in addition, gate and body bias, $\boldsymbol{p} = (T, V_{GS}, V_{DS}, V_{BS})$ (cf. section 4.2). Further parameters of the sensor system, like light intensity or pressure, can be included as long as they can be controlled.

Keeping the input signal, i. e., the concentration of a gas, constant, it is obvious that the sensor response can be varied by varying one or more working point parameters over time. The output signal can then be described by a time-dependent Equation 1.5:

$$s_{\text{out}}(t) = s_0(\boldsymbol{p}(t)) + \int_0^{s_{\text{in}}} S(s, \boldsymbol{p}(t))\,\mathrm{d}s. \tag{1.10}$$

This equation implies that through variation of $\boldsymbol{p}$ one (or more) ideally sensitive working point can be found for each gas. Cycling through these working points then results in a "fingerprint" of the atmosphere. One idealized example could be response peaks at certain temperatures which can be related, through previous calibration measurements, to type and quantity of specific compounds. Assuming generally different sensitivity curves for different compounds, this method thus increases both sensitivity and selectivity of a single sensor [57].

Equation 1.10 assumes that s_0 and S are not influenced by their history. Recent studies have, however, shown that the thermodynamic non-equilibrium condition induced by a quick temperature drop can induce highly sensitive states which relax over time in MOS sensors [58], [59]. This requires a re-definition of Equation 1.10 taking into account the sensor's history:

$$s_{\text{out}}(t) = s_0(\boldsymbol{p}(t), t) + \int_0^{s_{\text{in}}} S(s, \boldsymbol{p}(t), t)\,\mathrm{d}s. \tag{1.11}$$

The additionally introduced, explicit dependence on time can be very simple, e. g., when modeling linear drift, but is, practically, usually very complex to reflect, for instance, hysteresis and relaxation effects. While the necessary parameters, i. e., basically the sensitivity at different working points, in Equation 1.10 can be determined experimentally with reasonable effort, it is obvious from Equation 1.11 that the parameter space "explodes" if non-equilibrium effects are considered. Hence, a model describing the processes at play becomes very desirable to optimize this operating mode.

Temperature-cycled operation (TCO) has first been proposed by Eicker in the 1970s [60] and has since been applied to MOS sensors [57], pellistors [61], and *silicon-carbide-based field-effect transistor* (SiC-FET) sensors [62] to improve selectivity.*Gate bias-cycled operation* (GBCO) has been used to further improve the selectivity of SiC-FET sensors [63] and the aging of amperometric oxygen sensors can be quantified using a voltammetric approach [64], to mention only a few examples of cyclic operation. *Ultraviolet* (UV) light is another parameter commonly used to influence the sensor response [65], [66]. Despite its strong impact and quick time constant, very few works have used it in cyclic operation yet [67].

1.3. The need for chemical sensors

Gas sensors have been used in certain, specialized applications for several decades now, but are just starting to appear in more and more consumer products at the time of writing this thesis. The following list of established, emerging, and potential future applications is loosely based on [68] and is supposed to give an idea, not an exhaustive overview, of the potential market and the challenges still to overcome.

1.3.1. Safety and security

One of the first large-scale commercial gas sensor applications was the domestic detection of combustible gases, like propane, with a MOS sensor developed by Taguchi in 1970 [12], [69], [70]. The potential danger of certain gases had, however, been known for much longer from mining accidents involving carbon monoxide (CO) poisoning or methane (CH_4) explosions [71], which led to the development of detection appliances as early as in the 1920s [72]. In today's industrial environments, pellistors are used instead of MOS sensors due to their better accuracy [73]. With the advent of hydrogen as an alternative fuel, also here the detection of leaks to prevent explosions becomes more and more important and is often done by MOS or GasFET sensors [74], [75]. MOS sensors are also replacing or complementing the optical detection in smoke detectors, enabling earlier detection of fires with fewer false alarms by measuring the ratio between hydrogen and carbon monoxide [45]–[47], [76]. Hypoxic air venting, i. e., lowering the oxygen content in a room to approximately 15 %, is used in, e. g., archives and warehouses to prevent fire outbreaks [77] and requires oxygen sensors, often potentiometric or amperometric solid-state devices [78]. Death by carbon monoxide poisoning is, unfortunately, a regular occurrence [79], as carbon monoxide easily accumulates in toxic concentrations in enclosed spaces when open fire, like in chimneys or gas heaters, is combined with insufficient ventilation. The color- and odorless gas cannot be detected by humans, which is why carbon monoxide detectors based on MOS sensors or electrochemical cells have been developed as early warning systems [38], [80], [81].

Further, the detection of explosives or nerve agents with gas sensors is examined in many works [82], [83] and is an interesting application for security-sensitive zones like, e. g., airports.

1.3.2. Process control

Gas sensors are a crucial element in many feedback loops for the control of combustion processes. A well-known example is the lambda sensor [32], a solid-state potentiometric sensor based on YSZ for determining the rest oxygen content in exhaust gas, mostly of cars, but also domestic boilers. This information can be used to control the combustion process to reduce carbon monoxide production and allow the three-way catalyst to oxidize hydrocarbons, CO, and nitrogen oxides (NO_x) [78], [84]. In Diesel engines, toxic NO_x emissions are of special concern due to the higher combustion temperatures. Addition of ammonia (NH_3) in the form of urea can lower the NO_x emissions through *selective (non-)catalytic reduction* (S(N)CR) [85]–[87]. To prevent ammonia slip in this application, selective detection in the harsh environment of the exhaust stream is necessary for a closed-loop control, which can be achieved with SiC-FETs [31], [88]. They have also been used in power plants to measure the amount of sulfur dioxide (SO_2) [89]. Emission control is closely related to air quality (section 1.3.3) since proper process control reduces pollution in the first place and, thus, improves air quality.

Regarding sensitivity and selectivity, process control can often be considered simpler compared to other applications “in the open field” as gas composition and concentrations are usually well-defined by the underlying process. Moreover, for cyclic processes, taking into account expected changes can facilitate the detection task [90], [91]. On the other hand, these applications impose other requirements on sensor systems, like sufficient speed and temporal resolution to enable closed-loop control and stable operation in harsh environments like exhaust streams.

1.3.3. Air quality monitoring

Like fresh food and clean water, clean air is essential for life. The increasing pollution since the start of industrialization has affected the quality of all three; however, the omnipresence of air makes quality control prior to human consumption considerably more challenging compared to food and water. Air quality control can help to identify long-term threats from hazardous substances. A distinction is often made between indoor air quality and ambient (or outdoor) air quality, with *indoor air quality* (IAQ) having a potentially larger impact on human health in developed countries due to people spending 80 % of their time indoors [92]. Outdoor pollutants will, however, also influence indoor pollution [93].

A review of significant pollutants of both indoor and outdoor air, including their health effects and exposure limit recommendations, is given in the *World Health Organization* (WHO) reports [93] and [94]. Inorganic pollutants like asbestos and heavy metal compounds as well as particulate matter are, while important factors for air quality, mostly irrelevant for chemical sensors. Thus, the reader is referred to the above-mentioned reports for further information about these substances.

Common outdoor pollutants besides particulate matter are SO_2, nitrogen dioxide (NO_2), and ozone (O_3), the main source of the first two being poorly controlled or treated exhaust gases [93]. Tropospheric ozone is mostly created from precursors like NO_x and VOCs under the influence of UV light, i. e., sunlight [95], [96]. Both short- and long-term exposure to all these substances have been linked to decreased lung function and other diseases of the respiratory system [93]. The guideline values in Table 1.1 have been chosen to stay well below (typically around 50 %) the lowest value which has shown adverse health effects in all studies reviewed in the WHO report.

While indoor air quality is affected by outdoor air pollution, there are specific indoor sources of contaminants which can lead to aggregation of hazardous substances in enclosed spaces. One which is specifically mentioned in [93] is tobacco smoke, a mixture of many substances causing, amongst others, lung cancer, cardiovascular disease, pneumonia, and bronchitis, even, and explicitly so, in the case of passive smoking. Tobacco smoke is listed as one of the main sources of indoor pollutants like benzene, formaldehyde (a carcinogen [99] and the most common indoor pollutant [100]–[102]), naphthalene, and carbon monoxide. Together with NO_2, these five compounds have been identified as the most hazardous out of a list of 40 candidates by the INDEX project [103]. Additional sources are combustion processes, evaporation of gasoline, and chemicals used in consumer products like solvents, paints, and the formerly common mothballs (naphthalene) [93], [94].

Table 1.1.: Exposure limits of common gaseous air pollutants.

substance	limit / µg/m^3	limit / ppb$_v$	remark	source
NO_2	200	97	one-hour average	[93]
NO_2	40	19	long-term	[97]
SO_2	125	40	24-hour average	[93]
SO_2	50	16	annual	[93]
O_3	120	56	<8 h per day	[93]
benzene	0	0	no safe limit	[93]
naphthalene	10	1.7	annual average	[94]
formaldehyde	100	74	30-min average	[93]
TVOC	200	-	long-term	[98]

Benzene, formaldehyde, and naphthalene are examples of VOCs, a loosely defined class of substances with sometimes serious effects on human health already at very low concentrations. VOCs have been linked to the sick building syndrome [104]–[106] causing eye and nose irritation, headache, and dizziness, amongst others. Additionally, like NO_x, they are a precursor for tropospheric ozone [95], [96]. The most prominent example is the genotoxic carcinogen benzene for which the WHO report does not give any safe exposure limit, but, instead, only a unit risk of leukemia of $6 \cdot 10^{-6}$ per 1 µg/m^3. Other VOCs, like ethanol for example, are relatively harmless and can be tolerated in the *parts per million* (ppm$_v$) range. The loose definitions of VOCs, ranging from boiling points [107], [108] over vapor pressures [109], [110] to participation in atmospheric photochemical reactions [110], [111] indicate a problem with the *total volatile organic compounds* (TVOC) value [112], [113] which has replaced carbon dioxide (CO_2) as the *de facto* standard indicator for IAQ. Introduced by Mølhave *et al.* in an experiment using a mixture of 22 VOCs [113], its universal use has since been criticized by many researchers including Mølhave himself [114], [115]. The original TVOC definition was the output of a *flame ionization detector* (FID) in mg/m^3 whereas the number of molecules could be more relevant [114]. Even then, the widely different hazardous potentials of VOCs (compare ethanol and benzene) are not accounted for in the TVOC value which is recognized in a newer definition [115] providing a list of known, hazardous VOCs. No effects on humans have been reported below 200 µg/m^3 TVOC [98].

As a simple working definition in this thesis, any organic gas except methane which can be generated at concentrations in the ppb$_v$ range at room temperature and atmospheric pressure shall be considered VOCs. This definition has a large overlap with the commonly cited WHO definition of VOCs which fixes the minimum and maximum boiling point of a VOC at 50 and 260 °C, respectively [107], [108], [116]. The definition also includes boiling points for *very* and *semi*-volatile organic compounds (above 0 °C and below 400 °C, respectively). Notably, the same standard which cites the WHO definition, ISO16000-6 [116], defines TVOC as the sum of all substances appearing between and including n-hexane and n-hexadecane when using a *gas chromatograph with mass spectrometer* (GC-MS) with a non-polar column. This excludes many substances which would be considered VOCs by most other definitions, like ethanol or formaldehyde. This discrepancy between defintions is one hurdle to overcome when bridging the gap between sensor science and analytical chemistry (cf. chapter 11).

IAQ monitoring can be used for demand-controlled ventilation to achieve a healthy indoor environment with optimized energy usage. Current systems, if at all, regulate the ventilation based on CO_2 [117] or TVOC measurements [118] and could save more energy if hazardous VOCs can be selectively detected and quantified.

1.3.4. Olfaction

Odor is a part of air quality: bad odors can cause discomfort and impede the quality of life. The sources of bad odors are manifold: from industrial facilities [119] over waste water treatment [120] and landfills [121] to farms [122]. Odor is, however, a subjective sensation interpreted by the brain based on complex biochemical interactions between dozens of compounds. Many compounds are not chemically similar, but have a similar smell, e. g., sulfur-containing compounds. Moreover, the human odor threshold for some substances is in the *parts per trillion* (ppt_v) range [123]. All this makes odor detection with gas sensors a great challenge. Indeed, the only European norms for the determination of odor and concentration are based on human panels. In EN13725:2003, [124], dynamic olfactometry is used where an air sample is diluted until a human tester cannot perceive any odor anymore. The dilution then relates the gas concentration to the *odor unit* (ou), where 1 ou/m^3 is the threshold where the average tester does just not perceive any odor. The norms EN16841-1/2:2016 [125], [126] define odor detection in the field through a human panel with either a grid approach or following the odor plume from a source. These tests are tedious and expensive, not only due to the personnel effort, and can never provide a continuous monitoring. Especially the latter is, however, very important if odor events are seldom. Hence, sensor systems for odor detection, classification, and quantification are desirable as replacement of, or supplement to, human panels.

Many works have supposedly shown successful classification of odors of coffee, olive oil, or fruits [127]–[131]. However, in all cases the terms odor and compound are used interchangeably, ignoring the fact that different compounds can have similar smells or *vice versa*. Thus, true odor classification remains a challenge.

1.3.5. Health

Studies have conclusively shown that dogs can be trained to identify many different types of cancer [132], including lung [133], gastric [134], prostate [135], and bladder [136], in human urine or breath samples, suggesting that the presence of cancer and diseases in general, even including epileptic seizures [137], is associated with certain VOC markers. Identification and the ability to measure these markers would have huge implications on routine screenings and facilitate early detection of diseases.

For diabetes, acetone has long been identified as marker gas [138]. Its concentration in human breath ($< 900\,\mathrm{ppb_v}$ for healthy individuals [139]) at least doubles for diabetes patients. A commercially available, reliable sensor system could replace the current, blood-based testing with a non-invasive method. Many other markers have already been identified, e. g., NO for asthma and NH_3 for liver and kidney malfunction [140]. Recently, an ingestible sensor pill was developed and tested for gas composition measurements directly in the guts [141].

1.4. Sensor systems and measurement chain

In this work, the term *sensor system* shall refer to one or more sensor elements integrated with the required mechanical construction, electronics, and possibly software to operate the sensor in the intended way and produce a useful output. This definition, like the distinction between sensor and instrument, is not clear-cut, with sensor systems residing between sensors and instruments. Hence, a sensor system is part of the measurement chain which starts with an analyte concentration being converted to an electric signal through a sensor. This signal is then, usually, converted from analog to digital and, especially if a sensor array or virtual multisensor is used, processed further by software. This thesis consists of three parts, each of which focuses on a different element in this measurement chain.

Part I introduces the basics of multivariate signal processing, machine learning, and pattern recognition. A MATLAB-based software called DAV^{3}E is presented which integrates many new processing strategies specific to cyclic operation into one easy-to-use toolbox. Data fusion algorithms and model selection criteria are investigated based on simulated and real datasets, as well as strategies pointed out to avoid wrong results during validation and testing. Further application examples are the results presented in the other parts of the thesis.

Part II, after a short introduction to gas-sensitive field-effect devices, reports on improvements made regarding the performance, especially selectivity, of SiC-FET sensors through WO_3 as a new insulator material. A simple model is proposed and verified explaining the effects observed during gate bias cycling with and without light exposure.

Part III focuses on the efficient generation of stable analyte concentrations and mixtures for sensor calibration with rigorous error propagation. This includes software to control and model the calibration equipment as well as a a novel gas sensor calibration strategy. In addition, the results of an interlaboratory study and a field test are presented and discussed.

Part I.

Data evaluation

2. Multivariate data and data-driven models

As mentioned in the introduction, virtual or real sensor arrays are often used to improve the selectivity of chemical sensors. With only one sensor in static operation, its output value usually corresponds directly to the measurand. Sensor arrays, on the other hand, produce multiple and up to several thousand data values for each sample, one value for each real or virtual sensor. The resulting signal patterns increase the amount of available information and, thus, enable identification and quantification of individual gases even in complex mixtures. The complexity of the reactions on the sensor surface as well as the variance in sensor manufacturing, however, hinder the development of a general, theoretical model. Instead, individually calibrated data-driven models are used to relate the observed patterns to type and concentration of certain compounds.

The following sections will cover basic concepts of this kind of multivariate data evaluation with a focus on sensor signals from dynamic operation. Extensive reviews and in-depth discussions of all these and many more concepts can be found in [142]–[144].

2.1. Nomenclature and data format

Throughout this work, all multivariate data will be considered to have the same format unless stated otherwise. This format is a numeric, two-dimensional $N \times M$ matrix $\mathbf{X}$ where rows correspond to *observations* and columns correspond to *features*[1] (Figure 2.1). Hence, each observation is a row vector of M feature values. In the case of a virtual multisensor, one observation is one cycle, so that the sensor system's effective sampling pe-

---

[1] The term *feature* can refer to one specific data value (categorical or numeric), the entirety of these values over all *observations* in the form of a vector, or to the method of extracting these values from a dataset. Taking face recognition as an example, "pupillary distance" could be a *feature*, as well as its realization, e. g., "60 mm" is a *feature (value)*. One *observation* is made up of several *feature values* extracted from the same face according to the methods defined by the *features*.

riod is the length of a cycle (in the range of 10 s to 10 min) while the actual sampling rate is usually much faster (Hz to kHz).

During training, i. e., fitting the model to a calibration dataset, the model establishes a relation between feature and target values. Target values are a column vector, categorical or numeric, containing the known label of each observation, e. g., a gas type or concentration. For categorical values, the categories are also called classes or groups.

$$\begin{array}{rc}
 & \begin{array}{cccc}\text{feature 1} & \text{feature 2} & \cdots & \text{feature } M\end{array} \\
\begin{array}{r}\text{observation 1}\\ \text{observation 2}\\ \vdots \\ \text{observation } N\end{array} & \begin{pmatrix} x_{1,1} & x_{1,2} & \cdots & x_{1,M} \\ x_{2,1} & x_{2,2} & \cdots & x_{2,M} \\ \vdots & \vdots & \ddots & \vdots \\ x_{N,1} & x_{N,2} & \cdots & x_{N,M} \end{pmatrix}
\end{array}$$

Figure 2.1.: General structure of multivariate data.

2.2. Preprocessing

Data preprocessing can serve several purposes. It is, first of all, used to remove obvious imperfections like outliers or missing data points from training data in order to omit a negative impact on model training. It can further be used to remove noise through cycle averaging or smoothing. Especially the latter must be done with caution as smoothing can alter the shape of a sensor cycle and, thus, the information contained within. Preprocessing is also used to highlight or suppress certain effects, e. g., by subtracting a reference cycle from all cycles to show only the differences and not the "large signal". It should be noted that this kind of preprocessing does not change the contained information because the reference signal is the same for each cycle. This is different for cycle-based preprocessing, e. g., dividing each cycle by its own mean value, an approach which has been used to suppress baseline drift or the reaction to humidity in MOS sensors [145]. The possibility of this kind of preprocessing is an additional strength of multivariate data compared to single values as each sample, i. e., cycle, potentially contains its own reference value.

2.3. Dimensionality reduction, feature extraction and selection

The number of features M can be interpreted as the dimensionality of a sample. While each dimension, i. e., feature, can potentially add information, too many dimensions lead to a multitude of adverse effects generally referred to as the *curse of dimensionality*, for example [142], [146]:

- The distance d between two arbitrary points approaches 1 for many dimensions M, i. e., $\lim_{M\to\infty} d = 1$, which makes distance-based classification impossible.

- Observations sample the feature space so that the sampling density approaches 0 for high dimensionality if the number of observations does not increase at least exponentially.

- When the number of observations equals (or exceeds) the number of features, i. e., $M = N$, each observation can be identified in one unique dimension, resulting in overfitting.

In order to omit these effects, the dimensionality of any dataset should be reduced as much as possible, but without the loss of important information, before it is used to train a classifier or regressor.

One approach to dimensionality reduction is feature extraction. This step is particularly important for cyclic data as it contains many strongly correlated data points. A cycle is typically comprised of hundreds or thousands of data points which are sampled in quick succession. Hence, in most instances, the value of a data point is strongly related to the value of the previous data point, reducing the effective amount of information but not the dimensionality. Feature extraction "concentrates" the available information in fewer dimensions. Methods achieving this on the whole cycle are, for example, Fourier analysis or wavelet transform, resulting in M' components, the new features, of decreasing importance. With the assumption that the main information is contained in the first components, all others can be discarded to achieve dimensionality reduction with little information loss[2]. A more manual method is the extraction of shape-describing features like mean value, slope or other fit parameters over certain parts of the cycle. This method uses humans natural ability for pattern recognition and can, thus, achieve better results than the previously mentioned, purely mathematical methods [145].

---

[2] This is similar to how the JPEG compression uses discrete cosine transformation and quantization matrices to discard small details.

A hybrid of both methods is the extraction of shape-describing features where the best segmentation of the cycle is found through algorithms like *adaptive linear approximation* (ALA) [147], [148], allowing for automation of the whole process. Instead of shape, features can also describe higher statistical moments, like variance or skewness [149], or other parameters of a cycle segment, even noise [150], as long as the resulting value is reproducible for the same experimental conditions.

Depending on the dataset, the dimensionality can still be too high after feature extraction. In these cases, feature selection can further reduce the dimensionality by identifying and discarding non-important features. A simple approach is the selection of features with high correlation to the target value [149]. However, the resulting features can then contain very similar and, therefore, redundant information. Such collinear features can even lead to instabilities in many subsequent algorithms. Moreover, interactions between features, i. e., when information is encoded in the combination of two features, cannot be identified. Feature selection can be done bottom-up or top-down, by building and testing a model, then adding (bottom-up) or removing (top-down) a feature, and keeping the new model if it performs better (bottom-up) or not significantly worse (top-down) than the previous one. This approach, however, can take a considerable amount of computing time for large feature sets. Automatic feature selection methods like *recursive feature elimination support vector machine* (RFESVM) for linear separability [151] and ReliefF for non-linear separability [152] have shown good performance on many different datasets [148].

Finally, the third type of dimensionality reduction, and the one which is usually meant in literature when using this term, is based on multivariate statistical methods projecting the data into a new subspace, the most popular of which are *principal component analysis* (PCA) and *canonical discriminant analysis* (CDA). The latter is usually called *linear discriminant analysis* (LDA) in literature which is, however, confusing given the fact that there is a classifier with the same name. The original LDA algorithm described by Fisher [153] was a combination of dimensionality reduction to one dimension and subsequent classification. This algorithm has later been extended for multi-class problems in higher dimensions, and especially the dimensionality reduction part, i. e., CDA, is often used by itself for visualization purposes. Both methods use statistics to reduce the dimension of extracted features even further, often to one, two, or three dimensions due to the simple visualization. PCA is unsupervised, i. e., it operates on the data only, without knowledge of the target values. It projects the data into a new, orthogonal *principal component* (PC) space where the largest variance lies along the first axis, the second-largest along the second axis, and so on. CDA, on the other hand, is supervised and can, thus, use the target values to achieve better class separation. It minimizes the ratio of interclass variance to intraclass variance to arrive at a projection with compact, separated clusters in a new *discriminant function* (DF) space. Both methods can at most produce M dimensions, while the number of dimensions for CDA must, additionally, be less or equal than the number of classes minus 1[3]. Both algorithms achieve dimensionality reduction, similar to Fourier analysis, by discarding higher dimensions containing only noise. Both PCA and CDA produce one set of M coefficients (*loadings*) $\boldsymbol{c}$ per dimension, so that the projected data points (*scores*) $\boldsymbol{x}_{\text{score}}$ can be computed as the scalar product, or linear combination, of feature values $\boldsymbol{x}$ and coefficients values $\boldsymbol{c}$. Written as matrices to account for arbitrary numbers of dimensions and observations, the scores are computed as:

$$\mathbf{X}_{\text{score}} = \mathbf{X} \cdot \mathbf{C} \tag{2.1}$$

2.4. Classification and quantification

Classification or quantification of unknown observations is the ultimate goal of any model. All of the steps discussed in the previous sections only prepare the data which are eventually fed to a classifier or regressor. It is important to distinguish between classification and quantification problems as they answer different questions. This influences the choice of algorithms as well as experimental design. Note that there are additional algorithm families like clustering [142] or novelty detection [154]. Their goal is to find structures in unlabeled datasets (clustering) or to identify new types of observations which cannot be classified with the current model (novelty detection).

Classification assigns one category from a predefined set to each observation. An example is the inference of the type of activity (sitting, standing, walking, etc.) from smartphone sensor data [155]. For gas sensors, classification could determine whether the current atmosphere is oxidizing or reducing, or the type of one and only one currently present gas. The latter problem, however, cannot be applied to many real-life scenarios since, most often, gas mixtures of several compounds and concentrations are present. This disqualifies the use of a classification algorithm as gas concentrations may assume an infinite number of values which would require an infinite number of classes to represent, defeating the purpose of classification. Instead, a regression algorithm should be used to determine the concentration

---

[3] Higher dimensions are meaningless. When two classes are separated in two dimensions, a line between the class centroids defines a new, one-dimensional space with equally good separation.

of one or several target compounds. From the predicted concentration, a classification in the sense of alarm/no alarm is easily achieved by setting a threshold value.

One of the simplest classifiers is the distance to group centroids, i. e., the group centroids (in the reduced feature space) are the parameters determined during the training, and new observations are classified as the group closest to a new observation. Variations are possible with different distance metrics like Euclidean, Mahalanobis, Manhattan, or others. The *k nearest neighbors* (knn) classifier finds the *k* observations in the training dataset closest to the new observation, and classifies it as the group to which most of the neighbors belong. As mentioned before, the original LDA algorithm is now usually split into CDA[4] for dimensionality reduction and LDA for classification. It assumes normal distribution of the classes and, from this, creates linear boundaries which minimize the chance of picking the wrong class. This normality assumption is usually violated in real data, e. g., if the classes consist of sub-classes. While LDA is generally quite robust against violation of this assumption, it can sometimes be beneficial to chose a classifier like *logistic regression* (LR) that does not make any assumptions about the data. During training, it finds a set of coefficients which project the observations on a probability scale from 0 to 1 determining class membership. The output of a probability measure and the robustness against collinear features are additional advantages. A *support vector machine* (SVM) finds hyperplanes between classes, similar to LDA, but, instead of assuming normal distribution, fits the hyperplane so that the distance between hyperplane and class boundaries becomes as large as possible. Using suitable kernel functions, SVMs can be extended to non-linear classification problems. Also *artificial neural networks* (ANNs) enable non-linear classification which is heavily used in the recent deep learning approaches. They are, however, a black box [156] and need much training data due to their high flexibility. It should be noted that this flexibility makes them more prone to overfitting.

The *de facto* standard for quantification in chemosensing is *partial least squares regression* (PLSR) [142], [157], a linear regressor. It accepts multiple independent variables, i. e., features, and eliminates the instability often arising in *multiple linear regression* (MLR) from collinear features by a built-in dimensionality reduction similar to PCA, but with respect to maintaining a good linear model. In this respect, the acronym PLS is sometimes also interpreted as *projection to latent structures*, i. e., PLSR identifies the “true” (latent) variables and uses them for the regression. It can fit multiple targets at the same time and find the best compromise. Another algorithm is called

---

[4] Which is usually also referred to as LDA.

Elastic Net [158]. It generalizes the LASSO (least absolute shrinkage and selection operator) [159] and *ridge regression* [160], both of which can be used for implicit feature selection through a penalty term in the cost function which discourages the addition of features (*regularization*). All of these regressors determine one set of coefficients so that the prediction for a new observation can be directly computed as in Equation 2.1.

Both classification and quantification algorithms have the goal of minimizing the respective error. For classification, the error is usually given in percent of misclassified samples. The error of quantification, i. e., regression, can be given in several measures like the *coefficient of determination*, R^2, or the *mean square error* (MSE). In this work, errors will always be given as *root mean square error* (RMSE) as it has the same unit as the target and can be interpreted as *standard deviation* (std). The RMSE is computed from the differences between actual values x and predicted values $\hat{x}$:

$$\mathrm{RMSE} = \sqrt{\frac{1}{N}\sum_{i=1}^{N}(x-\hat{x})^2} \tag{2.2}$$

Note that both classifiers and regressors are always supervised, i. e., they require a training phase where they establish the relationship between input and desired outcome. This makes them prone to overfitting.

2.5. Training, validation, and testing

So far, only the *training* phase of model building has been considered. However, there are another two equally important phases, *validation* and *testing*, to make sure that the model generalizes well and can predict new data accurately [144]. Each of the three phases has a distinct purpose:

- training determines the model's parameters
- validation determines the model's hyperparameters
- testing checks the model's performance on new data

The term parameters refers to internal parameters of the model, e. g., the coefficients of CDA, PCA, or PLSR. Hyperparameters, on the other hand, are external parameters, e. g., the number of neighbors in knn or the number of dimensions/latent variables for CDA, PCA, or PLSR. The wrong choice of hyperparameters leads to either an under- or overfitted model, both of which diminishes its prediction performance. Therefore, a trained model must be validated with a new, independent dataset to determine the optimal values of all hyperparameters. As a rule of thumb, the hyperparameter value resulting in the smallest validation error should be chosen (see also section 3.9.3). However, in doing so, the hyperparameters are tuned so that the model performs well on the validation dataset which, again, can lead to overfitting. Hence, a third step with a third independent dataset, testing, is necessary to assess the model's true performance on new data. Further sources of overfitting are discussed in chapter 9.

Data generation is usually expensive in regards of time, money, personnel effort, and other resources. Consequently, people often hesitate to set aside portions of their dataset for validation and testing since only training data actually improve the true model performance. There are, however, methods to produce synthetic validation and testing datasets[5]. One of the most common is k-fold [144], [161]. It divides the dataset randomly into k parts, then uses $k-1$ to train a model, and the remaining part to determine the validation or testing error. This is done k times until each part had been left out once. The parts are usually chosen *stratified* to approximately represent the ratio of classes in the whole dataset. A special case of k-fold is leave-one-out where $k = N$, i. e., in each fold, only one point is left out. Leave-one-out is advantageous for very small datasets, but has shown no benefits for larger datasets compared to 10-fold [161]. All methods creating synthetic datasets usually have a slight pessimistic bias, i. e., the resulting error is larger than the actual average error of the model on new data, because fewer training data are available. Larger k values decrease this bias, but increase the variance (of outcomes between folds) as the smaller number of tested points increases the impact of misclassifications. The variance can be reduced through several iterations of k-fold, but it has been argued that the error is often dominated by the bias [162].

---

[5] Potentially, even synthetic training datasets can be generated. This can decrease the cost considerably, but must always be weighed against the loss of real-world information. An example for synthetic data generation is shown in section 3.8.2. The novel calibration method described in chapter 13 could be used to determine some basic parameters for the simulation, e. g., correlation coefficients of a real sensor device, relatively quickly. In addition to efficient dataset generation, synthetic data can also simulate conditions difficult to control in a lab setting, like drift or certain device failures.

3. DAV^{3}E

3.1. History and motivation

DAV^{3}E (Data Analysis and Verification/Visualization/Validation Environment) is the latest iteration of MATLAB-based software tools for sensor data evaluation at the *Lab for Measurement Technology* (LMT). It has replaced the *LDAPCAGUI* for classification model building and validation, the *FEGUI* for feature extraction as well as the *RegressGUI* for regression model building and validation. *FEGUI* and *RegressGUI* had been developed by the author of this thesis in a seminar work and Master's thesis, respectively, under supervision of Christian Bur. Having one integrated tool instead of three separate ones significantly increases the speed of the often tedious trial-and-error process in multivariate data evaluation. Moreover, in comparison to the older tools, DAV^{3}E is completely object-oriented, has a clean and maintainable interface, can be used with either *graphical user interface* (GUI) or command line, and implements new, user-friendly concepts like semi-automatic data fusion.

There are many commercial or open-source software tools already available which enable sophisticated data evaluation with a plethora of methods and algorithms. Commercial programs (closed-source) include *SPSS Statistics* (IBM), *Minitab* (Minitab, Inc.), *Statistica* (StatSoft), to mention only a few examples. Open-source alternatives include *Weka* (University of Waikato) as well as libraries like *scikit-learn* for Python or dedicated programming languages like *R* (The R Foundation). Both *scikit-learn* and *R* can be extended with third-party GUIs like *orange* (University of Ljubljana) and *RStudio* (RStudio).

However, virtually all of these tools assume a feature matrix as input, i. e., the important step of feature extraction is often skipped. If it is implemented, it usually provides only mathematical feature extraction methods like Fourier analysis. Recent works have, however, shown that shape-describing features in combination with knowledge from a simple, physical sensor model can give excellent model performance [58], [163], [164]. The physical model predicts, in this case, that certain segments of the cycle will change their slope depending on gas concentration, information which can be easily extracted graphically with shape-describing features, but hardly with Fourier analysis. This is why DAV^{3}E provides manual and automatic graphical feature extraction methods and emphasizes the importance of visualizing data in an interactive way to quickly identify issues in large datasets. It provides an easy means of annotating data from different, non-synchronized systems with potentially different sampling rates and cycle lengths, as well as cycle-based preprocessing, fusion, and validation methods missing from other software tools. Especially visualization as well as robust and capable validation and testing methods are often neglected in machine learning which has led to the publication of many peer-reviewed articles presenting models with significant, but hard to detect, overfitting [165].

The following sections describe the main concepts and features of the most recent version of DAV^{3}E published open-source under the GNU *Affero General Public License* (AGPL) license [166]. This version was written entirely from scratch based on the previous version described in [167]. The author would like to thank Tobias Baur for considerable contributions to concept and code of the older version as well as valuable discussions during the rewriting process. Further thanks to Tizian Schneider and Jannis Morsch for implementing the automatic feature extraction and selection methods.

3.2. General programmatic concepts

One goal during the development of the toolbox was to enable easy extendability with basic MATLAB proficiency. MATLAB was chosen as programming language because it is widely used in engineering, has an easy-to-learn syntax, and is much easier to set up and maintain than other frameworks, like Python, for the average user. It further provides many features of *object-oriented programming* (OOP) which is key to writing extensible software.

DAV^{3}E provides two interfaces for extension: *modules* to extend the GUI, and *plug-ins* to extend the functionality. Six modules are implemented in the current version:

- *Start* acts as welcome screen.
- *Preprocessing* visualizes cycles and quasistatic signals and enables creation of arbitrary preprocessing chains.
- *CycleRanges* enables cycle-wise data selection.
- *Grouping* enables preparation of data annotation and target vectors for different problems.

- *FeatureDefinition* visualizes group-wise cycle shapes and enables graphical feature extraction and preview.
- *Model* enables building, training, validation, testing, and visualization of the results of data-driven models.

Figure 3.1 shows the main GUI containing the Start module within the red, dotted rectangle. The module can be changed by clicking a button on the left side. The bottom table displays all sensors in the project and allows changing the currently displayed sensor data as well as the sensor's properties.

A module is derived from a module base class and defines its GUI elements and how they can be used to display or alter the underlying data. However, it never defines functions acting on the data. Instead, this is done in plug-ins of which there are currently 14 different types:

- RawDataImport: file import methods
- VirtualSensor: functions to create virtual sensors from real sensors
- RawDataPreprocessing: cycle-based preprocessing methods

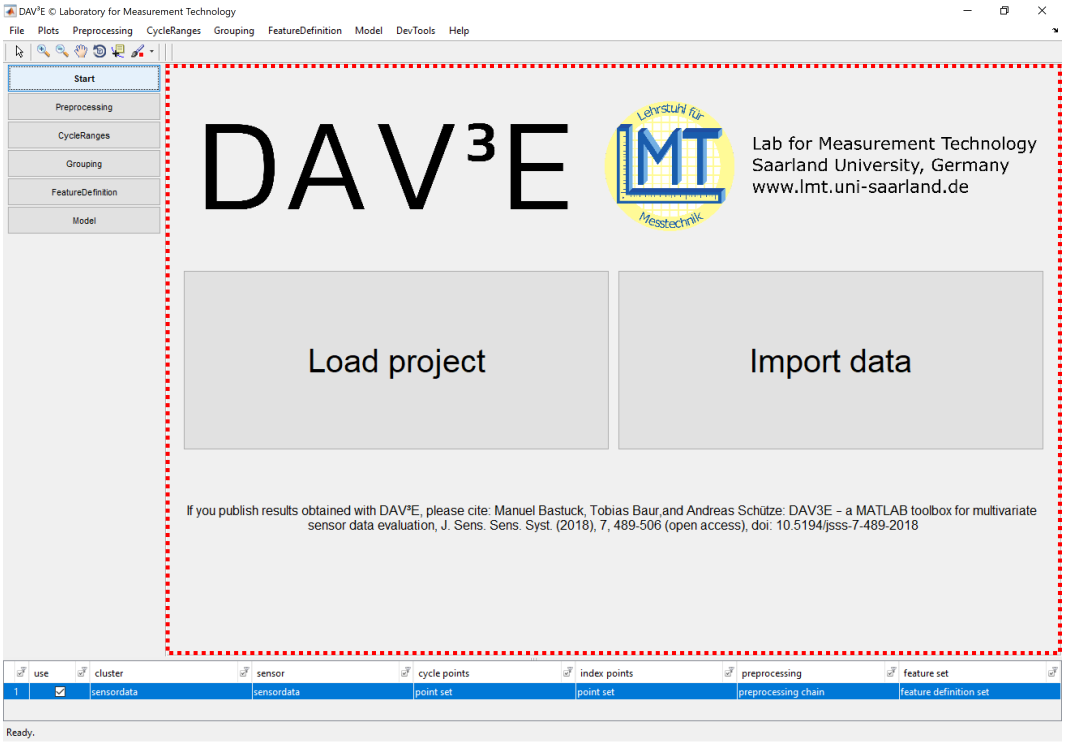

If you publish results obtained with DAV³E, please cite: Manuel Bastuck, Tobias Baur,and Andreas Schütze: DAV3E – a MATLAB toolbox for multivariate sensor data evaluation, J. Sens. Sens. Syst. (2018), 7, 489-506 (open access), doi: 10.5194/jsss-7-489-2018

	use	cluster	sensor	cycle points	index points	preprocessing	feature set
1	☑	sensordata	sensordata	point set	point set	preprocessing chain	feature definition set

Ready.

Figure 3.1.: DAV^{3}E's main GUI, here showing the *Start* module.

- FeatureCycleAverage: methods to compute average cycles
- FeatureExtraction: feature extraction methods
- Annotation: selects data and annotation to use in a model
- DataReduction: data reduction and augmentation algorithms
- FeaturePreprocessing: feature preprocessing methods
- TargetPreprocessing: target preprocessing methods (and inversion)
- DimensionalityReduction: dimensionality reduction algorithms
- Classification: classification algorithms
- Regression: regression algorithms
- Validation: validation dataset generation methods
- Testing: testing dataset generation methods

Plug-ins are a collection of functions which are used at runtime to initialize `DataProcessingBlock` objects. This results in a very easy syntax and almost no overhead in the actual plug-in file so that no understanding of OOP or other, more advanced, programming concepts is necessary. Each plug-in has, at least, a name, description, and an `apply` function. Depending on the type, other properties or predefined functions like `train` or `revert` (to transform predictions of a model trained on a preprocessed target back to the original scale) can be required. Plug-ins are the building blocks of the entire data evaluation chain, as outlined in Figure 3.2 and Figure 3.3, where also a list of all currently implemented plug-in functions is found.

Plug-in functions are usually supplied with a `Data` object and a `struct` of parameters (if applicable). A `Data` object can be generated from a `Sensor` and, stores, besides the data matrix, meta-data like real cycle number and start time for each row as well as selected cycles and features, amongst others. It also generates mutually exclusive training, validation, and testing datasets and stores model predictions and errors for each of these datasets. When used in a `Model` object, a `Data` object further keeps track of the current phase (training, validation, testing) as well as fold and iteration where applicable, so that simply calling `getSelectedData()` on the `Data` object supplied to a plug-in function always returns the correct part of the dataset which can then be directly used in the actual implementation of the algorithm. This kind of internal handling removes a great potential for errors from the plug-ins and lets the user focus on the implementation of the algorithm instead of program logic.

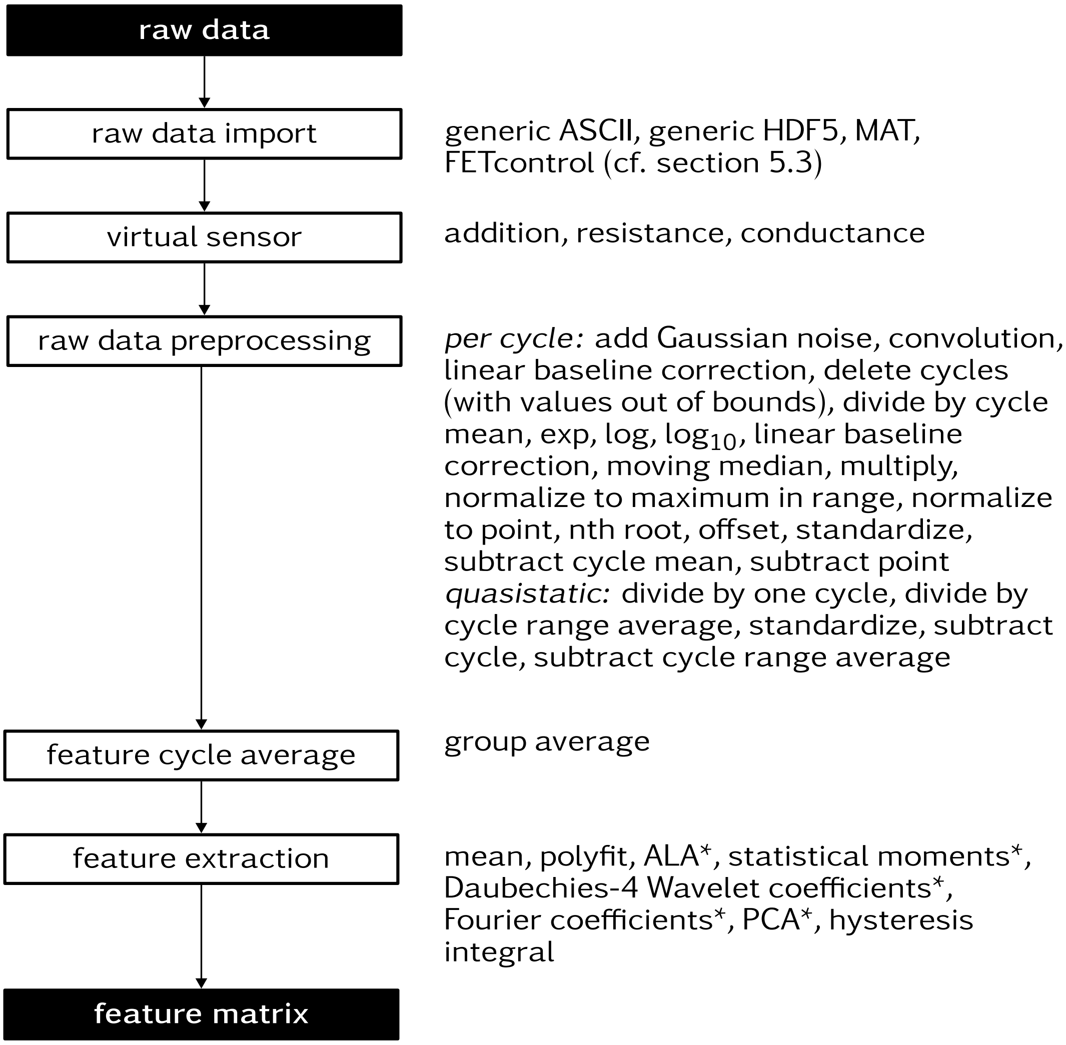

Figure 3.2.: The workflow in DAV^{3}E from raw data to a feature matrix which is then used to build a model (cf. Figure 3.3). In comparison with Figure 3.3, the number of currently implemented methods (on the right) shows that this part of the data evaluation chain is the main focus in DAV^{3}E. Note that quasistatic preprocessing cannot or may not be used to improve the model performance since they can only be applied to finished measurements. Methods marked with * have been implemented by Tizian Schneider and Jannis Morsch as described in [168].

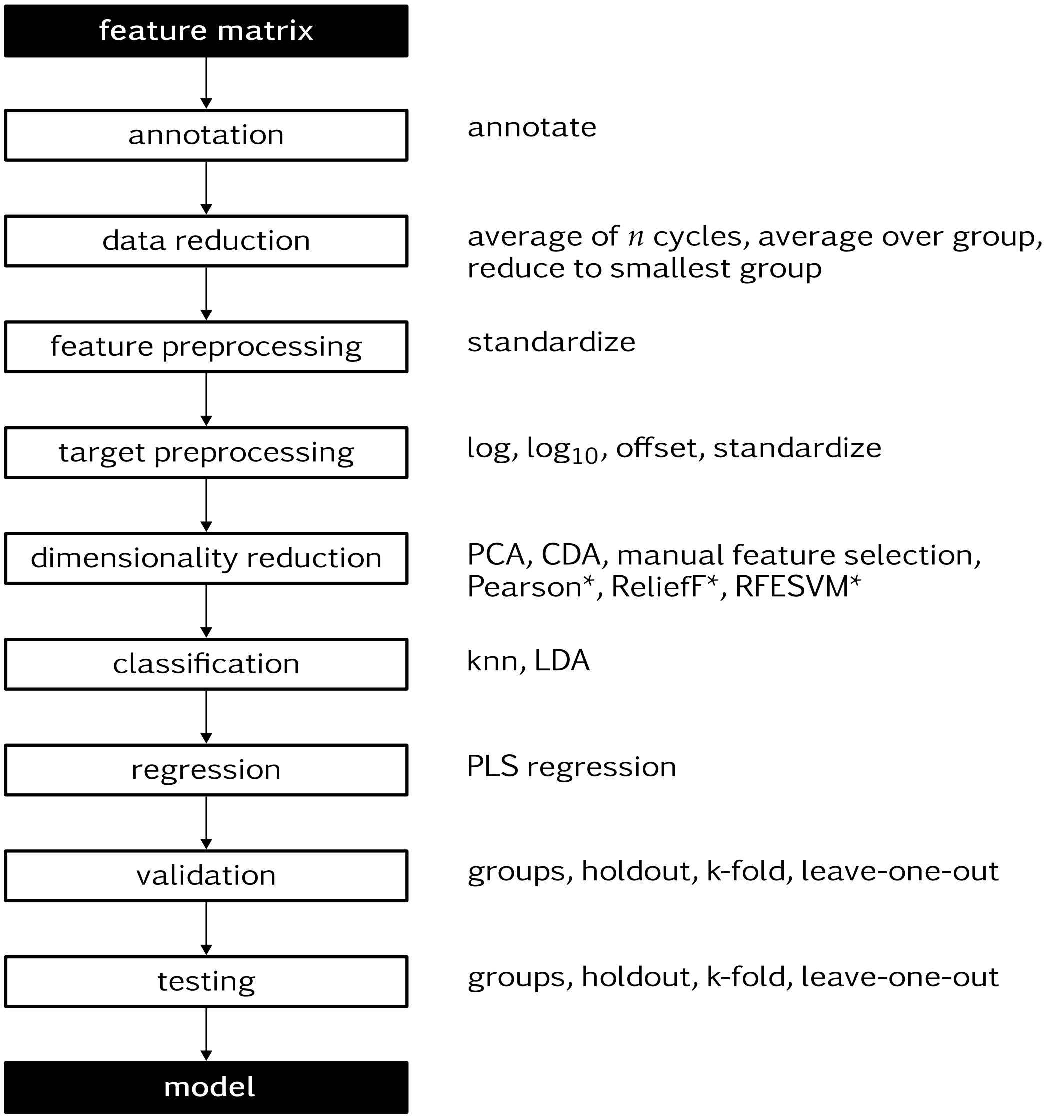

Figure 3.3.: The workflow in DAV^{3}E from the feature matrix (cf. Figure 3.2) to a model, with currently implemented methods on the right. Many steps, e. g., preprocessing, are optional or are usually not used together, e. g., classification and regression. A custom workflow can be created from these building blocks in the GUI or command-line. Methods marked with * have been implemented by Tizian Schneider and Jannis Morsch as described in [168].

3.3. Data structure

DAV^{3}E structures data into `Sensors` and `Clusters`. A `Sensor` is the smallest unit of data and represents one numeric data matrix with N rows and M columns. Each row corresponds to one observation (or cycle), and each column to one data point (or feature). Each `Sensor` can be assigned an individual *preprocessing chain*, *cycle point set*, *index point set*, and *feature definition set*, as described in section 3.6. Moreover, any `Sensor` can serve as the abscissa of another `Sensor`. This is, for example, useful for impedance spectroscopy data which typically results in three `Sensors`, i. e., data matrices: frequency, real part, and imaginary part. Real and imaginary part can have the frequency as abscissa, or the real part can be chosen as the abscissa of the imaginary part to produce a Nyquist plot. By default, sensor data are plotted over time or data points.

The time of each data value is dynamically computed from the given sampling period which is, together with the time offset, stored in the `Cluster` containing the respective `Sensors`. The `Cluster` class is only a helper structure and not strictly necessary, but is has proven useful for real data. This is because most instruments put out more than one data stream: a sourcemeter, for example, measures time, voltage, and current, resulting in three `Sensors` with identical sampling periods and time offsets. A `Cluster` thus groups `Sensors` from the same source and ensures they are always treated in the same way.

The previous version of DAV^{3}E also defined `Measurements` as a structure containing a group of `Clusters` which happened during the same time. It was intended to facilitate data fusion as all `Clusters` within one measurement could automatically be fused in parallel, and all `measurements` in series (see also section 3.8). This mechanism turned out to be too inflexible for many real-world datasets and was replaced with the *track system* in the new version (cf. section 3.8.1).

3.4. Interactive visualization

Large amounts of training data are required to build a data-driven model. Visualizing these data at each processing step helps to detect errors or outliers in the measurement, selecting better features, and interpreting the results. Graphics and pictures can convey information much more efficiently than tables or numbers, especially if individual data values are of less importance than overall data integrity. Added interactivity, i. e., the ability to change plots instantly to look at different aspects of the data, eventually helps to make otherwise opaque datasets more transparent and get a better "feel" for the data. Data-driven modeling contains many pitfalls, like overfitting, easily leading to deceivingly and only seemingly good results. Such results can only be critically questioned if, for instance, through interactive data visualization, a realistic estimate about the data's quality can be made.

Many plots are specific to certain methods and algorithms and will, rather than here, be explained when they are actually used in this thesis. There are, however, some very general plots related to multivariate data analysis and certain families of algorithms which shall be presented in the following paragraphs.

The first is a pair of two plots, quasistatic and cyclic plot. These plots can visualize both dimensions of a data matrix which is very useful for cyclic data in particular. The idea for these plots predates the *FEGUI*; however, the added interactivity in DAV^{3}E was a big improvement to usability and ease of use. The general principle is shown in Figure 3.4. The quasistatic plot shows the same point in each cycle one after the other, creating a signal as if the sensor was driven statically at the selected point of the cycle. In Figure 3.4, two working points have been selected, one in the middle of the cycle and one between the middle and the end, resulting in two quasistatic signals which show, for a temperature cycle, the sensor's gas response at two different temperatures. In the other dimension, particular cycles can be selected, e. g., one before a gas exposure (gray), one during exposure to gas A (green), and a third during exposure to gas B (orange). This allows easy comparison of the cycle shapes in different atmospheres. The two plots are co-dependent as the selection of what to show in one plot is done in the other plot, respectively.

Considering the actual implementation in Figure 3.5a, the vertical lines in the top plot can be added (double-click), removed (right-click) and moved (drag) with the mouse to select which cycles to show in the bottom plot as indicated by the color coding. Similarly, the vertical lines in the bottom plot determine the points in the cycle used to create the quasistatic signals in the top plot. The data shown in Figure 3.4 and Figure 3.5a are the same, only zoomed and cropped to cycles from 830 to 1080 for clarity in Figure 3.4. This plot pair is implemented in DAV^{3}E's *Preprocessing* module so that the effectiveness of the applied preprocessing can be determined immediately.

Another pair of plots newly introduced in DAV^{3}E appears in the *Feature-Definition* module Figure 3.5b. As before, the bottom plot shows cycles. Each cycle is, however, the average of many cycles as defined by a grouping (see section 3.5). Averaging reduces noise and can highlight identical parts in all considered cycles, eventually helping to select good features. Feature selection is done by first choosing the desired extraction method, e. g., *mean* or *polynomial fit*, and then using the mouse to draw ranges over parts of the cycle where this method shall be evaluated. In the example, the slope is computed as the non-constant coefficient of a first-order polynomial fit in ten equidistant ranges. The features are immediately extracted from the averaged cycles and their values centered and plotted over the span of the respective range in the top plot. This quick feedback showing the spread (for classification) or order (for quantification) of feature values aids range selection and can help novices understanding the step from cycles to features.

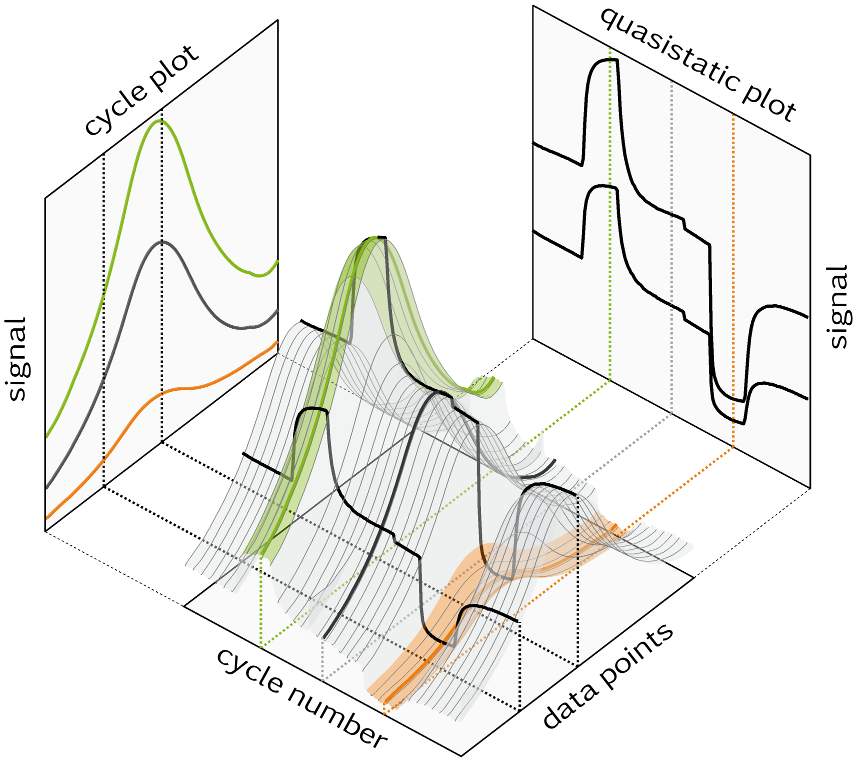

Figure 3.4.: Three-dimensional representation of a data matrix as in Figure 2.1 for cyclic data and the projections on both dimensions.

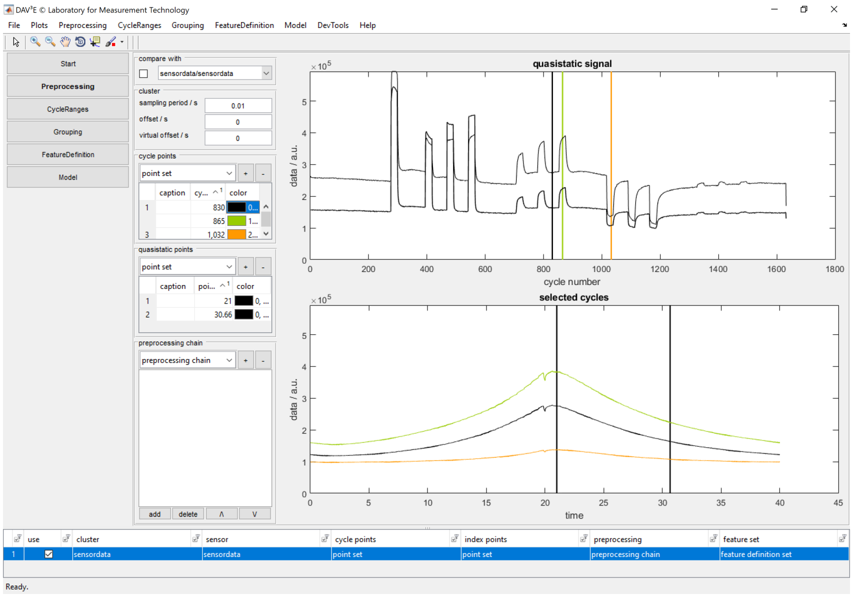

☐ compare with: sensordata/sensordata

sampling period / s: 0.01

offset / s: 0

virtual offset / s: 0

cycle points: point set

	caption	cy...	color
1		830	0...
		865	1...
3		1,032	2...

quasistatic points: point set

	caption	poi...	color
1		21	0, ...
2		30.66	0, ...

preprocessing chain: preprocessing chain

	use	cluster	sensor	cycle points	index points	preprocessing	feature set
1	☑	sensordata	sensordata	point set	point set	preprocessing chain	feature definition set

(a) *Preprocessing* module implementing the projected plots from Figure 3.4.

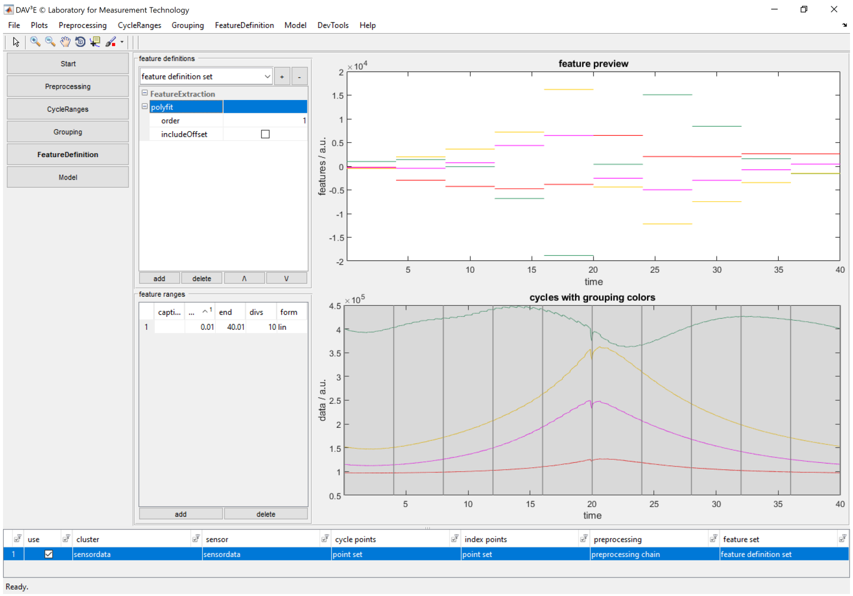

feature definitions: feature definition set

FeatureExtraction
- polyfit
  - order: 1
  - includeOffset: ☐

	capti...	...	end	divs	form
1		0.01	40.01	10	lin

	use	cluster	sensor	cycle points	index points	preprocessing	feature set
1	☑	sensordata	sensordata	point set	point set	preprocessing chain	feature definition set

(b) *FeatureDefinition* module enabling graphic feature extraction and feature preview.

Figure 3.5.: *Preprocessing* and *FeatureDefinition* modules in DAV^{3}E.

3.5. Data selection and annotation

In many cases, not all the data recorded during an experiment are to be included in the modeling process. Outliers, defects, and data recorded in undefined conditions, for example, ought to be be excluded. Especially the latter is a common occurrence with gas sensor data, as changing the gas atmosphere can take minutes depending on chamber volume and gas “stickiness”. Therefore, the gas mixing system and the sensor system run in parallel without interruption, and the sensor cycles which were recorded in equilibrated gas conditions are identified after the experiment. Both systems usually run independently since the amount of work necessary to couple and perfectly synchronize both systems in software rarely outweighs the gain, especially when many different experimental sensor systems are used. Efforts for interface standardization have started recently at LMT, but are not easily transferable when sensor systems are to be tested in other labs.

Selecting sensor cycles of interest is done in the *CycleRanges* module (Figure 3.6a). It displays the quasistatic signal chosen in the *Preprocessing* module as orientation: in most cases, gas exposures are clearly visible here. The user can then either define *ranges of interest* (ROIs) with the mouse or load them from a *JavaScript object notation* (JSON) file if such a file has been created by the gas mixing system. In most cases, however, manual changes are still necessary even with loaded ranges to account for long fluidic time constants. To this end, range batch processing is implemented in DAV^{3}E to, e. g., delay the start of each range for a certain number of cycles.

In the next module, *Grouping* (Figure 3.6b), a label can be assigned to each range which is then automatically assigned to each cycle in this range, creating a target vector to train the model. For classification, the label name is arbitrary; for quantification, it must be numeric. One set of labels is referred to as *grouping*, and an arbitrary number of groupings can be created. For example, one grouping can label each range with the name of the test gas present to train a classification model, whereas a second grouping could encode the concentration in ppm_v of one specific test gas in all ranges to achieve selective quantification. One grouping can be used to filter another grouping which is especially useful for gas mixtures, e. g., if a model shall only be trained with data where *relative humidity* (RH) was above 50 %. The label `<ignore>` excludes all contained cycles from the dataset, e. g., to ignore all data recorded below 50 %RH. Additionally, labels can be marked with an arbitrary number of trailing asterisks, e. g., `A`, `A*`, and `A**`. Internally, all three labels would be handled as `A`, however, when choosing groups, they are shown as three distinct labels to the user. This makes it possible to use one portion of data for training, and another, well-defined portion, for validation

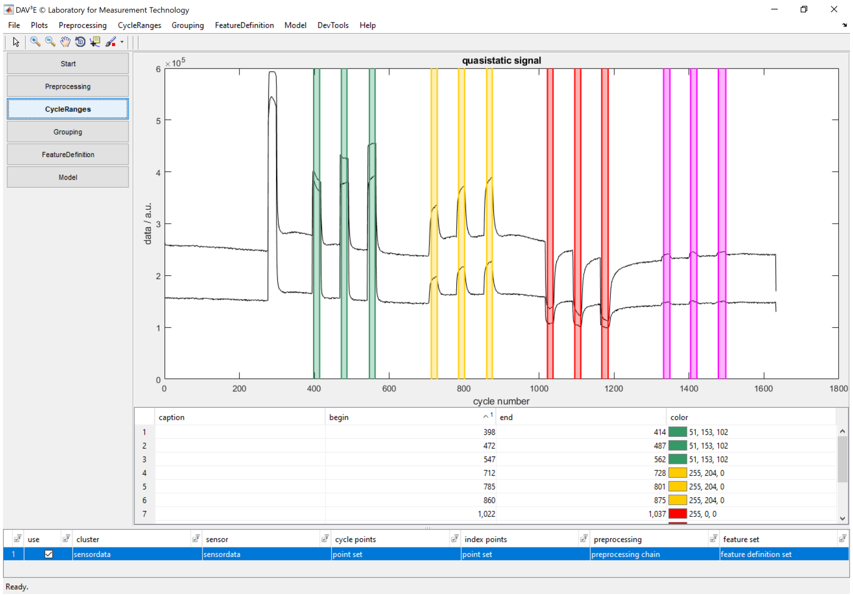

	caption	begin	end	color
1		398	414	🟩 51, 153, 102
2		472	487	🟩 51, 153, 102
3		547	562	🟩 51, 153, 102
4		712	728	🟨 255, 204, 0
5		785	801	🟨 255, 204, 0
6		860	875	🟨 255, 204, 0
7		1,022	1,037	🟥 255, 0, 0

	use	cluster	sensor	cycle points	index points	preprocessing	feature set
1	☑	sensordata	sensordata	point set	point set	preprocessing chain	feature definition set

Ready.

(a) *CycleRange* module displaying quasistatic signals as guide to select ranges of consecutive cycles in similar experimental conditions.

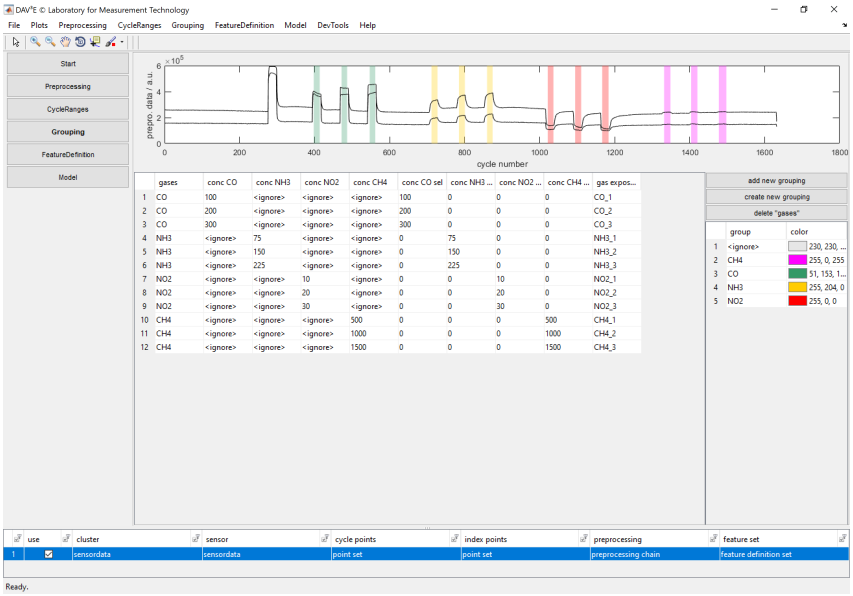

	gases	conc CO	conc NH3	conc NO2	conc CH4	conc CO sel	conc NH3 ...	conc NO2 ...	conc CH4 ...	gas expos...
1	CO	100	<ignore>	<ignore>	<ignore>	100	0	0	0	CO_1
2	CO	200	<ignore>	<ignore>	<ignore>	200	0	0	0	CO_2
3	CO	300	<ignore>	<ignore>	<ignore>	300	0	0	0	CO_3
4	NH3	<ignore>	75	<ignore>	<ignore>	0	75	0	0	NH3_1
5	NH3	<ignore>	150	<ignore>	<ignore>	0	150	0	0	NH3_2
6	NH3	<ignore>	225	<ignore>	<ignore>	0	225	0	0	NH3_3
7	NO2	<ignore>	<ignore>	10	<ignore>	0	0	10	0	NO2_1
8	NO2	<ignore>	<ignore>	20	<ignore>	0	0	20	0	NO2_2
9	NO2	<ignore>	<ignore>	30	<ignore>	0	0	30	0	NO2_3
10	CH4	<ignore>	<ignore>	<ignore>	500	0	0	0	500	CH4_1
11	CH4	<ignore>	<ignore>	<ignore>	1000	0	0	0	1000	CH4_2
12	CH4	<ignore>	<ignore>	<ignore>	1500	0	0	0	1500	CH4_3

	group	color
1	<ignore>	⬜ 230, 230, ...
2	CH4	🟪 255, 0, 255
3	CO	🟩 51, 153, 1...
4	NH3	🟨 255, 204, 0
5	NO2	🟥 255, 0, 0

	use	cluster	sensor	cycle points	index points	preprocessing	feature set
1	☑	sensordata	sensordata	point set	point set	preprocessing chain	feature definition set

Ready.

(b) *Grouping* module to label each cycle range. Several groupings are shown, e. g., the first column for classification of gas type, the second for quantification of CO, and the sixth for selective quantification of CO, i. e., the model shall predict 0 even in the presence of other test gases.

Figure 3.6.: *CycleRange* and *Groupings* modules in DAV^{3}E.

or testing. For example, the labels of a second measurement can be marked with an asterisk to use them for testing instead of creating synthetic testing data with k-fold. Asterisks can be applied to labels manually or using the filter function.

The *Grouping* module also color-codes ranges based on their label. This makes it easy to spot errors when groupings are defined manually. Alternatively, they can be loaded from a JSON file. For numeric groupings, a saturation gradient can automatically be produced from one base color.

3.6. Global pools

DAV^{3}E was built with data fusion from many different sources in mind. They can, for example, differ in sensor type, operating mode, cycle shape and length, which poses several challenges to data fusion (see section 3.8). But even before the actual fusion, it must be ensured that data from the same sensor is always treated in the same way. In most cases, changing, e. g., the feature extraction between two experiments which are then used to build one common model means adding "insider knowledge" which would not be available in a real-world setting. If the number of features would be changed between measurements, fusion would even become impossible since matrices with non-equal column number cannot be concatenated vertically. Instead, if the same sensor is used in several consecutive measurements, its data should always be processed and, for fair comparison, also be visualized in the same way. To achieve this, DAV^{3}E defines four *global pools* each containing one of the following:

- cycle point set: markers in the quasistatic signal defining displayed cycles
- index point set: markers in the cyclic plot defining the points in the cycle from which the quasistatic signal is created
- preprocessing chain: list of preprocessing methods applied to the sensor data from top to bottom
- feature definition set: list of applied feature extraction methods and ranges

Each pool can contain an arbitrary number of elements, and each `Sensor` is assigned one and only one element from each pool. Taking the feature definition set as an example, one set can be defined for `Sensor A` and a different set for `Sensor B`. The global pool has, thus, two elements, which can now be assigned to the respective sensors again when they are used in a second experiment. Changing the feature definition set in any sensor will change the element in the global pool and, thus, affect all sensors which have been assigned the respective set, maintaining consistency. The same is true for the other global pools.

Index point sets, *preprocessing chains*, and *feature definition sets* should always be the same for the same `Sensor`, i. e., they are defined for columns of the data matrix. *Cycle point sets*, instead, are defined for rows as they select cycles from the quasistatic signal, i. e., on a global time scale.

3.7. Scales

In order to be able to handle different cycle lengths and sampling rates together with simple, user-friendly data fusion, DAV^{3}E maintains four different scales for the data: the time scale, the index scale, the cycle scale, and the abscissa scale (Figure 3.7).

The time scale assigns a global time to each data value. This time is calculated from the given sampling rate (assumed constant) and the cluster's time offset. The time offset is given relative to the project's time origin which is sufficient to figure out the concurrency of observations during data fusion. If necessary, the project's time origin can be fixed in absolute time, i. e., day, month, year, etc., in order to transform all relative times to absolute times.

The index and cycle scale count columns and rows of the feature matrix,

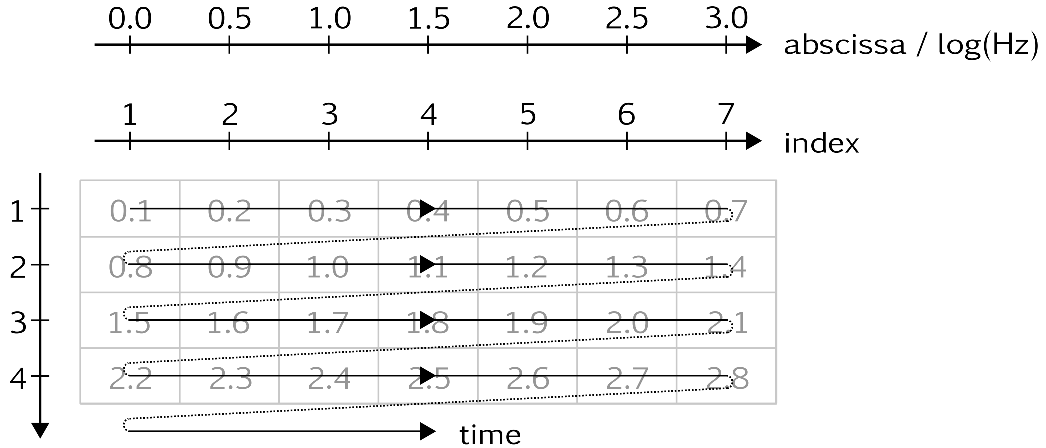

Figure 3.7.: The four scales used in DAV^{3}E. The unit of the abscissa scale is chosen as an example for impedance spectroscopy data.

respectively. Thus, converting the time scale into cycle scale and index scale is equivalent to converting the linear stream of data into a feature matrix (cf. Figure 3.4). These internal conversions are essential for the intuitive selection of data in quasistatic and cycle plots. Listing 3.1 shows the conversion functions used between time (`tPos`), index (`iPos`) and cycle (`cPos`) for point markers. They include out-of-range checks and round the time to the nearest index or cycle. The conversion functions for a range look similar, but ensure that a range never grows bigger than intended, i. e., the start point is always rounded up and the end point is always rounded down. Otherwise, a range defined on a high-resolution scale, i. e., short cycles, could contain cycles outside of the defined time range on a low-resolution scale.

In addition to the time offset, an additional *virtual offset* (`vOffset`) can shift the data by no more than half a cycle's duration on the time axis for these calculations. This makes sure that the cycles of two intermittent measurements fall into the same "grid" and saves computing power during serial fusion (cf. next section).

In some cases, the assumption of a constant sampling rate is not valid or the data is conventionally plotted against a non-time abscissa, for example in impedance spectroscopy. Therefore, each point of the index scale can be related to a point on the abscissa scale which, for impedance spectroscopy, would contain frequency values instead of times. Giving an average sampling time can still result in correct cycle lengths and allow for correct synchronization with other systems.

3.8. Data fusion

3.8.1. Cycles of equal length

Data fusion, in this context, means joining raw data or features from multiple `Sensors` (or `Clusters`) into one continuous data matrix. Challenges include the correct handling of different sampling rates (in the raw data space) or cycle lengths (in the feature space) and time offsets in order to make sure that the data joined were recorded at the same absolute time, i. e., during identical experimental conditions. Joining data over time, i. e., vertical concatenation of data matrices, increases the number of observations and will subsequently be termed *serial fusion*. In contrast, the term *parallel fusion* stands for a horizontal concatenation of data matrices, i. e., increasing the number of features.

In the older version of DAV^{3}E, serial fusion was achieved by joining `Clusters` with the same (user-defined) name from each `Measurement`. Parallel

Listing 3.1.: Functions to convert between time, cycle, and index position for points.

```
function iPos = timeToIndex(tPos,cluster)
    iPos = mod((tPos - cluster.offset - cluster.vOffset) / ...
        cluster.samplingPeriod, cluster.nCyclePoints);
    iPos = floor(iPos) + 1;
end

function cPos = timeToCycleNumber(tPos,cluster)
    cPos = (tPos - cluster.offset - cluster.vOffset) / ...
        (cluster.samplingPeriod * cluster.nCyclePoints);
    cPos = floor(cPos) + 1;
    cPos(cPos < 1) = nan;
    cPos(cPos > cluster.nCycles) = nan;
end

function tPos = indexToTime(iPos,cluster)
    iPos(iPos < 1) = 1;
    iPos(iPos > cluster.nCyclePoints) = cluster.nCyclePoints;
    tPos = (iPos - 0.5) * cluster.samplingPeriod...
        + cluster.offset + cluster.vOffset;
end

function tPos = cycleNumberToTime(cPos,cluster)
    cPos(cPos < 1) = 1;
    cPos(cPos > cluster.nCycles) = cluster.nCycles;
    cLen = cluster.samplingPeriod * cluster.nCyclePoints;
    tPos = (cPos - 0.5) * cLen ...
        + cluster.offset + cluster.vOffset;
end
```

fusion was done within the `Measurement` under the assumption that all `Clusters` start with the `Measurement`.

While this structure worked reasonably well for specifically designed measurements recorded in a lab environment, it became obvious that field test data, often generated with several independent instruments on the same location, could not be represented well with the `Measurement` approach. The main issue are arbitrary interruptions in the data streams, each creating a new logical `Cluster`. These `Clusters`, however, cannot generally be distributed to a common number of `Measurements` (Figure 3.8a), leading to time ranges where data fusion becomes impossible because `Measurements` are not allowed to overlap.

To resolve this issue, the newer version of DAV^{3}E replaced the `Measurement` concept with *tracks* and a common time origin for all `Clusters` (Figure 3.8b). Each `Cluster` is assigned a track which determines the `Clusters` for serial fusion. The track concept additionally allows arbitrary names for all `Clusters`. The lack of `Measurement` containers complicates the algorithm to find parallel cycles but, eventually, provides a much more flexible approach which can handle data with an arbitrary number of `Clusters`.

Having defined the data structure with tracks and common time origin, the data fusion algorithm provides two main ways to resolve missing data. The algorithm can insist on having all tracks present and, hence, puts only such times in the final data matrix (time-based resolution, Figure 3.9a). This approach leads to the maximum number of features, but can reduce the number of observations. Alternatively, certain tracks can be dismissed beforehand (track-based resolution, Figure 3.9b), which results in more observations with fewer features. Which resolution method should be chosen depends strongly on the application or research question.

The fusion algorithm first searches for all points in time where a `Cluster` starts or ends, including only `Clusters` in the considered tracks (track-based resolution). The final data matrix is then built by first joining data from all time regions with all `Clusters` present (time-based resolution) in parallel, and then fusing all the resulting matrices in series.

3.8.2. Cycles with different lengths

The previously described procedure requires equal cycle lengths of all `Sensors` joined in parallel [169]. In reality, different sensor technologies might require quicker or slower cycles, or there might be reference instruments recording with a sampling rate which is not a multiple of any other cycle length in the system. Data fusion for such multirate systems has been intensively investigated especially for combinations of visual and inertial

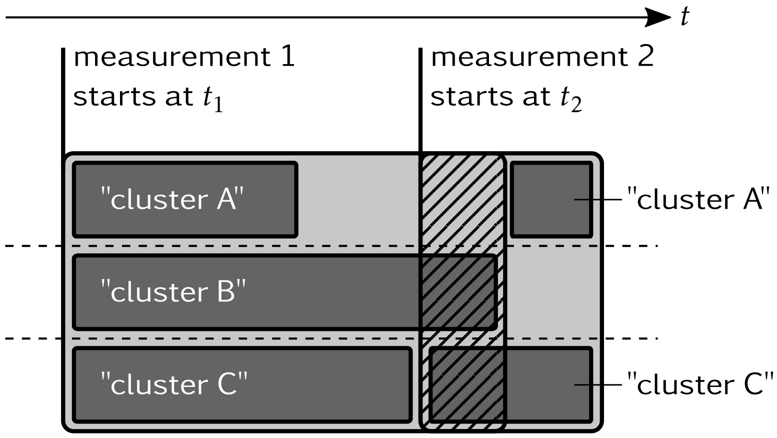

(a) The *measurement concept* in the older version requires identical names to fuse `Clusters` correctly and is not able to fuse overlapping `Clusters`.

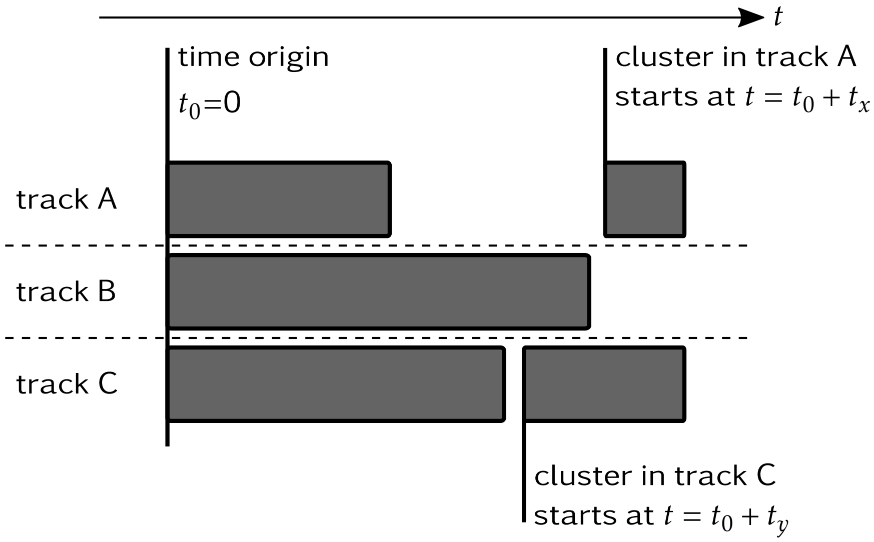

(b) The *track concept* in the newer version fuses `Clusters` based on their track and time offset measured from a common time origin.

Figure 3.8.: Comparison between the *measurement* and the *track* concept for data fusion.

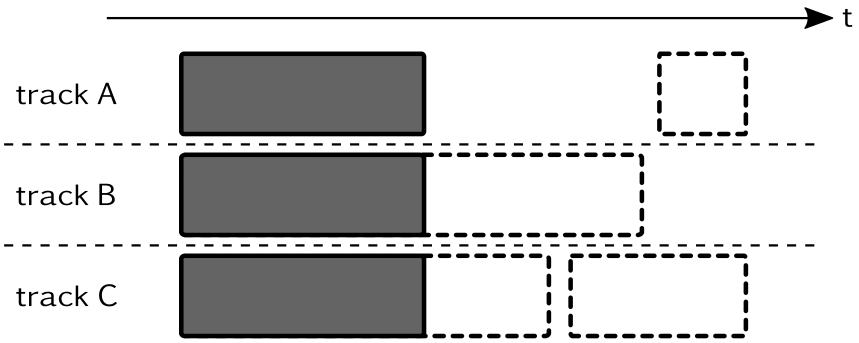

(a) Time-based resolution.

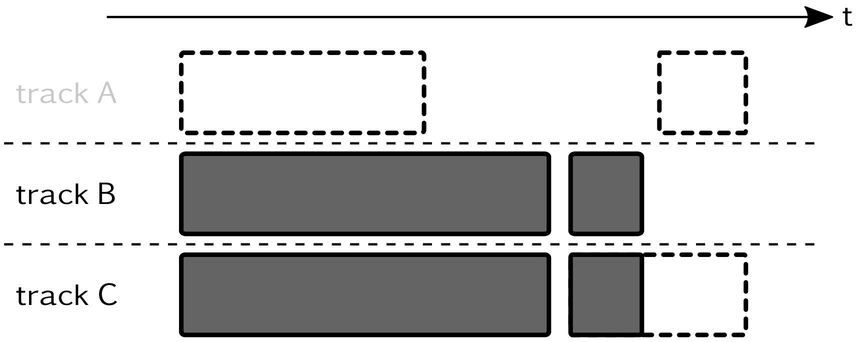

(b) Track-based resolution.

Figure 3.9.: Data fusion with missing data can be resolved in two ways: (a) fusing only data at times where all tracks are available, or (b) discarding one or more incomplete tracks.

data together with information from the *Global Positioning System* (GPS) for navigation [170], [171]. The Kalman filter or one of its variants [172] are common choices when the state of a system can be predicted by a physical model whose prediction is updated by sensor readings. This kind of modeling is, however, difficult to do for gas sensor system. Instead, this section describes and examines three simple fusion strategies developed during this PhD project. The reader is referred to page 56 for the continuation of the general description of DAV^{3}E.

Fusion strategies

There are several strategies to handle cases of different cycle lengths or significant time offsets between two cycled sensors. Three such strategies have been developed and simulated in this thesis [173]: *hold*, *combine*, and *mean*.

Consider two sensors running in parallel, one with a shorter cycle than the other. No phase shift and an integer ratio r for the number of short cycles in a long cycle can be assumed without loss of generality. Figure 3.10 shows an example for $r = 3$ with a triangular cycle shape (only for illustration).

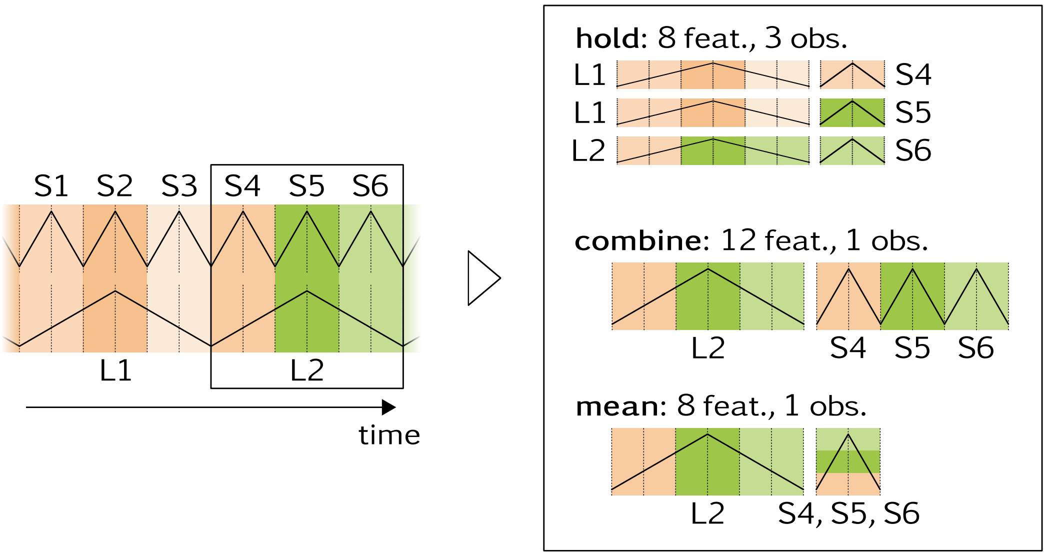

Figure 3.10.: Two systems L and S with unequal cycle lengths running in parallel and the three proposed strategies for simple and transparent fusion of the resulting matrices. The colors (green, orange) and their intensity represent gas exposures to two different gases with varying concentrations (adapted from [173]).

The simulated gas exposure (type and/or concentration) is changed after each short cycle, indicated as different colors (green, orange) with varying intensities. Two features are extracted from the short cycle (S) and six from the long cycle (L). The resulting feature matrices $\mathbf{X}_S$ and $\mathbf{X}_L$ have the dimensions $n_S \times m_S$ and $n_L \times m_L$, respectively, with $n_S/n_L = r$. The goal of the fusion algorithms described in the following paragraphs is to combine $\mathbf{X}_S$ and $\mathbf{X}_L$ into one matrix $\mathbf{X}$ with dimensions depending on the distinct algorithm. In the following, $\boldsymbol{x}_i$ means the i^{th} row vector from matrix $\mathbf{X}$, $\lfloor\cdot\rfloor$ means the floor operation, and the operator $[\cdot]$ concatenates its arguments horizontally.

The *hold* strategy combines data from a finished short cycle with data from the latest complete long cycle, i. e., it holds the long cycle until a new one is available. This leads to features being repeated in several operations but maintains the quick sampling period of the short cycle. The resulting dimensions of $\mathbf{X}$ are $n_S \times (m_L + m_S)$ (see Equation 3.1), i. e., there is one new observation for each short cycle so that at least those features are updated with their original frequency. The long cycle's features, however, become more and more outdated over time, so that diminishing their influence by weighting with $1/r$ is also tested.

$$\boldsymbol{x}_{\mathrm{hold},i} = \left[\boldsymbol{x}_{\mathrm{L},\lfloor i/n \rfloor}, \boldsymbol{x}_{\mathrm{S}}, i\right] \quad \text{with} \quad i = 1 \dots n_{\mathrm{S}} \tag{3.1}$$

The *combine* strategy reduces the resulting sampling period to the one of the long cycle. Every time a long cycle finishes it combines its features with the features from all short cycles which happened in the same time interval, i. e., $\mathbf{X}$ has the dimensions $n_L \times (r \cdot m_S)$ (see Equation 3.2). Combining features from the same cycle in one observation can make them highly redundant and correlated which can pose a problem for methods like LDA. On the other hand, however, these features were sampled quicker than the features from the long cycle, so that also for the *combine* strategy a variant with $\frac{1}{r}$-weighting of the long cycle's features is tested.

$$\boldsymbol{x}_{\mathrm{combine},i} = \left[\boldsymbol{x}_{\mathrm{L},i}, \left[\boldsymbol{x}_{\mathrm{S},i(r-1)+j}\right]_{j=0}^{r-1}\right] \quad \text{with} \quad i = 1 \dots n_{\mathrm{L}} \tag{3.2}$$

The *mean* strategy works similar to the *combine* strategy, but instead of adding all the short cycles' features to $\mathbf{X}$, it only adds the mean, resulting in dimensions of $n_L \times (m_L + m_S)$ (see Equation 3.3). The averaging directly decreases the random noise with $1/\sqrt{r}$ assuming the features are, in fact, similar (which would lead to collinearity with the *combine* strategy). In order to determine whether the lower number of features from the short cycle can be counteracted, also this strategy will additionally be tested with a weighting of $\frac{1}{n}$ on the long cycle's features.

$$\boldsymbol{x}_{\text{mean},i} = \left[\boldsymbol{x}_{\text{L},i}, \frac{1}{r} \sum_{j=0}^{r-1} \boldsymbol{x}_{\text{S},i+j} \right] \quad \text{with} \quad i = 1 \dots n_\text{L} \tag{3.3}$$

Simulation

The performances of the three described fusion strategies were tested with 100 000 simulated datasets generated with the MATLAB code found in the appendix (section 1). As many parameters as possible were varied to achieve a good estimation of the influence of the data fusion; the only constant parameters were the number of sensors (2) and the number of simulated gases (3) with each gas appearing for roughly 33 % of all observations (1000. . . 10 000). Each exposure contained one and only one gas. The influence of gas on a feature was determined by a random correlation coefficient between −1 and 1 assigned to each feature individually. Gaussian noise is additionally added with a random amplitude between 0 and 2. The gas concentration is drawn from a normal distribution (mean 1, std 0.1) for each observation, and one observation lasts for the duration of the short cycle. It is further assumed that all features are distributed equally over the cycle, i. e., the longer cycle will produce features influenced by several gas exposures which can easily happen in applications when the gas mixture varies during the cycle. The target value for a long cycle spanning multiple exposures is always chosen based on the exposure during which the cycle started. The number of short cycles within a long cycle, r, varies between 1 and 6, i. e., there are roughly 16 000 datasets with equal cycle lengths which can act as reference. The number of features in the long cycle varies between 7 and 16, and between 3 and 6 for the short cycle. All parameters are listed in Table 3.1. Note that, while these parameters are mostly chosen arbitrary, they could be tuned to be much more similar to a real sensor system with few data from a real calibration run. A novel, potentially well-suited calibration method is described and discussed in chapter 13.

All features are standardized which is a common procedure in practice to achieve equal scaling and influence of all features. This is especially important since the data are projected into two dimensions using PCA to avoid overfitting. The 10-fold cross-validated classification error, based on the smallest Mahalanobis distance in this projection, is used as performance measure of the respective fusion strategy.

Alongside the three described strategies, the performance of the long and short cycles alone will also be given and, additionally, the performance of

Table 3.1.: Simulation parameters (adapted from [173]).

parameter	distribution	value
observations n	uniform	$1000 \dots 10000$
observations per class	uniform	$(1/3 \pm 0.1) \cdot n$
classes	constant	3
concentrations c	normal	mean $= 1$, std $= 0.1$
sensors	constant	2
short cycles per long cycle r	uniform	$1 \dots 6$
features m_L	uniform	$7 \dots 16$
features m_S	uniform	$3 \dots 6$
feature correlation to c	uniform	$-1 \dots 1$
noise amplitude per feature a	uniform	$0 \dots 2$
noise per feature	normal	mean $= 0$, std $= a$

each fusion strategy where the cycles of the long cycles were weighted with $1/r$. This accounts for the (arbitrarily chosen) dominance of the long cycle's features as there are always more of them and all features carry, on average, the same amount of information. Further, r determines the difference of temporal resolution between the long and short cycle as there is one new gas exposure for each short cycle which influences different parts of the same long cycle.

Figure 3.11a shows the mean classification errors of all strategies for 100 000 simulated datasets. This high number of samples leads to very small, almost imperceivable, 95 % confidence intervals, while the variance is naturally much larger due to the many parameter variations.

As expected, the long cycle performs better than the short cycle which can simply be ascribed to its consistently higher number of features. The same argument explains the increased error for *weighted hold* and *weighted combine*. Interestingly, weighting the long cycle down improves the classification error of *mean*, suggesting a considerable decrease in noise through the averaging so that the overall classification performance benefits from a stronger influence of the short cycles' features. Overall, all strategies improve the classification significantly (*hold* should be compared to the short cycle due to having the same temporal resolution). Relatively spoken, *hold* improves the classification error by 85 %, *combine* by 76 %, and *mean* by 59 %. *Combine* and *weighted mean* produce the lowest absolute error with 2.1 %.

Figure 3.11b shows the classification error for all strategies over r. Obviously, the classification performance of the long and short cycle alone

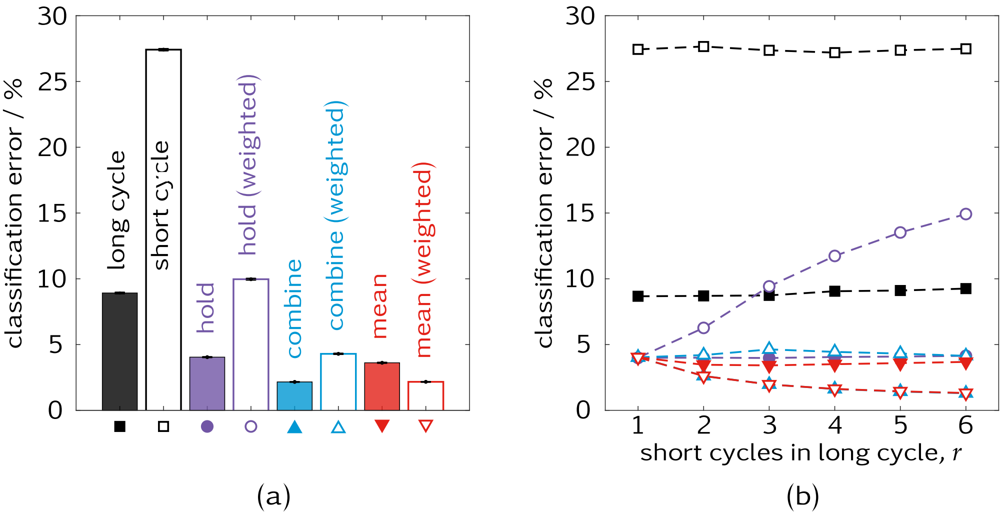

Figure 3.11.: (a) The average classification error for all strategies and the long cycles as baseline, and (b) the dependence of the error on the ratio between long and short cycle length r. The marker types used in (b) are indicated below the bars in (a).

does not depend on r. Furthermore, all fusion strategies produce the same performance for $r = 1$, which is expected as the resulting $\mathbf{X}$ is identical for all strategies in this case. These results validate the correctness of the simulation.

No obvious correlation of *hold*, *mean*, and *weighted combine* with r is observed. The *combine* and *weighted mean* strategies, however, behave identical approaching a value close to 1 % (1.3 % at $r = 6$) with increasing r. This validates the choice of the weighting factor $1/r$ as adding features from r short cycles has the same effect as downweighting the long cycle's features when adding features from only one short cycle. The PCA then averages the features by dismissing the noisy dimensions, giving, effectively, the same result for *combine* and *weighted mean*. *Weighted hold* notably produces a larger classification error with increasing r since the number of features added cannot counteract the reduced information from the long cycle's features. The average numbers of features are 11.5 for the long and 4.5 for the short cycle, i. e., a ratio of 2.6 which explains the position of the point of intersection of *weighted hold* with the long cycle.

The weighting factor has been arbitrarily chosen as the inverse of r. However, the influence of the weighting factor alone, as shown in Figure 3.12, can also be of interest. The optimum for *hold* and *combine* lies at equal weighting, i. e., 10^0, and is slightly shifted towards lower weights for *mean*.

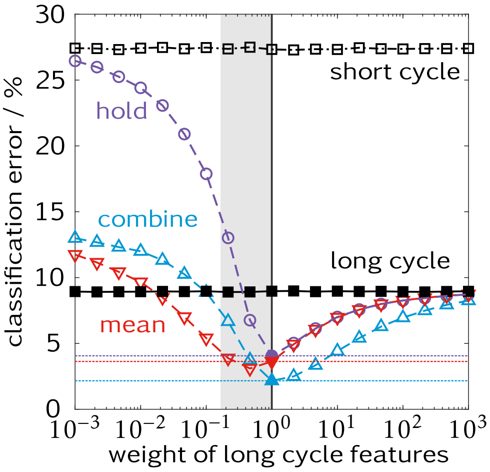

Figure 3.12.: Dependence of the average classification error on the relative weight of the long cycle.

While the sampling is not dense enough to determine the exact minimum, it is reasonable to assume 1/2.6 with the same argument as before. The performances of all strategies approach the performance of the long cycle with increasing weight which is reasonable as the short cycle becomes more and more insignificant. *Hold* and *mean* follow almost exactly the same behavior for weights greater than 1, approaching the long cycle's performance. *Combine*, on the other hand, while also approaching the same limit, stays longer at a lower classification error due to the increased number of short cycle features. Weights below 1 quickly worsen *hold*'s performance to the one of the short cycle while *combine* and *mean* stay considerably below this value. *Mean* performs even better than *combine*, suggesting that the explicit averaging is slightly more efficient than the implicit averaging done by PCA.

Evaluation with real data

The fusion strategies have been validated with real sensor data. To this end, two MOS sensors were run in parallel: one GGS5330 (UST Umwelt-SensorTechnik GmbH, Geschwenda, Germany), and one AS-MLV (ams AG, Premstätten, Austria). The GGS5330 has a ceramic substrate resulting in a thermal time constant of several seconds which requires a relatively slow temperature cycle. A triangular shape was chosen, increasing the temperature linearly from 150 °C to 450 °C during 15 s, and back to 150 °C during another 15 s. The AS-MLV has a thermal time constant of 7 ms [164] which allows for sharp temperature steps. Its cycle consists of two 5 s temperature plateaus at 450 °C and 200 °C. The resulting cycle lengths are $t_L = 30\,\mathrm{s}$ and $t_S = 10\,\mathrm{s}$, i. e., $r = 3$. The sensors are exposed to 100 ppb$_\mathrm{v}$ of ethanol and benzene in air (50 %RH) for 20 min each, with 20 min of only humid air after each exposure, respectively. The cycles were chosen such that the three classes, i. e., ethanol, benzene, and air, have similar sizes, resulting in 304 (n_S) and 912 (n_L) observations. The triangular cycle is divided into six equal parts on which the signal mean value are computed as features. For the step cycle, mean and slope of the low temperature plateau are extracted as features, i. e., $m_L = 6$ and $m_S = 2$.

The slope features show good correlation with the gas exposures, but are, numerically, considerably smaller than the mean features. This gives the opportunity to take a look at the influence of feature preprocessing. In addition to no preprocessing and standardization, Pareto scaling which subtracts the mean and divides by $\sqrt{\mathrm{std}}$, is considered [174]. As the classification was fairly good to begin with, Gaussian noise with one standard deviation of the respective feature in air was added to each feature. The processing is done as in the simulation and the results are shown in Figure 3.13.

Obviously, the short cycle produces a much better classification despite having fewer features. This deviation from the simulation is easily explained by the fact that not all features carry the same amount of information in real data. It is, further, evident that the short cycle must be preprocessed to have any influence since the classification error of all strategies in the first column (a, d, g) is similar to the long cycle's performance. A notable exception is *weighted combine* in (a) where, presumably, the increased number of features from the short cycle increases their influence. This effect vanishes, however, when the long cycle is preprocessed and overpowers the short cycle again. This explains the large classification errors in (h) as well as the difference between centering and Pareto scaling being the same as the difference between Pareto-scaled and standardized data, i. e., $\sqrt{\mathrm{std}}$. Hence, Pareto scaling "lies between" centering and standardization.

When the short cycle is preprocessed "more" than the long cycle, it starts to gain influence which is most prominently seen in (c) and (f) where all strategies produce the same error as the short cycle alone. In (e), the short cycle benefits from downweighting the long cycle more than in (a), depicting the non-linear character of the preprocessing. While unweighted *hold* and *mean* are still on the level of the long cycle, the weighted variants and both *combines* produce an error at short cycle level or lower, approaching the optimum. This trend continues with (i) where *combine*, *mean*, and their weighted variants perform perfectly, with *hold* still being significantly better than the short cycle alone. Variant (b) stands out as it achieves the same result with different preprocessing of both cycles. Here, the optimum weighting for this specific dataset has been found. This becomes clear when comparing the first row with Figure 3.12 where all classification errors approach the long cycle for small, and the short cycle for large weights with a global minimum in between, which is exactly what happens in (a), (b), and (c).

When this work was first published [173], mean and slope were computed for both plateaus of the step cycle. However, the resulting features were very noisy for the static high-temperature plateau, and it was proposed in this work that noisy features were the reason for poor performance when both cycles were standardized. Especially PCA is sensitive to noise and outliers [175] and the *combine* strategy was the most influenced. By excluding these features in this reevaluation, this assumption has been validated. In both evaluations, parameters resulting in perfect or near-perfect classification could be found for this dataset. At the point of writing, *unweighted mean* has been implemented as default fusion strategy into DAV^{3}E as it provides

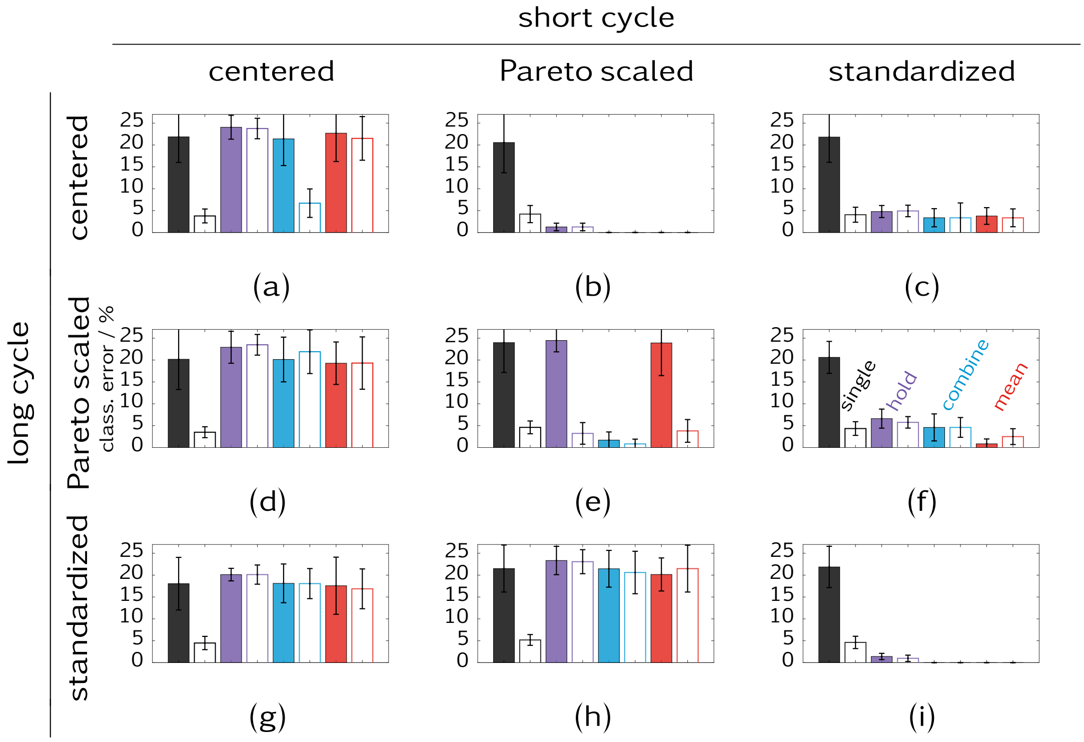

Figure 3.13.: Classification errors (10-fold cross-validated) for real data with different combinations of preprocessing for all proposed strategies. Hollow bars indicate the weighted variant of the method or the short cycle (black), respectively.

a constant performance and can handle non-integer r relatively easily. The same is true for *unweighted hold* which should be implemented in the future as an alternative strategy to keep the temporal resolution.

3.9. Data-driven models

3.9.1. Data reduction and augmentation

Groups are not always of equal size but sometimes show a strong imbalance. One typical example concerns cycles in carrier gas being more common than cycles in test gas due to pauses, i. e., carrier gas only, between test gas exposures. Classifiers aim to minimize the classification error which, with large variations in group sizes, is often very easily achieved by classifying all observations into the largest class. The resulting good classification rate is deceiving as the model is not able to classify observations correctly, but just relies on the fact that most observations belong to one specific class. Quite often, smaller groups are the interesting "alarm cases" which, with such a model, could be detected at all.

This kind of error can only be identified in a *confusion matrix*[1] and not in the overall classification rate. It can, however, be avoided in the first place by eliminating the differences in group size by either adding or removing data points. Removal is the safer option, as all remaining data points are real. It is implemented in DAV^{3}E as random selection of points in each group. While it can severely reduce the amount of available training data, it has been found on several occasions during this PhD project that models trained with equal class sizes show a significantly better performance even when predicting the whole training dataset. Adding data points can be done by estimating the mean and covariance matrix of a group and generate samples that fit in this distribution. This approach, however, assumes a normal distribution of the class, which is often not the case. Adding new data points can severely distort the resulting model and must be done very carefully.

Another occasion where data reduction can be useful is to avoid having to apply group-based validation. Instead, the data is reduced to mean values of each respective group. This requires a sufficiently large number of groups and reduces the noise and variance through averaging which can seemingly improve the results. Given an appropriate experimental design, this kind of data reduction prevents data pollution and speeds up the model building process by reducing the total number of very similar observations.

---

[1] A confusion matrix shows with which classes wrongly predicted classes were "confused". An example can be found in Figure 7.10 in section 7.3.

3.9.2. Preprocessing

Both feature and (numeric) target values can be preprocessed. Feature preprocessing, standardization in particular, is often done to equalize the scales of all features and, thus, make model parameters like the coefficients of CDA or PLSR comparable and an indicator for the importance of each feature (cf. section 3.8.2). The second reason for preprocessing is linearization. The output of chemical sensors seldom varies linearly with the analyte concentration, but instead follows a power law [15] or logarithmic [17] behavior. Training the model with logarithmic target and/or feature values can linearize both behaviors, making a simple, linear model applicable. Preprocessing target values lead to predictions on the preprocessed scale which are automatically transformed back to the original scale by DAV^{3}E when a revert function is implemented for the respective preprocessing method.

3.9.3. Validation and testing

As stated in section 2.5, validating a model is crucial to make sure it will perform satisfactory on new data. Most often, a dedicated validation dataset is not available, so that methods like leave-one-out and k-fold are used to generate synthetic validation datasets. However, care must be taken not to "pollute" the training dataset with observations from the validation or testing set, leading to over-optimistic results.

In DAV^{3}E, the complete feature matrix is managed by one `Data` object. The `Data` object provides three methods to select data from the feature matrix: `setAvailable()`, `setValidation()`, and `setTesting()`. The `setAvailable()` method takes row numbers (or a logical vector) describing which observations should be considered in the model at all and deselects all other observations. Deselected observations can later be predicted as unknown values, but will not influence the model building process.

The `setTesting()` method takes one of the available data generation algorithms and its parameters: *none*, *leave-one-out*, *k-fold*, *holdout*, or *groups*. *Leave-one-out*, *k-fold*, and *holdout* produce synthetic testing datasets as described in section 2.5. *Groups* allows the selection of specific groups which will then be used as testing data. Some methods, like k-fold, produce several folds, i. e., k_{test} distinct dataset pairs will be created. Additionally, the number of iterations i_{test} can be defined, resulting in $k_{\text{test}} \cdot i_{\text{test}}$ distinct dataset pairs. Several iterations are often used to reduce the variance of the resulting error; however, it should be kept in mind that any bias will not be affected so that more iterations will not necessarily lead to a better result [162].

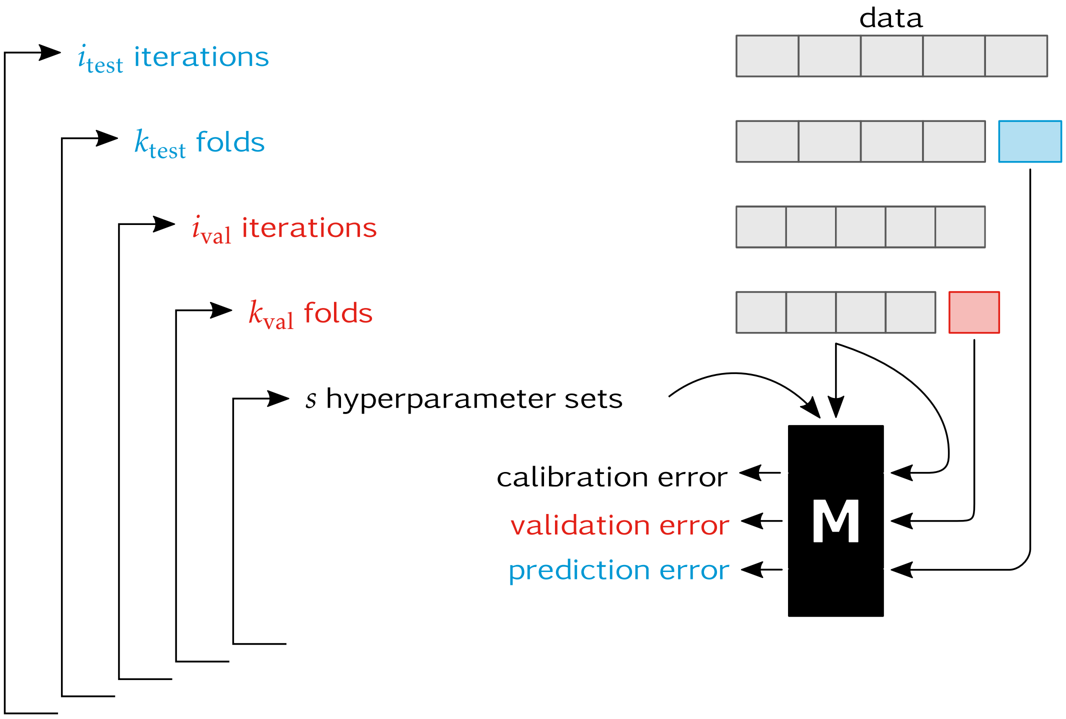

Figure 3.14.: Scheme of model training, validation, and testing loops in DAV^{3}E. Iterations repartition the data, folds (here both 5) reserve one part for prediction after training.

The third method, `setValidation()`, works identical to `setTesting()`. The only difference is that it choses its data from the data which is not deselected by `setAvailable()` and which was not put in the testing set by `setTesting()`. Similar to `setTesting()`, it can produce several folds k_{val} in several iterations i_{val}. The final result are three 5-dimensional, boolean matrices $(n \times k_{\text{val}} \times i_{\text{val}} \times k_{\text{test}} \times i_{\text{test}})$ which define for each fold and iteration whether an observation is part of training, validation, or testing. The associated errors, quantifying the deviance of the model prediction from the target values, are the calibration error, validation error, and prediction error. The standard deviation or confidence interval of these errors can be computed from the values over all folds and iterations for one set of hyperparameters. Model training, validation, and testing happen in five nested loops as depicted in Figure 3.14.

This compact representation of training, validation, and testing as boolean matrices makes it easy to implement a safeguard in `checkIntegrity()`. This method takes the logical `AND` of all three matrices and raises an error if any element of the result is true. This simple mechanism protects effectively and

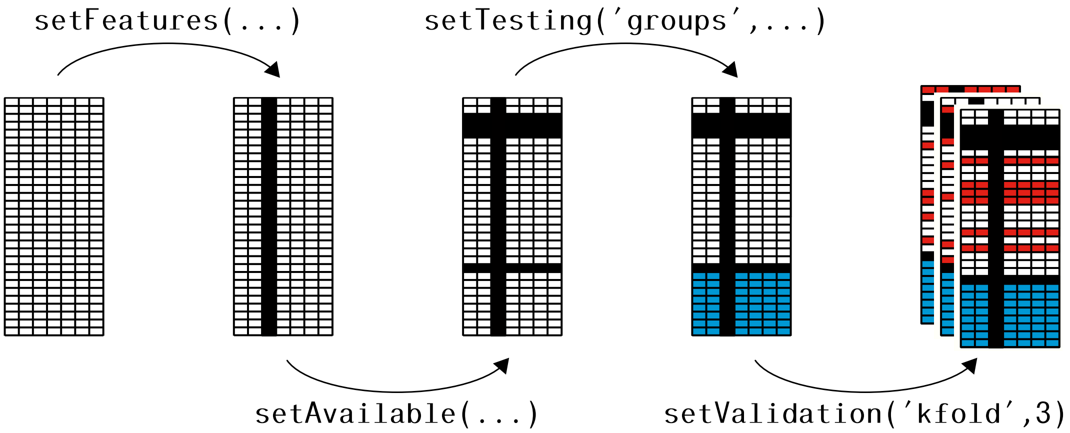

Figure 3.15.: Progression of data selection and synthetic data generation in DAV^{3}E. The commands can be executed in any order.

efficiently against mistakes in the implementation and, thus, prevents any data pollution during validation or testing.

Features can be selected and deselected independently of the selection of observations. All steps of data selection from the bare feature matrix to several (virtual) datasets with selected features are shown in Figure 3.15. The datasets are "virtual" because the actual data is stored only once. The information about the different virtual datasets is stored in boolean vectors.

The experimental design with gas sensors consists, classically, of one gas exposure after the other. Within one gas exposure, the environmental conditions are kept constant and its duration is usually chosen to contain at least several sensor cycles. This allows for the time it takes to establish new gas concentrations and let the sensor react to them. This means, however, that once everything is in a steady state, all observations will be extremely similar, with variations only through noise (in the sensor, the electronics, or the gas mixing system). Since all these parts are designed to have as little variance as possible, the final dataset contains many very similar observations. When leave-one-out or k-fold are "blindly" applied to such data, the results often appear to be much better than they are in reality due to dataset pollution. One of the most extreme combinations is leave-one-out with a 1nn classifier: the cycle which is left out is very similar to the cycles which were recorded just before and after it, so that one of these will most likely be its closest neighbor after projection, leading to a seemingly correct classification even if a time-dependent effect like drift is involved. Newly recorded cycles, on the other hand, are not part of these time series and could be projected entirely elsewhere. While this is the most extreme example, the principle is true for

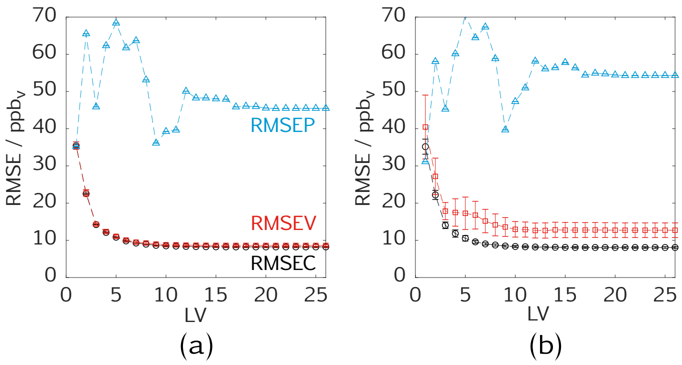

Figure 3.16.: Different variants of 10-fold cross-validation on a dataset with many quasi-identical observations: (a) uses the classical approach of removing random data points, (b) removes complete groups of consecutive cycles, and (c) removes all cycles in specific concentrations of the target gas in each fold.

any validation methods and predictors.

This effect must be avoided in order to prevent overfitting of the model. Several strategies are implemented in DAV^{3}E. One is data reduction, which is discussed in section 3.9.1. The other is group-based validation (and testing): Instead of applying k-fold, leave-one-out, or holdout to select unique rows of the feature matrix, they are applied to groups, e. g., gas exposures with the same concentration settings.

Figure 3.16 shows the difference between three variants of 10-fold cross-validation on a regression problem which will be further discussed in chapter 11. The objective is quantification of formaldehyde concentration in a background of varying interfering gases. The same formaldehyde concentrations are repeatedly set in different backgrounds. Figure 3.16a shows the result with conventional 10-fold cross-validation, i. e., ten folds where, randomly, 10 % of observations are left out as validation set. The similarity between *root mean square error of validation* (RMSEV) and *root mean square error of calibration* (RMSEC) and the low validation variance clearly shows that the validation data was already contained in the training data. No distinct optimum can be found. In Figure 3.16b, 10-fold cross-validation was applied on groups instead of individual cycles. The groups consisted of all cycles recorded in the same environmental conditions, i. e., usually during the same gas exposure. Of those groups, 10 % are used for validation in each fold, resulting in a much more distinct RMSEV with higher variance and an obvious break at three *latent variables* (LVs). The last figure, Figure 3.16c, is the result of group-based 10-fold cross-validation where formaldehyde concentrations were taken as groups, leading to an even more distinct optimum at three LVs.

Note that shape and value of the *root mean square error of prediction* (RMSEP) is identical in all three plots because the model performance is not dependent on the validation method. The final model is, however, selected based on its RMSEV, e. g., by selecting the model with the lowest error. A realistic (as compared to optimistic or pessimistic) validation method will, given that the validation data is appropriate, select a model which performs as well as possible on new data. This performance is then measured with the RMSEP. Indeed, the relation between validation and RMSEP is considerably more pronounced in Figure 3.16c compared to Figure 3.16a.

Given the experimental design as previously described, the variants (a) to (c) can be interpreted as increasingly rigorous tests of the model performance. Non-group-based validation (a) tests the model for stability against noise of the measurement equipment. While this is important, it is in most cases negligible and, therefore, not suitable for model selection. Exposure-based validation (b) tests for stability against noise as well as for selectivity since the same target gas concentration must be quantified correctly in background conditions not contained in the training. Concentration-based validation (c) tests for stability against noise, selectivity, and interpolation ability as the model must predict target gas concentrations not contained in the training.

Following the above argumentation, models built from data with similar observations should always be validated with group-based validation. Concentration-based validation (c) is not applicable to classification problems as it would remove whole classes from the training set. It further leads to problems with quantification, too, when only few target gas concentrations are available, or when one of the outermost concentrations is left out and the model is forced to extrapolate. Extrapolation generally leads to a considerably higher error compared to interpolation, skewing the results. To mitigate this problem, DAV^{3}E allows to fix individual groups, e. g., the outermost concentrations, in the training set (which was done in (c)). Exposure-based validation is a good compromise which works well in all cases.

3.9.4. Hyperparameter optimization

Hyperparameter optimization is done based on the validation error. In the *Model* module, the value for each hyperparameter can be either fixed, or a list of values. In the latter case, models will be trained, validated and tested for all possible hyperparameter sets. They are always sorted from high to low values because, in many cases, the training for higher values already includes the training for lower values. For example, a CDA trained for three DFs can also be evaluated for one and two, saving computing time. If only one hyperparameter is varied, the resulting errors are plotted as in Figure 3.16. For two hyperparameters, the calibration, validation, and prediction errors can be plotted as three-dimensional surface, and for more than two, the remaining ones must be set to fixed values for visualization. In the case of many hyperparameters, like for (deep) neural networks, random search instead of grid search could be more efficient [176]. The result of such complex dimensionality reduction or classification algorithms is, however, often hard to interpret [156] and cannot be used to improve the physical sensor model, which is often the case for simpler algorithms like CDA. Therefore, DAV^{3}E is deliberately restricted to such simple algorithms, resulting in models which seldom exceed two hyperparameters. Hence, the implementation of random search had not been prioritized.

Several criteria to determine the optimal hyperparameter value from the validation error are implemented in DAV^{3}E. The minimum criterion (*min*) selects the parameter value with the absolute lowest error. It can easily be influenced by slight variations in the error, especially when the change with the parameter becomes negligible. The *min (conf.)* criterion determines the absolute minimum and its confidence interval over all folds and iterations and then selects the hyperparameter set that produces a validation error just below the upper bound of the confidence interval. The *max t* criterion computes the t value of each error by dividing its mean value through its standard deviation. It selects the model with the largest t value. The *elbow* criterion computes the two-dimensional Euclidean distance of all error points to a line defined by the first and last error point and selects the parameter value with the largest distance from this line [177]. The *quotient* criterion [157] computes the fraction

$$\frac{\text{validation error}_{\alpha}}{\text{calibration error}_{\alpha-1}} \tag{3.4}$$

for all hyperparameter value indexes from 1 to α. It selects the last parameter value that produces a quotient below a given threshold. Suggested values for this threshold can be found in the range between 0.9 and 1.00 [157], [178]. Here, 0.95 and 0.99 are tested. Criteria like these are mainly investigated related to clustering, i. e., assigning a label to similar observations in an unlabeled dataset, to determine the optimal number of clusters. A review of 30 different algorithms can be found in [179].

In Figure 3.17, these six criteria are tested against subjective selection of the optimal number of LVs for PLSR models. Negative numbers mean that the criterion has selected fewer features than the author for the specific

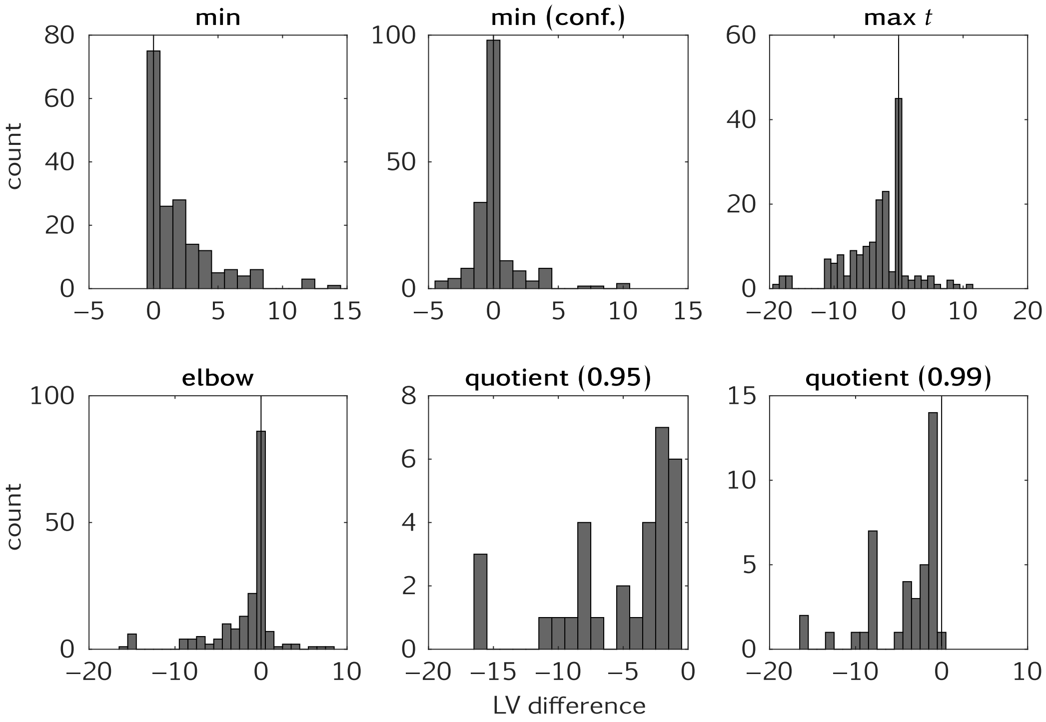

Figure 3.17.: Distribution of LVs selected by various criteria in relation to the subjectively determined number of LVs. Zero means that the subjective selection and the criterion selection are equal, negative numbers mean that the criterion has selected fewer features.

model. The histograms are based on the 90 models trained with the experimental data presented in section 13.2. For each model, the number of LVs was determined based on both the validation error and the cross-validated correlation coefficient between prediction and target, amounting to 180 data points for this comparison.

The *min* criterion is the only one out of the tested set of criteria which consistently selects at least as many or more LVs as the subjective selection. In most cases, the gain in the validation error reduction from these additional LVs is so small that the selection can change between runs due to the random nature of k-fold. This is, obviously, not compatible with the parsimony principle, i. e., to choose the lowest number of LVs feasible, and can even lead to overfitting of the model. All other tested criteria choose the number of LVs more conservatively. Both *quotient* criteria always (with the exception of one outlier) select considerably fewer LVs than subjective selection. In the majority of cases, however, the threshold is exceeded even for the first LV which was interpreted as rejecting the model entirely. The fact that subjective selection and other criteria were able to select a reasonable number of LVs resulting in well-performing models suggests that the threshold should be increased. Consequently, this criterion requires parameter tuning by the user, which is a drawback to all other tested criteria. The three remaining criteria, i. e., *min (conf.)*, *max t*, and *elbow*, all choose the same number of LVs as subjective selection with the highest probability. The *max t* still has a strong tendency to select fewer LVs which is less pronounced for *elbow*. The selections of *min (conf.)* are centered around the subjective selection and, approximately, normally distributed. In most cases, the conservative selection made by *elbow* resulted in a well-performing model. It can, however, fail to catch slow, but continuous decreases which can add up to a significant reduction. Moreover, *elbow* in particular depends on the overall shape of the error curve and can, in rare cases, end up selecting the model with the largest validation error instead. These edge cases could be caught, but it would complicate the criterion. Overall, *min (conf.)* seems like the best choice out of the six tested criteria.

3.9.5. Hierarchical models

Especially in complex environments, it can be difficult to find one comprehensive model which works in all cases. It can, therefore, be beneficial to use several, more and more specialized, models to arrive at a prediction [56], [145], [180], [181]. For example, if humidity has a big influence, a first model could classify observations as low, medium, or high humidity, and subsequently feed the data to a specialized quantification model which has been trained only at the respective humidity level. The idea is that the specialized model can perform better because it experiences less “noise” through interferents.

This type of hierarchical modeling is not yet included in the newer version of DAV^{3}E, but a prototype has been implemented in the older version. It lets the user build a tree out of all defined models where models are the nodes, and classes are the branches. This tree structure enables targeted training of all models with only the data it will later evaluate. For example, the model for quantification in medium humidity levels is not trained with data from low and high humidity levels. This is crucial to actually improve the performance of the lower-hierarchy models and would otherwise require many specialized groupings. The whole model tree can then be validated and tested.

3.10. DAV^{3}E in research and teaching

DAV^{3}E has become the *de facto* standard for gas sensor data evaluation at LMT since several years. More recently, it is also used for impedance data, condition monitoring data, and even image data. The same version used for productive data evaluation is also part of LMT’s graduate lecture *Measurement technology IV: Multi sensor signal processing* to teach students the basics of data-driven model building. The fact that DAV^{3}E guides the user from raw data to a tested model usually leads to quick and practical understanding of the fundamental concepts. The interactive plots further allow for a better grasp of the consequences of different configurations and preprocessing steps.

DAV^{3}E is also used at the International Iberian Nanotechnology Laboratory (INL), Portugal, to analyze data from Raman spectroscopy, at the Copenhagen Centrum for Atmospheric Research group at the University of Copenhagen, Denmark, and at the Materials Center Leoben Forschung GmbH (MCL), Austria, for gas sensor data [182], as well as at the Indian Institute of Technology (IIT) Kharagpur, India, for data of fractional order sensors. It has further been used in teaching at the Applied Sensor Science group at Linköping University in a project course for Master’s students (*TFYA92 Project Course in Applied Physics*), as well as in workshops in Denmark (*Current and future Air Pollution management – Perspectives on new sensor technologies*) and at IIT Kharagpur (*Data Analysis in Instrumentation Systems*).

The quick acceptance and international recognition of DAV^{3}E shows that the toolbox satisfies a need in the scientific community and is flexible enough to be applied to data from other groups and research fields.

In addition, the scientific results presented in the following chapters of this thesis are examples for the application of DAV^{3}E on real data. Important features and visualizations are mentioned and discussed directly where they occur during the evaluation of different datasets, extending the basic explanations given in this chapter.

Part II.

Gas-sensitive field effect transistors

4. Gas-sensitive field-effect devices

4.1. MIS capacitor

One of the simplest field-effect devices is the *metal-insulator-oxide* (MIS) capacitor. It generally consists of a metal (or highly doped poly-Si) electrode insulated from a lightly doped semiconductor - hence the structure's name. A common insulator is SiO_2 which is why the structure is often also called MOS (for *metal-oxide-semiconductor*) [183]. However, to prevent confusion with the resistive-type MOS sensor where the acronym describes one type of material and not a material stack, field-effect devices will be referred to as MIS in this thesis while the terms insulator and oxide will be used interchangeably.

The semiconductor, or *body*, is at a fixed potential $\phi_B = 0\,\mathrm{V}$ acting as the reference for the voltage V_{GB} applied to the metallic electrode, or *gate*. Figure 4.1 shows the basic design of a MIS capacitor as well as the energy band diagram of an ideal device. *Ideal* here means that (1) the work functions of metal and semiconductor are equal, and (2) there are no charges at the

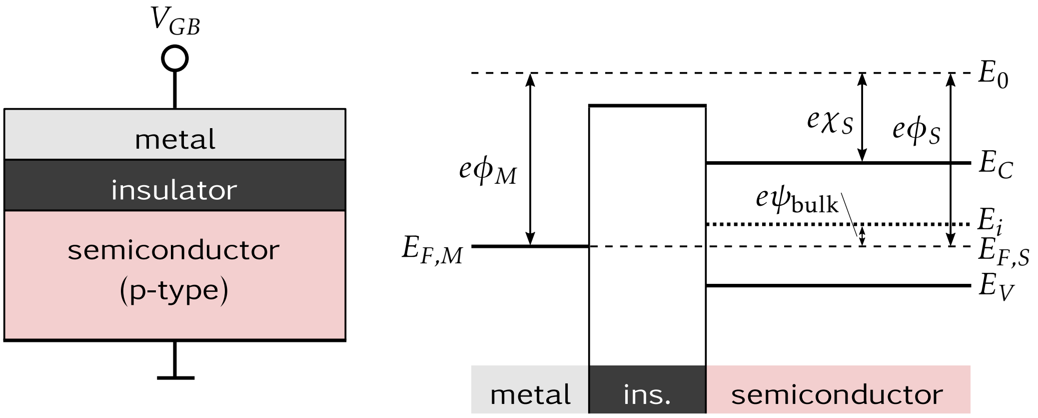

Figure 4.1.: Simple MIS capacitor setup and associated band diagram (adapted from [184]).

insulator/semiconductor interface, i. e., the whole device is devoid of electric fields [185]. The work function ϕ is the work $e\phi$ necessary to move a charge, here an electron with charge e, from the highest available energy state in the bulk, the Fermi level E_F, to the vacuum level E_0. Doping the semiconductor moves the Fermi level away from the intrinsic Fermi level E_i by $e\psi_{\mathrm{bulk}}$ in the bulk. Two material constants are further defined: the band gap E_g as the energy difference between valence band E_V and conduction band E_C, and the electron affinity χ as the energy difference between E_C and E_0.

In reality, metal and semiconductor work functions are generally not equal, but the flat band state can still be reached by applying the flat band voltage V_{fb} to the gate which compensates the work function difference ϕ_{MS} and any additional charges Q_S in or at the insulator capacitor [183]:

$$V_{\mathrm{fb}} = \phi_{\mathrm{MS}} - \frac{Q_S}{C^*_{\mathrm{ins}}} \tag{4.1}$$

This difference is also called the *built-in potential* since it adds a constant bias to the effective gate voltage, determining the direction of band bending at $V_{GB} = 0$. The following discussions are mainly based on [184] and [183] and refer, without loss of generality, to a device with p-type bulk, i. e., with electrons as minority charge carriers. The relations for n-type devices are, generally, the same with switched arithmetic signs.

For $V_{GB} < V_{\mathrm{fb}}$, the bands at the semiconductor/insulator interface are bent upwards. Majority charge carriers, i. e., holes, are drawn towards the interface and accumulate there, which is known as *accumulation state*. In this state, gate electrode and semiconductor act as the two plates of a capacitor with the insulator as dielectric. The measured capacitance per unit area, C^*, is:

$$C^*_{\mathrm{acc}} = C^*_{\mathrm{ins}} = \frac{\varepsilon_{\mathrm{ins}}}{d_{\mathrm{ins}}} \quad \text{with} \quad \varepsilon_{\mathrm{ins}} = \varepsilon_0 \varepsilon_{r,\mathrm{ins}} \tag{4.2}$$

For $V_{GB} > V_{\mathrm{fb}}$, the bands are bent downwards, leading to a *depletion* of holes in the layer below the electrode. This adds a capacitance in series with the capacitance across the insulator, the depletion region (DR) acting as a dielectric:

$$C^*_{\mathrm{DR}} = \frac{\varepsilon_s}{d_{\mathrm{DR}}} \tag{4.3}$$

$$C^*_{\mathrm{dep}} = \frac{C^*_{\mathrm{ins}} \cdot C^*_{\mathrm{DR}}}{C^*_{\mathrm{ins}} + C^*_{\mathrm{DR}}} = \frac{\varepsilon_{\mathrm{ins}}}{d_{\mathrm{ins}} + d_{\mathrm{DR}} \cdot \frac{\varepsilon_{\mathrm{ins}}}{\varepsilon_s}} \tag{4.4}$$

The width of the depletion region is given by

$$d_{DR} = \sqrt{\frac{2\epsilon_S \psi_{\text{surf}}}{eN_A}} \quad \text{with} \quad V_{GS} = \psi_{\text{surf}} + \frac{\sqrt{2\varepsilon_S e N_A \psi_{\text{surf}}}}{C^*_{\text{ins}}} \tag{4.5}$$

where N_A is the density of acceptors per unit volume in the semiconductor [185].

When the gate voltage increases above a certain threshold voltage V_{th}, electrons begin to dominate charge transport in the layer below the gate. This is known as *inversion state*. The threshold voltage is defined as the gate voltage at which the electron density at the semiconductor surface equals the hole density in the bulk (Figure 4.2), or $\psi_{\text{surf}} = 2\psi_{\text{bulk}}$. The threshold voltage can be broken down into three separate contributions: the flat band voltage defined in Equation 4.1, the actual potential change at the semiconductor surface, and the voltage drop over the oxide [184]:

$$V_{\text{th}} = V_{\text{fb}} + 2\psi_{\text{bulk}} + \frac{\sqrt{4\varepsilon_S e N_A \psi_{\text{bulk}}}}{C^*_{\text{ins}}} \tag{4.6}$$

The measured capacitance in the inversion region depends on the *alternating current* (AC) frequency because of the finite generation and recombination rates of the minority charge carriers. At low frequencies (LF), the electron density at the interface can follow the changes in the electric field, and the capacitance is the same as in the accumulation region. For high frequencies (HF), generation becomes too slow to maintain the electron density, creating,

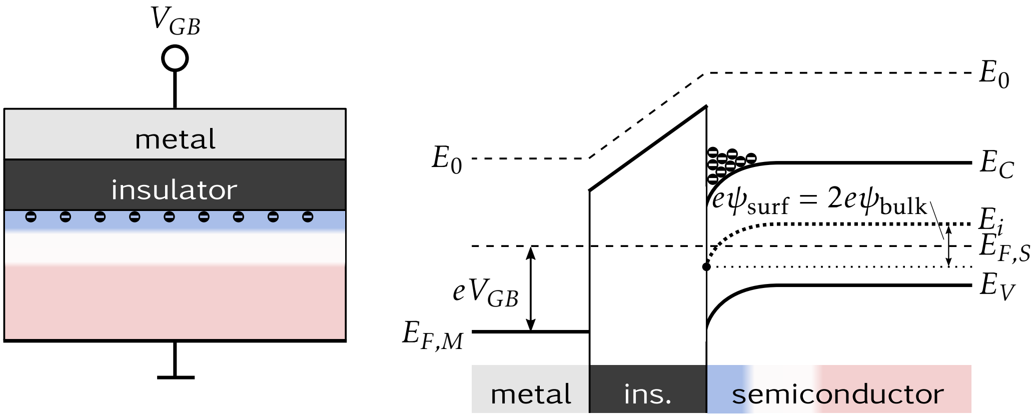

Figure 4.2.: MIS capacitor and band diagram at $V_{\text{GB}} = V_{\text{th}}$ (adapted from [184]).

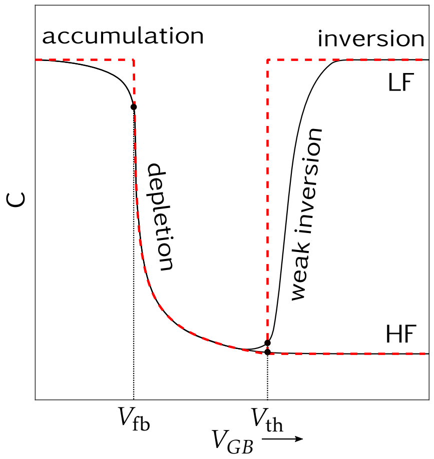

Figure 4.3.: Capacitance over gate bias according to the simple model equations presented here (red, dashed) and more realistically (adapted from [183], [184]).

again, a depletion zone, thus [183]:

$$C_{\mathrm{inv,LF}} = C^*_{\mathrm{acc}} \tag{4.7}$$

$$C_{\mathrm{inv,HF}} = C^*_{\mathrm{dep}} \quad \text{with} \quad d_{\mathrm{DR}} = \sqrt{\frac{4\epsilon_S \psi_{\mathrm{bulk}}}{eN_A}} \tag{4.8}$$

The characteristic curve gained from the simple model is shown in Figure 4.3 alongside a more realistic curve. The gas sensor effect (cf. section 4.3) exploits the change of the flat band voltage (Equation 4.1) with the charge Q_S on the oxide which, in turn, changes the threshold voltage (Equation 4.6) of the device. This leads to a shift of the characteristic curve in Figure 4.3 to the left with positive charges and *vice versa*, resulting in a capacitance change at a constant external gate bias.

The region at $V_{GB} = 0$ and, therefore, the arithmetic sign of the flat band voltage, determines whether the device is of the enhancement type (depletion or inversion region at $V_{GB} = 0$) or depletion type (accumulation region at $V_{GB} = 0$).

4.2. MIS field-effect transistor

The *metal-oxide-semiconductor field-effect transistor* (MISFET) can be seen as a MIS capacitor with a laterally elongated semiconductor part which includes one additional contact per side (Figure 4.4). These contacts are referred to as *drain* and *source* and are directly adjacent to, but isolated from, the gate. They are strongly n-doped (still considering a p-type bulk without loss of generality) so that a depletion region builds up around both contacts, i. e., no current can flow between drain and source. In the inversion region ($V_{GS} > V_{\mathrm{th}}$), on the other hand, an n-type channel forms below the insulator, connecting drain with source and enabling current flow. Hence, the main advantage of a MISFET over a MIS capacitor is, when used as a sensor, the significantly simpler readout, i. e., measuring a current instead of a capacitance.

The drain-source voltage V_{DS} adds an additional degree of freedom to the set of characteristic curves of the MIS capacitor. For *field-effect transistors* (FETs), source instead of body is usually considered the reference potential. For most applications, both are at the same potential to prevent current flow through the body diode, i. e., the pn-junction at the source/body interface.

In the *cutoff* region, i. e., $V_{GS} < V_{\mathrm{th}}$, the number of electrons in the channel below the insulator is negligible, just like the resulting drain current I_D. Above the cutoff region, i. e., $V_{GS} > V_{\mathrm{th}}$, the device can operate either in the *linear* region ($V_{GS} > V_{DS}$) or the *saturation* region ($V_{GS} < V_{DS}$). In the linear, or ohmic, region, the device acts like an ohmic resistor whose resistance can be adjusted through the gate bias:

$$I_{D,\mathrm{lin}} = K \cdot \left((V_{GS} - V_{\mathrm{th}}) - \frac{V_{DS}}{2} \right) \cdot V_{DS} \quad \text{with} \quad K = \frac{W}{L} \mu_n C^*_{\mathrm{ins}} \tag{4.9}$$

W and L are the channel's width and length, μ_n is the electron mobility in the channel.

The current I_D is influenced by the lateral electric field between drain and source as well as the transversal electric field between gate and body. When V_{DS} is increased in the saturation region, the potential difference between gate and body decreases close to the drain region. Once the effective potential difference drops below V_{th}, inversion is lost and the channel detaches from the drain region (*pinch-off*). The lateral electric field becomes very strong due to the almost infinitesimally small channel depth at the pinch-off point so that all electrons leaving the channel move at their (constant) saturation speed towards the drain. Consequently, the drain current becomes independent of V_{DS} in the saturation region. The dependence $I_D(V_{GS})$ is found as Equation 4.9 with $V_{DS} = V_{DS,\mathrm{sat}} = V_{GS} - V_{\mathrm{th}}$:

$$I_{D,\mathrm{sat}} = \frac{K}{2} \cdot (V_{GS} - V_{\mathrm{th}})^2 \tag{4.10}$$

The change of I_D with V_{DS} and V_{GS} is shown in Figure 4.5 for the simple model as well as with some non-ideal effects relevant to this work. The linear

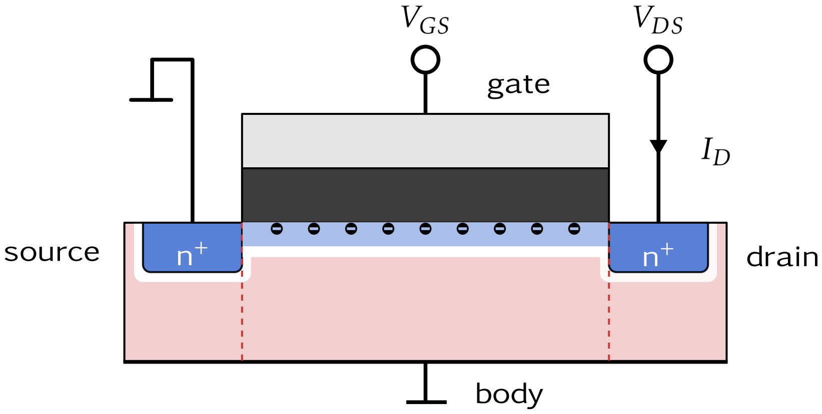

(a) Linear mode.

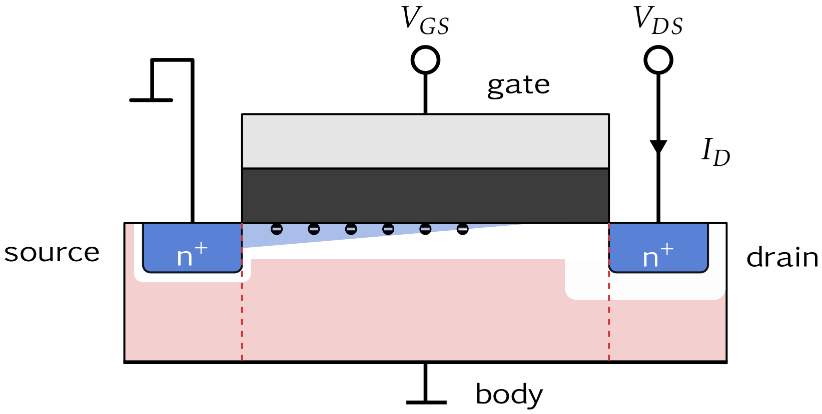

(b) Saturation mode.

Figure 4.4.: MISFET with indicated channel in (a) linear and (b) saturation mode (adapted from [184]).

current increase in the saturation region in Figure 4.5a is due to channel-length modulation [184], i. e., shortening of the effective channel length L with increasing V_{DS} because the pinch-off point moves closer to source. It can be accounted for by the channel-length modulation parameter λ, so that Equation 4.10 becomes:

$$I_{D,\text{sat}} = \frac{K}{2} \cdot (V_{GS} - V_{\text{th}})^2 \cdot (1 + \lambda V_{DS}) \tag{4.11}$$

Obviously, the drain current cannot increase infinitely with the gate bias as Equation 4.10 suggests. Figure 4.5b shows the characteristic curve leveling off above a certain gate bias which is due to both the limited number of electrons available and the electrons moving closer to the interface, thus being affected more by defect scattering [184].

The parameters summarized in the factor K (Equation 4.9) define, to a large portion, the FET's properties. One important property is the transconductance g_m,

$$g_m = \frac{\partial I_D}{\partial V_{GS}}, \tag{4.12}$$

which, in the saturation region, is the slope of the curve shown in Figure 4.5b. From a sensor point of view, it is the device's sensitivity with respect to

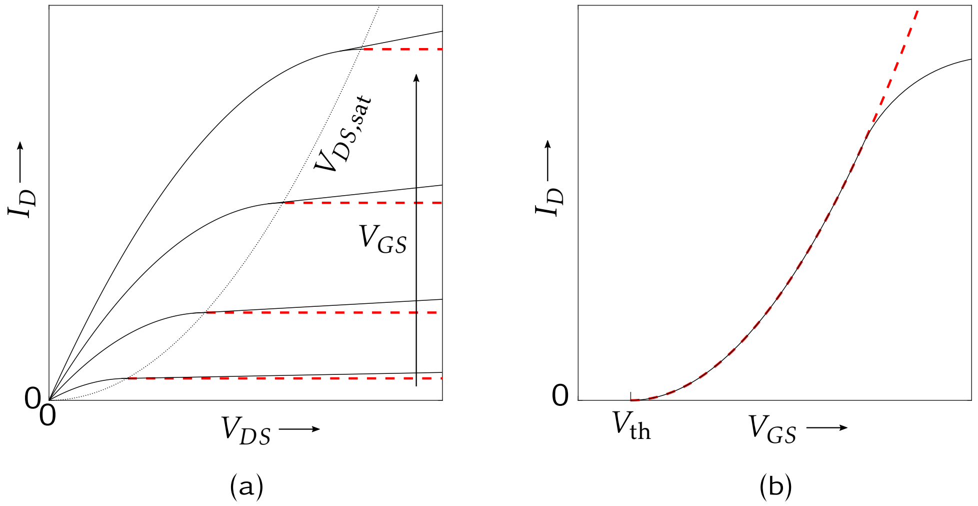

Figure 4.5.: Simple models (red, dashed) for (a) MISFET I/V curves over drain-source voltage and (b) over gate bias in saturation mode. The black lines incorporate non-ideal effects like (a) channel-length modulation and (b) mobility reduction (adapted from [184]).

changes in the effective gate bias. As pointed out in section 4.1, the effective gate bias is changed by oxide charges like adsorbed gas molecules (see also section 4.3).

A MISFET's temperature dependence is mainly governed by the electron mobility $\mu_n(T)$ which decreases with temperature due to phonon scattering:

$$\mu_n \propto T^{-x} \quad \text{with} \quad x = \frac{3}{2}. \tag{4.13}$$

At the same time, the threshold voltage decreases slightly with temperature due to a decrease of the Fermi level ψ_{bulk}:

$$\psi_{\text{bulk}} \propto \ln(T^{-x}) \quad \text{with} \quad x = \frac{3}{2} \tag{4.14}$$

The first effect decreases, the second increases the drain current, generally leading to a decrease of drain current with increasing temperature [184].

All transistors used in this work are normally-on (depletion-type), n-type MISFETs, i. e., an n-type channel exists between drain and source for $V_{GS} = 0\,\text{V}$.

4.3. Gas-sensitive field-effect transistor

The first GasFET, conceived in 1975 by Lundström *et al.* [37], was a MISFET structure, as described in section 4.2, with a dense palladium layer as gate electrode on a SiO_2 insulator. Palladium acts as a catalyst for many reactions, and here in particular for the dissociation and subsequent ionization or polarization of hydrogen (or hydrogen-containing) molecules. The resulting protons, i. e., H^+, or hydrogen atoms, can move almost freely through the metal [186] and quickly form an equilibrium between the surface, bulk and gas phase hydrogen concentration. Some of the protons move to the metal/insulator interface, adsorb on the oxygen atoms of the oxide (or, more rarely, on the metal [187]) and form dipoles with mirror charges in the metal (Figure 4.6) [188]. These dipoles add to the effective gate bias, changing the capacitance of a MOS capacitor or, here, the current flowing through the MISFET channel. Notably, surface dipoles in general also change a material's work function [189]. Hydrogen adsorption on palladium in vacuum (or in the gas phase) usually increases the metal's work function. Adsorption at the metal/insulator interface, however, decreases it. The hydrogen-induced dipole moment at the interface has further been found to be in the range of 2 to 4 Debye which is significantly larger than in vacuum [188]. The adsorption at the interface follows a Temkin isotherm, i. e., the adsorption

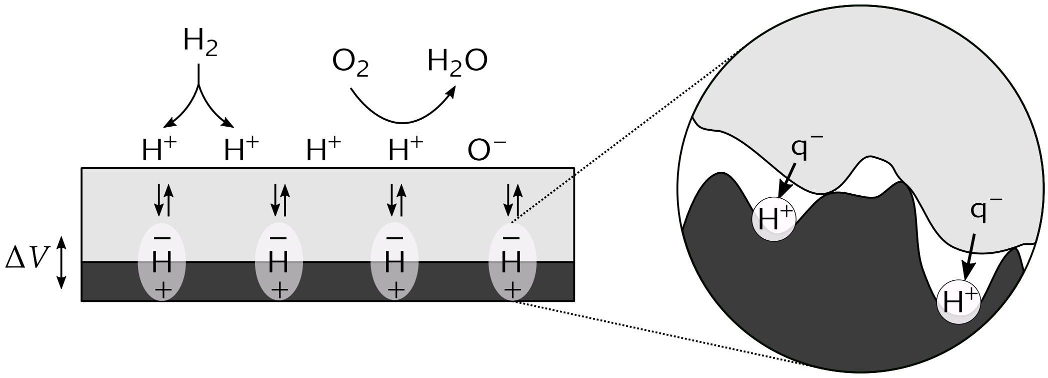

Figure 4.6.: Reactions on a GasFET with dense gate (left, adapted from [191]), and a microscopic view explaining dipole formation and direction at the interface (right, after [188]).

energy decreases linearly with the number of adsorbents [17], [190]. Both interaction between the adsorbents or adsorption sites at different energy levels have been proposed as reasons [187], [188].

In general, adsorption at the interface is favored over adsorption at the gas-facing surface, resulting in the interesting effect that the inactivation of surface adsorption sites (within certain limits), e. g., through poisoning, slows the response but does not decrease its equilibrium response [192]. Further, different from resistive-type metal oxide sensors, no oxygen has to be present to induce a sensor response. Actually, hydrogen and oxygen adsorbed on a catalyst react to water through the Langmuir-Hinshelwood mechanism [186], [193] so that oxygen lowers the hydrogen surface concentration and, thus, the sensor response.

The dense palladium layer is not only the gate electrode and a catalyst, but also acts as a filter allowing only protons to pass. This makes the sensor selective to hydrogen and certain hydrogen-containing gases, e. g., hydrocarbons [31], [191] which, however, at the same time limits its potential applications. A closer inspection of an "accidental" sensitivity to ammonia caused by cracks in a thin metal layer showed that a non-continuous or porous gate[1] (Figure 4.7) gives rise to a much wider range of detectable gases [191]. For the case of ammonia, it was shown that the three-phase boundaries between gas phase, metal, and insulator promote dissociation of ammonia [191], [195], possibly by the formation of acidic sites through proton adsorption on the bare oxide [188]. It was further shown that oxygen

---

[1] Other developments include FETs with *suspended* or *floating* gate [194] where an air gap between the sensitive layer and the oxide lifts the restriction of permeability and allows for a wide range of sensitive materials/structures to be used.

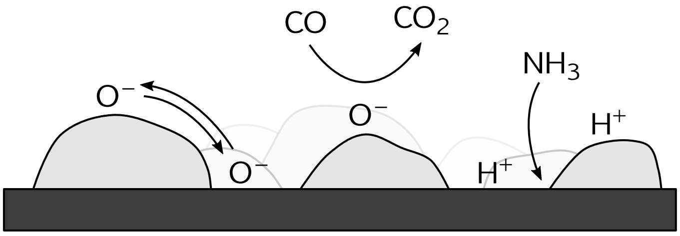

Figure 4.7.: Additional reactions (cf. Figure 4.6) on a GasFET with porous gate including spill-over, oxidation, and dissociation at three-phase boundaries (after [31]).

is necessary for ammonia to dissociate at temperatures up to 523 K [196]. The resulting hydrogen atoms are then detected as charges on the oxide or dipoles at the interface.

A porous gate further enables the detection of reducing and oxidizing gases like CO and NO_2, respectively. The involved process is believed to be very similar to the process on resistive-type metal oxide sensors [197] where the oxygen surface coverage determines the device's conductivity (see also section 1.2.3). Oxygen in the form of negatively charged ions spills over from the catalyst "islands" to the bare oxide, adding a surface charge which, after Equation 4.1 and Equation 4.6, influences the threshold voltage. The oxygen anions on the surface lower the effective gate voltage which, for an n-type device, lowers the drain current. Oxidizing or reducing gases increase or reduce the oxygen surface coverage, respectively, and, thus, influence the sensor signal.

All of the discussed sensing mechanisms are also valid for gas-sensitive MIS capacitors with the same gate structure. The GasFET's main advantage is the easier readout. Instead of measuring capacitance or impedance in the kHz or MHz range, the sensor signal is the channel conductance. It can be measured as voltage change at a fixed current or current change at a fixed voltage. Considering the characteristic curve in Figure 4.5a and Equation 4.11, the sensitivity in the saturation region with respect to changes in the effective gate bias for the respective operating mode is:

$$S_{\mathrm{Ifix,sat}} = -\frac{4I_{DS,\mathrm{sat}}}{\lambda K}(V_{GS} - V_{\mathrm{th}})^{-3} \tag{4.15}$$

$$S_{\mathrm{Vfix,sat}} = K(V_{GS} - V_{\mathrm{th}}) \tag{4.16}$$

Typically, $K, \lambda \ll 1$ hold, and $I_{DS,\mathrm{sat}}$ is in the range of µA or low mA for GasFETs, so that the sensitivity is larger for fixed current operation close to the threshold voltage. Without a very stable and low-noise current source, however, this mode of measurement results in a poor signal-to-noise ratio. Moreover, constant current can quickly lead to unintended operation in the linear region with a different behavior. Hence, the more stable fixed voltage operation is used in this PhD project. If not indicated otherwise, the sensor signal is the drain current at $V_{DS} = 4\,\mathrm{V}$, i. e., in the saturation region.

The first GasFET generations were based on a silicon substrate, limiting their operating temperature to 250 °C [198] due to silicon's relatively small band gap of $E_{g,Si} \approx 1.1\,\mathrm{eV}$. A high operation temperature (range) is desirable to accelerate reactions on the sensor like ad- and desorption, influencing speed and repeatability, and to change the catalytic activity or induce non-equilibrium states with TCO, influencing selectivity and sensitivity. The temperature limitation was overcome with the development of SiC-FETs with a considerably larger band gap[2] than silicon ($E_{g,4H-SiC} \approx 3.3\,\mathrm{eV}$). SiC-based field-effect devices can operate up to 1000 °C with a time constant for gas responses in the order of milliseconds [198]. In combination with its chemical inertness, such devices are well-suited for measurements in flue gases and exhaust streams [31]. Gas-sensitive field-effect devices can be produced in standard semiconductor processes with exception of the gas-sensitive gate contact (commonly a noble metal catalyst) which can be added in one additional step at the end. This compatibility potentially offers cheap large-scale fabrication of GasFET/SiC-FET devices [191].

---

[2] Alternatively, higher operating temperatures of more than 400 °C can be achieved with the Silicon-On-Insulator (SOI) technology [199].

5. Hardware and software

5.1. Sensor devices

In this work, two types of device structures were used: depletion-type MIS capacitors with n-doped bulk, and normally-on, n-type SiC-FETs. The SiC-FET samples were kindly provided by SenSiC AB, Kista, Sweden, and the capacitor samples were processed by Dr. Mike Andersson at Linköping University. A detailed description of the fabrication process is given in [31]. The thickness of the porous gate metalization is approximately 25 nm with elongated pores of up to 30 nm width and 200 nm length for platinum on SiO_2 [200]. The whole gate has a length L of 8 µm to 10 µm and a width W of 300 µm. The substrate is 4H-SiC and the gate material stack consists of 50 nm SiO_2, 25 nm Si_3N_4, and 5 nm SiO_2 as the top layer.

It should be noted that the properties of devices within one batch and between batches can vary significantly. The threshold voltage for depletion-type devices varies from −3 V to 0 V on one wafer, supposedly due to changes in thickness of the active n-type layer or the doping level close to the wafer edges [31]. The variation is much less for enhancement devices (3 V to 4 V), but the temperature dependence of their threshold voltage is one magnitude larger compared to depletion devices [31]. Variations and drift of the saturation current have also been observed [201].

Each SiC-FET chip contains up to four independent FET structures, two of which usually have the gate contact grounded, while an arbitrary gate bias can be applied to the other two. Newer designs feature only two FET structures, both with accessible gate, on the chip. Each chip further contains an internal temperature sensor at the front and an internal heater at the backside (Figure 5.1b). However, both of these structures are currently still being optimized for stability and reproducibility. Instead, each sensor chip is mounted on a ceramic heater (Heraeus Holding GmbH, Hanau, Germany) along with a commercial Pt-100 temperature sensor. Both the sensor chip and the Pt-100 are glued side by side with a two-component ceramic bonding agent (Ceramabond 571 by Aremco, Valley Cottage, USA). As a result, the temperature measured by the Pt-100 can only give a rough indication of the chip's actual front-side temperature. The manually applied ceramic glue

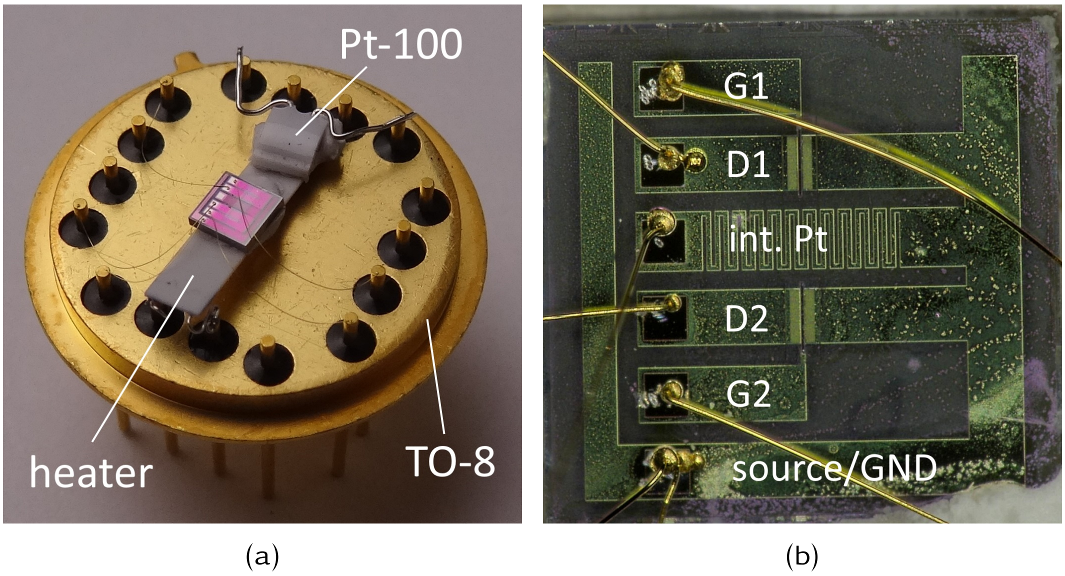

(a) (b)

Figure 5.1.: (a) SiC-FET and Pt-100 temperature sensor glued onto a ceramic heater and mounted on a TO-8 header, and (b) zoom on the chip structure with two FET structures.

adds a certain individual temperature error per device, and dynamic errors can arise from quick front-side temperature changes through turbulences. Moreover, the whole setup is relatively large and leads to a large thermal time constant in the range of seconds. Note that with the more mature Si technology, thermal time constants of 100 ms could be achieved instead [202]. The ceramic heater is bonded to a TO-8 header with 16 pins, as are the internal contacts of the sensor chip (Figure 5.1a).

5.2. Hardware and electronics

All measurements are done with the sensor(s) mounted in a stainless-steel measurement chamber. There are two chamber types, one which holds one sensor, and the other which holds up to three, each rotated by 90°. The gas channel runs perpendicular to the sensor surface and can be connected to the gas mixing system with 1/8 inches Swagelok connectors. The dead volume is around 3 ml. More details are given in [200].

The TO-8 header is connected with a custom-made *printed circuit board* (PCB) and a 15-pin D-SUB connector to an electronics board (Figure 5.2) developed and manufactured by 3S GmbH, Saarbrücken, Germany. It can set and measure the voltage and/or current of one FET structure per chip. It further sets gate and body bias, and sets and measures the heater temperature. Temperature control is achieved with a Wheatstone bridge which keeps the heater resistance at an adjustable ratio to a reference resistance. All specifications for the latest version of the electronics board are given in Table 5.1. Compared to the previous version, the new board implements some minor improvements, like a switchable current measurement range, a *general purpose input/output* (GPIO) pin, and easier mechanical connectivity. The board communicates via *Universal Serial Bus* (USB) and a simple protocol with a host PC.

An extension board was later designed and built in this PhD project. It can be used to reroute any of the header pins 1-4 to the temperature sensor pins which gave more flexibility when bonding the internal temperature sensor. Further, the bulk bias can be intercepted and used to switch an external heater on or off or to supply a variable current between -70 and +70 mA to, e. g., a *light-emitting diode* (LED). The circuit diagram and PCB design can be found in the appendix (section 1).

5.3. Software

At the start of this project, a LabVIEW software was available for communication and data recording with the 3S board [200]. Temperature and gate bias cycles could be configured, saved and loaded, and live manipulation of all sensor parameters was possible.

Nevertheless, a new software was developed in Python during this PhD project (Figure 5.3). In contrast to LabVIEW, Python, as a text-based programming language, enables efficient use of version control systems like git or *Apache Subversion* (SVN). Such systems log all changes to the source code, increasing transparency, allow for different versions (*branches*) in the same repository, and enable collaboration on software projects in general. The new software, *FETcontrol*, is OOP-based, increasing maintainability and extendability. It is publicly available under the MIT License on GitLab [203].

The new program supports communication with an arbitrary number of boards in one instance. With the LabVIEW version, one instance had to be started for each board, which made, e. g., thermal crosstalk between sensors in the same measurement chamber harder to identify due to the phase shift between the instances. The new program further detects all connected boards automatically based on the ID of their FTDI USB chips. This improves the older, manual, error-prone selection of boards based on a non-indicative port number. Once the board is identified, both programs can automatically load a predefined set of individual calibration parameters.

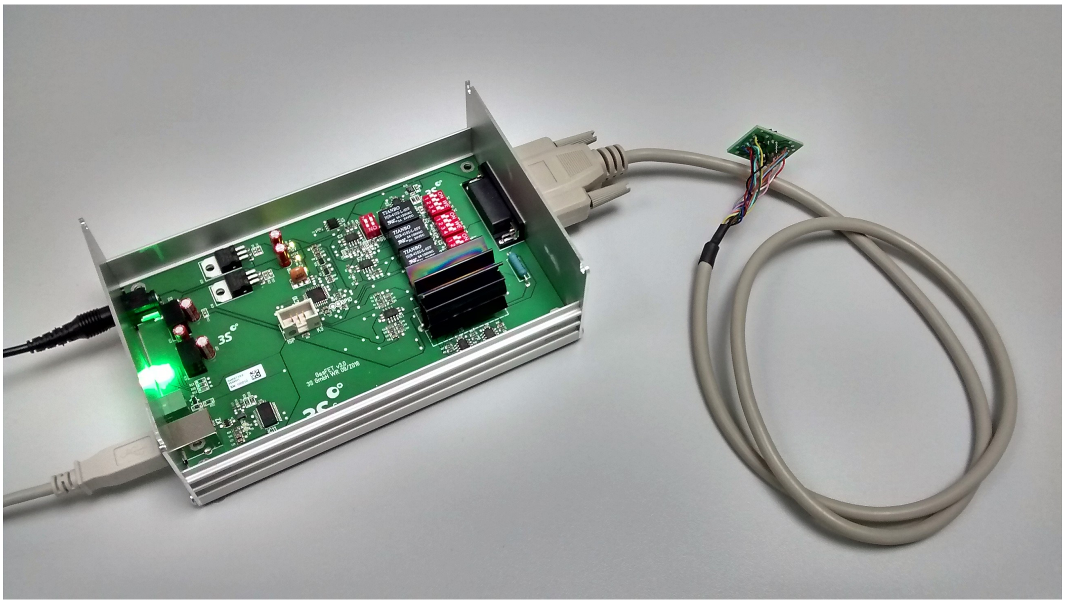

Figure 5.2.: Picture of the hardware board with kind permission from Wolfhard Reimringer, *3S GmbH - Sensors, Signal Processing, Systems, Saarbrücken, Germany* (3S GmbH). The red *dual in-line package* (DIP) switches allow chosing measurement range, temperature sensor (internal/external) and sensor structure on the chip to measure.

Table 5.1.: Specifications of the GasFET hardware board.

parameter	action	range	resolution	
drain-source voltage V_{DS}	set	0. . . 12 V	8 bit	46.9 mV
drain-source voltage V_{DS}	measure	0. . . 12 V	14 bit	732.4 µV
drain current I_D	set	0. . . 500 µA	8 bit	2.0 µA
		0. . . 1000 µA	8 bit	3.9 µA
drain current I_D	measure	0. . . 500 µA	14 bit	30.5 nA
		0. . . 1000 µA	14 bit	61.0 nA
gate bias V_{GS}	set	−7. . . 7 V	13 bit	1.7 mV
bulk bias V_{BS}	set	−7. . . 7 V	13 bit	1.7 mV
temperature T	set	40. . . 550 °C	8 bit	2.0 °C
temperature T	measure	40. . . 550 °C	10 bit	0.5 °C

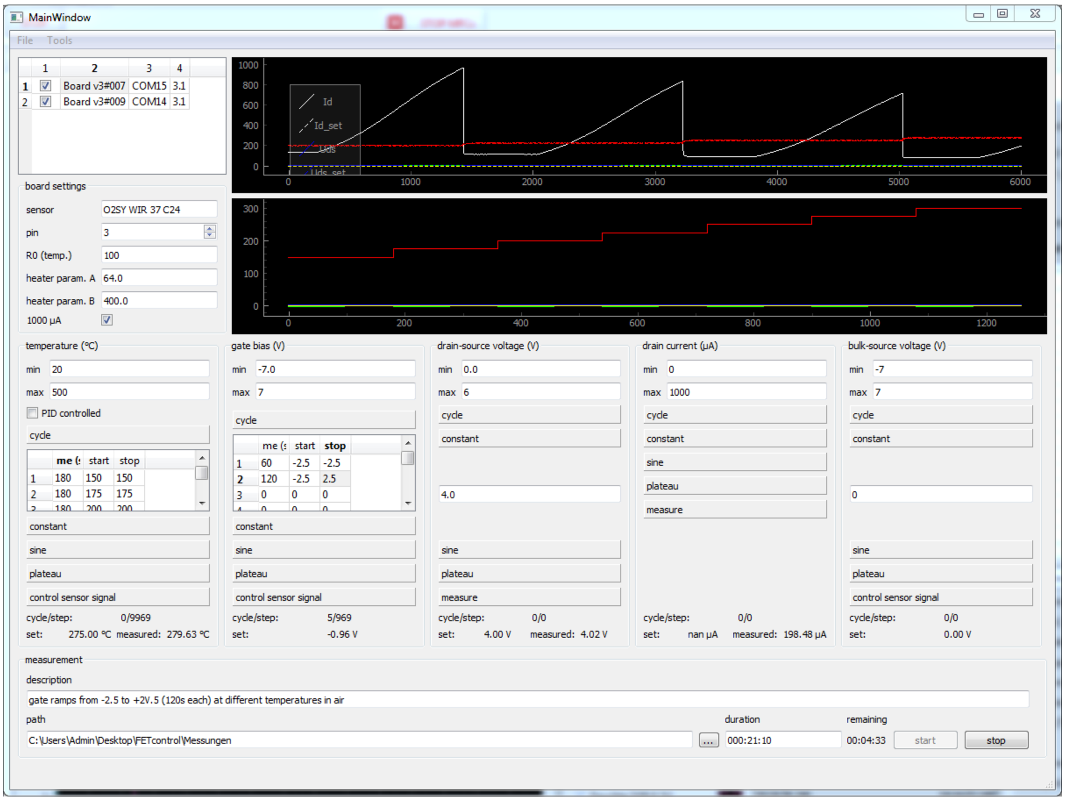

	1	2	3	4
1	☑	Board v3#007	COM15	3.1
2	☑	Board v3#009	COM14	3.1

board settings
sensor O2SY WIR 37 C24
pin 3
R0 (temp.) 100
heater param. A 64.0
heater param. B 400.0
1000 µA ☑

temperature (°C)
min 20
max 500
☐ PID controlled

	me (s	start	stop
1	180	150	150
2	180	175	175
3	180	200	200

cycle/step: 0/9969
set: 275.00 °C measured: 279.63 °C

gate bias (V)
min -7.0
max 7

	me (s	start	stop
1	60	-2.5	-2.5
2	120	-2.5	2.5
3	0	0	0
4	0	0	0

cycle/step: 5/969
set: -0.96 V

drain-source voltage (V)
min 0.0
max 6
4.0
cycle/step: 0/0
set: 4.00 V measured: 4.02 V

drain current (µA)
min 0
max 1000
cycle/step: 0/0
set: nan µA measured: 198.48 µA

bulk-source voltage (V)
min -7
max 7
0
cycle/step: 0/0
set: 0.00 V

measurement
description
gate ramps from -2.5 to +2V.5 (120s each) at different temperatures in air
path
C:\Users\Admin\Desktop\FETcontrol\Messungen
duration
000:21:10
remaining
00:04:33

Figure 5.3.: GUI of the latest version of *FETcontrol* showing a signal history (top plot) and all configured cycles (bottom plot). Connected boards are shown in the top-left table with user-definable parameters below. Each cycle type (five columns below the plots) has several modes to choose from.

The old LabVIEW program handled temperature and gate bias in a special way since these were the only parameters being cycled. The new program, however, abstracts all parameters, i. e., drain-source voltage, drain current, gate bias, bulk bias, and temperature, as cycles whose values are generated from predefined functions. Each function is active for a certain time window, which is then followed by the next time window. The cycle's total duration is the sum of all time window durations. Several functions are implemented, like constant, slope, and sine wave. The first two can be quickly defined in a three-column table with duration, start value, and end value, inspired by a user interface implemented by 3S GmbH. Compared to the old LabVIEW software, abstracting all values as cycles simplifies some tasks greatly. For example, recording an I/V curve like in Figure 4.5a could not be done in the old program, but can now simply be defined as a linear increase of V_{DS}. Similarly, the bulk bias, while seldom (and not at all in this work) used with the sensor itself, can be used to control external hardware like the heater of a pre-concentrator or an UV-LED, which would have required major changes in the old software.

Some parameter's cycles can be extended with special functionality. For example, there is a software *proportional–integral–derivative* (PID) controller implemented for the temperature cycle which establishes a closed-loop control of the temperature based on the external Pt-100. Without closed-loop control, an experimental characteristic curve has to be determined prior to each measurement with a new sensor with a two-point heater power calibration. It is described by the temperature offset and slope. With closed-loop control, this step is no longer required, making it especially beneficial for use in the field and/or by untrained users. In theory, closed-loop control can also counteract sudden temperature changes through turbulences or air temperature changes. Unfortunately, this is not possible at the moment for two reasons. Firstly, the external Pt-100 reacts much slower than the sensor surface. Secondly, the maximum sampling rate of the board is around 20 Hz (10 Hz is used in all measurement for reliability) because each measurement must be explicitly requested. This rate is too low for effective control and leads to higher noise compared to open-loop control, which is why most measurements presented here were made in the open-loop configuration.

Another parameter with special functionality is the gate bias. It can be used to keep the drain current at a constant level through a software PID controller. To enable this mode, PID parameters for the gate bias must be given, and both drain-source voltage and drain current must be set in the software. The gate bias used for compensation is then equal to the internally added gate bias through the gas and, thus, gives a reading "closer to the actual physics". This compensation operation also means that the effective gate bias, and, thus, according to Equation 4.16, the sensitivity, are constant. A similar principle can be used to improve the linearity of magnetic sensors [204] and gate bias compensation in particular has been employed to read out gas-sensitive MIS capacitors [205].

One more improvement in the new program concerns data recording. The old program could only save plain text *comma-separated values* (CSV) files, either a data matrix with one chosen cycle per row, or all parameter values over time with one parameter per column. Some meta-data were saved in the filename which is very unsafe and can easily lead to information loss. Now, all parameters are written to a *Hierarchical Data Format 5* (HDF5) file, a widely used binary file format [206]. A binary format stores data much more effectively compared to plain text which, in combination with the built-in compression, can decrease file size and loading times drastically. The file can be divided in directories (*groups*) and files (*datasets*), so that each board is represented as one dataset. The complete configuration, including cycles, PID and board parameters, start time, and user-supplied information like sensor ID and comment, is encoded as JSON and saved as meta-data directly in the HDF5 file. This JSON has the same format as normal configuration files saved in the program, so that the whole configuration can directly be loaded and executed from the same file as the data. Documenting all these parameters manually would be tedious and error-prone and, potentially, require additional work if they are needed later for data evaluation in a different program.

In its current version, HDF5 is missing journaling, which means that complete data loss can occur when the file is open and the program ends unexpectedly, e. g., through power loss. The chance of this happening is minimized by collecting the data in volatile memory and writing it only once every minute to the file.

6. Materials

6.1. Overview

The response of field-effect devices depends on structure and composition of both the gate electrode and insulator material. Several insulator materials have been examined, including SiO_2, Al_2O_3, Si_3N_4, and Ta_2O_5 [205], [207]. With a dense gate electrode, differences between these materials have been found in regard to detection limit, saturation limit (ranging from $10\,\mathrm{ppm_v}$ to $> 10\,000\,\mathrm{ppm_v}$), saturation response, and speed of recovery for hydrogen [205]. In the same work it has been shown that the response increases with the density of oxygen atoms in the surface of the oxide. Indeed, oxidation of Si_3N_4 in a porous-gate device could significantly increase the hydrogen response, and another work confirms its dependence on oxygen presence for GaN [208]. Slow drift effects associated with sodium contamination of SiO_2 [209] could further be eliminated by replacing it with any of the other mentioned oxide materials [207], [210]. Further works have found an increased response to hydrogen and hydrocarbons for metal-oxide layers like WO_3 [211], TiO_2 [212], Ga_2O_3–ZnO [213], and CeO_2 [214] between an electrode and a SiC bulk, creating a Schottky diode. This increase is, however, mostly attributed to a change in conductivity of the oxides rather than a field-effect.

Regarding the gate electrode electrode material, the most common materials are palladium, platinum, and iridium (Pd, Pt, Ir). As discussed before, changing the structure from a dense to a porous layer enables the detection of species other than hydrogen through exposing the oxide [191]. The level of porosity also plays a role [215]. First and foremost because smaller pores lead to a larger catalyst surface which can actually decrease the hydrogen response [191], as well as more three-phase boundaries important for dissociation of, e. g., NH_3. It also influences the switching point of the binary carbon monoxide response [33] caused by carbon monoxide temporarily poisoning the catalyst at high CO/O_2 ratios. With smaller metal “islands”, the oxygen coverage on the metal can more quickly be restored with oxygen from the insulator surface. The different types of material differ mainly in their catalytic activity. Platinum, for example, has a lower activation energy for the reaction of hydrogen and oxygen to hydroxyl groups, effectively lowering the hydrogen response of platinum as compared to palladium [216]. Iridium has, in general, higher working temperatures compared to platinum, e. g., for ammonia detection 225 °C were found optimal for platinum and 325 °C for iridium [191].

6.2. Tungsten trioxide

From the previously mentioned oxide materials, especially WO_3 is a prominent semiconductor used in MOS sensors [217], [218] and has shown good results for detection of NO_x [219]–[221], NH_3 [222], H_2 [223], and VOCs [224] like ethanol [222], [223], [225] acetone [222], and naphthalene [226], amongst others. It has, however, been studied very little with regard to field-effect devices. In [219], a GasFET with WO_3 gate was found suitable for NO_2 detection, despite cross-sensitivity to NO and humidity, and in [211], a WO_3 layer sandwiched between the Pt electrode and SiC bulk of a Schottky diode increased the hydrogen response by 300 %. However, to the best of the author's knowledge, WO_3 has never been used as oxide layer in a GasFET.

WO_3 is a non-stoichiometric material whose n-type semiconductor behavior arises from oxygen vacancies, similar to SnO_2, the classic material for MOS sensors. The sensing effect is, thus, similar (cf. section 1.2.3), however, not identical. Differences between SnO_2 and WO_3 have been reported, e. g., regarding the influence of humidity which reduces the former but oxidizes the latter [227]. With regard to field-effect devices, the relatively high oxygen ratio of WO_3 promises many adsorption sites for hydrogen and protons, increasing the response to VOCs in particular. At the same time, however, it should be noted that WO_3 is an acidic oxide and, thus, promotes formation of protons from water. Hence, a relatively strong dependence on humidity can be expected.

The following discussions are based on the data presented in [228] which have been reevaluated.

6.2.1. Preparation

A dense WO_3 layer was deposited on top of the native SiO_2 layer in the gate area using *pulsed laser deposition* (PLD) by the group of Prof. Jyrki Lappalainen at Oulu University, Finland. PLD is a *physical vapor deposition* (PVD) technique where material from a rotating target (here pure WO_3) is evaporated by a powerful laser, eliciting a local plasma plume, and then travels through a vacuum onto the sample. The laser used at Oulu University was a XeCl excimer laser with 308 nm wavelength, 25 ns pulse length, and a pulse frequency of 5 Hz [228]. The whole system was first evacuated down to 10×10^{-3} Pa, and then brought to 5 Pa by adding oxygen. The sample was heated to 550 °C during deposition, resulting in a 50 nm thick, dense, flat WO_3 layer (Figure 6.1) composed of monoclinic epsilon and gamma phases [228].

On top of the WO_3 layer, 30 nm of porous iridium was deposited at *Linköping University* (LiU) via *direct current* (DC) magnetron sputtering at 6.6 Pa. The PLD specimen is compared with an untreated specimen on which only iridium was deposited, i. e., the material stacks are Ir/WO_3/SiO_2 and Ir/SiO_2, respectively, both followed by Si_3N_4 and SiO_2 as described in section 5.1. For simplicity, the two specimens will from here on be referred to as *WO_3* and *SiO_2* after their exposed oxide.

The aim of this experiment was to compare the performance of the WO_3 and SiO_2 sensor under semi-real conditions for IAQ (or similar) applications. Ethanol was chosen as a common interfering background gas coming from perfume, cosmetics, or beverages. It should, ideally, not affect the sensor response as it does not pose a threat to human health in the low ppm_v concentration range. Naphthalene, on the other hand, has a recommended annual average exposure limit of 1.9 ppb_v, which is seldom exceeded, but significantly higher concentrations were found in some cases [229]. It is the simplest member of the group of *polycyclic aromatic hydrocarbonss* (PAHs), the exposure to which has been linked to increased cancer risk [230], [231]. Hence, the measurement profile in Figure 6.2a contains ramps from 0 ppb_v to 40 ppb_v naphthalene in steps of 5 ppb_v, measured on constant ethanol concentrations of 0, 1, 2.5, and 5 ppm_v, respectively. Each naphthalene exposure lasted 30 min, followed by 60 min of background gas. Zero air with

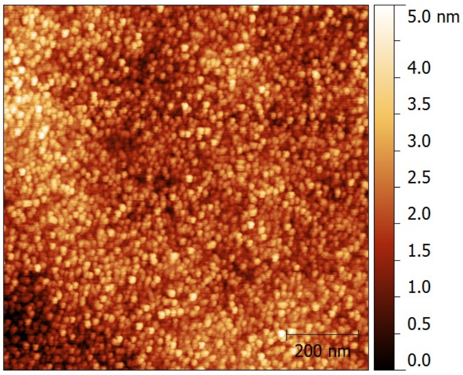

Figure 6.1.: AFM micrograph of the deposited WO_3 layer.

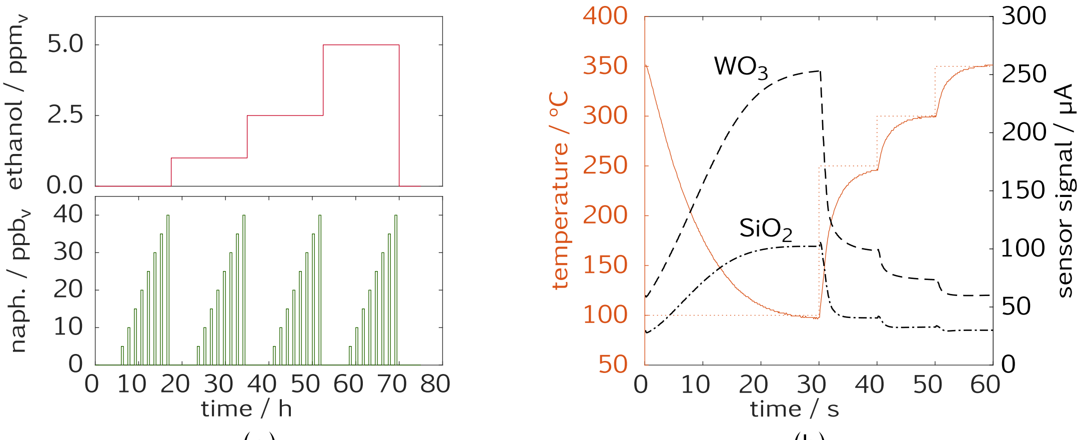

(a)

(b)

Figure 6.2.: (a) Gas profile with four ethanol background plateaus and naphthalene ramps. (b) Temperature cycle and resulting sensor signals.

50 %RH was used as the carrier gas.

The sensors were both driven with identical temperature cycles with a total duration of 60 s and four temperature plateaus of 100, 200, 250, and 300 °C (Figure 6.2b). The duration of the temperature plateaus was chosen so that the desired temperature was reached within the plateau. Figure 6.2b also shows the resulting sensor signals in air. The difference in amplitude is most likely due to electrical differences in the sensor chips, like a different doping level or varying oxide thickness. However, the qualitative behavior is the same for both sensors.

6.2.2. Response and features

The quasistatic signals in Figure 6.3 were extracted from the cyclic sensor signal by plotting the last point of the signal of each temperature plateau over the cycle number, that is, one point every minute. It shows an approximation of what the sensor would behave like if it was driven at a constant temperature. In order to emphasize the gas reaction, which is easily masked by the strong temperature dependence, the quasistatic signals were generated from difference cycles. To this end, the average cycle shape of the cycles 200 to 300, i. e., the baseline in air before the first naphthalene exposure, was subtracted from all cycles. This eliminates the large changes introduced by the electronic temperature dependence of the device and turns the sensor signal into a sensor response.

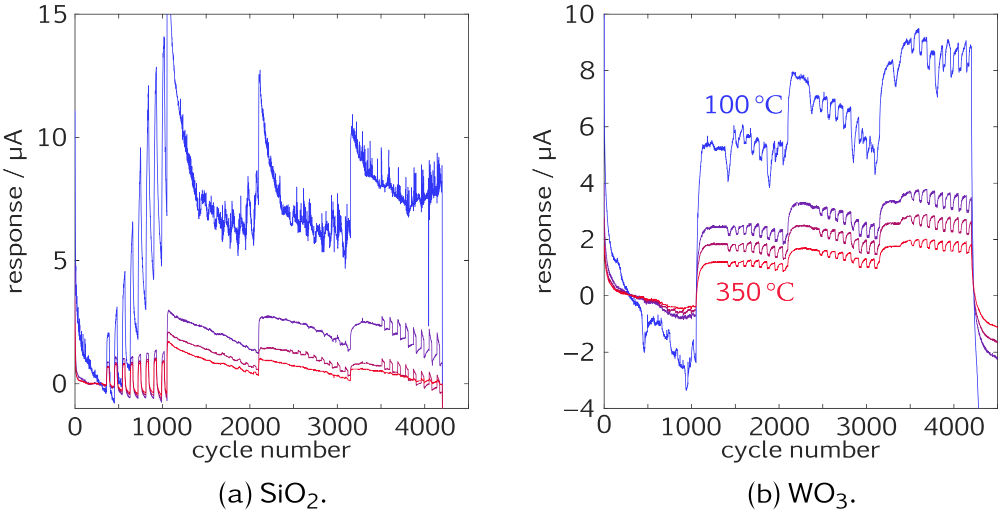

(a) SiO_2. (b) WO_3.

Figure 6.3.: The quasistatic signals produced from points at the end of each temperature plateau (cf. Figure 6.2b).

It is obvious that the lowest temperature (100 °C, blue) leads to a highly unstable signal with little response except for the first naphthalene ramp in Figure 6.3a. The SiO_2 specimen at 100 °C shows by far the highest sensitivity towards naphthalene, however with very long recovery times resulting in a strong upward drift. Also, the signal vanishes almost completely upon the introduction of ethanol at all temperatures. Remarkably, the response to naphthalene seems to return and even increase again with higher ethanol concentrations. The signal shape of these responses is, however, different from the reaction observed at 0 ppm_v ethanol, indicating a different sensing mechanism dominating in ethanol. The naphthalene response for WO_3 (Figure 6.3b) has the expected shape and only minor variations in magnitude for all three non-zero ethanol concentrations. For 0 ppm_v ethanol, however, the response disappears almost entirely. This comparison between the two top oxides is a clear indication of the influence of the oxide on the gas sensing.

Both sensors exhibit a continuous downward drift over time, the strongest being SiO_2 in ethanol between −260 and −62 nA/h, depending on temperature. The WO_3 specimen only drifts between −83 nA/h to −5 nA/h, which was determined as the slope of a linear fit over the 2.5 ppm_v ethanol plateau. A baseline correction done by subtracting a linear fit from the quasistatic signal of each cycle point was tested, but did not change the qualitative outcomes of the further evaluation. Moreover, this kind of baseline correction can only be done if the gas profile is known and has, thus, little relevance for real applications.

As the gas profile is, however, known in this case, the cycle shapes can easily be compared in different atmospheres. Figure 6.4 shows the average cycle shape of the last 15 cycles for each naphthalene exposure in 0 $\mathrm{ppm_v}$ ethanol (green, top plot), as well as the average cycle shape of the 15 cycles just before the first naphthalene exposure of each ethanol plateau (red, bottom plot). The darker the color, the higher the concentration, except for the black cycle in the top plot which stands for 0 $\mathrm{ppb_v}$ naphthalene. Both sensors exhibit a reaction to naphthalene with its amplitude increasing with the concentration. The reaction is larger for SiO_2, which could be expected from the quasistatic plot. An important observation is that the reaction to naphthalene is negative for WO_3 and positive for SiO_2, whereas both oxides exhibit a positive reaction to ethanol. This behavior can also be seen comparing the two quasistatic plots in Figure 6.3 and is another indication of two distinctly different sensing mechanisms for both materials.

The positive response towards naphthalene with SiO_2 is consistent with other, similar measurements [232]. Presumably, dehydrogenation or oxidation of naphthalene, or a combination of both, is causing this response. Dehydrogenation of benzene, C_6H_6, down to C_6H_3 has been reported to start around 150 °C on platinum [233], [234]. As naphthalene is the simplest polycyclic aromatic hydrocarbon made up of two fused benzene rings, a similar reaction can reasonably be assumed. Also oxidation of naphthalene to CO_2 and H_2O is possible and has been reported to start around 200 °C for Pt supported on SiO_2 [235]. The process removes oxygen and, therefore, negatively charged ions, from the sensor surface through the following reaction [236]:

$$\mathrm{C_{10}H_8 + 4.5\,O_2 \longrightarrow C_6H_4(CO)_2O + 2\,CO_2 + 2\,H_2O} \tag{6.1}$$

Regarding ethanol, similar processes are assumed to either release a proton or remove an oxygen ion [225], [237]–[239]:

$$\mathrm{CH_3CH_2OH + O \longrightarrow CH_3CHO + H_2O} \tag{6.2}$$

At the lowest temperature, 100 °C, recovery happens very slowly after each exposure which eventually leads to a pronounced upward drift with SiO_2 (Figure 6.3). This suggests slow desorption of naphthalene, blocking active sites or hindering the replacement of oxygen ions on the sensor surface. In 1 $\mathrm{ppm_v}$ ethanol, the low-temperature response returns to a smaller, more stable value which could be explained by ethanol blocking most active sites for naphthalene detection. Taking ethanol's two orders of magnitude higher vapor pressure at 100 °C [240] as a rough indicator, it should desorb relatively

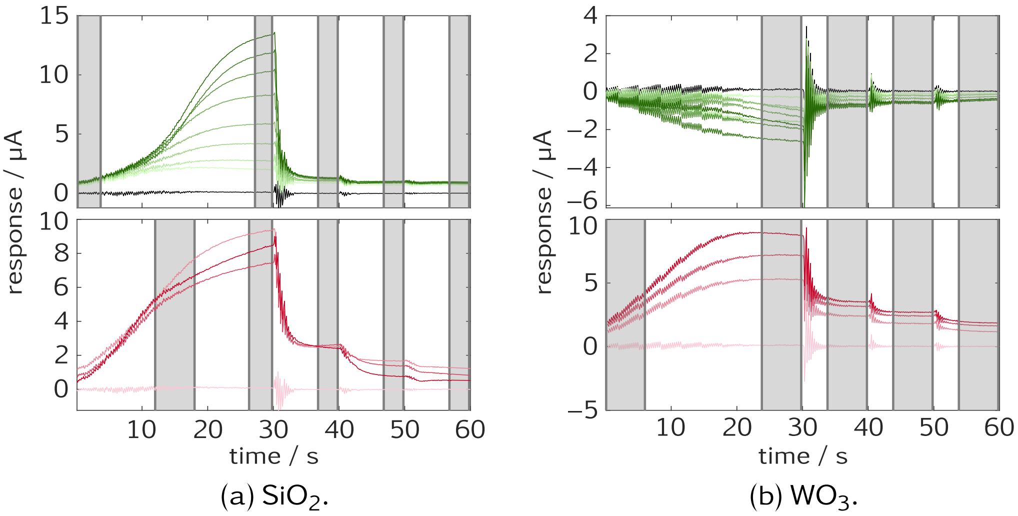

(a) SiO_2.

(b) WO_3.

Figure 6.4.: Average cycle shapes in naphthalene (top, green) and ethanol (bottom, red) at different concentrations without the respective other gas. Ranges (gray) in the upper plot define mean value features, ranges in the lower plot define slope features. Both feature types are always extracted and separated here only for visual clarity.

quickly compared to naphthalene[1]. Due to the much higher concentration of ethanol compared to naphthalene, however, ethanol nevertheless dominates the processes on the sensor surface and essentially masks any naphthalene response. The slowly increasing response (and its lower time constant) to naphthalene with higher ethanol concentration observed at intermediate temperatures requires further investigation. It can be speculated that protons from dissociated ethanol molecules act as Brønsted acid sites on the sensor surface. A similar effect is proposed for the dissociation of ammonia at three-phase boundaries [188]. Such sites have further been reported on WO_3 in humid air and promote ring fission of cyclic molecules [236] which could lead to a larger response to naphthalene the more ethanol is present and dehydrogenated. This can also be part of the explanation for the behavior of the WO_3 sensor which shows almost no response without ethanol. The inverse direction of the response on WO_3 should, however, be investigated in a future work.

---

[1] Vapor pressure is defined for an equilibrium between gas and liquid phase and, thus, does not necessarily describe ad- and desorption processes at a surface, i. e., solid phase, very well.

The gray ranges in Figure 6.4 mark the features extracted from the cycles: mean value features in the top plot, and slope features in the bottom plot. Note, however, that the separation of features and gases is only for visual clarity, i. e., both feature types are computed for all cycles. In the first evaluation of the data, as reported in [228], while the same types of features were used, many more features were extracted and later selected using a significance criterion. In this reevaluation, a more heuristic approach is employed using DAV^{3}E's feature preview (Figure 3.5b), i. e., the feature ranges were defined so that the resulting features from the average cycles showed a clear separation and order. Not only the average cycles shown in Figure 6.4 were used, but also average cycles including naphthalene in ethanol background and *vice versa*, as quantification of naphthalene independent of the ethanol background is the ultimate aim. The resulting cycle shapes are similar to superpositions of average naphthalene and ethanol cycles.

6.2.3. Classification and quantification

In a first step, the extracted features of all cycles, i. e., all naphthalene concentrations in all ethanol concentrations, were projected into 2D space using CDA with the ethanol concentrations as target (Figure 6.5). Both sensors clearly separate the concentrations on DF1, but SiO_2 produces uniformly spaced classes, whereas the response to ethanol with WO_3 seems to be almost binary, which fits the reactions seen in the quasistatic signal (Figure 6.3b). The order of separation on DF2 does not follow the ethanol concentration nor does it vanish if the naphthalene exposures are left out for either plot. One possible explanation for the variance in DF2 is the observed baseline drift. In conclusion, the first DF is sufficient to separate an ethanol from a non-ethanol environment.

CDA, i. e., class-based dimensionality reduction, is appropriate given the assumption that different ethanol concentrations actually lead to fundamentally changed reactions on the sensor surface. For the quantification of naphthalene concentrations on a continuous spectrum, however, regression should be used instead of classification, mainly because it provides interpolation capability and does not, falsely, try to separate close-by naphthalene concentrations into distinct classes. As a benchmark, PLSR calibration plots for naphthalene quantification without ethanol background are shown in Figure 6.6.

Both models were validated and tested with concentration-based leave-one-out, i. e., in each fold all cycles in one specific naphthalene concentration are set aside for validation or testing. In both cases it was made sure that 0 and 40 ppb_v were always in the training set because extrapolation would

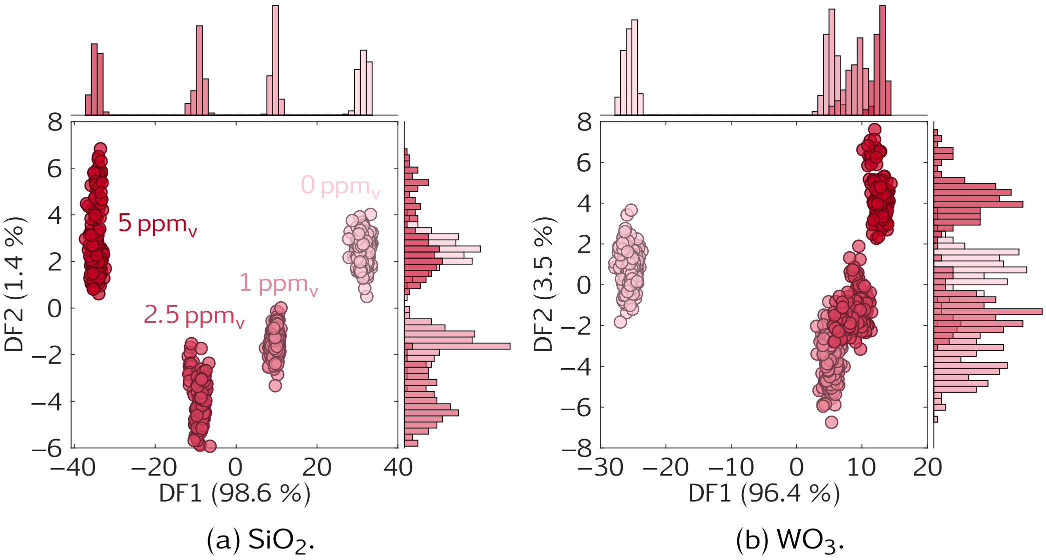

(a) SiO_2.

(b) WO_3.

Figure 6.5.: A 2D-CDA scatter plot showing the ability to discriminate ethanol concentrations independent of naphthalene addition. Histograms show the distribution of scores for the respective DF.

lead to over-pessimistic results. The graphs in Figure 6.6 depict one arbitrary testing fold without validation, i. e., the blue triangles are predicted with the model trained with the gray circles. The distance between the middle line and the dashed lines represents the RMSEV determined during validation. When testing errors are given, they always refer to the average RMSEP determined with all folds, not the error from the arbitrary fold shown in the graph. The uncertainty given for errors is always the standard deviation of all folds. The number of LVs in the PLSR model was determined manually by finding a compromise between the smallest RMSEV and the number of LVs, i. e., when the addition of one component improved the RMSEV only slightly compared to previous improvements, the lower number of components was chosen.

Both sensors show good linearity and acceptable precision (SiO_2-RMSEP: $(2.7 \pm 0.6)\,\text{ppb}_v$, WO_3-RMSEP: $(3.9 \pm 1.3)\,\text{ppb}_v$) with 5 ($SiO_2$) and 1 ($WO_3$) LVs, respectively. The need for so many LVs for SiO_2 seems to arise mainly from the baseline drift, as baseline corrected data produces an equally good model with 2 LVs (not shown). The WO_3 model exhibits two outlier groups, 10 and 40 ppb$_v$, which coincide with large, periodic dips observed in the quasistatic signal for 100 °C in Figure 6.3b around cycle 500, 1000, 1500, and so on. These dips appear regularly every eight hours and were later found to

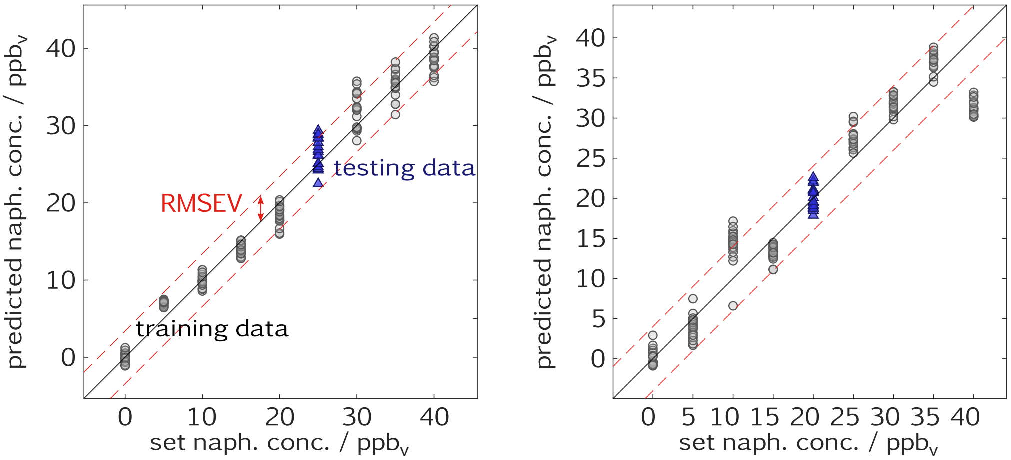

(a) SiO_2.

(b) WO_3.

Figure 6.6.: Calibration plot for naphthalene without ethanol background.

be correlated with an increase in ambient temperature of 2 °C caused by the thaw cycle of the air conditioning system. This temperature peak increased the absolute humidity temporarily by evaporating water droplets stuck in the humidification line. The issue was resolved in later measurements by adding an aerosol trap and minimizing surface areas. It shows, however, that WO_3 is, as expected, significantly more sensitive to humidity than SiO_2 which does not react to the humidity variations at all. The results presented in chapter 11 suggest that this cross-sensitivity could be suppressed with appropriate calibration.

Both sensors are also able to quantify naphthalene in 5 ppm_v ethanol satisfactorily (Figure 6.7), SiO_2 with an RMSEP of (3.2 ± 1.1) ppb_v (2 LV) and WO_3 with (3.7 ± 2.0) ppb_v (2 LV). However, removing the 0 concentration variations from the WO_3 model, which is affected by humidity, halves its error to (1.8 ± 0.8) ppb_v (not shown). It has then a considerably better precision and linearity than the SiO_2 model, i. e., WO_3 is better suited for naphthalene quantification in the highest ethanol concentration.

Figure 6.8 shows calibration plots for PLSR models for selective naphthalene quantification, independent of the background ethanol concentration. As expected, both models loose accuracy and precision compared to quantification in only one constant background. The RMSEP increases to (11.0 ± 4.7) ppb_v with 1 LV for SiO_2, and to (6.1 ± 1.3) ppb_v with 4 LV for WO_3. The use of only 1 LV in the SiO_2 model is surprising for such a complex problem, and consequently leads to very poor prediction, especially below 20 ppb_v where the predicted values stop decreasing with the actual

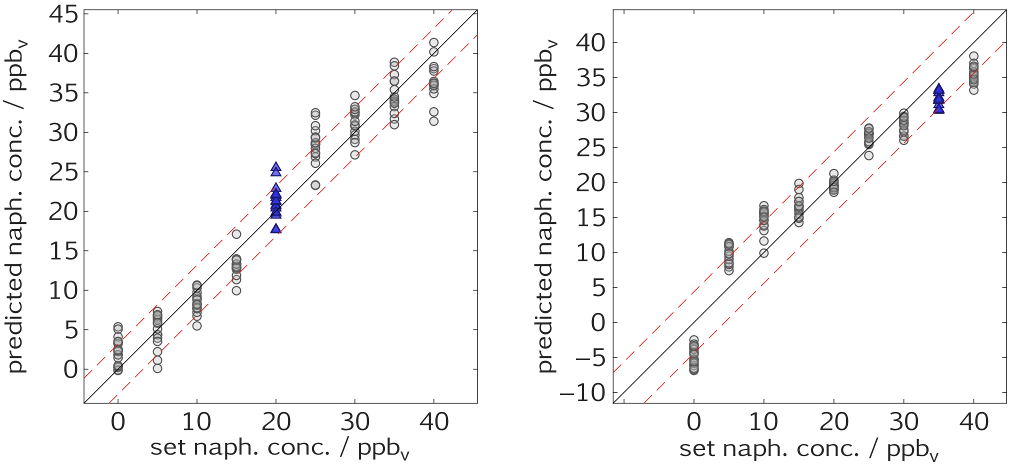

(a) SiO_2. (b) WO_3.

Figure 6.7.: Calibration plot for naphthalene in 5 ppm_v ethanol.

naphthalene concentration. The plot has been colored to show the strong influence of different ethanol backgrounds. WO_3, on the other hand, produces a better model which is considerably less dependent on the ethanol concentration (not shown in the coloring of Figure 6.8b). The main issue is the logarithmic behavior lowering the accuracy.

Upon closer inspection it was found that the 0/0 observation, i. e., 0 ppb_v naphthalene in 0 ppm_v ethanol, had by far the highest prediction error in the prediction of the SiO_2 model. Removing it from the training consequently lead to much better precision and linearity, with a RMSEP of (6.3 ± 2.0) ppb_v with 3 LVs (Figure 6.9a). The WO_3 model, on the other hand, could be improved by training it on (decadic) logarithmic concentrations offset by 1 to allow the inclusion of 0. In Figure 6.9b, the predictions have been converted back to the original scale by taking them to the power of 10 and subtracting 1 (which is automatically done in DAV^3E). This leads to a model with very good precision and accuracy in the range relevant for air quality monitoring below 10 ppb_v. While the average RMSEP for the whole model is at (7.4 ± 2.5) ppb_v which seems slightly worse than the SiO_2 model, the naphthalene concentration can be predicted, independent of the ethanol level, with a standard deviation of 0.37 ppb_v and 2.90 ppb_v at 0 and 10 ppb_v, respectively.

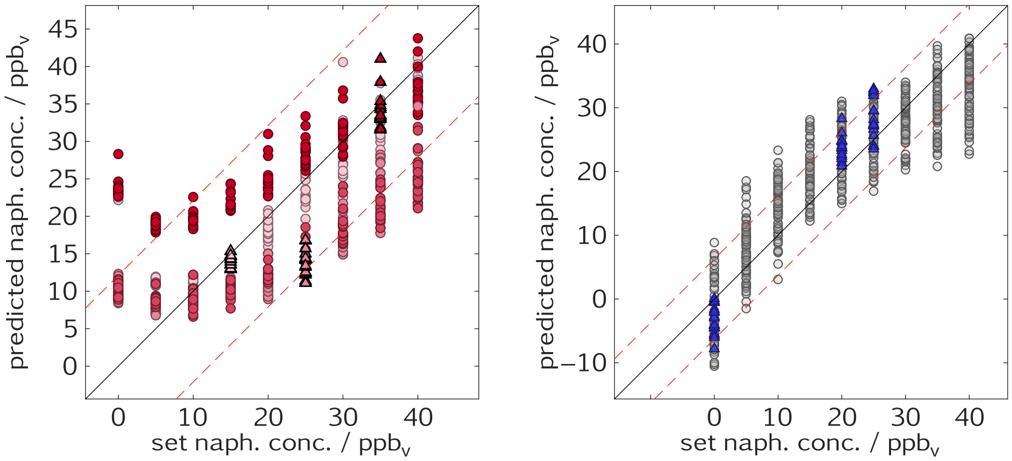

(a) SiO_2.

(b) WO_3.

Figure 6.8.: Calibration plot for naphthalene independent of ethanol background. The colors in (a) indicate different ethanol concentrations.

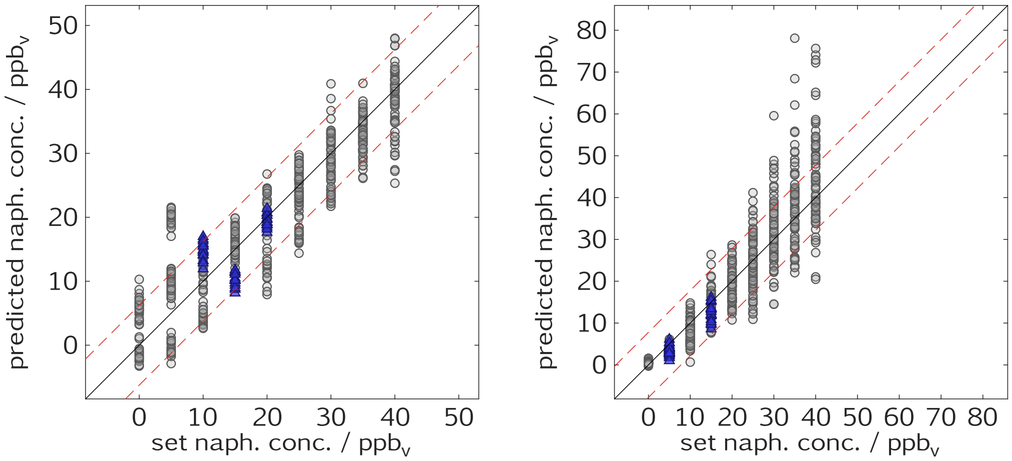

(a) SiO_2 without the 0 class in 0 ppm$_v$ ethanol.

(b) WO_3 trained on logarithmic concentrations.

Figure 6.9.: Calibration plot for naphthalene quantification independent of ethanol background with improvements to achieve the best possible result.

6.2.4. Stability

Two WO_3 SiC-FETs were also used in the interlaboratory study presented in chapter 11. The aim was to quantify target VOCs (benzene, naphthalene, and formaldehyde) in a varying background of other VOCs.

The quasistatic signals at 210 and 330 °C during a long calibration measurement (described in detail in chapter 11) are shown in Figure 6.10. Sensor (a) shows a pronounced upwards drift of roughly 60 nA/h, while (b) drifts slightly downwards with roughly −20 nA/h. The responses to the VOC background are very similar, e. g., a difference of 2 µA at the first step around cycle 700. Sensor (a), however, does not show any reaction to formaldehyde, while (b) does show a clear response. The other two target gases, benzene and naphthalene, could not be detected due to their low concentrations.

The only difference between both sensors was the operating mode: while (a) was driven with temperature plateaus between 210 and 330 °C at $V_{GB} = 0\,\mathrm{V}$ over two minutes, for (b) the gate bias was additionally cycled between −1 and +1 V on each temperature plateau. The total operating time of the sensors is not known, but estimated to be approximately two weeks, not counting pauses.

Micrographs of the gate area of both sensors were taken with a *scanning electron microscope* (SEM), revealing obvious differences in the topography (Figure 6.11). Sensor (a) seems to be covered by a relatively dense layer with only few visible cracks. Unfortunately, the layer was too thin to determine its composition with *energy dispersive X-ray spectroscopy* (EDX), and a more surface sensitive method like *X-ray photo electron spectroscopy* (XPS) was not readily available. If the material is assumed to be the catalyst, i. e., iridium, mainly due to a lack of other options, this could explain the missing formaldehyde response. The dense[2] metal layer on the gate would turn the sensor into a dense-gate SiC-FET, i. e., the response is mainly governed by hydrogen atoms or protons diffusing to the metal/insulator interface. While dehydrogenation of formaldehyde is possible, it requires special catalysts (ruthenium with certain ligands) to happen [241], [242]. Some of the VOCs in the background, on the other hand, can dissociate relatively easily and produce atomic hydrogen on the surface, causing a response.

Sensor (b) shows the distinct "web" pattern (Figure 6.11b) usually observed for a porous gate [200], with the lighter part being iridium. The pores are one order of magnitude larger as reported for platinum on SiO_2 (cf. section 5.1). It can, however, not be determined whether this is due to restructuring or due to deposition and annealing parameters. In any case, three-phase

---

[2] Not perfectly due to some visible and, possibly, invisible cracks, but dense in comparison to the expected porosity.

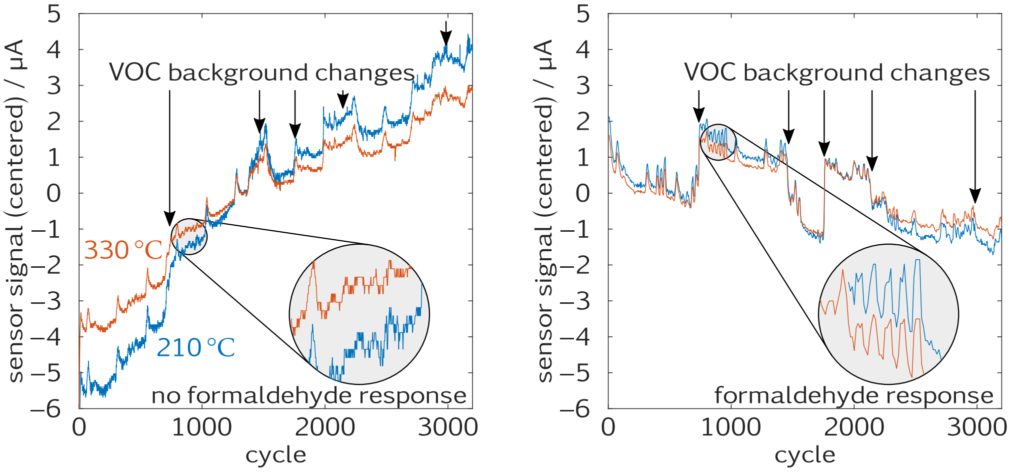

(a) TCO with constant gate bias.

(b) TCO with varied gate bias.

Figure 6.10.: Quasistatic signal of two SiC-FETs with Ir/WO_3 gate.

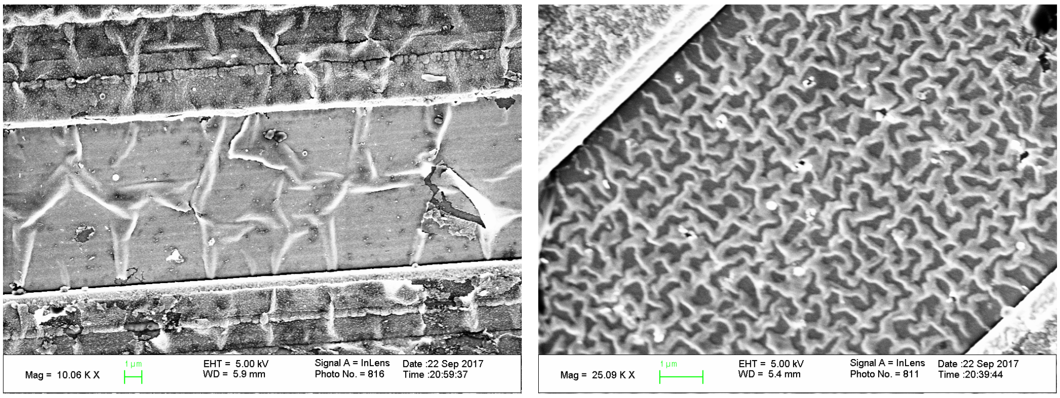

(a) TCO with constant gate bias.

(b) TCO with varied gate bias.

Figure 6.11.: Comparative SEM micrographs of the gate regions of the SiC-FETs from Figure 6.10.

boundaries and bare patches of oxide are still present, explaining the visible response to formaldehyde in Figure 6.10b.

In [31], restructuring of the gate has been observed after two weeks of continuous operation for negative gate biases and reducing conditions. These sensors were, however, never exposed to excessively strong reducing conditions and the specimen without gate bias is more deteriorated than the one with gate bias cycling, making also electro migration [31] an unlikely explanation. It can be speculated that the restructuring comes from a reversible phase transition (from γ-WO_3 to β-WO_3) which has been reported for WO_3 at 330 °C [243]. Both sensors should have been heated to no more than 330 °C during their temperature cycle, but undetected deviations between the two specimens of several 10 °C are possible due to the manual mounting process.

6.2.5. Conclusion

WO_3 was used, for the first time, as the "active oxide" of a SiC-FET and compared to the commonly used SiO_2. Quantification of low naphthalene concentrations (up to 40 $\mathrm{ppb_v}$) in large ethanol concentrations (up to 5 $\mathrm{ppm_v}$) was possible with both oxides, but WO_3 performed considerably better especially in a varying background. The best achieved uncertainty was 3 and 6 $\mathrm{ppb_v}$ naphthalene in the (health-wise relevant)range between 0 and 10 $\mathrm{ppb_v}$ for WO_3 and SiO_2, respectively. One reason could be the opposing response directions for ethanol and naphthalene with WO_3, and, additionally, more naturally occurring acidic sites on its surface. Both oxides show a strong dependence on gas interactions, i. e., the response of WO_3 to naphthalene is much smaller without ethanol than with, while the opposite is true for SiO_2. This observation shows that sensitivity and selectivity must always be defined in a suitable context.

Despite the better performance of WO_3, its application in SiC-FETs requires further investigations. It exhibits much stronger cross-sensitivity to humidity than SiO_2 and leads to unstable sensors. The latter is, tentatively, attributed to a phase transition of WO_3 taking place at 330 °C.

7. Influence of the gate bias

7.1. Signal compensation

As already mentioned in section 4.3, there are several ways to drive and read out the signal from field-effect devices. For MIS capacitors, the most obvious is measuring the capacitance or impedance and for MISFETs the channel conductivity can be measured in constant voltage or constant current mode. The signal from both devices can also be read out by controlling the gate bias to keep impedance, voltage, or current constant. The applied gate bias is then the sensor signal. In this *compensation mode*, the device's sensitivity with respect to the electric signal transduction is constant because the effective gate bias and, thus, the working point do not change. Moreover, the sensor response is equal to the additional gate bias caused by the gas, thereby simplifying the interpretation through the establishment of a more direct link between the sensor signal changes and underlying physical (real) properties and mechanisms. .

This kind of compensation mode was implemented in the old LabVIEW software by Claudia Daut during her Bachelor's thesis [244] supervised by the author. The concept was later ported to the new Python software, but all of the following results were achieved with the LabVIEW software. The compensation is based on a *proportional–integral* (PI) closed-loop controller with manually determined parameters. Due to the slow sampling rate (10 Hz) of the sensor setup, the controller produces some noise and can need up to a few seconds to reach a new stable value. Nevertheless, the experimentally determined signal-to-noise ratio is comparable to read-out in constant voltage mode, and the controller's time constant is below the fluidic and thermal time constants of the setup so that its influence can be neglected.

A comparison between fixed voltage mode and compensation mode was done with TCO. The temperature cycle was an asymmetric triangle, increasing from 180 °C to 270 °C during 25 s and back during 35 s. The resulting sensor signals are shown in the top plot of Figure 7.1. The sensor was exposed to NH_3 concentrations, in dry air, from 6 ppm_v to 30 ppm_v and back in steps of 6 ppm_v, i. e., two exposures separated in time for each concentration. Each exposure lasted 60 min and was followed by carrier gas only

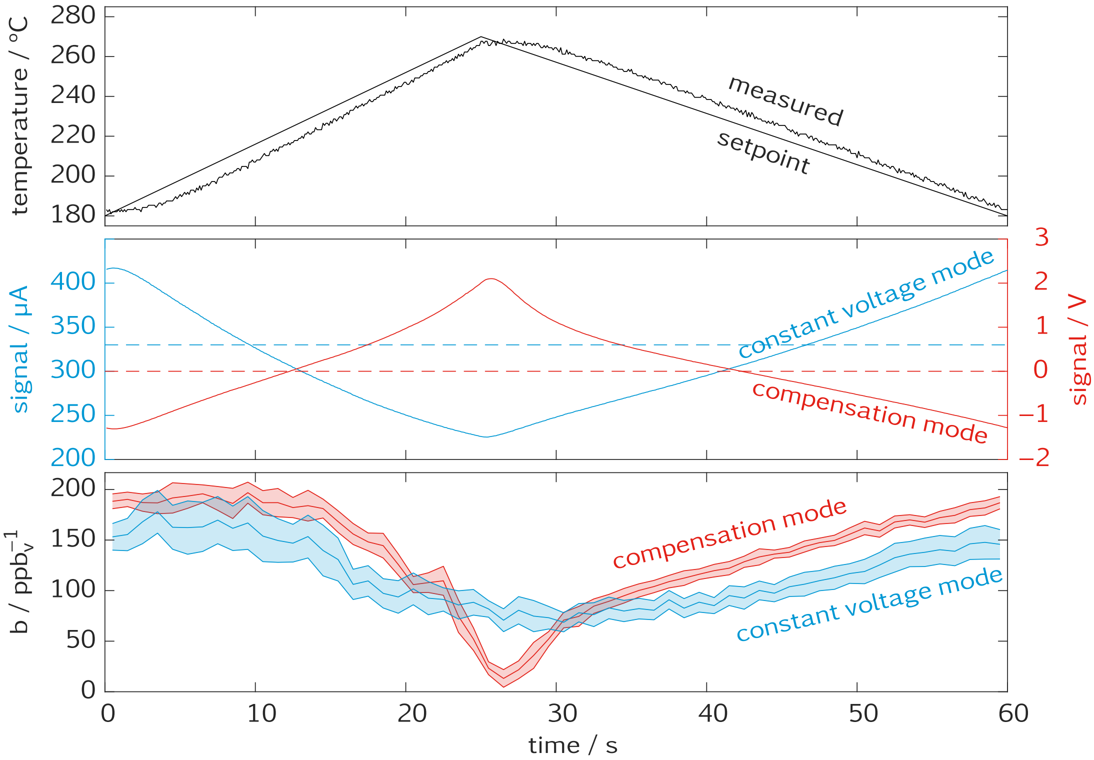

Figure 7.1.: (Top) sensor temperature, (middle) sensor signal for both modes, and (bottom) b values (cf. Equation 7.2) for both modes. The 95 % confidence intervals were computed by MATLAB's `fit` function. The dashed lines in the middle plot indicate the gate bias (0 V) in constant voltage mode, and the current (330 µA) in compensation mode. V_{DS} was 4 V in both modes.

for 150 min to allow for sensor recovery. This measurement was done twice with the same sensor, once in constant voltage mode using the GasFET board (3S GmbH), and once in compensation mode using a Keithley Sourcemeter 2016B (Tektronix, Inc., Beaverton, USA) for better gate bias resolution. Other differences in the performance of both instruments were determined to be negligible [244]. The sensor response in both modes was determined from the (absolute) difference between the last point just before and the last point within a gas exposure.

The results of this experiment have been published in [245] and will be reevaluated in the following. In both modes, the response over NH_3 concentration follows a logarithmic curve as expected. The non-linearity of the response changes, however, over the cycle and, in particular, can become almost linear for compensation mode [245]. To quantify these variations, the response for each gas exposure is computed for each of the 600 data points in the cycle, i. e., for all quasistatic signals. Sensor drift is compensated by subtracting a linear fit from each quasistatic signal. Additionally, to keep the influence of drift on the results as low as possible, only the later exposures (from 30 $\mathrm{ppm_v}$ downwards) are used and the lowest concentration, 6 $\mathrm{ppm_v}$, which turned out to be rather instable, was excluded. This reduces the available amount of data, but should make sure that the sensor was stable during the exposures considered. The response r is normalized to the response at 30 $\mathrm{ppm_v}$ to compensate the different scales of both modes, one being in µA and one in V, and then fitted with

$$r = a \cdot \log(b \cdot c + 1) \tag{7.1}$$

where c is the gas concentration, and a and b are fit parameters. The closer the curvature of this fit is to zero, the closer the relationship comes to being linear. Instead of the, relatively, complex derivative of Equation 7.1, the parameter b can as well be used to compare the deviation from linearity assuming an always negative curvature. Taking the quotient of the slope at minimum and maximum concentration yields:

$$\frac{\partial r(0\,\mathrm{ppm_v})}{\partial c} \cdot \left(\frac{\partial r(30\,\mathrm{ppm_v})}{\partial c} \right)^{-1} = ab \cdot \frac{b \cdot 30\,\mathrm{ppm_v} + 1}{ab} = b \cdot 30\,\mathrm{ppm_v} + 1 \tag{7.2}$$

$b = 0$ indicates linear behavior and $b > 0$ negative curvature, which is here assumed to indicate a logarithmic function.

The bottom plot in Figure 7.1 shows the values of b for fits of ten consecutive data points, i. e., each b value was determined from a one second time window in the temperature cycle. Both read-out modes show significant changes in linearity over the cycle, i. e., with temperature. In both modes, higher temperatures lead to a more linear behavior (b closer to 0). This can be understood as a change from adsorption-limited (logarithmic) to reaction-limited (linear) behavior at higher temperatures. However, the variance of b is larger in compensation mode, reaching almost $b = 0$ at the highest temperature (and gate bias) and $b = 200\,\mathrm{ppb_v^{-1}}$ at the lowest temperature (and gate bias). In constant voltage mode, b is between 70 $\mathrm{ppb_v^{-1}}$ and 160 $\mathrm{ppb_v^{-1}}$. The resulting change in sensor characteristics is shown in Figure 7.2.

In constant *current* mode, the gate bias has previously been used to modify the sensor response and measurement range [31]: larger biases increase the saturation voltage which “smoothens” the transition from linear to saturation region (cf. Figure 4.5a). This reduces the sensitivity, defers saturation

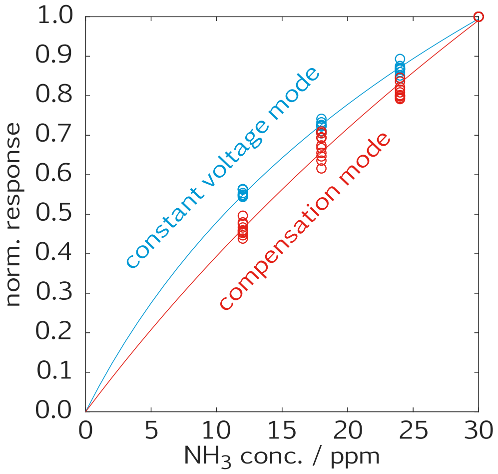

Figure 7.2.: Normalized sensor response and logarithmic fit for both operating modes for the time window from 25 s to 26 s in the cycle (point of lowest b for compensation mode, cf. Figure 7.1).

and, thus, increases the measurement range. In constant *voltage* mode, measurements are usually taken “deep” in the saturation region. It is, however, possible that the measurement point transitioned in the beginning of the linear region at higher gate bias, which could explain the distinct shape change of the red compensation mode curve above 1.5 V (Figure 7.1, middle).

The gate bias also influences the sensitivity g_m, which, if it were the only explanation, should result in identical behavior at the same temperature and gate bias values. The gate bias was kept at 0 V in constant voltage mode and changed, mainly through temperature variations, between −1.3 and +2.0 V in compensation mode. If the change in electrical characteristics were the sole explanation for the observed differences, b would be very similar for both modes at $V_{GS} = 0$ V, i. e., around 12 and 42 s, which is not the case.

One possible explanation is that charges on the sensor surface, most likely oxygen anions, can be moved between patches of metal and oxide through fringing electric fields; it has been suggested in [33] that the bare oxide could act as oxygen reservoir. Ammonia leads to an increase in current by either adding protons or removing oxygen anions. This increase is compensated by reducing the gate bias. The more negative gate bias transfers oxygen from the metal to the oxide, adding a negative internal gate bias so that the external gate bias does not have to be lowered as much. Although speculative, it is believed that such a process could flatten the sensor response characteristics under the right circumstances. The basics of this hypothesis are examined further in the next section.

7.2. Electrically promoted spill-over

While the variable gate bias is a promising advantage of FETs over MOS, adding an additional parameter to cycle, very few studies looking into its effects are available. Nakagomi *et al.* [246] have studied the effect of negative and positive static gate biases on the gas response of a SiC-FET with buried short channel. They found an increased gas response in combination with larger noise for positive gate biases, which was attributed to the channel moving closer to the insulator interface. Kreisl *et al.* have seen a quench-in effect for positive gate biases in GasFETs with presumably porous gate, i. e., charges becoming trapped on the sensor surface or in the bulk [247], [248]. They attribute their findings to protons being pushed into the oxide and forming a metastable state. Gate-pulsed read-out of floating gate GasFETs has been found to improve baseline stability and selectivity by evaluating the transient response [249].

It is assumed in this work that, given a porous catalyst, the gate bias influences the equilibrium surface density of charged species on the metal and the oxide. The equilibrium can be (re-)established through (reverse) spill-over between metal and oxide (Figure 7.3), possibly supported by fringing electric fields crossing the gap between metal and insulator. The dominating species is assumed to be oxygen anions (O^-, O_2^-, or O^{2-}) covering both the insulator and the catalyst. This assumption is strongly supported by many measurements showing strong reactions to the oxygen content where more oxygen leads to a signal decrease, i. e., negative charges on the gate for n-type FETs. These charges must be present on the insulator since the catalyst, which is kept at a fixed potential, screens any charges on top of it. An effect of species on top of the metal through the fringing fields is probably small or negligible [197]. Oxygen must also be present on the catalyst as many reactions involving oxygen as an important reaction partner are taking place, which can be seen by detecting the reaction products with a mass spectrometer [250].

The oxygen anions on the sensor surface can be described as a canonical ensemble, i. e., a system with a constant number of particles, temperature, and volume, where the latter refers to an area in the two-dimensional case. The associated thermodynamic potential is the Helmholtz energy A, defined as

$$A = U - TS, \tag{7.3}$$

where U is the internal energy and S the entropy of the system. T is the temperature of the surrounding heat bath (the sensor). The Helmholtz energy is minimal at equilibrium, i. e., the internal energy is minimized and

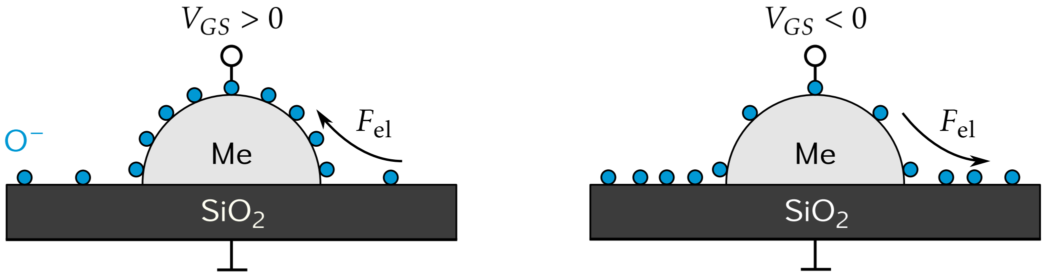

Figure 7.3.: Suggested principle of electrically promoted spill-over with negatively charged particles.

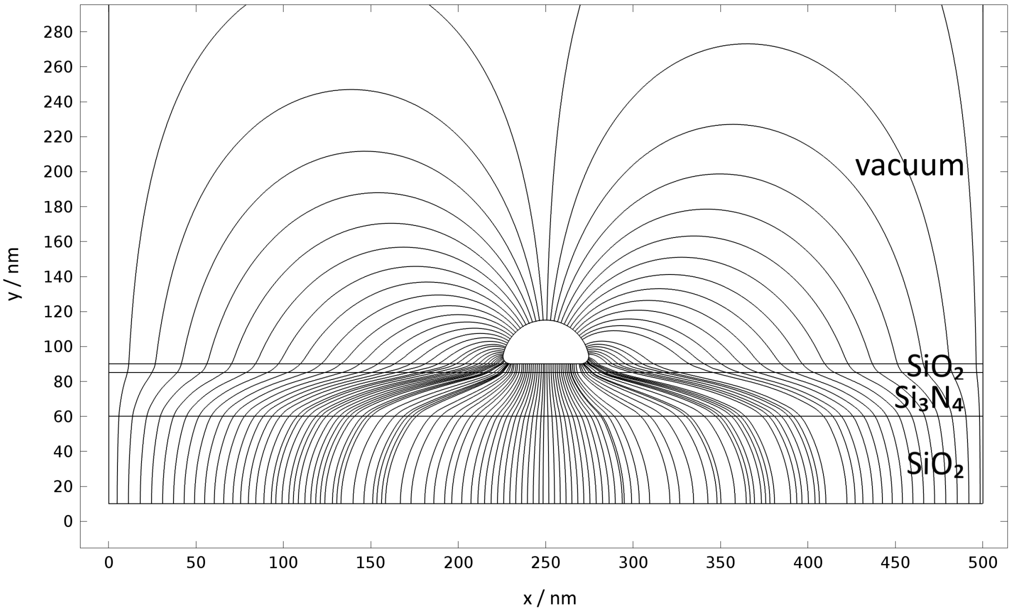

Figure 7.4.: Electrical field lines of a single metal hemisphere at +2 V going through the gate material stack and extending into the vacuum.

the entropy maximized. The latter leads to an entropic force, also known as pressure, trying to distribute all particles as evenly as possible across the surface. The internal energy is here assumed to be mainly electrostatic potential energy which increases with inverse distance of opposite charges. An anion on metal with a fixed potential is very close to its mirror charge. The distance of an anion on the insulator to a positive counter charge is considerably larger, so that energy minimization should favor anions on the metal. Minimizing A then leads to an equilibrium where the anions are distributed between metal and insulator which can be described by a partition coefficient R:

$$R = \frac{[\mathrm{O}^-]_{\mathrm{Me}}}{[\mathrm{O}^-]_{\mathrm{SiO_2}}} \tag{7.4}$$

Equation 7.3 shows that increasing temperature puts more weight on entropy, i. e., the distribution of anions evens out with increasing temperatures ($R \to 1$ for $T \to \infty$).

In this model, applying a potential to the gate should change the partition coefficient. The potential difference between gate and substrate causes an electric field, changing the potential energy of the anions and, therefore, the entire system's energy. Thus, a redistribution occurs to find the new minimum of A. Most of the electric field created by a metal hemisphere sitting on top of an insulating plane with a backside contact goes directly through the dielectric. There is, however, a fringing field extending into the surrounding vacuum. Figure 7.4 shows the simulation of the electric field lines in a very simple model[1].

To test the hypothesis, a SiC-FET with porous iridium gate was exposed to six different concentrations of oxygen between 0 and 20 %. True 0 % O_2 is difficult to reach and should be read as "almost zero". The measurements in 0 % were, however, significantly different from measurements in 1 %, retroactively confirming that concentrations far below 1 % have been reached. During the whole measurement, the gate potential was switched back and forth between −2 and +2 V. One gate bias cycle took 20 min (10 min per plateau). A constant oxygen concentration was set for 10 h each. During this time, the sensor temperature is set to 150, 150, 200, 250, and 300 °C for one hour each. This is done twice during one gas exposure, once with and once without LED (see chapter 8), however, only the second, non-LED temperature cycle, is evaluated here. The repetition of 150 °C is to give the sensor and the gas mixing system time to equilibrate after a change in oxygen concentration. For each temperature plateau, an average cycle is computed from the last two cycles (the first cycle allows the sensor to settle after the

---

[1] Thanks to Caroline Schultealbert for her help with COMSOL Multiphysics.

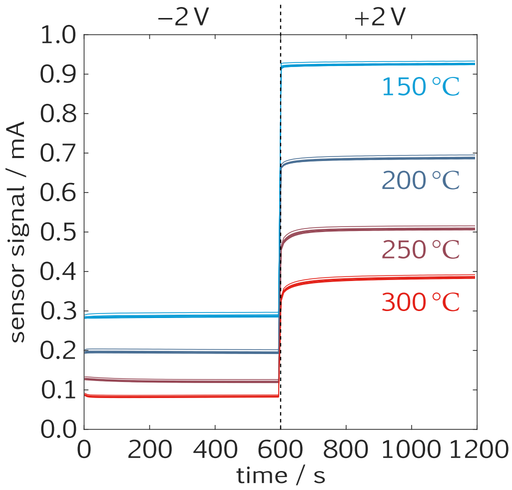

Figure 7.5.: Sensor signal in all different oxygen exposures. The gas influence is masked by the large changes through temperature and gate bias.

temperature change) and smoothed with a moving average filter of window width 10, corresponding to one second at 10 Hz sampling rate.

As mentioned before, FETs react much more strongly to changes in temperature or gate potential than to gas. Indeed, the raw signal, shown for cycles in all oxygen concentrations from 0 % to 20 % in Figure 7.5, seems to only depend on temperature and gate bias, with a negligible influence of the atmosphere. These masking influences must be eliminated to make the small effects a change in oxygen concentration has visible. The main effect of temperature dependence arises from changes in the electron mobility μ_n, but also the threshold voltage changes non-linearly with up to 8 mV/K (experimentally determined).

The simplest way to capture and eliminate all non-gas dependent temperature effects is to subtract a reference signal. Here, the sensor signal at 1 % O_2 is used as a reference. While 0 % O_2 would be more suitable as a reference, it is, as mentioned before, only “almost zero”, making its relative error large. It also happened to be the very first exposure of the measurement so that the sensor was potentially still drifting stronger as compared to later in the measurement, which could skew the results. As all involved signals were recorded in the same measurement with the same sensor, it should contain all temperature dependencies, so that the remaining signal is purely the influence of oxygen.

One thing to keep in mind is the change of the transconductance g_m with the gate bias. The change in current which is the measured sensor response is caused by a change in effective gate bias. Assuming oxygen anions on the insulator, the effective gate bias changes because a surface charge affects the threshold voltage. Hence, the effective gate bias is directly related to the physical quantity to be measured. As mentioned above, the changes through gas are significantly smaller than changes through gate bias or temperature, i. e., the effective gate voltage change in the working point $\boldsymbol{p} = (T, V_{GS})$ can be approximated as being linear:

$$\Delta V_{GS,\mathrm{eff}} = \frac{\Delta I_{DS}(c, T, V_{GS})}{g_m(T, V_{GS})} \tag{7.5}$$

The experimentally determined values for g_m can be found in Table 7.1.

The resulting responses for 2.5, 5, 10, and 20 % O_2 are shown in Figure 7.6. The overall response becomes more negative with increasing oxygen concentration. This is expected as the basic sensor principle relies on a relation between concentration in the gas phase and on the sensor surface. More oxygen leads to more oxygen anions on the surface, i. e., a negative surface charge, lowering the signal. The response becomes less negative for the positive gate bias compared to the negative gate bias which supports the hypothesis that the electric field moves oxygen anions away from the insulator. In addition, the response becomes more negative with increasing temperature for both gate biases. This can also be explained by the given hypothesis for the reasonable assumption of R being large over the whole temperature range, i. e., significantly more oxygen anions being on the metal compared to the insulator. Higher temperatures lead to a more even spread of anions over the surface, causing some to move from the “metal reservoir” to the oxide, lowering the sensor signal.

Those dependencies of the response become even clearer in Figure 7.7. As before, the logarithmic response is expected for a GasFET. It becomes also obvious in this depiction that the absolute response is always smaller, i. e., less negative, for positive gate biases. Interestingly, the spread between temperatures is considerably smaller at the negative gate bias, most likely due to the fact that the relative change of R is smaller when already high coverage of the metal is to be increased even more. The reasons for the deviance of the lowest temperature at −2 V is unknown, but could arise from very long time constants usually observed at low temperatures and gate bias. It is deemed ignorable since it is only minor and all other temperatures still follow the expected trend. Moreover, the difference between the response at −2 V and +2 V increases with oxygen concentration and decreases with temperature, as would be expected from the model.

Table 7.1.: Experimental values of transconductance g_m in µA/V. The values at temperatures marked with * have been linearly extrapolated from measurements at 225, 250, 275, and 300 °C.

	150 °C*	200 °C*	250 °C	300 °C
−2 V	100	80	59	42
+2 V	209	177	145	112

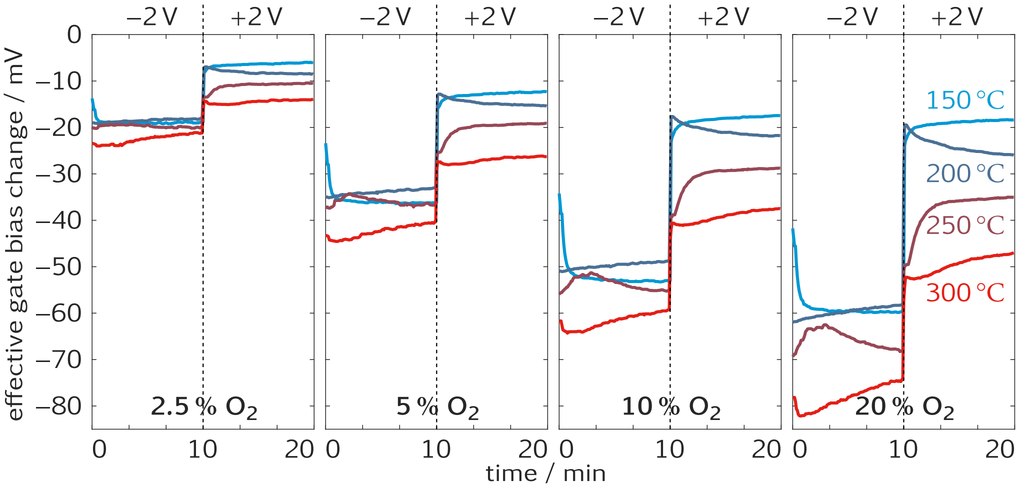

Figure 7.6.: Change in effective gate bias for 2.5, 5, 10, and 20 % oxygen with 1 % oxygen as reference. The effective gate bias change has been computed from the drain current after Equation 7.5.

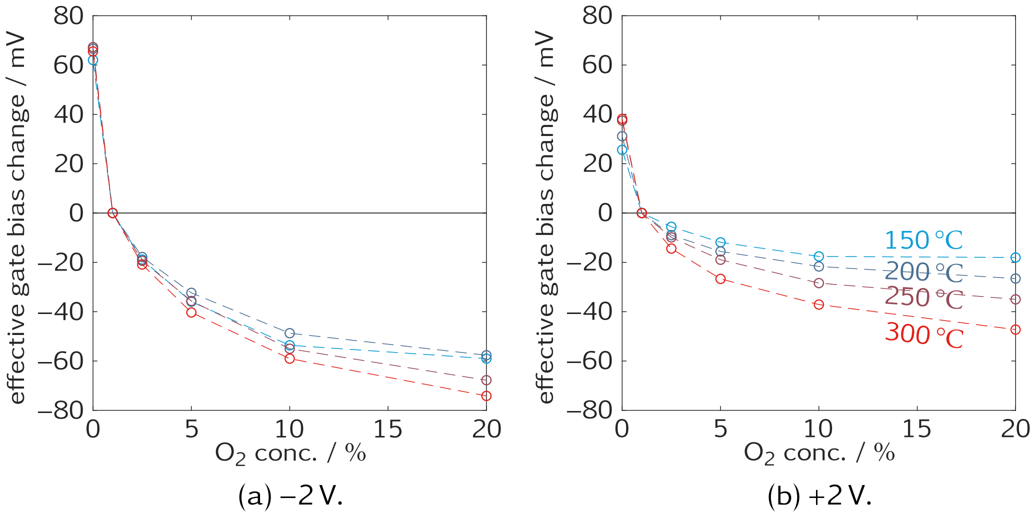

(a) −2 V.

(b) +2 V.

Figure 7.7.: Response in Figure 7.6 just before gate bias step.

7.3. Gate bias cycled operation

The previous experiments suggest that additional information can be extracted from a GasFET in gate bias cycled operation. The gate bias has an influence on the sensor response both statically and dynamically, i. e., on plateaus as well as after quick changes. With this in mind, the cycle used in [63], consisting of gate bias ramps from −1 V to +3 V at two different temperature plateaus, has been revised and optimized. The two temperature plateaus are kept in the new cycle, but moved to more extreme values to achieve more distinctive shapes of gate bias cycles. The temperature plateaus are now at 150 and 300 °C as compared to 200 and 260 °C before. Each plateau lasts 60 s. During this time, the gate is at −2 V for 40 s and then switches to +2 V for 20 s. The idea behind the asymmetric time intervals is to give more time to “store” oxygen on the insulator.

The sensor was exposed to different gas atmospheres in dry air for one hour each. Each atmosphere contained only one test gas. Gas types and concentrations were scrambled so that they do not appear in a particular order which reduces the potential for misinterpretation of sensor drift as gas response. The gases were NH_3 (17, 20, 33, and 50 ppm_v), CO (8, 17, 50, and 100 ppm_v), NO_2 (0.2, 0.3, 0.5, 0.7, and 1 ppm_v), and H_2 (1, 2, 4, 5, and 7 ppm_v). All these concentrations are considerably lower compared to the reference work [63] and measured in dry air compared to dry nitrogen with 5 % O_2.

In Figure 7.8, the average cycle shape in each gas type is shown. The

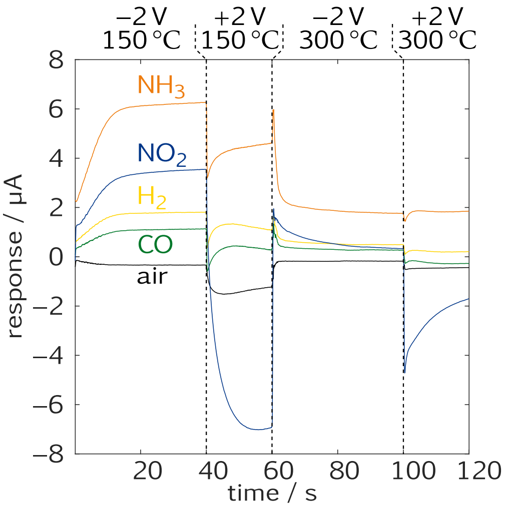

Figure 7.8.: Average cycle shapes of different gas types in varying concentrations offered one after the other in random order. The average cycle in air has been subtracted to emphasize gas-induced changes.

differences have been emphasized by subtracting the average cycle shape in air (sampled from start and end of the measurement), and smoothing the result with a moving median of window width 5 to remove spikes at sharp edges. The different gas types result in different, distinct cycle shapes. NO_2, the only oxidizing gas in the measurement, stands out as the most dynamic after the gate bias step from −2 V to +2 V. The non-zero line for air indicates the presence of some sensor drift over time. It is, however, mostly smaller than the gas-induced changes.

Interestingly, the response becomes more negative at positive gate biases for all gases. This is different from the response increase observed in pure air (Figure 7.6). The same behavior was seen with a sensor from the same batch running in parallel with the exception of NO_2 at 150 °C which exhibits a more positive response at positive gate bias. The exact nature of the gas interactions causing this change is yet unknown and should be subject to further studies. One possible explanation is the *electrochemical promotion of catalysis* (EPOC) or *non-Faradaic electrochemical modification of catalytic activity* (NEMCA) effect which is well-known in electrocatalysis to reversibly change a catalyst's activity and selectivity by orders of magnitude through the application of a voltage [251], [252]. It has been reported for many different porous catalysts supported on ionic conductors with a counter electrode, i. e., essentially the setup of an amperometric sensor. Ions pumped through the electrolyte reversely spill-over to the catalyst and build up a

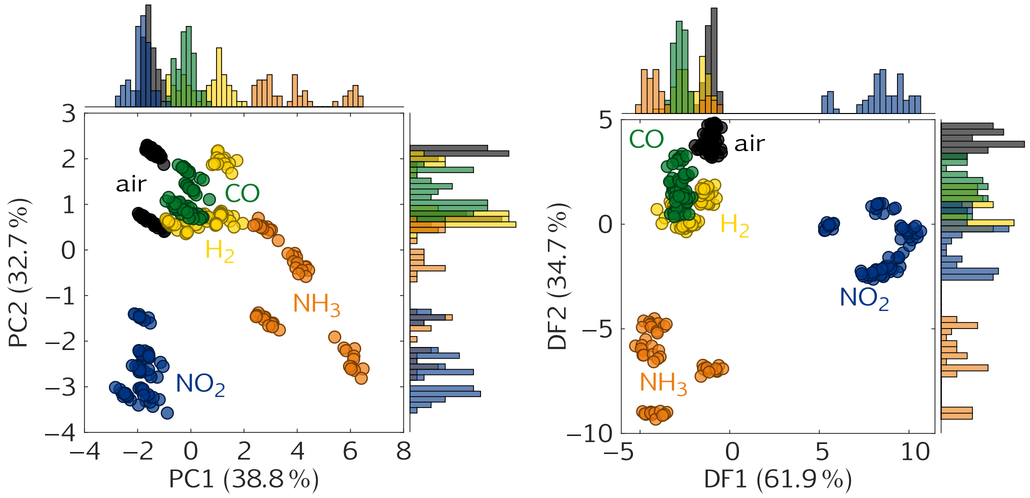

(a) PCA. (b) CDA.

Figure 7.9.: (a) PCA and (b) CDA (with gas types as target) computed with standardized features (four means, four slopes) from the cycle in Figure 7.8.

double-layer altering the metal's work function and binding energies of adsorbates. Removal of oxygen anions in particular speeds up adsorbate decomposition, and *vice versa* [251]. SiO_2 is generally not considered an ionic conductor, but considering its surface as oxygen reservoir [33] could cause a small, yet similar effect.

The gate bias cycle was designed based on the previously discussed experiments, focusing on sudden changes and long plateaus rather than continuous change. This makes feature extraction simple: the slope is computed right after each temperature or gate bias step, and the mean value from the end of each gate plateau is taken, resulting in 2×4 features. These features have been projected with PCA and CDA with the gas types as target (Figure 7.9). The differences between both methods are small, with CDA producing, as expected from the method, denser clusters. H_2 and CO are not well distinguished from air, probably owing to their low concentrations and resulting low, and very similar, signal changes in the range of the sensor drift. Both the static and dynamic response are stronger at lower temperature and especially pronounced for NO_2 which can clearly be detected in the sub-ppm_v range.

In order to examine the influence of the gate bias variation on the amount of information in the signal, two models were built using CDA, a 1nn classifier, and an exposure-based leave-one-out validation. One model was trained with two mean features at +2 V, the other with all four mean features, i. e.,

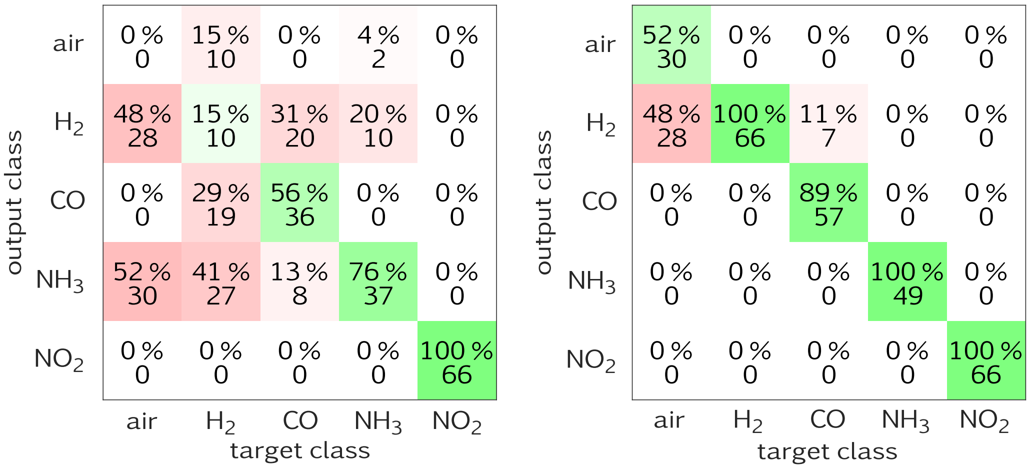

	air	H_2	CO	NH_3	NO_2
air	0 % 0	15 % 10	0 % 0	4 % 2	0 % 0
H_2	48 % 28	15 % 10	31 % 20	20 % 10	0 % 0
CO	0 % 0	29 % 19	56 % 36	0 % 0	0 % 0
NH_3	52 % 30	41 % 27	13 % 8	76 % 37	0 % 0
NO_2	0 % 0	0 % 0	0 % 0	0 % 0	100 % 66

(a) TCO.

	air	H_2	CO	NH_3	NO_2
air	52 % 30	0 % 0	0 % 0	0 % 0	0 % 0
H_2	48 % 28	100 % 66	11 % 7	0 % 0	0 % 0
CO	0 % 0	0 % 0	89 % 57	0 % 0	0 % 0
NH_3	0 % 0	0 % 0	0 % 0	100 % 49	0 % 0
NO_2	0 % 0	0 % 0	0 % 0	0 % 0	100 % 66

(b) TCO+GBCO.

Figure 7.10.: Confusion matrices showing the absolute and relative amount of correctly classified observations for a CDA model with 1nn classifier with (a) two features from TCO and (b) four features from combined TCO+GBCO.

at +2 and −2 V. The slope features were omitted for a fair comparison since they can only be computed with GBCO in this cycle. The validation error for predicting the gas type independent of concentration for the model with two features was (50.8 ± 49.7) %, while the four-feature model achieved significantly better (23.9 ± 11.6) %. The confusion matrices in Figure 7.10 show that NH_3 and NO_2 can be predicted relatively well with both models, while all other gases need the additional features produced by the gate bias variation. This dependence of the prediction performance on the class also explains the large uncertainty for the TCO-only model. This result clearly shows that gate bias cycled operation encodes a significant amount of gas-related information into the sensor signal.

In addition to classifying the gas type, attempts to quantify the concentration of each gas have been made (Table 7.2). A PLSR model was trained either on only the exposures of the target gas (*others ignored*) or at all exposures with the target value for all non-target gases set to 0 (*others 0*). The latter is a substantially more difficult task since it requires selectivity of the features which is reflected in the resulting RMSEV values. The two gases with the largest response and separability, NH_3 and NO_2, show considerably better results compared to H_2 and CO. The features were standardized and the 0 group was reduced, by discarding random data points, to the same size as all other target gas groups to prevent this group dominating the training. Vali-

Table 7.2.: Parameters for trained and validated PLSR models for each gas type and the resulting validation error.

gas	LVs	RMSEV/ppb_v	RMSEV/c_{max}
H_2 (others ignored)	1	1.11	0.16
H_2 (others 0)	1	2.76	0.39
CO (others ignored)	7	30.01	0.30
CO (others 0)	1	29.75	0.30
NH_3 (others ignored)	4	0.60	0.01
NH_3 (others 0)	1	5.55	0.11
NO_2 (others ignored)	5	0.13	0.13
NO_2 (others 0)	2	0.29	0.29

dation was done by exposure-based leave-one-out, excluding the respective highest (and lowest when *others ignored*) concentration to keep them in the training as “anchor points”.

A similar combination of TCO and GBCO has been used in the experiment presented in section 13.2 for a SiC-FET with dense palladium gate. The sensor was exposed to 350 unique gas mixtures comprising seven gases (including water vapor). The same type of sensor operated statically (at $V_{GB} = 0\,V$ and constant temperature) showed only weak selectivity to water at 100 °C and to hydrogen at 200 °C. Combining TCO with GBCO, as shown in Figure 7.11, increased the selectivity threefold compared to the best values achieved during static operation. The temperature cycle consisted of two plateaus at 100 and 200 °C and the gate bias was switched between −2 and +2 V.

The middle and bottom plot show the correlation coefficient of a mean and a slope feature, both computed with a window size of 5, with the target values for hydrogen and water. It is obvious that the features correlate much stronger with water than with hydrogen. This explains the poor selectivity in static operation: water masks the hydrogen’s influence on the signal, especially at the low temperature of 100 °C. Looking at the mean feature correlation first, the sensor’s correlation with hydrogen is between 0.3 and 0.4 at −2 V and drops to almost 0 at +2 V. The highest hydrogen correlation, 0.43, is found at 200 °C and −2 V, going hand in hand with a dip in water correlation. The higher temperature decreases the water surface coverage. As there are no spill-over effects on a dense gate, the influence of the gate bias cannot be explained with the presented model, but possible effects include proton trapping in the oxide as reported in [247], [248] or

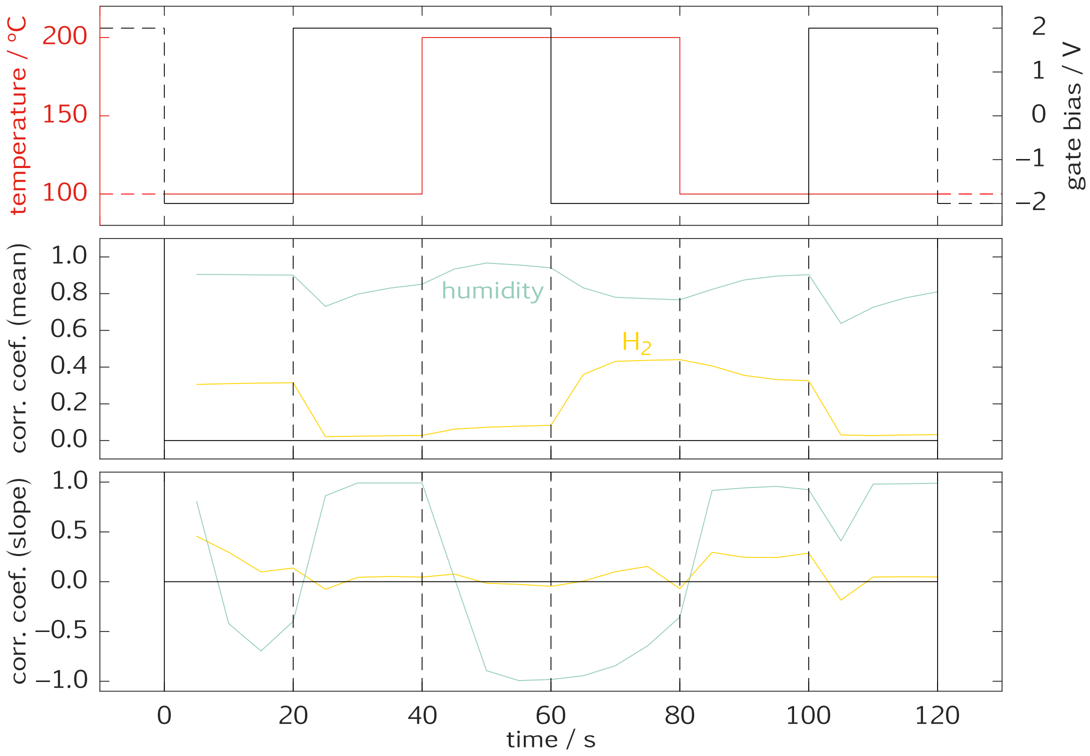

Figure 7.11.: Combined TCO+GBCO cycle (top) with correlations of mean (middle) and slope (bottom) features to hydrogen and water concentration. The dashed parts of the graph in the top plot indicate the previous and following cycle.

a change in the catalytic activity. There is, however, little doubt that this ability, i. e., to switch the hydrogen response on and off at will, improved the performance of the cycled sensor significantly over the statically driven ones. The resulting virtual sensor array then contains sensors with and without hydrogen response, facilitating the discrimination of hydrogen and water in the quantification model.

The correlation of slope features is very pronounced and dynamic for water, reaching from perfect positive to perfect negative correlation. This increase in dynamics is expected since the arithmetic sign of the response's slope changes with the direction of the temperature or gate bias step. It is, however, interesting that the correlation stays very strong in most sections even after 20 s. The correlation to hydrogen is mostly zero for the slope features with the notable exceptions of both sections at 100 °C and −2 V. The first is preceded by a downwards gate bias step, the second by a downwards temperature step. A smaller correlation is also observed at the remaining section at −2 V, which is where non-zero correlation was also observed for the mean features.

7.4. Conclusion

It has been found that controlling a GasFET's gate bias to keep the measured current constant influences its, usually logarithmic, response characteristics to become more logarithmic or almost linear. One possible explanation for this observation could be charges, likely oxygen anions, being moved onto or away from the oxide on the sensor surface through electric fields. This hypothesis has been tested with varying oxygen concentrations and can explain many of the observed effects. Combining TCO with GBCO produces features with additional information which significantly improve the classification of five different gases. Moreover, GBCO was able to greatly improve the selectivity of a SiC-FET with dense palladium gate for hydrogen and humidity: the hydrogen response is completely suppressed at positive gate biases.

8. Influence of light

Light-activated MOS sensors for gas detection have been studied for decades and extensive reviews on the topic are available [65], [253]. The consensus is that photons can increase the chemical activity of the semiconductor surface through electron-hole pair generation, effectively increasing the amount of free charge carriers available for ionization, e. g., electrons, to bind oxygen to the surface. This process is considerably more efficient than activation through temperature. Commercial state-of-the-art gas sensors (heated) require 35 mW or more [254], [255] whereas light-activated MOS sensors with power requirements of only 100 µW have been reported [66]. At the same time, photons can de-ionize adsorbed oxygen, increasing the desorption rate. Generally, irradiation changes the equilibrium coverage of oxygen and other species on the sensor surface and, thus, all sensor properties and in particular the *sensitivity, selectivity, and stability* (3S).

Little research has been directed to exploring the effects of light irradiation on field-effect gas sensors. Most of these works focus on 1D gate materials [256], [257] and one mentions UV irradiation to remove trapped electrons from an Al_2O_3 gate insulator [258]. The lack of motivation for this kind of research is not very surprising given that MOS sensors promise much larger effects upon irradiation due to their semiconducting nature. Nevertheless, the binding energies of gas molecules chemisorbed on a metallic catalyst (Pd, Pt, Ir) can be reached with UV light. Oxygen is bound at around 4 eV, and hydrogen at 2.5 eV to 3.5 eV [259], corresponding to wavelengths of 300 nm and 380 nm to 500 nm, respectively. Consequently, UV light should be able to influence, and, more specifically, speed up, desorption processes and change the equilibrium which can be especially interesting in combination with gate bias changes. This section discusses some preliminary results regarding UV irradiation of a SiC-FET with porous Ir gate which have partly been published in [260].

A UV-LED was mounted opposite the chip surface with a distance less than 5 mm. The LED's forward voltage is 3.8 V at 20 mA. Its experimentally determined spectrum[1] is shown in Figure 8.1. The peak wavelength is at 405 nm with significant output between 370 and 440 nm. The LED was cho-

---

[1] Thanks to Maxim Schmidt, Institute of Microelectronics, Saarland University.

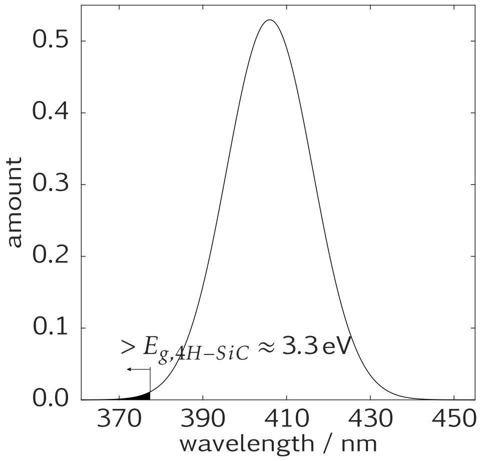

Figure 8.1.: Experimentally determined emission spectrum of the UV-LED.

sen to have little influence on the electrical properties of the SiC-FET, i. e., the output below 377 nm, corresponding to the band gap of around 3.3 eV for 4H-SiC[2], should be small. Otherwise, photo-induced electron-hole pair generation in the channel would constantly increase the charge carrier concentration in the channel, leading to higher currents and altered device behavior. The total thickness of the material stack (porous $\mathrm{Ir/SiO_2/Si_3N_4/SiO_2}$) from gas phase to SiC is around 100 nm and can be penetrated by UV light. Indeed, the sensor signal is 100 µA to 200 µA higher under UV irradiation.

The electrical changes caused by the UV light can be observed in the absolute sensor signal (Figure 8.2). For easier comparison, the main temperature effect, i. e., change of electron mobility, is compensated. The exponent x in Equation 4.13 was experimentally determined from a linear fit to a log-log plot of the drain current over temperature. The resulting values are 3.93 at −2 V, and 2.66 for +2 V (without UV irradiation). Values with an absolute value larger than the theoretical (3/2) have been reported in literature [261]. The difference between gate biases probably arises from electrons being closer to the interface at positive gate bias and, thus, affected more by defect scattering than phonon scattering. Dividing the drain current by $T^{-3.93}$ indeed compensates the temperature influence well with and without UV irradiation (Figure 8.2). However, dividing the signal at +2 V by

---

[2] The theoretical band gap is lowered through high doping and temperature by 0.1 V each, resulting in an experimentally determined band gap of 3.065 eV (405 nm) for the materials in the sensor device. However, SiC is an inactive band gap material, i. e., the low photon adsorption efficiency should still prevent excessive charge carrier generation. (*personal communication, Dr. Mike Andersson*)

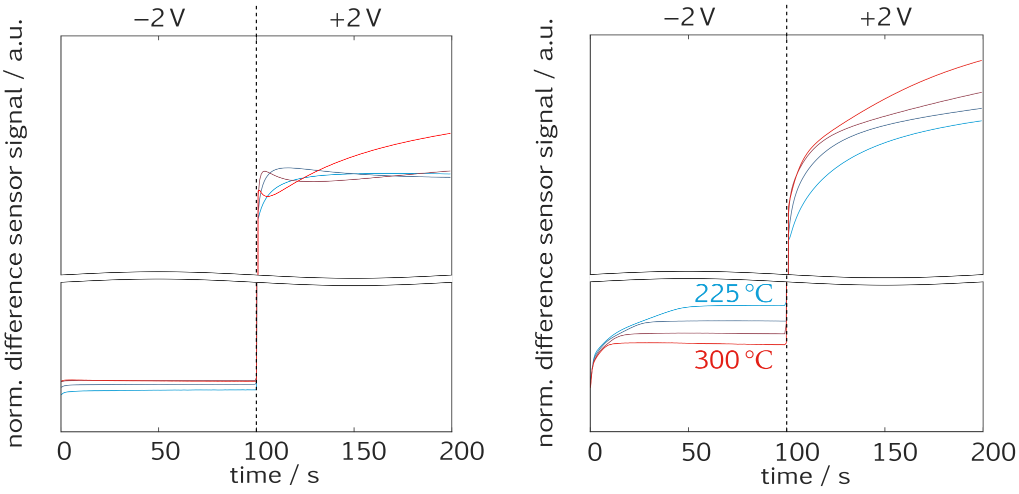

(a) LED off.

(b) LED on.

Figure 8.2.: Raw signal in 20 % O_2 with and without UV irradiation compensated for temperature-dependent change of electron mobility.

$T^{-2.66}$ leads to a signal three orders of magnitude smaller, suggesting an unidentified measurement error or the model being invalid in this range. Nevertheless, the compensation works reasonably well for the whole cycle and, moreover, the shape is of interest rather than absolute values. Note that the figure shows the temperature-compensated raw sensor signal from a separate measurement with shorter plateau durations (100 s) and a more narrow temperature range (225 °C to 300 °C in steps of 25 °C).

Dynamic effects appear with UV irradiation, causing a general upwards trend over time especially at positive gate bias. A tentative explanation which fits the direction of the drift is the removal of trapped electrons from the oxide which has been reported to happen only under UV light for Al_2O_3 as gate insulator [258]. Alternatively, the additional electron-hole pairs in the channel could increase the time constant until a new charge carrier equilibrium in the channel has been reached, which is accelerated through higher temperatures.

The data shown in Figure 8.3 and Figure 8.4 are from the "LED on" part of the measurement described in section 7.3, i. e., gate bias plateaus at −2 and +2 V in changing oxygen concentrations. It has been processed in the same way as before, this time using the values for g_m determined under UV irradiation (Table 8.1).

As before, the overall response becomes more negative with increasing oxygen concentration and the response is less negative at positive gate bias.

Table 8.1.: Experimental values of transconductance g_m in µA/V. The values at temperatures marked with * have been linearly extrapolated from measurements at 225, 250, 275, and 300 °C.

	150 °C*	200 °C*	250 °C	300 °C
−2 V	124	102	81	59
+2 V	168	157	146	136

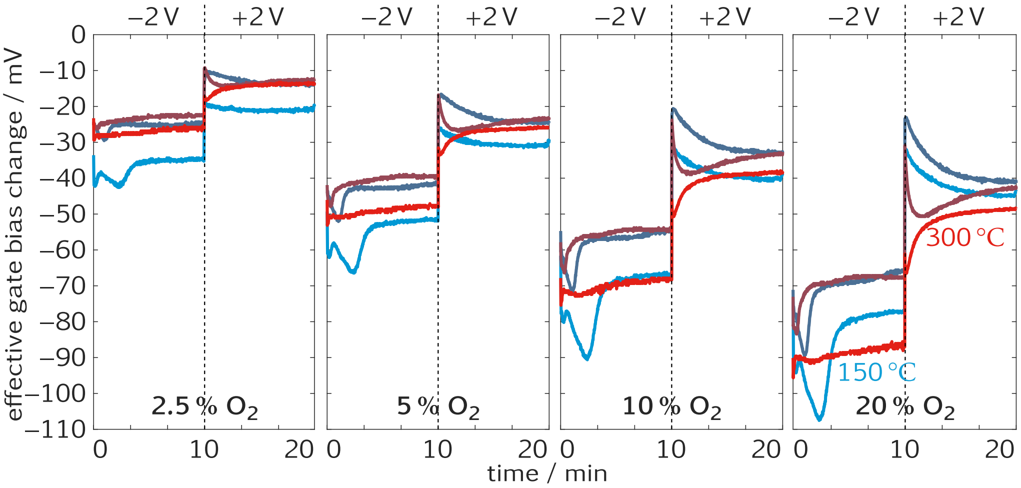

Figure 8.3.: Change in effective gate bias with UV irradiation for 2.5, 5, 10, and 20 % oxygen with 1 % oxygen as reference. The effective gate bias change has been computed from the drain current after Equation 7.5.

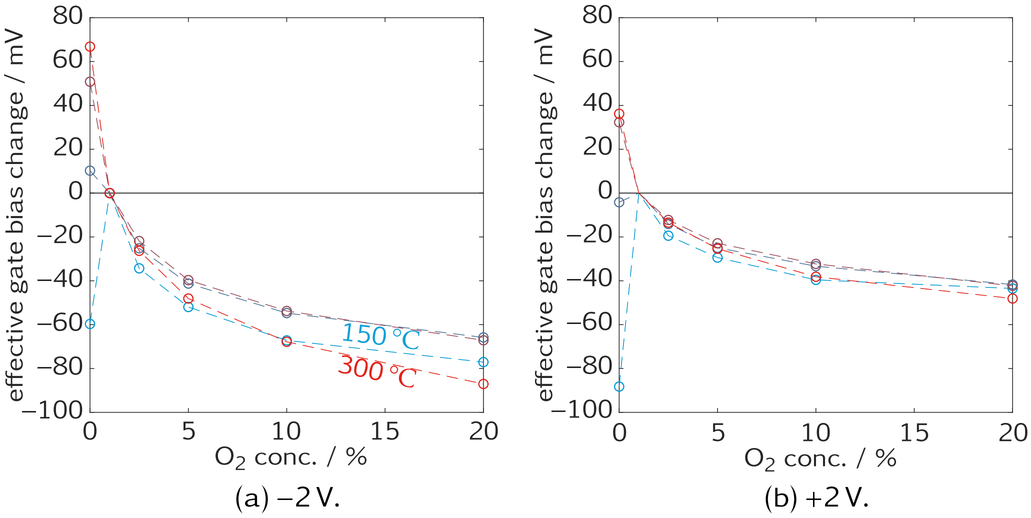

Figure 8.4.: Response in Figure 8.3 just before the gate bias step.

The negative shift with increasing temperature, while apparent in Figure 7.7, cannot be observed under UV irradiation (Figure 8.4). One possible explanation is that the surface mobility is dominated by the irradiated rather than the thermal energy, rendering the latter's influence negligible. The response, however, gains dynamic effects under UV light (compare Figure 7.6 and Figure 8.3). Most apparent is the clearly concentration-dependent dip at the beginning of the cycle, i. e., having switched from +2 V to −2 V. It is most pronounced at 150 °C, decreases in both duration and amplitude with temperature and vanishes at 300 °C. It fits well the idea of negative charges, i. e., oxygen anions, being pushed from the catalyst onto the oxide, decreasing the signal. The higher the temperature, the quicker is the process and the fewer charges have been moved in the first place since higher temperatures increase entropy. The exact reason of the signal rising again from the dip as well as the dynamic effects at positive gate bias cannot be consistently explained with the current model, showing the need for further investigations. The responses in different target gases are even more complex, but have many unique features enabling perfect classification at least in a simple measurement design [260].

In conclusion, the measurements with UV irradiation show, qualitatively, the same effects as without the irradiation (cf. section 7.3). The UV light adds, however, dynamic effects in the response not seen before which are consistent with a movement of charges on the surface when the gate bias is changed. Dynamic effects in the absolute sensor signal can be explained by trapped electrons being freed or the constant generation of electron-hole pairs through the light. The effects introduced with UV irradiation are significant and gas-dependent so that light should definitely be considered as a quick and effective parameter to be cycled in order to increase the information content of GasFET signals and other sensor technologies.

Part III.

Testing and evaluation

9. Gas sensor calibration

A reliable calibration is paramount for all sensors. It determines the relation between the sensor's electrical output and the actual physical or chemical quantity to be measured. While this relationship can, in principle, often be modeled theoretically for physical sensors, the finite manufacturing precision still makes calibration or at least controls necessary. This is even more the case for chemical sensor systems which are required to deliver selective outputs in a whole host of environments, each presenting a large variety of interferents. The complex interactions between sensor and gas or gases in-between each other, the often large number of target and interfering gases as well as sensor drift over time require long and complex calibration profiles to establish a stable, data-driven model (or, in theory, to prove the reliability of a theoretical model).

The calibration of gas sensors has been a long-standing issue and has spawned many publications in the past few decades. The long settling time after a gas concentration change could be reduced by one order of magnitude by a simple exponential model [262]. Calibration transfer methods have been applied to distribute the calibration from one master to several similar slave systems, and drift compensation makes an initial calibration model last for a longer period of time. Eventually, however, each system must be recalibrated. While the expense and effort for frequent recalibration is often justified by the cause in industrial or other professional environments, it is a major hurdle for the adoption of gas sensors in mainstream customer electronics like smartphones. One potential solution is the use of interconnected sensor networks with sensor units constantly recalibrating themselves with the measurements from nearby (mobile or stationary) sensor units [263], [264].

Even if the problem of sensor drift can be overcome, eliminating the need for recalibration, initial calibration is still an issue. The problem of overfitting a model to artifacts in data has been discussed in Part I, but such artifacts can manifest themselves on many levels (Figure 9.1). The use of validation and testing when building data-driven models has already been discussed. However, also the specific calibration equipment, i. e., gas mixing system, or, more generally, experimental unit [265], can introduce systematic errors, e. g., an unidentified offset in one of the gas flows. Such unknown influences can cause overfitting which cannot be detected using test data recorded with the same experimental unit. Instead, the testing data must come from a calibration run with another, independent system. This work has already shown an example of how slight temperature variations in the laboratory could influence the calibration for any system contained in the room (cf. section 6.2). Also the quality of carrier and test gases can vary between laboratories and institutes[1]. Thus, inter-lab tests are generally more reliable than intra-lab tests, i. e., using different calibration equipment in the same laboratory. If inter-lab tests have confirmed the stability of the sensor system, there is still no guarantee that it will work and perform as expected from the in-lab calibration in the field. It is rarely possible to model the environment of a certain field location so that a calibration model cannot simply be transfered between two different environments. Hence, field tests are required, usually with the help of costly and bulky reference instruments, often with long sampling periods and no on-line capability, since the gas composition cannot be changed at will. This kind of passive calibration, as compared to active calibration in a controlled gas mixing system, presents the additional challenge that rare events can easily become underrepresented so that a compromise between calibration time and model quality has to be made.

The levels of possible overfitting causes shown in Figure 9.1 are closely related to sources of variation in quality control and measurement systems analysis [266], [267]. Interlaboratory studies play an important role in improving data quality and confidence. Also called round robin tests, the conduct and statistical evaluation is described in at least two standards, one by the *American Society for Testing and Materials* (ASTM) [268] and the other from the *International Organization for Standardization* (ISO) [269]. Their application to gas sensor system testing is, however, just emerging. At the time of writing, only three independent interlaboratory studies to evaluate the performance of chemical gas sensor systems could be found [270]–[273][2], in contrast to many more for the testing of reference instruments or the validation of measured sample properties.

This part (Part III) of the thesis presents, in the following, three studies aimed at improving gas sensor calibration through field tests, interlaboratory studies, and improved experimental design for calibration profiles. Beforehand, the LMT gas mixing equipment is described and briefly compared to other such equipment. In this context, the features of a newly developed control software for such calibration equipment are presented.

---

[1] Or change with the delivery of a new gas cylinder.

[2] Including one which was performed during this PhD project.

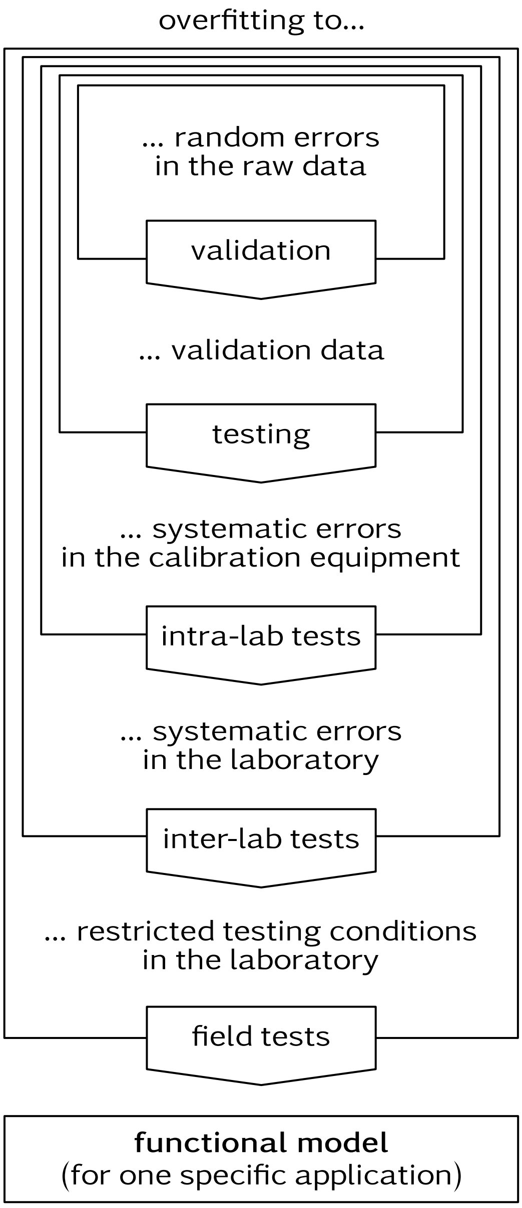

Figure 9.1.: Possible causes and associated testing strategies for overfitting.

10. Test gas generation

Reliable, accurate, and precise generation of gas mixtures is, obviously, a basic requirement for gas sensor testing and calibration. These systems are mostly custom-built and unique. One of the systems used at LMT is described in [274], [275]. The following sections will give a brief overview of the different components of the system in order to facilitate a better understanding of its limitations and provide a basis for the newly developed control software.. Different other gas mixing concepts relevant to this work are briefly described.

10.1. Hardware

10.1.1. LMT

The basic principle of the gas mixing system, dynamic dilution, is shown in Figure 10.1. A known gas mixture with relatively high pressure, typically from a gas cylinder or a zero air generator, is connected to a *mass flow controller* (MFC). The MFC creates a constant, adjustable gas flow, usually given in ml/min. The MFC is followed by an (optional) 3/2-way valve which redirects the gas flow either to the sensor or bypasses it, the main purpose of the latter being to avoid subjecting the sensor to gas flow fluctuations when an MFC settles on a new setpoint. Combining several of these gas lines enables automatically controlled creation of precise and dynamic gas mixtures. Fluidic details like dead volume and mixing length together with characterization and validation measurements of the newest LMT system are discussed in [275].

The usual carrier gas is zero air from a GT Plus ultra-zero air generator (VICI AG International, Schenkon, Switzerland). This device removes hydrocarbons ($\geq C_4$), sulfur oxides, and nitrous oxides (max. 0.1 ppm_v) with an activated carbon filter, CO_2 (max. 5 ppm_v) and humidity (min. dew point −50 °C) with a pressure swing, and remaining hydrocarbons (max. 0.1 ppm_v) as well as hydrogen and carbon monoxide (max. 0.1 ppm_v) through catalytic oxidation [276], [277]. Such low and especially stable interferent concentrations are an important prerequisite to produce reliable and credible mea-

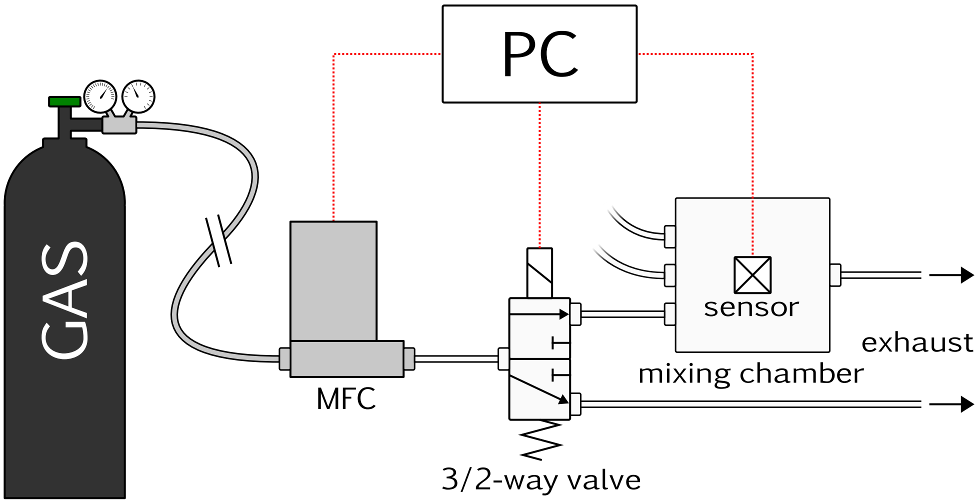

Figure 10.1.: Schematics of a gas mixing system with dynamic dilution.

surements of target gases at ppb$_v$ level. For a more realistic environment, typical atmospheric concentrations of hydrogen (500 ppb$_v$), carbon monoxide (150 ppb$_v$) and methane (1.8 ppm$_v$) [278]–[281] can be added separately from a commercial gas cylinder. Humidity is added in the system via a bubbler line (cf. next paragraph). The oxygen concentration can be varied between 0 and 20 % through the addition of pure nitrogen N5.0, i. e., a purity of 99.999 %. Some systems provide a dedicated MFC for nitrogen, others provide the choice to add either nitrogen or humidity to the carrier gas flow. Air, nitrogen, and humidity are supplied by one MFC with 500 ml/min maximum flow each, giving full dynamics up to a total flow of 500 ml/min.

The bubbler line (Figure 10.2) is essential for generating humidity, but can be used in general to bring any liquid into gas phase. An MFC produces a constant flow of carrier gas, usually air or nitrogen, which is then passed through a bubbler flask filled with *high-performance liquid chromatography* (HPLC)-grade water (or another liquid of choice). The gas is introduced below the surface of the liquid so that the bubbles saturate with vapor on their way up. As long as the gas phase can fully saturate, the headspace concentration is proportional to the liquid's vapor pressure, resulting in 100 %RH. This means, however, that the concentration depends strongly on the liquid's temperature. Therefore, the flask is usually kept in a temperature-regulated water bath slightly below room temperature to avoid condensation downstream. The bubbler flask can also be followed by a second flask in the same water bath which is filled with, e. g., glass wool and acts as aerosol and particle trap.

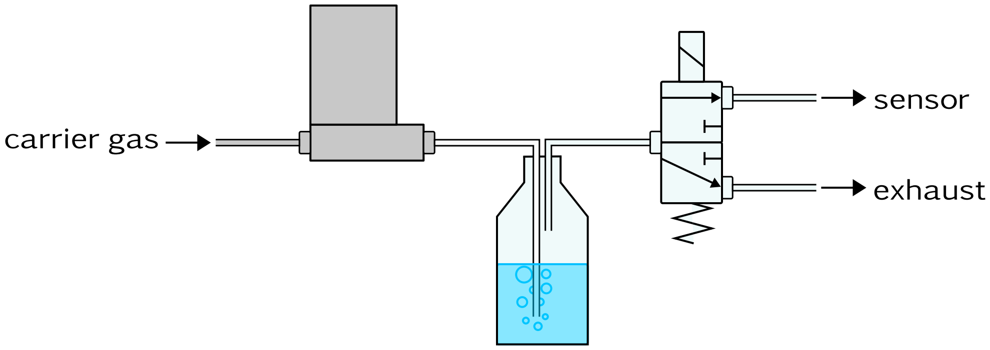

Figure 10.2.: Fluidic diagram of a bubbler line.

In this setup it is essential that the valve is located downstream of the flask. Otherwise, evaporating liquid could enter the gas stream even without any flow of carrier gas. For the same reason the outflow is always higher than the inflow which must be factored in especially for high evaporation rates, i. e., at high temperatures [282], [283].

Replacing the bubbler flask with a permeation oven transforms the bubbler into a permeation line (Figure 10.3). One or several permeation tubes are placed in the heated, airtight oven chamber. These tubes are made from *perfluoroalkoxy alkane* (PFA) or similar materials and contain the pure test substance which slowly diffuses through the tube walls. However, unlike the bubbler line, reaching equilibrium in the oven can take up to several hours, which is why, usually, neither the carrier gas flow nor the temperature are adjusted to generate different concentrations. Instead, the oven outflow is dosed into the main gas flow using a second MFC. Gas generation through permeation is compact and can, in principle, be very exact using gravimetry to determine the permeation tubes' mass loss. Components can be added or removed from gas mixtures and it also works for gases with very high vapor pressure, e. g., naphthalene, which cannot be kept in gaseous form in pressurized cylinders.

The permeation line setup requires a higher inlet pressure to compensate the pressure drop over one MFC. Additionally, the pressure between the two MFCs must be controlled with a pressure regulator and a higher inflow than outflow must always be ensured to maintain pressure.

Instead of diluting the test substance through permeation, carrier gas can be added by another MFC instead, yielding a predilution line (Figure 10.4). A typical configuration with 500 ml/min maximum carrier flow and 10 ml/min or 20 ml/min maximum test gas and injection flow achieves a dynamic dilution over more than four orders of magnitude [274], [275]. Thus, 100 ppm_v test gas can be diluted down to one-digit ppb_v concentrations. The same con-

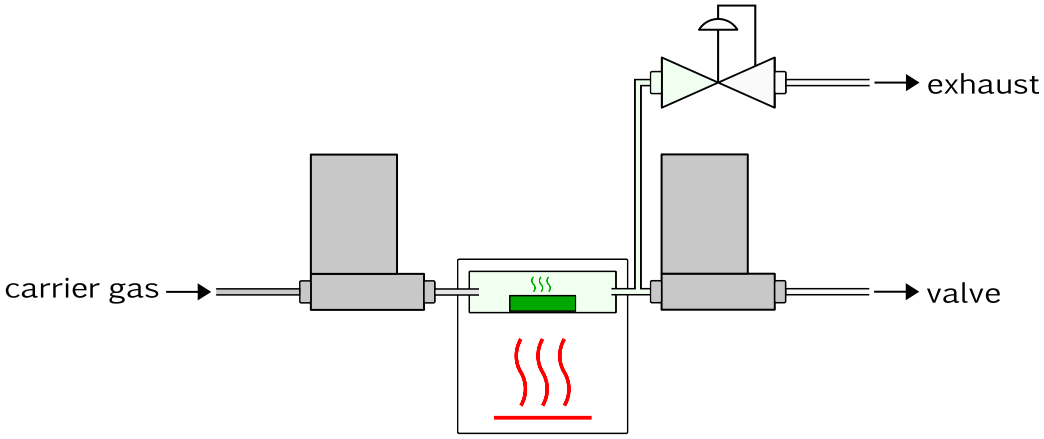

Figure 10.3.: Fluidic diagram of a permeation line.

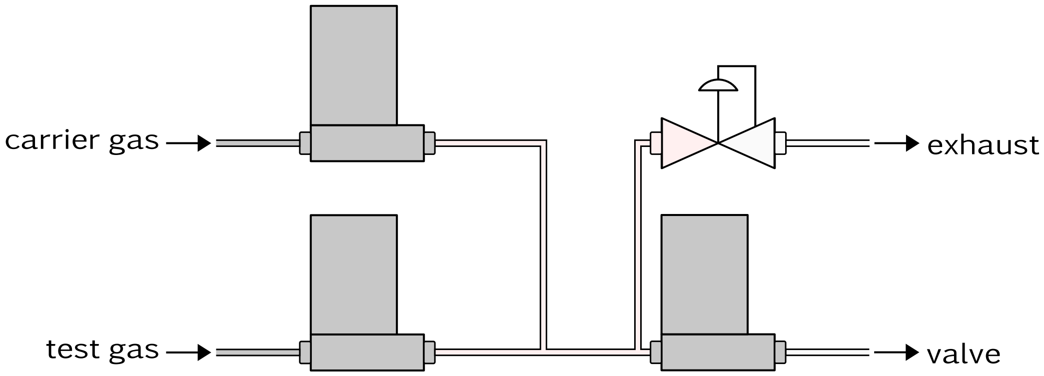

Figure 10.4.: Fluidic diagram of a predilution line.

centration range could be achieved with a test gas concentration of 1 ppm_v or less connected to a normal gas line. However, gas with a purity of N5.0 (sold as "ultra-high purity") contains 10 ppm_v of impurities in unknown ratios, almost completely masking the actual test gas. Hence, both permeation and predilution line aim for high dilution ratios so that high initial test gas concentrations far above the level of impurities can be used.

10.1.2. Other gas mixing concepts

Most of the measurements presented in this work were done on a system as described in the previous section. However, gas mixing systems at Linköping University (LiU) and the *Bundesanstalt für Materialforschung und -prüfung* (BAM) have also been used and shall, therefore, be briefly outlined here.

LiU has five gas mixing systems with similar setup. All gases are supplied from gas cylinders, including pure nitrogen and pure oxygen, and are injected into a common gas flow by computer-controlled MFCs. All test gas cylinders have pure nitrogen (N5.0) as background, which, in combination with separate MFCs for oxygen (N5.0) and nitrogen (from a liquid supply of unknown purity), allows for a freely adjustable oxygen concentration in the carrier gas. Instead of one valve per gas line, the whole gas flow enters a four-way valve which can direct the gas flow through the sensor chamber or directly to waste. To maintain a constant flow and atmosphere, a second branch with only two MFCs, nitrogen and oxygen, is connected to the four-way valve. When the valve switches, this gas flow is lead through the sensor chamber. This system enables sharp steps and time for a new gas mixture to settle, similar to the LMT system. Humidity can be added via an optional bubbler line. A mass spectrometer can be connected to any system for on-line monitoring of the gas mixture or certain other components, e. g., reaction products. Both the ability to easily change the oxygen concentration and to monitor reaction products downstream the sensor location were valuable features for many orientation measurements, in particular regarding the influence of the gate bias. Results of these measurements have been published in [250].

The system at BAM was designed to generate and maintain exact VOC mixtures with many components and low concentrations to, e. g., investigate the sorption properties of materials [284], [285]. Gases are generated through evaporation of pure, liquid substances at precise temperatures. Enclosed in stainless steel bottles, the resulting headspace concentration is extracted through a small nitrogen inflow and lead into a glass bottle to be mixed with 50 %RH air. Capillaries feed a main mixing bottle from any number of pure substances from which the final gas mixture can be extracted. The capillaries have precise length and (inner) diameter so that the gas flow is proportional to the (constant) pressure difference between substance and mixing bottle, i. e., they act as a static MFC. The background air in the system is dried and cleaned with an activated carbon filter which removes all contaminants relevant to materials tests. Environmental hydrogen and carbon monoxide can, however, pass. Many analytical methods are available in the same laboratory to determine exact gas concentrations, e. g., *high performance liquid chomatography with a diode array detector* (HPLC-DAD) or GC-MS [270].

10.2. Software

The gas mixer software[1] presented in this section is jointly developed by LMT (Manuel Bastuck, Tobias Baur, Henrik Lensch) and 3S GmbH (Julian Howes) with equal contributions. We would also like to thank Martin Leidinger for valuable discussions, especially during the conceptualization stage. The following descriptions will focus on the contributions made by the author.

10.2.1. Graph model

The gas mixing system has been modeled as a directed graph, i. e., a set of nodes connected by directional edges. The nodes act as gas reservoirs, i. e., they contain a certain volume of a certain gas mixture, and the edges allow this gas mixture to flow from one node to another with its direction representing the pressure difference. An edge's flow, q, can be restricted, e. g., through an MFC or valve. The model follows a simple set of rules:

- Supplies (gas cylinders and zero air generators, liquids, permeation tubes) are infinite reservoirs, i. e., they supply infinite outflow
- A reservoir's inflow is the sum of all ingoing edges' outflow, its outflow is the sum of all outgoing edges' inflow
- A reservoir can only have one infinite inflow, but many restricted inflows
- A reservoir's outflow can be lower, but not higher than its inflow
- The outflow of an unrestricted edge is the same as its inflow

---

[1] working title: grupy, for *Gas Research Unit in PYthon*

- The outflow of a restricted edge is its restricted flow or its inflow, whichever is smaller

With this setup, all of the gas line types mentioned before can be modeled as subgraphs. The internals of a subgraph are hidden from the user (and can be regarded as a "black box") and the only interface are the outer nodes which can be connected via unrestricted edges to the outer nodes of other subgraphs.

One of the simplest subgraphs is a gas supply (Figure 10.5a), modeling, e. g., a gas cylinder. It consists of only one outflow node which is static, i. e., it is an infinite reservoir of a predefined gas mixture. The subgraph for a liquid supply looks identical but extends the gas supply subgraph with a method to calculate the liquid's vapor pressure at a given temperature. The permeation tube subgraph (Figure 10.5b) also contains a static gas node which is, however, entirely internal. It feeds the outflow node via a restricted internal edge whose flow is automatically set to the tube's permeation rate at a given temperature.

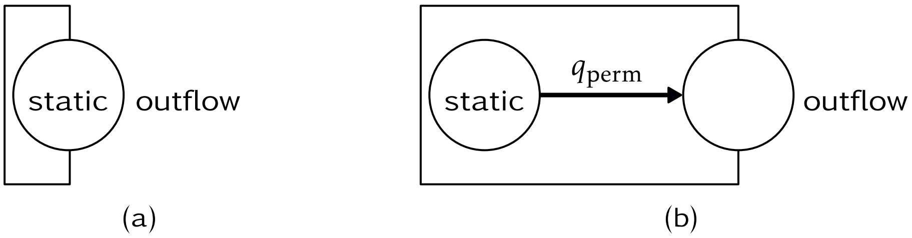

Figure 10.5.: Subgraphs for (a) a gas supply and (b) a permeation tube.

The outflow nodes of all these supplies can be connected to the inflow node of a gas line (Figure 10.6). It comprises one inflow and one outflow node connected with an internal edge. The flow of this edge is restricted by a mandatory MFC and an optional valve assigned to the gas line. Thus, a gas line can provide a defined outflow from a gas supply, just like in the real system.

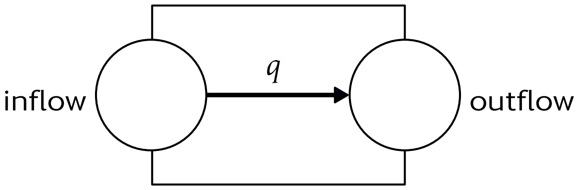

Figure 10.6.: Subgraph of a gas line with a gas flow q between two reservoirs.

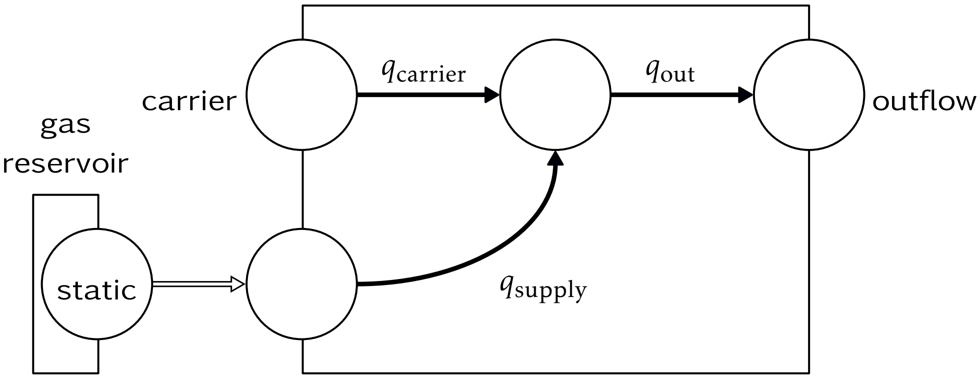

Figure 10.7.: Subgraph of a predilution line (with supply).

The subgraph concept can easily accommodate more complex assemblies. The structures of bubbler, permeation, and predilution line are all derived from of the same template with only the test gas flow restriction being adapted. Figure 10.7 shows the subgraph for a predilution line. A gas supply is connected to the test gas inflow node. Another gas supply would usually be connected to the carrier inflow node, but is omitted here for visual clarity. The subgraph replicates the fluidic connections from Figure 10.4. Each edge represents one MFC, and the edge between the internal reservoir and the outflow node can also be restricted by a valve, if desired. Keeping all these structures internal provides a very simple user interface: the only connections the user has to define are unrestricted edges between the subgraphs.

As stated, the predilution subgraph can be transformed into a bubbler subgraph (Figure 10.8) with only small changes. The outflow q_{out} is only restricted by a valve, but no more by an MFC, according to the bubbler line concept shown in Figure 10.2. The supply flow q_{supply} is controlled internally to be a fraction of the carrier flow q_{carrier}. This fraction is the liquid's vapor pressure p_v divided by the total pressure [282],

$$\Phi(T) = \frac{p_v(T)}{p + p_v(T)}, \tag{10.1}$$

where p is the atmospheric pressure. This fraction can be requested from the liquid supply connected to the bubbler, the latter of which supplies the current temperature. The implementation is such that the temperature can either be supplied by the user or read from a sensor.

The permeation subgraph Figure 10.9 follows the same concept. The supply flow is unrestricted because it just forwards the flow coming from the permeation tube supply. This flow is equal to the permeation rate P_0

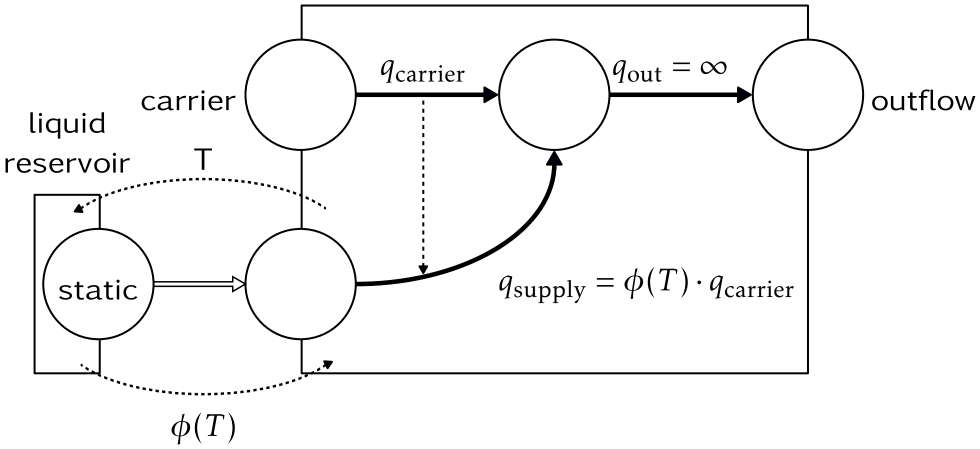

Figure 10.8.: Subgraph of a bubbler line (with supply).

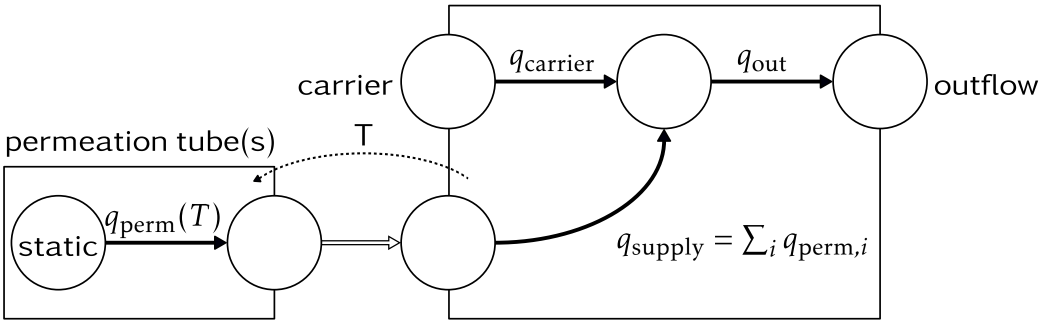

Figure 10.9.: Subgraph of a permeation line (with supply).

which is calibrated by the manufacturer for a temperature T_0. For other oven temperatures T, the new permeation rate P can be estimated [286]:

$$\log(P) = \log(P_0) + 0.034(T - T_0) \tag{10.2}$$

Note that the uncertainty of the calibrated permeation rate can be as high as 50 %.

10.2.2. User interface

The implementation of the graph provides both a command line and a GUI. The GUI consists of a canvas Figure 10.10 in which gas supplies and subgraphs (called assemblies) can be placed by drag and drop. The outer nodes are highlighted and color-coded making the connection of subgraphs easy and intuitive. The underlying implementation checks automatically if the connection between two nodes is allowed based on their categories

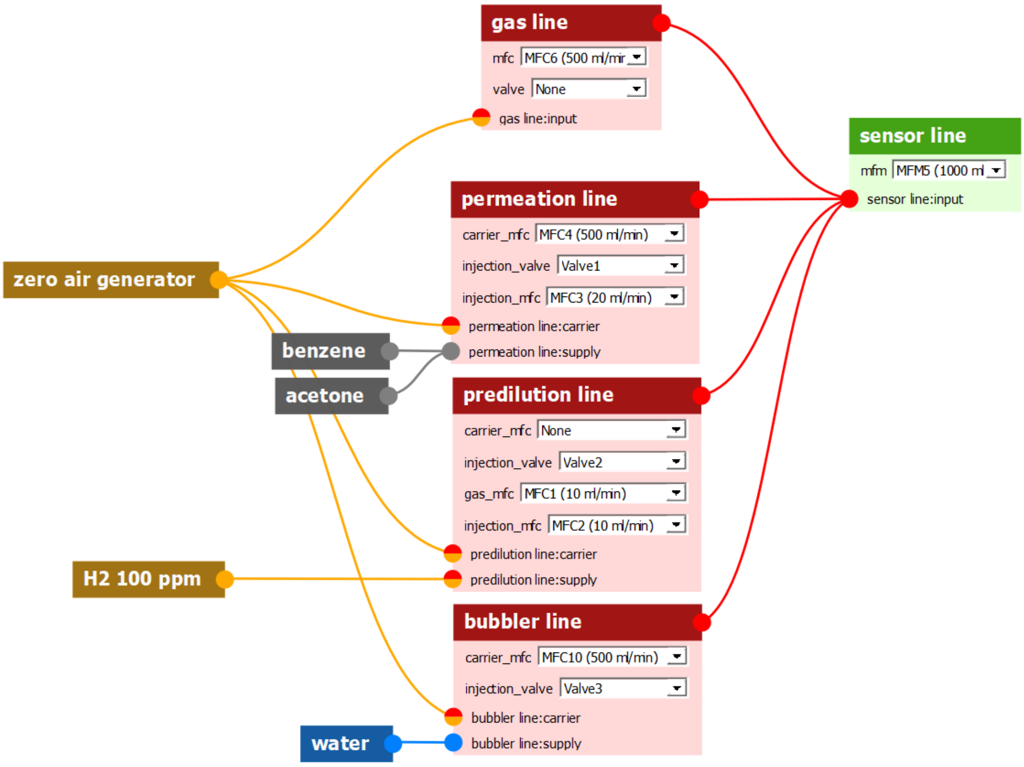

mfc MFC6 (500 ml/mir
valve None

mfm MFM5 (1000 ml

carrier_mfc MFC4 (500 ml/min)
injection_valve Valve1
injection_mfc MFC3 (20 ml/min)

carrier_mfc None
injection_valve Valve2
gas_mfc MFC1 (10 ml/min)
injection_mfc MFC2 (10 ml/min)

carrier_mfc MFC10 (500 ml/min)
injection_valve Valve3

Figure 10.10.: GUI of the graph editor.

and maximum number of connections and rejects wrong connections. The system can handle multiple categories for a node, which is indicated by the red/yellow coloring of red assembly nodes, indicating the possibility to add either a (yellow) gas supply or many (red) assemblies. Due to the previously discussed limitations, the blue liquid node allows only one incoming connection, while the grey permeation tube node allows many. All assemblies feed the green sensor line which represents the mixing chamber. All assemblies have predefined parameters for devices like MFCs, *mass flow meters* (MFMs) and valves. The available devices are predefined in a hardware configuration file and can be chosen from a dropdown menu which prevents choosing the same device twice.

Instead of using the GUI, the same graph can be produced programatically as shown in Listing 10.1. In a first step, the supplies are loaded from an external JSON file. Then, the assemblies are created, named, and the devices are set from a predefined list. Flows between nodes can be created with `target_node.create_inflow_from(source_node)`. These flows correspond to the colored lines in Figure 10.10.

Listing 10.1.: Python code to recreate the graph in Figure 10.10.

```python
# getting supplies
supply_hydrogen = get_registry().get_gas_source('h2 1000 ppm')
supply_air = get_registry().get_gas_source('zero air
 ↪  generator')
supply_water = get_registry().get_liquid('water')
supply_benzene = get_registry().get_permeation_tube('benzene')
supply_acetone = get_registry().get_permeation_tube('acetone')

# creating gas lines
gl_carrier = GasLine('gas line', mfc=mfcs[5])
gl_permeation = PermeationLine('permeation line',
 ↪  carrier_mfc=mfcs[3], injection_mfc=mfcs[2],
 ↪  injection_valve=valves[0])
gl_predilution = PredilutionLine('predilution line',
 ↪  gas_mfc=mfcs[0], carrier_mfc=mfcs[3],
 ↪  injection_mfc=mfcs[1], injection_valve=valves[1])
gl_bubbler = BubblerLine('bubbler line', carrier_mfc=mfcs[9],
 ↪  injection_valve=valves[2])
sensor = SensorLine('sensor', mfm=mfcs[4])

# creating flows from supplies to gas lines
gl_carrier.inflow_node.create_inflow_from(supply_air.outflow_node)
gl_permeation.carrier_node.create_inflow_from(supply_air)
gl_permeation.supply_node.create_inflow_from(supply_benzene)
gl_permeation.supply_node.create_inflow_from(supply_acetone)
gl_predilution.carrier_node.create_inflow_from(supply_air)
gl_predilution.supply_node.create_inflow_from(supply_hydrogen)
gl_bubbler.carrier_node.create_inflow_from(supply_air)
gl_bubbler.supply_node.create_inflow_from(supply_water)

# creating inflows to sensor line
sensor.inflow_node.create_inflow_from(gl_carrier.outflow_node)
sensor.inflow_node.create_inflow_from(gl_permeation.outflow_node)
sensor.inflow_node.create_inflow_from(gl_predilution.outflow_node)
sensor.inflow_node.create_inflow_from(gl_bubbler.outflow_node)
```

The whole graph can be saved to and loaded from a GraphML file. GraphML is based on *Extensible Markup Language* (XML), a human-readable markup language, and has structures to define nodes, edges, subgraphs, data for all these, and many more. Listing 10.2 shows excerpts from the example graph as GraphML.

10.2.3. Solving the graph

One main feature of user-friendliness is the software's ability to hide "physical implementation details" from the user, at least to a certain degree. The user designing the gas profile for a sensor test should not have to figure out the flow setpoints for all MFCs in the system during each instant. Instead, she should be able to simply enter the desired gas concentrations and leave all details to the software. This is the reason why the graph model is necessary in the first place.

There are two ways to arrive from gas setpoints to device setpoints: analytically or through optimization. The analytic approach guarantees exact and deterministic results, but can impose certain restrictions on the graph. Optimization is often able to lift these restrictions, but requires tight supervision or even parameter tuning to ensure the integrity of the results. The current system employs an analytic approach to solve the overall graph with the help of optimization in predilution subgraphs.

For the whole graph, the linear equation system

$$\mathbf{Q} \cdot \boldsymbol{q} = \hat{\boldsymbol{q}} \tag{10.3}$$

must be solved, where $\hat{\boldsymbol{q}}$ are the desired gas flows, $\boldsymbol{q}$ the required MFC flows, and $\mathbf{Q}$ a matrix of maximum gas outflows for each subgraph, with one row per gas and one column per subgraph. The desired gas flows are easily calculated from the desired gas concentrations c_i with the given total flow q_{total} as:

$$\hat{q}_i = q_{\text{total}} \cdot \frac{c_i}{\sum_i c_i} \tag{10.4}$$

The maximum outflow matrix $\mathbf{Q}$ is determined by iterating over all subgraphs and all gases and noting the theoretical maximum outflow in the respective place.

The matrix $\mathbf{Q}$ must be square for the equation system to have a unique (or no) solution. This is the case when there are as many subgraphs as varied gases. This requirement poses some practical problems. For example, air is a mixture of nitrogen and oxygen supplied by only one carrier gas MFC.

Listing 10.2.: GraphML of the example graph in Figure 10.10.

```
<?xml version='1.0' encoding='UTF-8'?>
<graphml ...>
  <key atrr.name="mfc" id="mfc" attr.type="str"/>
  <key atrr.name="y" id="y" attr.type="float"/>
  <key atrr.name="x" id="x" attr.type="float"/>
  <key atrr.name="class" id="class" attr.type="str"/>
  <graph edgedefault="directed" id="main">
    <graph edgedefault="directed" id="sensor line">
      <data key="class">SensorLine</data>
      <data key="x">625.490</data>
      <data key="y">81.139</data>
      <node id="sensor line:input"/>
      <node id="sensor line:exhaust"/>
      <edge id="sensor line:exhaust_flow" source="sensor line:input"
      ↪   target="sensor line:exhaust"/>
    </graph>
    <graph edgedefault="directed" id="gas line">
      <data key="class">GasLine</data>
      ...
      <node id="gas line:input"/>
      <node id="gas line:output"/>
      <edge id="gas line:flow" source="gas line:input" target="gas
      ↪   line:output">
        <data key="mfc">MFC6</data>
      </edge>
    </graph>
    ...
    <graph edgedefault="directed" id="zero air generator">
      <data key="class">GasSource</data>
      ...
      <node id="zero air generator:reservoir"/>
    </graph>
    ...
    <edge id="e3" source="gas line:output" target="sensor line:input"/>
    <edge id="e7" source="zero air generator:reservoir" target="gas
    ↪   line:input"/>
    ...
  </graph>
</graphml>
```

Moreover, most test gases have air (or nitrogen) as background gas, so that it is not immediately obvious which test gas is associated with which subgraph. These dependencies can, however, be found iteratively by finding at least one subgraph containing a gas which is not contained in any other subgraph. If no two subgraphs are connected to gas sources with the same set of gases (which is one of the limitations of the linear approach), the carrier gas line will usually be the last one remaining. If it is connected to a mixture and no unique gas, the resulting equation system would be over-determined. In most cases, this would render it unsolvable because the final concentrations of nitrogen and oxygen vary with the addition of test gas and can, therefore, not be given by the user. To solve this dilemma, the last remaining subgraph is discarded under the assumption that it is the carrier gas line. Instead, the equation system is extended by one row forcing the summed up flow of all subgraphs to be equal to the user-supplied total flow. The resulting equation system is, eventually, solved with the `solve` command from the `numpy.linalg` module and the solution is checked for valid results, i. e., in $[0;1]$.

For the predilution line, the maximum outflow of gases cannot be determined directly. This is because the outflow MFC is connected to the internal mixing node whose gas mixture is controlled by q_{supply} and q_{carrier}. Hence, these two values must first be determined based on the desired outflow of test gas. Moreover, there are often multiple possible solutions for one desired test gas outflow, making optimization a good choice to solve the predilution subgraph. In the implementation, the *Sequential Least Squares Programming* (SLSQP) algorithm from the Python SciPy module is used [287], [288]. It can solve bounded non-linear problems with constraints by minimizing an objective function. For the predilution line, all variables are restricted to flow fractions in $[0;1]$, and the only (inequality) constraint is that the sum of inflows must be a certain percentage larger than the outflow. The latter is necessary to maintain a constant pressure in the mixing node before the outflow MFC. The objective function was chosen as

$$f(\boldsymbol{q}) = (\boldsymbol{q} - \hat{\boldsymbol{q}})^2 + p(\boldsymbol{q}) \tag{10.5}$$

where $p(\boldsymbol{q})$ is a penalty function which can be tuned to achieve different results. Specifically, this means that the optimization can try to find solutions with the smallest possible deviations between actual and desired flow under the following conditions:

- The supply MFC is opened as little as possible to consume as little gas as possible and run the system more economically.

- The carrier MFC is opened as wide as possible to increase the flow through the mixing node and speed up flushing the gas line.

- The outflow MFC is opened as little as possible to allow for more variation and flexibility with other injected gases in the total flow.

Figure 10.11 shows the setpoint of a carbon monoxide predilution line and the sensor response of an AS-MLV-P2 sensor (ams AG, Premstätten, Austria) which was linearly mapped to the expected concentration. The type of optimization makes a clear difference and it is obvious that reaching an equilibrium can take 30 min or more when the predilution line is optimized for test gas consumption. With optimized flush time, the signal change is almost instantaneous. One idea for an advanced gas profile is to change the prediluted concentration quickly with optimized flush time and then switch to minimized test gas consumption when the equilibrium has been reached.

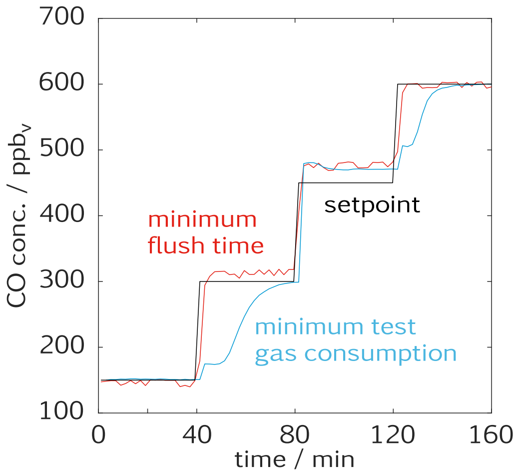

Figure 10.11.: Influence of the optimization on the predilution line's speed. The concentrations are estimated from the linearly mapped sensor signal of an AS-MLV-P2 ssensor.

All three terms are weighted with a user-defined coefficient k, so that $p(\boldsymbol{q})$ becomes:

$$p(\boldsymbol{q}) = \frac{1}{\sum k} \cdot (k_{\text{eco}} \cdot q_{\text{supply}} - k_{\text{flush}} \cdot q_{\text{carrier}} + k_{\text{outflow}} \cdot q_{\text{out}}) \tag{10.6}$$

Solving the predilution line poses one more problem which is, at the same time, the reason for the predilution line's very existence: the "forbidden" flow region of MFCs. An MFC cannot control the flow with arbitrary accuracy;

instead, the lower limit is about 2 % of the maximum flow for most modern MFCs. Hence, the need for predilution. The optimization, however, does not know about this forbidden region (0; 2)[2] and will produce solutions there as well. Coming from the right side, this issue could be handled by designing a steady function which increases the penalty drastically below 2 %. The single allowed point (0) surrounded by two infinitely high walls (negative values as well as values just above 0 are equally forbidden) is a big problem to virtually all optimization algorithms as they assume smooth functions. Some algorithms, like genetic ones, do not have this formal requirement, but tests have shown that "0" is still not found most of the time, with the additional issues of a longer running time and indeterministic results. Hence, an approach requiring two SLSQP runs was chosen, one trying to solve the problem within the whole parameter space, and the other with q_{carrier} fixed to 0. Both results are compared and the better one is chosen, given that its deviation is below a user-defined acceptance value. Otherwise, the problem will be deemed unsolvable in order to provide exact results in accordance to what would be expected from the linear solver applied to the whole graph.

As the linear solver cannot handle more complex cases, it is thinkable to apply the optimization algorithm used with the predilution line to the entire graph. This has been tested in a prototype implementation and found to work satisfactorily, despite largely increased runtimes due to the number of runs needed to find the optimal flows, including zero. The naïve approach, testing all permutations of zero and non-zero flows, is not feasible even for moderately complex systems with ten MFCs, resulting in roughly 2^{10} possible combinations. LMT's predilution system has over 20 MFCs. The number of combinations to check can, however, be largely reduced with a heuristic approach. The initial optimization is done in the full parameter space, i. e., [0; 100] % of the maximum flow. In each of the following runs, one of the flows below 2 % is fixed to 0 which is only kept as the final value if the objective function's value decreases. Otherwise, the flow is constrained to [2; 100] % and the next run is performed. This process ends as soon as there is no flow in (0; 2) left. The result of the latest run becomes the final result which is, again, checked for deviations outside certain limits from the desired concentrations.

Solving the entire graph with optimization gives more freedom to the user considering the system design. For example, chains of subgraphs and subgraphs connected to identical gas supplies are not possible to solve with the analytic approach.

---

[2] Parentheses indicate an open side (point not included), square brackets a closed side (point included) of an interval.

10.2.4. Substances and concentration units

Each substance to be used with the software must once be registered in a JSON file holding all substances with their relevant data. Ethanol is given as an example in Listing 10.3. The substance can be identified in the program by its name, its chemical formula, any of its alternative names, or its *Chemical Abstracts Service* (CAS) identifier. The molar mass is necessary to convert mass to volume, and the specific heat to compute the *gas correction factor* (GCF) which accounts for deviations from calibration gas and temperature of an MFC. The Antoine parameters allow to compute the vapor pressure in a given temperature range and, thus, enable using the substance also in liquid form. Hazard and precautionary statements (H, P and EUH) inform the user about potential threats from pure substances or mixtures, and the common unit can be set to personal preference (e. g., % for nitrogen or %RH for humidity).

The defined substances can then be used to define supplies like gas cylinders, permeation tubes, and liquids. Listing 10.4 shows an example for a gas cylinder containing approximately 1000 ppm_v ethanol in air. Concentrations are always given either as positive numbers in ppm_v, or as negative numbers, indicating ratios. This is helpful in such a case because the software will automatically fill the non-ethanol part of the bottle in a ratio of 79/21 of nitrogen/oxygen.

While ppm_v is the base concentration unit for all calculations in the software, it is not a practical unit for user input in all cases. This is especially true for relative humidity (or relative saturation, more generally), where calculating the absolute concentration requires temperature, pressure, and the related vapor pressure of the substance in question. Thus, the software contains functions to convert all these units to ppm_v in a very concise way: `ppb(13)` will return 0.013, and `relsat(25, sensor_line)` will return the absolute water vapor concentration in ppm_v at 25 %RH in the sensor line (i. e., mixing chamber).

10.2.5. Uncertainties

One important aspect often ignored in experimental work, especially when it comes to data-driven models, is the consideration of measurement errors or uncertainties. They are, however, worth a closer look, not only to adhere to good scientific practice, but also because they can quickly accumulate in complex systems and, eventually, make the test result look worse than the sensor's actual performance.

The sources of uncertainties in a *gas mixing apparatus* (GMA) are manifold.

Listing 10.3.: Example of the ethanol parameters in substances.json.

```json
{
  "ethanol": {
    "chemical formula": "C2H6O",
    "alternative names": [],
    "CAS": "64-17-5",
    "molar mass": 46.0684,
    "H": ["225", "319"],
    "P": ["210", "240", "305+351+338", "403+233"],
    "EUH": [],
    "specific heat cp": 2435,
    "antoine parameters": [
      {
        "tempmin": 273.0,
        "tempmax": 351.7,
        "a": 5.37229,
        "b": 1670.409,
        "c": -40.191
      }
    ],
    "common unit": "ppm"
  }
}
```

Listing 10.4.: Example of an ethanol cylinder in supplies.json. Note that "systematic error" here stands for the analytic confidence interval given on the gas cylinder's certificate.

```json
{
  "ethanol 1000 ppm": {
    "type": "bottle",
    "substances": {
      "ethanol": {
        "concentration": 985,
        "systematic_error": 12,
        "random_error": 0
      },
      "nitrogen": {
        "concentration": -79,
        "systematic_error": 0,
        "random_error": 0
      },
      "oxygen": {
        "concentration": -21,
        "systematic_error": 0,
        "random_error": 0
      }
    }
  }
}
```

Starting at the supply, all gas generation methods come with an uncertainty, be it systematic (i. e., an offset), random (i. e., noise) or both. Commercial gas cylinders, for example, commonly have a systematic uncertainty of 1 % of the measured test gas concentration (with an additional deviation from the ordered concentration), going as high as 20 %. Permeation tubes can even have systematic errors as high as 50 %. The random error for gas cylinders is, for all intents and purposes, zero, but permeation tubes and bubbler flasks strongly depend on the temperature stability. In addition, all gas supplies contain more or fewer impurities like water, carbon monoxide, hydrogen or hydrocarbons, i. e., VOCs, which can offset concentrations from their theoretical values in the final mixture.

A second source of uncertainties are MFCs with both a systematic and random error as per the respective data sheet. The MF1 (MKS Instruments, Inc., Andover, USA), for example, has an accuracy of ±(0.5 % of reading + 0.2 % fullscale) and a repeatability of 0.2 % fullscale [289]. In a simple gas line, the uncertainty of the final test gas concentration can directly be computed as

$$\mathrm{u}_{\text{gasline}}(c) = c_0 \cdot \frac{\mathrm{u}(q)}{q_t}, \tag{10.7}$$

with c_0 as the test gas concentration in the gas cylinder, $\mathrm{u}(q)$ the uncertainty of the MFC flow, and q_t the total flow over the sensor. Replacing the uncertainty with the actual flow computes the actual concentration instead.

For a predilution line, the final concentration c at the sensor is

$$c_{\text{predil}} = c_0 \cdot \frac{q_s}{q_s + q_c} \cdot \frac{q_o}{q_t}, \tag{10.8}$$

with q_s being the flow from the gas cylinder, q_c the flow of carrier gas, and q_o the flow injected into the main gas stream. The influence of the flow uncertainties of the three MFCs can then be computed using error propagation:

$$\mathrm{u}_{\text{predil}}(c) = \sqrt{\sum_{x=\{q_s,q_c,q_o\}} \left(\frac{\partial c}{\partial x} \cdot \mathrm{u}(x)\right)^2} \tag{10.9}$$

$$= \frac{c_0}{(q_s + q_c)^2} \cdot \frac{q_o}{q_t} \sqrt{(q_c \mathrm{u}(q_s))^2 + (q_c \mathrm{u}(q_c))^2 + \left(q_s \frac{q_s + q_c}{q_o} \mathrm{u}(q_o)\right)^2} \tag{10.10}$$

Equation 10.8 and Equation 10.10 are visualized in Figure 10.12 for a predilution line made out of three MF1 with $c_0 = 100\,\mathrm{ppm_v}$, $q_{s,max} = 10\,\mathrm{ml/min}$,

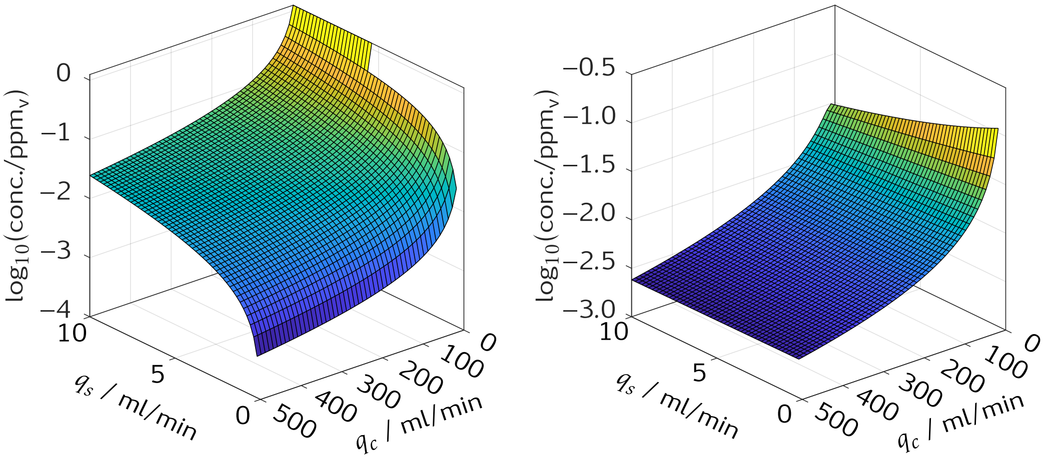

(a) (b)

Figure 10.12.: (a) Logarithmic concentration and (b) repeatability uncertainty of a predilution line at a fixed, intermediate outflow.

$q_{c,max} = 500\,\text{ml/min}$, $q_o = 5\,\text{ml/min}$, $q_t = 400\,\text{ml/min}$ and a safety margin of a 5 % larger outflow than inflow. The minimal and maximal concentrations and repeatability uncertainties achievable with this specific setup are listed in Table 10.1. Comparing the last two rows, which produce the same concentration with widely different uncertainties, shows the importance of finding the most suitable flow values.

All these uncertainties can be annotated and propagated based on the graph with the `uncertainties` package so that confidence intervals can be given for the final concentrations. Both types of uncertainties, random and

Table 10.1.: Minimum/maximum (bold) concentrations and repeatability uncertainty with associated MFC flows for a predilution line. The last row produces the same concentration as above, but with a much smaller uncertainty by choosing more suitable flows.

conc. / ppb_v	unc. / ppb_v	q_s / ml/min	q_c / ml/min	q_o / ml/min
0.02	**0.01**	0.2	500.0	0.2
2350.00	5.00	10.0	0.0	9.4
0.02	0.10	0.2	500.0	0.2
47.06	**230.73**	0.2	10.0	9.6
47.06	4.44	10.0	160.0	3.2

systematic, are computed. Only random uncertainties are to be considered within the same experimental unit, but random and systematic uncertainties are necessary to evaluate the results from two different setups.

For different setups, also the uncertainty of the gas supply concentration $\mathrm{u}(c_0)$ should be taken into account. In this case, Equation 10.7 becomes:

$$\mathrm{u}_{\text{gasline}}(c) = \frac{1}{q_t} \cdot \sqrt{(c_0 \cdot \mathrm{u}(q))^2 + (q \cdot \mathrm{u}(c_0))^2}, \tag{10.11}$$

and another summand is added to Equation 10.10:

$$\mathrm{u}_{\text{predil}}(c) = \frac{c_0}{(q_s + q_c)^2} \cdot \frac{q_o}{q_t} \sqrt{\cdots + \left(q_s \frac{q_s + q_c}{c_0} \cdot \mathrm{u}(c_0)\right)^2} \tag{10.12}$$

Uncertainties of the calibration equipment have long been, and still are, neglected in many works about chemical sensors. This is understandable as their manual computation is time-consuming and automated computation requires a suitable model of the calibration equipment. Moreover, the meta-data needed, like MFC flows, is often not available or difficult to work with. All these issues have been addressed in this PhD project through the joint development of a new software.

Often, the calibration equipment's uncertainties are simply assumed negligible compared to the sensor's quantification ability. This assumption has been proven wrong, as, with predilution lines, poorly chosen parameters can produce an uncertainty of five times the desired concentration. The following chapters, and section 13.2 in particular, further show that modern gas sensors with optimized temperature cycling are well capable to detect and quantify concentrations around the limit of uncertainty of the used calibration equipment.

11. Interlaboratory study

An interlaboratory study has been conducted between LMT and BAM as part of this PhD project to assess the performance of several experimental gas sensor systems. Target gases were the VOCs benzene, naphthalene, and formaldehyde in a varying background of interferents, including harmless VOCs. The results have been published in [270] and are reevaluated in this chapter.

11.1. Experimental setup

Six different types of experimental sensor systems (Table 11.1) were tested in parallel. To avoid interference between systems, e. g., through reaction products influencing systems downstream, they were mounted in parallel fluidic branches. To prevent widely different flows through each branch due to varying sensor chamber geometry and, thus, flow resistance, each branch was fitted with a restriction of 10 cm long pipe with 1/16 inches inner diameter. Note that in this evaluation, only the best performing system (branch 2) will be considered. One other, conceptually similar system (branch 1) performed only slightly worse, one system suffered a technical fault (branch 6), and the remaining three systems (branches 3, 4, 5) had very poor results with the applied, challenging calibration profile.

The initial measurements were done at BAM with the gas mixing system described in section 10.1.2. Formaldehyde was added to the mixture via a common gas line from the same bottle that was used for the later measurements. The systems were exposed to five different gas profiles (Figure 11.1), over 24 h, with the concentrations determined according to ISO 16000-3:2011 [290] (formaldehyde) and ISO 16000-6:2011 [116] (rest) before each measurement. VOC mix C adds a relatively constant background of toluene (1.7 $\mathrm{ppb_v}$), hexanal (15 $\mathrm{ppb_v}$), n-decane (4.5 $\mathrm{ppb_v}$), limonene (0.6 $\mathrm{ppb_v}$), α-pinene (10 $\mathrm{ppb_v}$), and n-dodecane (7 $\mathrm{ppb_v}$). The total flow was 240 ml/min, the carrier gas was humid air (50 %RH) cleaned with an activated carbon filter.

After the sensor systems had been used in several other measurements, a calibration measurement was done at LMT around one month after the mea-

Table 11.1.: Overview of the gas sensor systems used in the interlab study.

branch	type	gas transport	electronics
1	MOS (AS-MLV)* (TCO/DSR)	diffusion in chamber	log. amp.
2	MOS (AS-MLV)* (TCO/DSR)	flow normal to sensor surface	log. amp.
3	SiC-FET (Ir/WO_3) (TCO)**	diffusion in chamber	GasFET board
3	SiC-FET (Ir/WO_3) (TCO+GBCO)**	diffusion in chamber	GasFET board
4	MOS (WO_3+preconc.)*** (triangular TCO)	diffusion in long tube	log. amp.
5	MOS (WO_3+preconc.)*** (triangular TCO)	diffusion in long tube	log. amp.
6	MOS (WO_3+preconc.)*** (triangular TCO)	diffusion in chamber	log. amp.

* Description follows on page 159.

** Temperature plateaus at 210, 240, 270, 300, and 330 °C, gate plateaus at −2 and +2 V, further discussed in section 6.2.4.

*** Sensor, preconcentrator, and TCO further described in [44], [226].

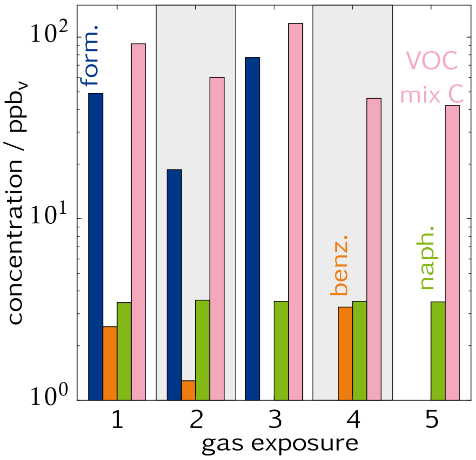

Figure 11.1.: Calibration profile at BAM.

surement at BAM. The LMT gas mixing system has the benefit of working automatically and quicker due to its lower volumes, but the gas composition cannot be determined analytically due to lack of suitable equipment. The systems were exposed to around 175 unique gas exposures, the theoretical values of which are shown in Figure 11.2. VOC mix A (acetaldehyde, acetone, n-decane, hexanal, toluene)[1] and VOC mix B (limonene, α-pinene)[2] were provided by one permeation line each where the oven was filled with one permeation tube per substance. Note that n-dodecane is not present in these mixtures as compared to the BAM measurement and the ratios between VOCs are different as well, essentially simulating a relocation of the sensor system. Naphthalene was provided by a third permeation line, benzene and formaldehyde were supplied from commercial gas cylinders with concentrations of 100 ppm or higher and injected in the main gas flow through predilution lines. The total flow was 400 ml/min. The carrier gas was humid air (30 %RH and 50 %RH) from a ultra-zero air generator (cf. section 10.1.1). Constant amounts of H_2 (500 ppb$_v$), CO (150 ppb$_v$) and CH_4 (1840 ppb$_v$) were added for a more realistic baseline. An exhaustive table of all test gas exposures can be found in [270].

The most promising sensor system was based on a commercial MOS sensor, the AS-MLV (ams Sensor Solutions Germany GmbH), with an optimized temperature cycle. The basic principle of this cycle is the measurement of

---

[1] With a component ratio of, roughly: 1:3.2:0.4:1:1.2, with acetaldehyde as the reference varying between 1.5 and 15.8 ppb$_v$.

[2] With a component ratio of, roughly: 1:0.65, with limonene as the reference varying between 0.4 and 1.7 ppb$_v$.

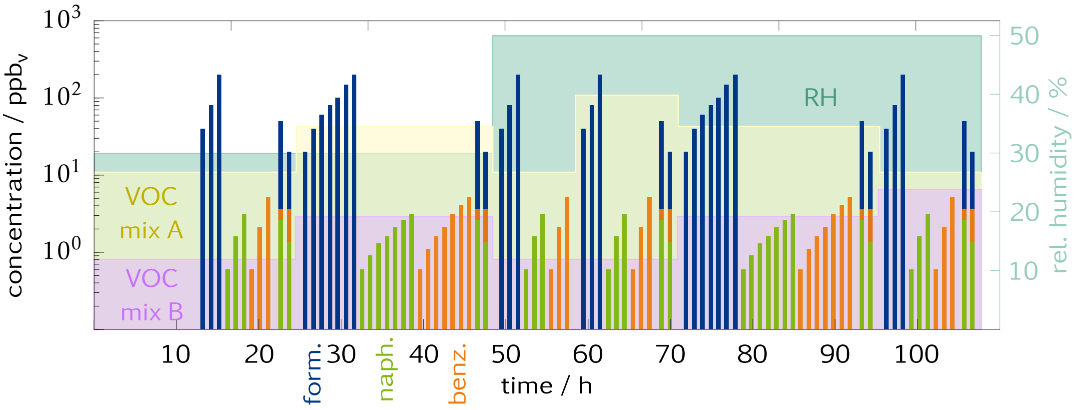

Figure 11.2.: Calibration profile at LMT.

differential surface reduction (DSR) [164], [291]. It employs a high temperature plateau to enrich the surface with adsorbed oxygen and then reaches a very sensitive state through a quick temperature reduction. The rate at which the surface is reduced is specific to gas type and concentration and can be measured as the slope of the logarithmic signal at the low temperature plateau. The low temperature plateaus were 150, 200, 250, and 300 °C, each preceded by a plateau at 450 °C. The logarithm of the resulting sensor signal is shown in Figure 11.3. The slope was computed for all cycles in the selected ranges. The ranges are shorter at the beginning of the plateau to account for the larger changes. This notion is confirmed by the large spread of the feature values at the beginning of the plateau. In total, 26 slopes, i. e., features, were extracted from each cycle. The evaluation starting at the raw data and finishing with tested models was done entirely in DAV^{3}E (cf. chapter 3).

11.2. Formaldehyde quantification

Formaldehyde was the only target gas which the system was able to quantify. Its exposure limit is 80 ppb$_v$ as compared to benzene (1 ppb$_v$) and naphthalene (2 ppb$_v$), so that the concentrations offered were around two orders of magnitude higher.

Figure 11.4a shows a PLSR model with 4 LVs. It was trained on 1942 cycles from the LMT dataset, most of which (1623) represent only background variations, i. e., 0 ppb$_v$ formaldehyde. The number of cycles for non-zero formaldehyde concentrations is between 23 and 65, depending on the concentration. Removing or reducing the zero-group impaired the model performance, most likely due to the lost information on background

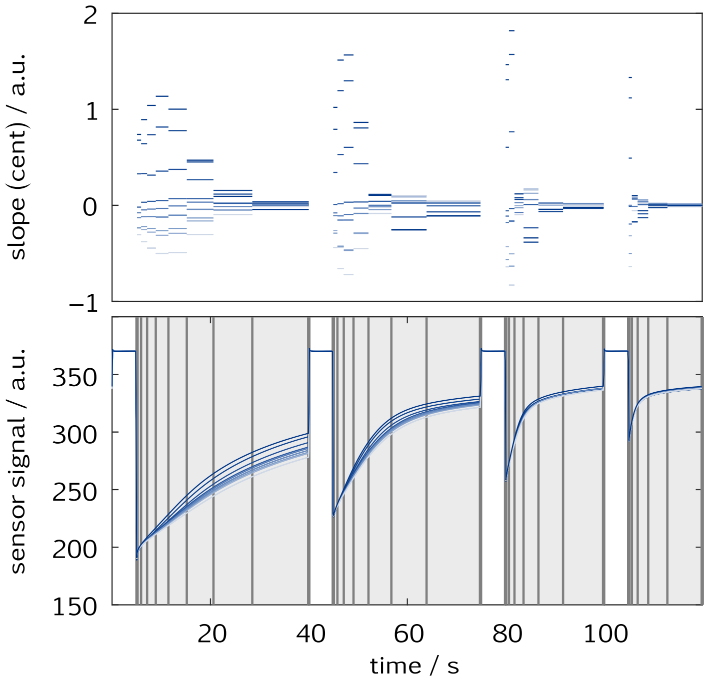

Figure 11.3.: Logarithmic sensor signal in different formaldehyde concentrations (blue shades), the extracted slope features (gray ranges), and, in the top plot, the centered slope values for each formaldehyde concentration.

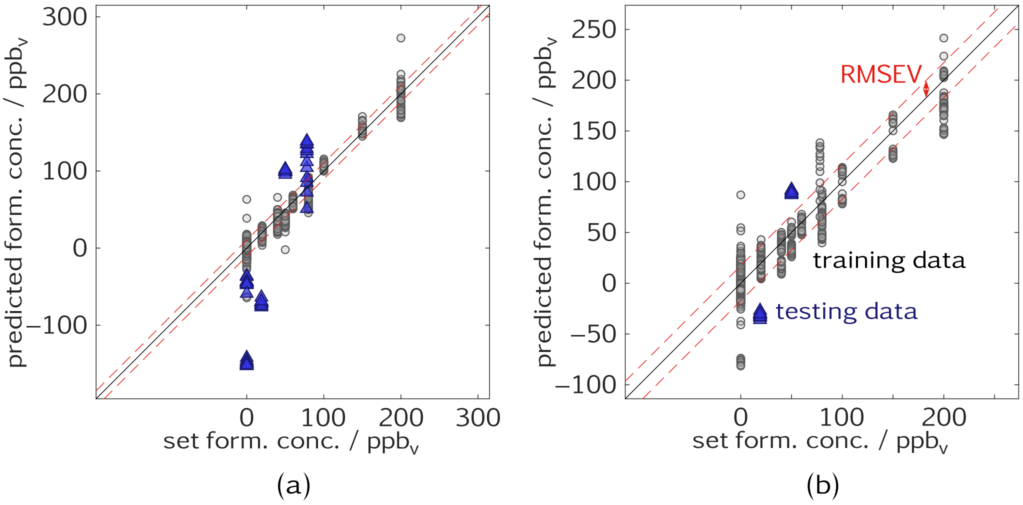

(a)

(b)

Figure 11.4.: PLSR model for formaldehyde trained with LMT data, predicting BAM data (a) before and (b) after updating with three exposures from BAM data.

variations. Validation was done with the exposure-based 10-fold algorithm, and testing with the BAM dataset resulted in an RMSEP of 90 ppb$_v$.

Updating this model with three exposures, 130 cycles, representing the extreme values from the BAM measurement, i. e., 0 and 80 ppb$_v$, reduces the RMSEP by almost half to 48 ppb$_v$ with 3 LVs (Figure 11.4b). Simply leaving out the three exposures from the test dataset only improves the RMSEP to 80 ppb$_v$. This shows that already a relatively small amount of additional information, in this case 2 % (3 exposures added to 175 exposures), can considerably increase the model performance in a slightly different new environment. Hence, a model based on an exhaustive lab calibration could quickly be updated in a new environment, e. g., when the system is deployed in the field.

In [270], a quite large validation error of 39 ppb$_v$ is reported for a model trained on the BAM dataset. This error was mainly caused by the bias of the two exposures at 0 ppb$_v$ formaldehyde. Only 1 LV had been chosen for this model due to the large error of the validation, suggesting that the addition of further LVs could not improve the model's true performance. The validation was, however, done with the exposure-based leave-one-out algorithm so that one out of five folds had to extrapolate the highest concentration. Excluding the highest concentration from the validation and using it as anchor point in the training (which was not possible in the older version of DAV^{3}E) instead yields a model with 3 LVs and a validation error of only 18.6 ppb$_v$ for the

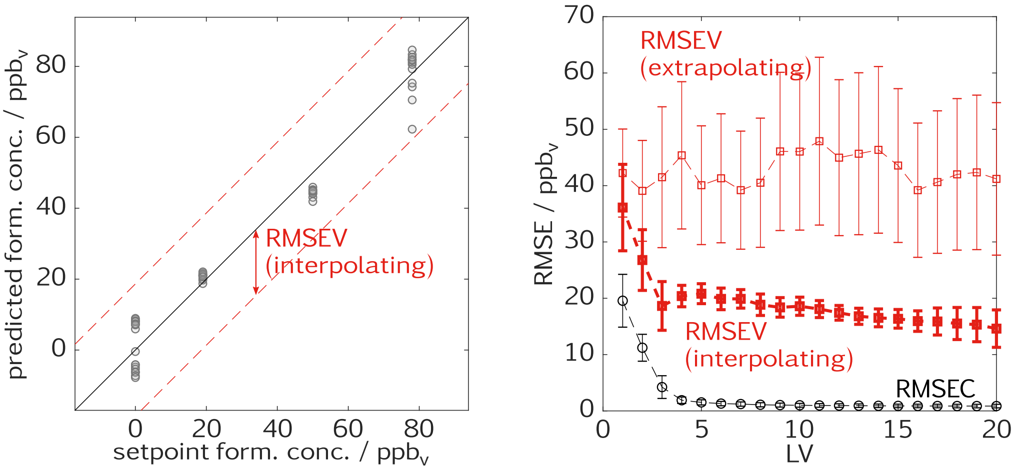

(a)

(b)

Figure 11.5.: (a) PLSR model for formaldehyde trained with BAM data. (b) Extrapolation, i. e., predicting the highest concentration, in a validation fold, leads to over-pessimistic results compared to validation with only interpolating folds.

same dataset (Figure 11.5). The validation error has a clear minimum at 3 LVs and follows the lower boundary of the confidence interval computed for the extrapolating error. No dedicated testing is done for this model because that would leave only three exposures in each training fold and impact the result heavily.

The variance of the highest formaldehyde concentration in the BAM dataset is significantly larger than that of the other groups. It does not arise from random noise, but from a signal change over time. This observation shows the benefit of including many cycles from the same exposure into the model instead of just taking one or the average of all cycles. This exposure was the third of five with all others showing less variance, so that an undetected, temporary issue of the BAM gas mixing system is a likely cause. One explanation could be a varying hydrogen or carbon monoxide concentration which is not removed from the carrier gas by the activated carbon filter. Especially hydrogen is irrelevant for the usual purpose of the system because it cannot be detected by most analytic instruments and is not hazardous to human health. Most gas sensors, however, react strongly to hydrogen (and carbon monoxide). More evidence for this assumption is found with TVOC quantification.

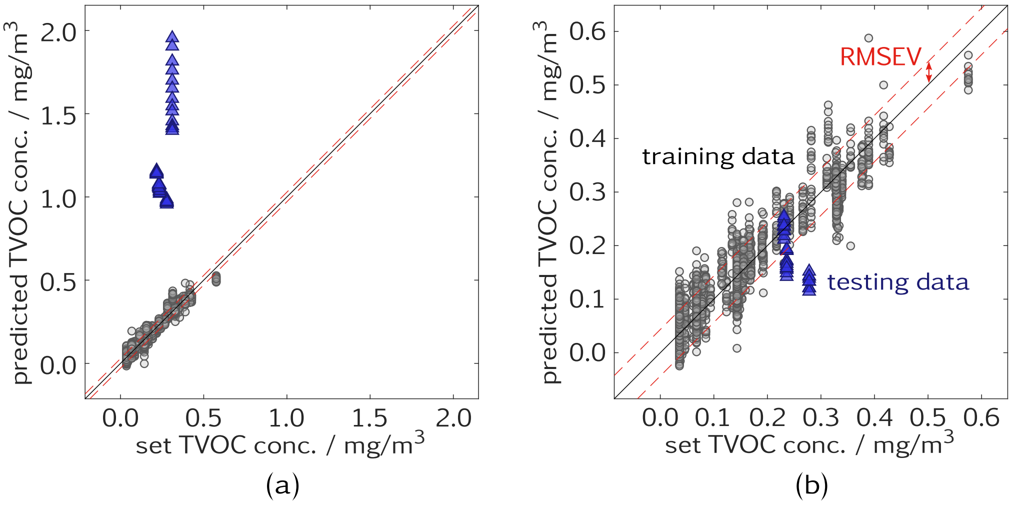

Figure 11.6.: PLSR model for TVOC trained with LMT data (a) before and (b) after updating with two exposures from BAM data.

11.3. TVOC quantification

Despite the issues related to TVOC (cf. section 1.3.3), it is the most common indicator for air quality in current systems and studies. Thus, being able to predict a reliable TVOC value in addition to selective quantification of hazardous VOCs can raise the overall confidence in a gas sensor system.

Similar to the model for formaldehyde, a PLSR is trained on all data from the LMT dataset. Most concentration levels are represented by 10 or 20 cycles, with two containing 160, one 260, and one 580 cycles. The RMSEP of the predicted BAM dataset is 950 $\mu g/m^3$ at 9 LVs while the maximum actual value is around 500 $\mu g/m^3$ (Figure 11.6a). Updating the model with the cycles from the lowest and the highest TVOC concentration in the BAM dataset reduces the RMSEP by one order of magnitude to 92 $\mu g/m^3$ (Figure 11.6b). In particular, the bias is almost completely removed.

The model for TVOC quantification must react to a wide range of different gases whereas the model for formaldehyde must mainly suppress those gases. Thus, it is reasonable to assume that the TVOC model is more sensitive to changes in the atmosphere, explaining the large error in Figure 11.6a. N-dodecane is present at a relatively constant concentration of 7 ppb_v in the BAM dataset and missing from the LMT dataset, providing a possible cause. However, benzene and naphthalene, provided at maximum concentrations of 3 and 5 ppb_v, respectively, could not be detected or quantified with this system, casting doubt on such a high influence of n-dodecane. As suggested

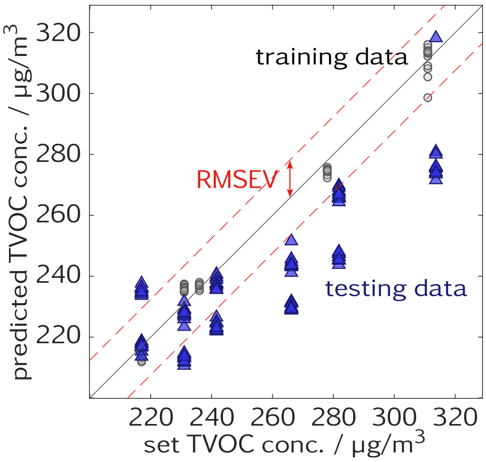

Figure 11.7.: PLSR model for TVOC trained with BAM data, predicting LMT data.

earlier, uncontrolled hydrogen or carbon monoxide, with a baseline value of 500 $\mathrm{ppb_v}$ and 150 $\mathrm{ppm_v}$, respectively, in environmental air, in the BAM system is another and, arguably, more likely explanation.

Turning the model training around can give an indication to which component has the larger influence. If it is n-dodecane, a strong bias towards the other direction should be present when predicting data from the LMT dataset with a model trained on the BAM dataset. If, however, hydrogen or carbon monoxide is the cause, which was present in both datasets but, presumably, only varied in one, the BAM model has possibly learned to ignore the variations of these gases. Indeed, predicting LMT data with a model trained on BAM data results in a very small prediction error of 32 $\mu g/m^3$ with 3 LVs (Figure 11.7). An even smaller error was reported in [270] with 13 LVs, but, as before, the use of anchor points in the training produced a more reliable but still well-performing model.

12. Field tests

12.1. GasFET field test system

For the field tests with GasFET sensors during the SENSIndoor project[1], a basic field test system was built by Peter Möller[2]. It was based on the LabVIEW sensor control software (cf. section 5.3), the GasFET Board 2.0 by 3S GmbH (section 5.2), and an *Intel Compute-Stick* running Windows 10 for control and read-out. Reference data (T, RH, CO_2) was recorded through the commercial sensor system *tSENSE Display* (Senseair, Delsbo, Sweden) [292], and remote communication was possible using either the Compute-Stick's built-in WiFi module or an external 4G modem. This system was used to collect the data in section 12.2. However, several shortcomings were discovered over time, many related to the use through non-trained users at remote locations. Consequently, an improved prototype (*new system* or *V2.0*, Figure 12.1b) was built during this PhD project which will be described and compared to the older version (*old system* or *V1.0*, Figure 12.1a) in the following paragraphs. A side-by-side comparison can be found in Table 12.1.

One of the main issues of V1.0 was the missing feedback to the user. It did not actively communicate problems or errors; instead, a screen and input devices had to be connected to the Compute-Stick to check the correct functioning of the software. This required not only intricate knowledge of the (lab-grade) software, but also seriously impacted the system's mobility, in particular due to the need for an external screen. V2.0 has replaced both screen and input devices with one built-in touchscreen (7 inches) which enables basic configuration and feedback in a web-based interface. To further increase mobility, the new system's dimensions have been shrunk considerably from 60 cm × 30 cm × 15 cm (not considering screen, mouse, and keyboard) to 24 cm × 16 cm × 12 cm.

The V1.0 system had the GasFET mounted on the outside of its box and shielded from direct light by a glued-on, black plastic cap. Test measure-

---

[1] Research project within the European FP7 program, grant agreement no. 604311, *Nanotechnology-based intelligent multi-SENsor System with selective pre-concentration for Indoor air quality control*, www.sensindoor.eu.

[2] Formerly research engineer at LiU.

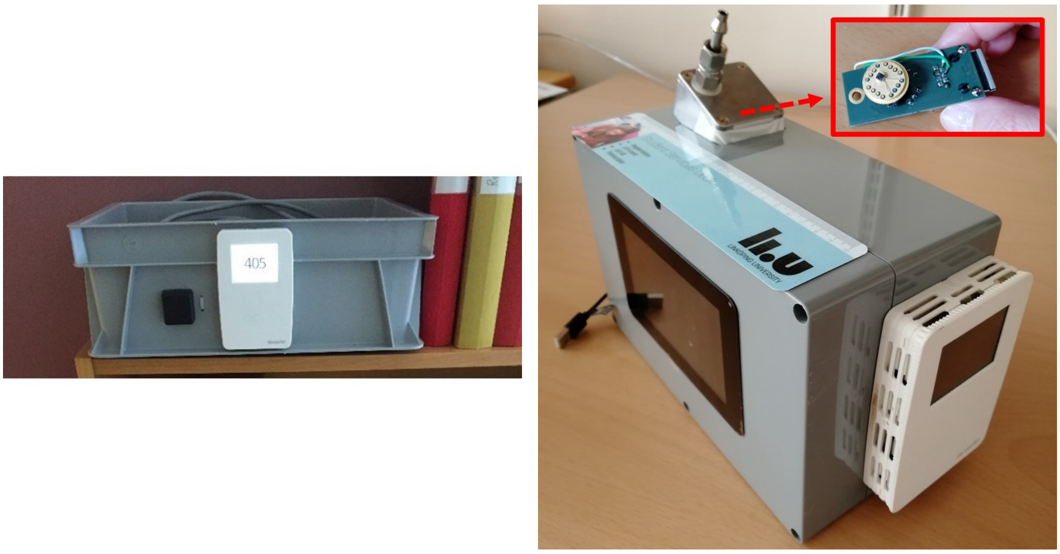

(a) Old system (V1.0). (b) New system (V2.0).

Figure 12.1.: Old and new field-test system prototype.

ments showed no influence of external light and no evidence of influence from vapors coming from the plastics was found. However, especially the latter cannot be excluded, so that a signal dependence on room temperature mediated by vapors could arise. Further issues were the missing electrical shielding of the sensor as well as the complicated sensor replacement. The new system uses a sealed measurement chamber made from cast aluminum (Figure 12.2). The gas inlet is a 2 cm long metal tube of 1/8 inches outer diameter with a Swagelok fitting on the outside. It reaches almost to the bottom of the measurement chamber, effectively preventing any light from hitting the sensor surface. The dimensions of the pipe severely limit gas diffusion so that a small fan is used to obtain a slightly lower pressure in the chamber, creating an in-flow of outside air. The external Swagelok fitting also makes gas calibration possible without removing the sensor from the system. Additionally, a new adapter PCB for the GasFET was developed (cf. appendix, section 2). It replaces the direct soldering of wires used in the old design with a RJ45 connector, adds a screw hole for mounting and grounding as well as two jumpers (see next paragraph). This PCB improves the user-friendliness considerably because, unlike the old one which was soldered directly to the wires leading to the GasFET board, it can be exchanged as a whole instead of handling the sensitive, 16-pinned sensor. The attachment mechanism in the measurement chamber is designed such that the chamber is grounded when the PCB is fixed in the chamber. This, together with the

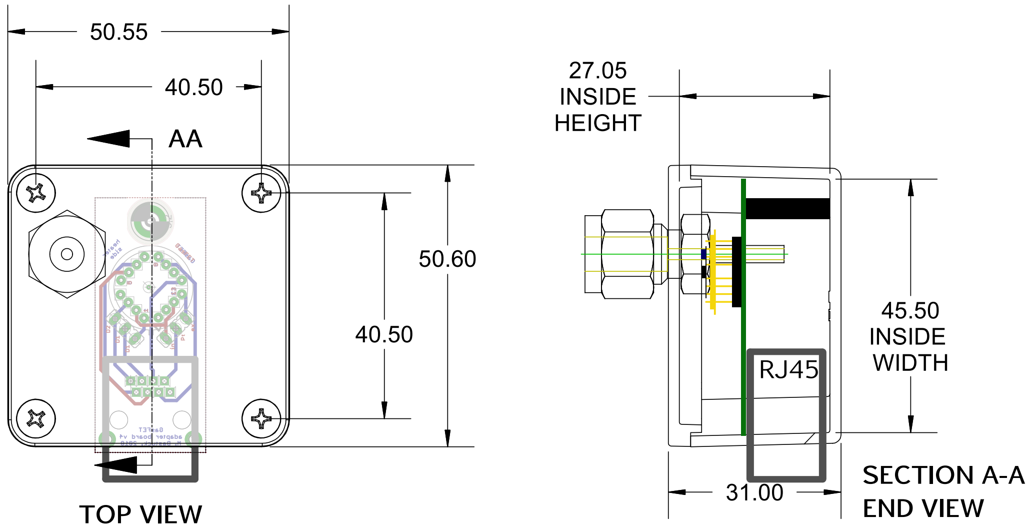

Figure 12.2.: Measurement chamber (chamber design adapted from [293], all measurements in mm).

use of a CAT6-Ethernet cable has effectively removed noise which had been observed in certain environments with the old system.

With an easily exchangeable sensor the need for automatic adaption to new sensors arose. One sensor chip can have up to four transistor structures which, in a lab environment, are selected with a DIP switch on the GasFET board. The same goes for external or internal temperature sensors. The GasFET board is more difficult to reach in V2.0 compared to V1.0, and changing these parameters requires knowledge an untrained user does not have. Instead, with the new PCB, sensors can be tested in the lab, mounted onto the PCB, and the jumpers set to select one out of two transistor structures and whether to use the internal or external temperature sensor. This effectively prevents user configuration errors upon sensor change. Each PCB carries a unique ID which can be entered on the touchscreen for documentation purposes. Different sensors also generally have slightly different heater control parameters which had to be determined manually in the software in V1.0. In V2.0, this process has been automated. First, the heater power is set to zero and the measured temperature is stored as the offset. In a second step, the power is slowly increased until the highest temperature in the cycle is measured. When the temperature has been stable for 10 s, this point completes the two-point calibration of the heater power.

The old system was lacking a mechanism for an orderly shutdown when no input devices were connected. This in combination with the tendency of HDF5 files to become corrupted when a power loss occurs during writing led to data loss on several occasions. The new system provides a button on the touchscreen for shutdown, uses a write buffer so that writing operations only happen once every five minutes, and splits the measurements into separate files of one hour length each. This has in many cases prevented data loss or limited it to less than 60 min.

The new system is based, as far as possible, on free hard- and software to reduce cost. The Intel Compute-Stick (120 € in the cheapest configuration) has been replaced with the *BeagleBone Black* (BBB) (60 €), a single-board computer similar to the Raspberry Pi. Windows 10 (120 € in the cheapest configuration, 10 € as OEM version with the Intel Compute-Stick) has been replaced by the free Debian 9, and the programming language was changed from the commercial LabVIEW (400 €/year in the cheapest configuration) to the freely available Python. The NI-DAQ (110 € in the cheapest configuration) is replaced by the internal *analog-digital converters* (ADCs) of the BBB and a custom-made PCB with voltage dividers to adjust the signal range. All in all, the cost for the new system is dominated by the 60 € for the BBB and around 20 € for the other components (housing, measurement chamber, etc.). This sums up to at least 160 € less per system, plus 400 €/year running costs for a LabVIEW license.

Several aspects of V2.0 can be improved upon in the future. Currently, the volume of the measurement chamber is unnecessarily large and the fan should be replaced by a small pump with more power. While the sensor mounting mechanism is a significant improvement compared to V1.0, a redesign of the chip header, e. g., based on an alumina substrate and spring-loaded contact pins in the chamber lid, could enable easier and more reliable mounting. The GasFET board was developed for lab use and exploratory measurements with permanent connection to a PC. A new revision with a full stand-alone microcontroller could be designed to fit better in the concept of a field-test system. Neither system is hermetically sealed which makes them unfit for outdoor use. However, using, e. g., a heat exchanger instead of ventilation slits in the new system would seal the electronics completely from the environment.

Table 12.1.: Side-by-side comparison of the two field test system prototypes.

property	V1.0	V2.0
dimensions	60 cm × 30 cm × 15 cm	24 cm × 16 cm × 12 cm
controller	Intel Compute-Stick	BeagleBone Black
operating system	Microsoft Windows 10	GNU/Linux Debian 9
programming language	LabVIEW 2014	Python 3.6
sensor hardware	GasFET Board 2.0 (3S GmbH)	GasFET Board 3.0 (3S GmbH)
sensor connection interface	16-pin TO-8 header	RJ45 connector
sensor hardware configuration	change on GasFET Board manually	encoded on sensor PCB
measurement chamber	black plastic shielding	cast aluminum with 1/8 inches inlet
gas sampling	passive, diffusion-based	active, flow-based
temperature control	open-loop with manual parameter settings	open-loop with auto-calibration on startup
autostart	yes; ca. 1 min boot time	yes; ca. 1 min boot time plus 10 min time for user interactions
calibration	dismount sensor and test in usual GMA measurement chamber	connect GMA outlet to Swagelok inlet on field-test measurement chamber
user interface	none; optional Windows interface with additional screen/mouse/keyboard	touchscreen for most important options and feedback
reference instrument	SenseAir T/RH/CO_2; read-out with NI-DAQ	SenseAir T/RH/CO_2; read-out with BBB's ADCs
resilience against power loss	complete data loss likely	data loss limited to < 60 min
data collection	locally on SD card, remotely via RemoteDesktop (WiFi or mobile internet)	locally on SD card, downloadable via USB, remotely via Dropbox or similar (WiFi)

12.2. Field test

A field test was conducted over several weeks from June to September 2016 at the Montessori school Trilobiten in Linköping (published in [294]). The field test system V1.0 was installed in a classroom with automated ventilation at a height of 1.2 m. Formaldehyde, being the most common indoor pollutant [100], [102], was chosen as target gas and recorded with the Graywolf FM-801 [295] as reference instrument. This colorimetric system shows very little cross-sensitivity to other gases and records one value every 30 min. Its detection limit is given as "$< 20\,\mathrm{ppb_v}$" with an accuracy of $\pm 4\,\mathrm{ppb_v}$ below $40\,\mathrm{ppb_v}$. Experimentally, values could be obtained as low as $10\,\mathrm{ppb_v}$. The very low formaldehyde concentrations found in the classroom during the field test likely have an impact on the quality of the final model.

The SiC-FET sensor had a porous iridium gate on top of a PLD-WO_3 layer as described in section 6.2. The sensor was operated in a temperature-cycled mode, the temperature cycle consisting of four plateaus (330, 300, 270, and 240 °C) with a duration of 80 s each. The mean value of the stable signal on each plateau was extracted, resulting in four features. Nine days of continuous measurement with all data stream available, except for one short break, could be evaluated. The data is shown in Figure 12.3. For this graph and the following evaluation, the data streams from all systems have been resampled to a sampling period of 80 s, i. e., the sensor's cycle length. Linear interpolation was used for both up- (FM-801) and downsampling (other systems). The correlation between the data streams is shown in Table 12.2 for nine days in August where data from all instruments was available (except for a short period in the evening of August 24).

The temperature clearly follows a day/night cycle. RH and CO_2 are occupancy indicators, increasing when humans are present. CO_2 can even resolve distinct events, most likely individual lessons in the classroom. A meeting in the classroom was confirmed from 6 pm to 11 pm on August 23, explaining the increased CO_2 concentration during this time. No spikes during weekends (August 20/21 and August 28/29) show that the room was empty. However, a sharp, sudden decrease of all measured variables just before August 28 suggests the ventilation being switched on or a window being opened for a brief period of time. The ventilation schedule displayed in the graph is the scheduled one. Manual overrides are not fed back to the system. Nevertheless, a quick build up of formaldehyde can be noticed as soon as the ventilation is switched off at 6 pm on normal weekdays as well as over the weekends. It stabilizes somewhere in the range of $20\,\mathrm{ppb_v}$ to $30\,\mathrm{ppb_v}$ after several hours. Three hours of ventilation at 50 % reduce the concentration to between 10 and $15\,\mathrm{ppb_v}$, followed by an instantaneous drop

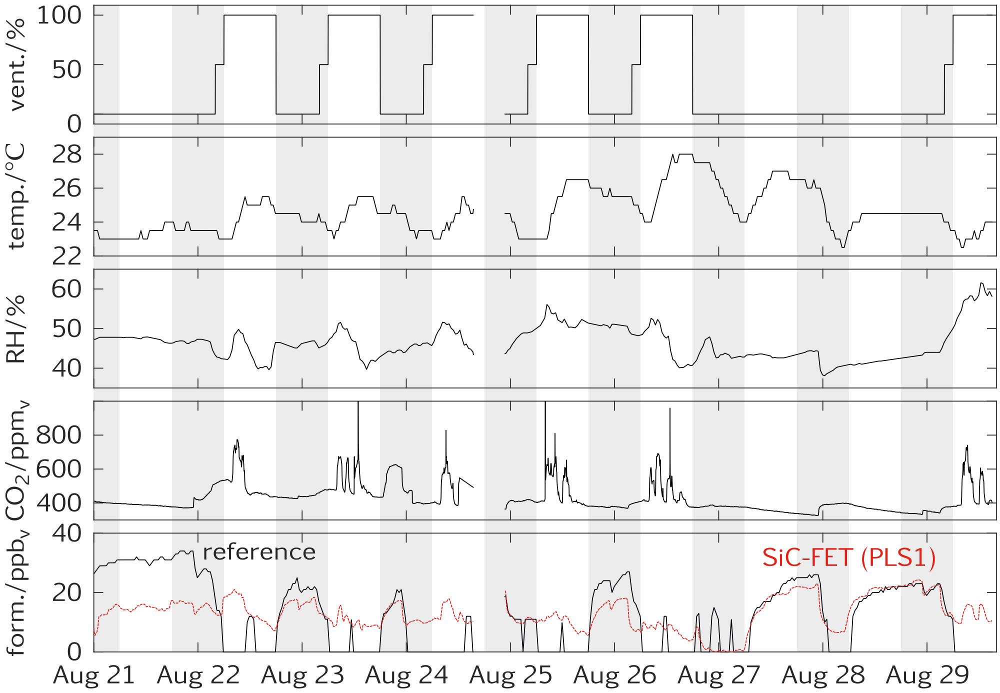

Figure 12.3.: Field test data over nine days. Night (6 pm to 6 am) is marked as dark areas. The bottom plot shows the output of a PLSR model with 1 LV (red) based on the SiC-FET data in addition to the reference instrument data.

Table 12.2.: Correlation coefficients (in percent) between data streams. Txxx refers to the four features, PC1 is the first PCA component and PLS1 is the prediction of a PLSR model with 1 LV.

	form.	T	RH	CO$_2$	T330	T300	T270	T240	PC1	PLS1
ref.	100	−14	−12	−44	46	49	46	40	47	48
T	−14	100	−26	−15	−22	−32	−8	2	−11	−13
RH	−12	−26	100	32	−6	−6	−3	−3	−4	−4
CO$_2$	−44	−15	32	100	4	13	−10	−18	−8	−6
T330	46	−22	−6	4	100	94	91	78	93	95
T300	49	−32	−6	13	94	100	79	62	83	86
T270	46	−8	−3	−10	91	79	100	95	99	99
T240	40	2	−3	−18	78	62	95	100	95	93
PC1	47	−11	−4	−8	93	83	99	95	100	100
PLS1	48	−13	−4	−6	95	86	99	93	100	100

below the detection limit of the reference instrument at 100 % ventilation.

Generally, formaldehyde concentration is positively correlated to both temperature and RH [296], [297]. The reason for the observed negative values (Table 12.2) is the influence of the ventilation pattern on all variables. The ventilation decreases the formaldehyde concentration effectively to zero during the day, i. e., at the same time when higher outside temperatures and RH are present. The same effect explains the strong negative correlation between formaldehyde and carbon dioxide of −44 %: both gases appear anti-cyclically due to the time patterns of ventilation and room occupancy. Hence, any sensor with perfect formaldehyde selectivity (assuming the reference instrument as perfect) should produce the same correlation pattern. Any deviation can be interpreted as cross-sensitivity.

Table 12.2 compares the four single features with each other as well as the first PC and the prediction of a 1-LV PLSR model based on the extracted features and trained with the reference instrument data as target. All of these except for the signal at 240 °C (T240) result in a correlation with formaldehyde between 46 % to 49 %. These close values suggest that the TCO has only a small effect and any selectivity must come mainly from the sensor itself. The single feature T300 has the best correlation for formaldehyde with 49 %, but deviates from the “perfect correlation pattern” particularly regarding ambient temperature T and CO_2. PCA and PLSR can reduce the cross-sensitivity to ambient temperature, but maintain a large influence of, seemingly, CO_2.

Such relatively small concentrations of CO_2, a relatively inert molecule, can usually not be detected with chemical sensors. The sensor reacts more likely to other substances which are linked to CO_2 as indicator for human presence. Acetone and isoprene are components of human breath at concentrations of around 4 and 2 % of the CO_2 content [298], [299]. With a CO_2 baseline of 400 $\mathrm{ppm_v}$ and an average peak concentration around 700 $\mathrm{ppm_v}$, human presence should increase acetone and isoprene levels by 12 and 6 $\mathrm{ppm_v}$, respectively. Human presence is further associated with a variable increase in hydrogen concentration, usually in the low $\mathrm{ppm_v}$ range depending on occupant density. Due to instability of the sensor, it could not undergo further tests to determine the sensitivity to these gases; however, they are likely to elicit a sensor response at such relatively high concentrations.

The sensor’s response amplitude associated with CO_2 peaks varies, but is never larger than the response to formaldehyde despite the assumed total gas concentrations being three orders of magnitude larger (20 $\mathrm{ppm_v}$ breath components and 20 $\mathrm{ppb_v}$ formaldehyde). Theoretically, this could suggest a selectivity of $> 1000 : 1$ to formaldehyde in comparison with interfering gases. It is, however, very likely that other gases present in a fixed ratio to formaldehyde influence the sensor as well. This would explain the similar shapes of reference instrument and model prediction, especially at high formaldehyde concentrations with, however, a varying bias of up to 15 ppb_v (Figure 12.3). If the ratios of these gases can always be expected to be similar, the sensor signal would be sufficient for a simple ventilation control after a calibration with a reference instrument. Another issue is the relatively high baseline of the model prediction compared to the reference instrument. But since 10 ppb_v are the absolute detection limit of the reference instrument, and taking into account the accuracy of 4 ppb_v, determination of the true baseline is not possible with this setup in this environment.

When this field test is repeated, the sensor response to common interfering gases should be determined beforehand. Ideally, reference instruments for these gases should be present at the site or, at least, air samples should be taken and analyzed, e. g., one during night and one during day, to get an idea of the air composition. Carbon dioxide is a valuable indicator for human presence and helps to check for cross-sensitivity to gases linked to human presence even without other references. Common influences, like ventilation, must be kept in mind during evaluation to understand and correctly interpret the correlation patterns.

13. Random mixtures calibration

13.1. Calibration profile

Despite calibration being a crucial part of gas sensor research, very few publications can be found concerning the design of calibration methods and profiles (not systems) in particular [164], [300]–[303]. The majority of publications uses a classical calibration profile where the sensor is exposed to increasing (or decreasing) concentrations of one test gas in carrier gas. Repetitions or random shuffling of exposures are sometimes used to prevent confounding of effects, e. g., sensor response, memory effects, and long-term baseline drift [265], [301], [303], [304].

Calibration profiles with one and only one test gas per exposure (but changing between exposures) are usually easy to interpret and can give a first idea of the sensitivity, speed, and even selectivity of a sensor[1]. However, there are very few, if any, applications where only one specific gas is present in a constant background. Instead, a mixture of many gases with constantly varying concentrations makes the task of selective detection or quantification considerably harder due to masking and other interactions. This issue is the reason for the very existence of sensor arrays and virtual multisensors. Simulating this during sensor calibration requires better performing sensor systems, especially in terms of selectivity, a more sophisticated experimental design as well as data evaluation compared to the simple one-gas (*sequential*) approach. It should, however, result in significantly better models and a more realistic estimate of the sensor system's performance in the field.

Thousands of publications and several extensive datasets [305]–[308] are available for the sequential approach. This number becomes much smaller for gas mixtures. In [309], two mixtures of two gases each (ethylene, methane, CO) with random concentrations are considered, and in [301], sixteen combinations of three VOCs at three fixed concentration levels are generated in several runs. Fixed concentration levels are also used in [310] to generate up to 24 different gas mixtures comprising up to five different gases.

---

[1] Determination of stability requires long calibration profiles which stands in contrast with the usually desired short profiles for time efficiency.

Fixed concentration levels have the benefit of simpler evaluation and interpretation, but squeeze the actually continuous concentration into only a few concentration levels. This quantization enables the use of factorial design [265] or similar methods to plan the calibration run, but can also – especially with highly non-linear sensor responses – conceal information if the number of levels is too small. Moreover, there is evidence that grid search or other "ordered" methods are less effective than random sampling especially in higher-dimensional spaces [176]. Therefore, the design method of *random effects* [265] uses random variations of variables drawn from defined distributions.

Figure 13.1 shows a proposed design scheme for gas sensor calibration related to IAQ applications based on random effects. It is based on "nested ratios" of binary gas mixtures within predefined concentration ranges. First, the amount of TVOC in a background gas, usually in $\mu g/m^3$, is drawn from a uniform distribution. This TVOC mixture is divided into target and interfering VOCs, which both can be divided again into a ratio of specific substances. The last step can be repeated for more granular control or more gases of interest. The background contains varying concentrations of CO, H_2, and humidity, three permanent gases in the atmosphere relevant for chemical gas sensors. The resulting gas profile has seven *degrees of freedom*, indicated by arrows in Figure 13.1 which are chosen randomly for each exposure to achieve a large variety of gas compositions. Each of the VOCs is removed from the mixture with a certain, low probability to generate zero-samples for it.

All ratios are drawn from uniform distributions between 0 and 1. A possible issue is that the specific VOC distributions are, therefore, generated from the multiplication of two uniform distributions (target/interfering VOC ratio, and specific VOC ratio). It is easy to see that, with an expected value of 0.5 for each ratio's distribution, the product's expected value tends to zero for a large number of factors. In [311], the exact distribution for the number of factors n has been derived to be:

$$f(x) = \frac{(-\log(x))^{n-1}}{(n-1)!} \quad \text{for} \quad 0 < x \leq 1 \tag{13.1}$$

A slightly higher data density in lower concentration regions can be desirable to improve the model performance in this critical range, but a too large density gradient can impair the model's overall prediction ability, as discussed later in this chapter.

The resulting dataset can be used in several ways to train or validate a sensor system. The quasi-standard today and, thus, the minimum requirement for a new system, is the quantification of TVOC. The profile makes sure that

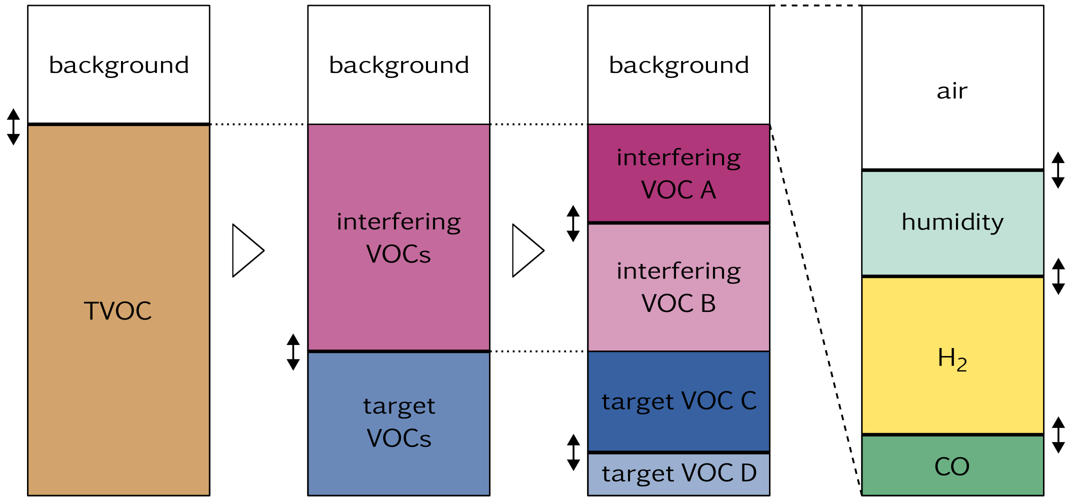

Figure 13.1.: Calibration and validation gas profile for IAQ monitoring systems (ratios not to scale).

many different concentrations are contained in the gas profile, so that a first model covering most of the predefined TVOC concentration range can be trained and validated after relatively few exposures. The different ratios in TVOC composition make sure that the system actually detects TVOC and is not specific to any of the components. It should, however, be noted that TVOC here refers to only four specific VOCs, and not to hundreds as in reality.

In a second step, the system can be trained to detect the amount of target, i. e., hazardous, VOCs, and to discriminate them from non-hazardous, interfering VOCs. And, in a third step, the system can be trained on individual substances to be able to report much more distinct hazards. Hence, the performance of a system on the presented gas profile can be used to place the system in one of three categories with respect to its abilities.

In each exposure, CO, H_2, and humidity is varied. It is a basic requirement of any IAQ monitoring system to minimize cross-sensitivity to variations of these three background gases. Systems failing this basic requirement are unfit for further tests in their current form and, e. g., need reference sensors to compensate reactions to the background gases.

A Python program for the generation of an arbitrary number of random exposures can be found in the appendix (Listing 3). The range from which each ratio is randomly chosen can be defined, as can the range of the absolute concentrations of each substance.

13.2. Sensor system performance

The concentration ranges for TVOC and each substance in the mixture have been chosen according to an extensive survey of VOC concentrations in buildings [229]. Around 750 unique, random exposures, each lasting 20 min, have been created and measured, 350 of which are evaluated here. For the remaining exposures, not all of the signals of the regarded sensor systems are available. The measurement was divided in eight sessions with 100 exposures each[2], preceded by 2 h of 50 %RH air with 150 ppb_v carbon monoxide and 500 ppb_v hydrogen. The concentrations of carbon monoxide and hydrogen were never lower than 100 and 300 ppb_v, respectively, to maintain a realistic background. Due to a mistake in the experimental setup, toluene and benzene were switched during the measurements so that benzene is provided at unusually high concentrations, and *vice versa*. While this impairs the transferability of the calibration to real-world IAQ applications to a degree, it does not invalidate the calibration itself. The distributions of all gases are shown in Figure 13.2.

In addition to the random mixture exposures, all tested sensor systems (cf. Table 13.2) have also been calibrated with the classic sequential approach. Each gas was, alone in a background of 500 ppb_v H_2 and 150 ppb_v CO, provided at four distinct, increasing concentration levels (Table 13.1). These exposures were repeated at 25, 50, and 75 %RH, resulting in 72 distinct exposures of 20 min duration each. Between two gas exposures, 20 min of carrier gas was supplied to see the recovery behavior of the sensor systems.

Hydrogen and water were supplied by gas lines with a maximum flow and 20 and 500 ml/min, respectively. Carbon monoxide and acetone were supplied by predilution lines with 10 ml/min maximum supply and outflow and 500 ml/min maximum carrier flow. All other gases were supplied by predilution lines with 20 ml/min instead of 10 ml/min.

Ten different sensor systems were tested in parallel. As before, they were distributed into four branches with restrictions to cancel out variations in flow resistance. The total flow was 400 ml/min. Out of three SiC-FETs with dense palladium gate (*Pd-FET*), two were operated at a constant temperature, and one with a combination of TCO and GBCO (Figure 7.11). Another SiC-FET with porous iridium gate (*Ir-FET*) was operated with the same combination of cycles. All MOS sensor systems were operated with a variant of the temperature cycle used in chapter 11, i. e., quick temperature drops. *UST* refers to a thin, ceramic substrate with a sensing layer manufactured by UST UmweltSensorTechnik GmbH, Geschwenda, Germany. The *AS-MLV* is a

---

[2] Due to technical problems, one of the sessions had only 50 complete exposures.

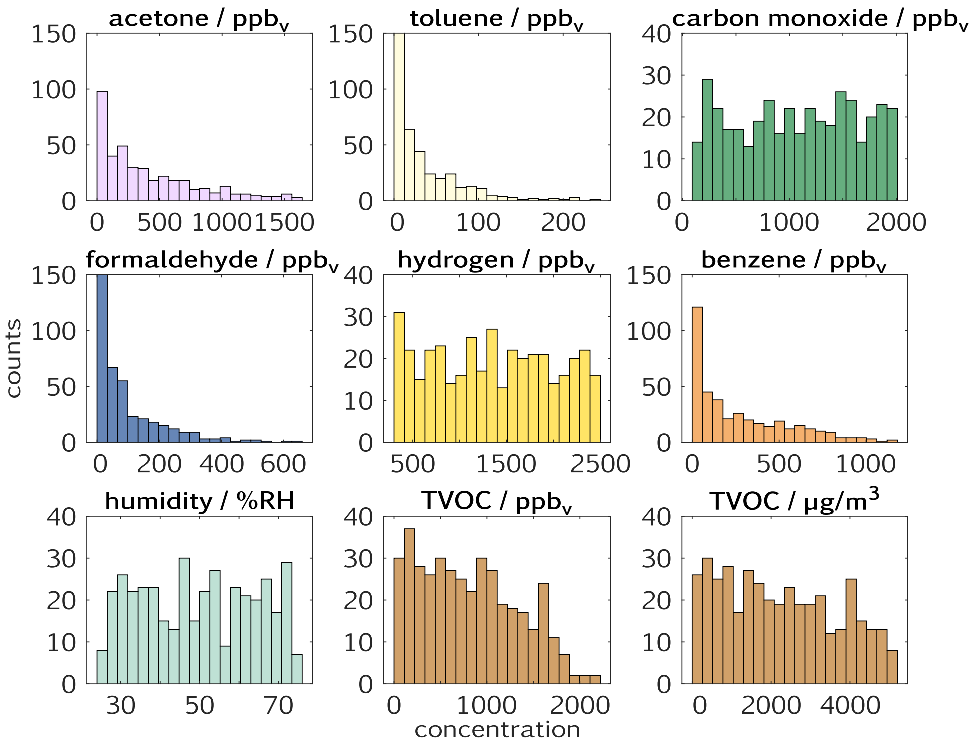

Figure 13.2.: Histograms of gas concentrations in the random-mixtures calibration.

Table 13.1.: Concentration levels used in the sequential calibration. The uncertainty of water cannot be computed due to its dependence on (uncontrolled) temperature.

		concentration level / ppb$_v$			
gas	supply conc. / ppm$_v$	1	2	3	4
acetone	506 ± 10	250	500	750	1000
benzene	100 ± 5	250	500	750	1000
hydrogen	98 ± 2	500	750	1000	1250
carbon monoxide	1000 ± 20	150	300	450	600
toluene	106 ± 2	5	25	45	65
formaldehyde	56 ± 11	40	80	120	160
water / %RH	100	25	50	75	-

discontinued version of a MOS sensor by ams AG, Premstätten, Austria. The *AS-MLV-P2* is its replacement. The suffix *(cond.)* stands for *conditioned* and corresponds to the sensor being exposed to HMDSO prior to the tests in an attempt to passivate its surface and make it selective to hydrogen [20], [312]. The *BME680* (Bosch Sensortec GmbH, Reutlingen, Germany) and *SGP30* (Sensirion AG, Staefa, Switzerland) have their own operating profiles defined by the manufacturer, but the provided *application programming interface* (API) allows overriding the temperature profile within the abilities of the sensor. This means that the results presented here for these two sensors do not reflect the performance of the sensors as sold by the manufacturers. The SGP30 has four different sensitive layers which are evaluated as one sensor array. Additional built-in sensors for temperature, pressure, or humidity are not included in the evaluation. The sensor systems, operating modes, and extracted features are listed in Table 13.2. Note that for all MOS sensor systems, in accordance with the DSR model (cf. section 11.1), the logarithm of the sensor signal is evaluated. The author would like to thank Caroline Schultealbert and Tobias Baur for preparing and setting up the MOS sensor systems, including electronics and software, and for the discussions during the planning phase of this measurement.

Classically, a sensor's selectivity is determined from sequential measurements of one test gas at a time. It can then easily be computed as the ratio of the response to the target gas and the response to another, interfering gas according to Equation 1.9. With random mixture calibration, this is no longer possible since the sensor is exposed to all gases at the same time in each exposure. Quantification is done by training a PLSR model for each gas, i. e., there is no classic sensor response available in this case. Instead, the new measure *performance* is defined for each gas g as

$$\text{performance} = \frac{\text{std}(c(g))}{\text{RMSEP}(g)} - 1 \tag{13.2}$$

where $\text{std}(c(g))$ is the standard deviation of the concentration distribution of gas g, and $\text{RMSEP}(g)$ is the RMSE of prediction of a PLSR regression model quantifying this gas. If the model performs well, its standard deviation, i. e., RMSEP, is significantly lower than the standard deviation of the input distribution. Instead, if both values are equal, the model cannot quantify the gas satisfactorily. The fraction becomes 1 in this worst case, so one is subtracted to obtain a zero baseline. Noise can lead to values slightly below zero, which are cut-off in all graphs for clarity. Figure 13.3 gives an overview of the performances of all tested systems and gases.

This definition of performance is closely related to the *coefficient of determination*, R^2, which follows the same logic and is often used to describe the

Table 13.2.: Tested sensor systems, operating modes, and applied feature extraction. For the DSR temperature cycle, the base temperature is given first, followed by a list of measure temperatures.

sensor system	operating mode	features
Pd-FET (100 °C)	static, 100 °C	1× mean over 2 min
Pd-FET (200 °C)	static, 200 °C	1× mean over 2 min
Pd-FET (cycled)	TCO+GBCO (Figure 7.11) (100/200 °C, ±2 V)	6× mean over plateaus 7× slope over transients
Ir-FET (cycled)	TCO+GBCO (Figure 7.11) (100/200 °C, ±2 V)	6× mean over plateaus 7× slope over transients
UST	TCO (DSR), 12 steps (450 °C to 75, 100, ..., 350 °C)	12× slope
BME680	TCO (DSR), 9 steps (400 °C to 150, 175, ..., 350 °C)	9× slope
AS-MLV-P2 (cond.)	TCO (DSR), 6 steps (450 °C to 150, 200, ..., 400 °C)	6× slope
AS-MLV-P2	TCO (DSR), 12 steps (450 °C to 75, 100, ..., 350 °C)	12× slope
AS-MLV	TCO (DSR), 12 steps (450 °C to 75, 100, ..., 350 °C)	12× slope
SGP30	TCO (DSR), 12 steps (14 to 2, 3, ..., 13)[*]	4×17× slope[**]

[*] API and documentation of the SGP30 only specify arbitrary levels, presumably proportional to the temperature.

[**] The SGP30 has four separate sensitive layers and, due to strong dynamic effects, more than one slope was extracted from some temperature plateaus.

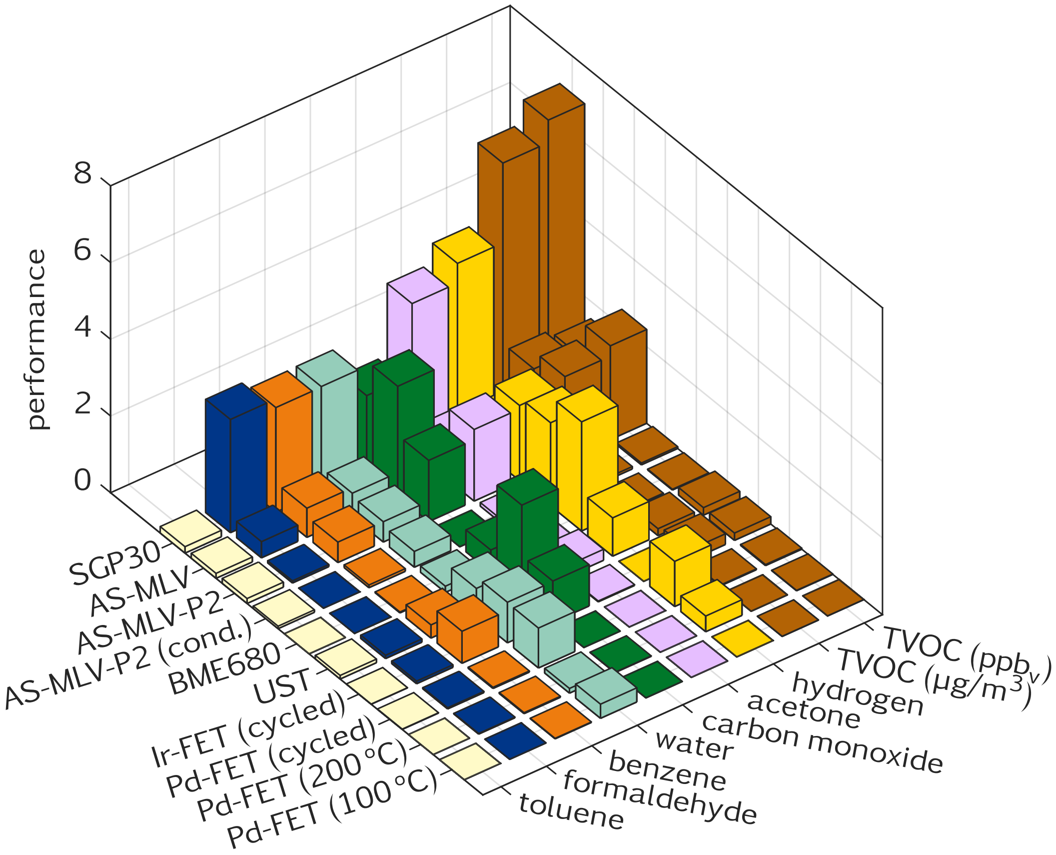

Figure 13.3.: Overview of system performance.

goodness of fit [313]:

$$R^2 = 1 - \frac{\mathrm{SS}_{\mathrm{res}}}{\mathrm{SS}_{\mathrm{tot}}} = 1 - \frac{\sum_{i=1}^{N} (y - \hat{y})^2}{\sum_{i=1}^{N} (y - \bar{y})^2} \tag{13.3}$$

The fraction of the residual and total *sum of squares* (SS) gives the unexplained variance and is the inverse square root of the fraction in Equation 13.2. Hence, the performance grows without bounds the more variance is explained by the model, i. e., the better the prediction follows the target values.

A high performance value states that the sensor system can quantify the associated gas well. The Pd-FET at 100 °C reacts slightly to water, but cannot quantify any gas satisfactorily. In theory, it should be selective to hydrogen (and hydrogen-containing compounds), but the very low operating temperature most likely leads to a large influence of humidity on the response, masking the hydrogen signal. This is supported by the Pd-FET operated at 200 °C showing a clear response[3] to hydrogen and only hydrogen, as expected[4]. This performance is roughly tripled for the cycled Pd-FET with a similarly good performance for water. Presumably, the high and low temperature part of the cycle are selective to hydrogen and water, respectively, allowing for better discrimination and, thus, selective quantification of both. The (porous) Ir-FET, on the other hand, is not able to quantify hydrogen with the same cycle, likely due to Ir requiring higher temperatures in general [191]. It can, however, quantify benzene, carbon monoxide, and water with similar, only slightly lower performance. The UST provides excellent carbon monoxide and decent hydrogen performance. The latter is, however, surpassed thrice by the conditioned AS-MLV-P2 which otherwise shows only a small reaction to carbon monoxide and basically none to other gases, i. e., the conditioning works as expected. The AS-MLV-P2 greatly expands the list of detectable gases with respect to the sensor systems discussed so far: the only gases with negligible performance are toluene (which has close to zero performance for all systems) and formaldehyde. Notably, TVOC can be quantified better than any unique gas. The older AS-MLV shows a similar pattern, however, with better performance for carbon monoxide, but close to zero performance for both acetone and hydrogen. Finally, the SGP30 shows superior performance for five gases (formaldehyde, benzene, water, acetone, and hydrogen) with double to four times the performance of the second best-performing system for the respective gas, as well as for TVOC. Only the carbon monoxide performance is third to the AS-MLV and the UST. The

---

[3] with the meaning of: good selective quantification ability

[4] The relatively low temperatures were chosen in an attempt to reduce cross-sensitivity to hydrocarbons. Higher temperatures could improve the hydrogen response

Table 13.3.: Performance measures for sensors.

	average performance		
sensor system	mean	median	threshold (0.5)
Pd-FET (100 °C)	0.043	0	0
Pd-FET (200 °C)	0.067	0.010	0
Pd-FET (cycled)	0.260	0.027	2
Ir-FET (cycled)	0.393	0.192	3
UST	0.594	0.287	3
BME680	0.406	0.023	2
AS-MLV-P2 (cond.)	0.325	0.068	1
AS-MLV-P2	1.255	1.560	7
AS-MLV	1.063	0.760	7
SGP30	3.578	2.951	8

good performance is, most likely, a result of the four distinct sensitive layers in combination with TCO.

Table 13.3 lists the performance of each sensor system averaged over all gases. Ordering the systems according to mean or median results in only minor differences in the middle field. The threshold value, here the number of gases with a performance above 0.5, is an additional, simple number of merit. It is also the only one of the three which can convey classical selectivity (as low numbers just above zero), i. e., where the sensor itself reacts only to, e. g., hydrogen.

The number of LVs has been manually determined for each model. In this case, however, two separate numbers were chosen: one to minimize the RMSEP, and one to maximize the correlation coefficient between prediction and target data. The model performance was then computed for the larger of the two, sometimes resulting in a better and never in a worse model. RMSEP is not always the best parameter to optimize as it can be small for models with virtually no correlation so that all points are close to the ideal line. When correlation appears at a higher number of LVs, the RMSEP can become worse because the spread increases. However, good correlation, i. e., accuracy, is, arguably, more important than a low RMSEP, i. e., precision.

Interestingly, the number of LVs is, for some criteria (cf. section 3.9.4), distinctly correlated with the average sensor system performance (Table 13.4). The highest correlation with 92.7 % is found between *min (conf.)* and the average sensor system performance. Both *min* and *min (conf.)* result in correlation coefficients over 85 % for all three performance statistics. The

Table 13.4.: Correlation between average selected number of LVs and average system performance.

	correlation coef. / %		
LV criterion	mean	median	threshold (0.5)
min	88.9	84.8	87.8
min (conf.)	92.7	89.7	85.3
max t	45.8	39.5	58.0
elbow	48.9	49.2	72.9
quotient (0.95)	76.2	72.0	80.8
quotient (0.99)	70.4	69.4	87.3
subjective	87.7	85.4	83.2

Table 13.5.: Correlation between selected number of LVs for the hydrogen model and average system performance.

	correlation coef. / %		
LV criterion	mean	median	threshold (0.5)
min	83.7	76.6	71.6
min (conf.)	84.1	79.3	69.6
max t	−12.8	−11.8	−18.4
elbow	31.8	37.3	72.6
quotient (0.95)	-	-	-
quotient (0.99)	-	-	-
subjective	85.3	80.0	69.4

subjective selection, which was eventually used to compute the model performance, reaches good, but overall slightly lower values. Interestingly, the correlation is poor between the *elbow* criterion and mean/median, but increases by 20 percentage points for the threshold measure, i. e., the number of well-performing gases. Compared to *min* and *min (conf.)*, *elbow* is more conservative and selects only LVs leading to a considerable decrease in RMSEP which are, in turn, presumably related to the number of best performing gases or, possibly, sensing mechanisms. The correlation for *max t* is the overall poorest, whereas the better performing *quotient* criteria are very strict and often do not even select one LV, disqualifying them as indirect performance measure.

This correlation is interesting because, if it holds for the performance of a distinct gas, it could greatly reduce the number of models to build in order to screen a set of sensor systems for overall performance. Table 13.5 shows the correlations between the average system performance and the number of LVs selected for only the hydrogen model. Hydrogen was chosen because, here, it has the highest average performance over all systems with 1.46. Indeed, the correlation between the promising selection criteria (*min*, *min (conf.)*, and *subjective*) and the average system performance decreases only slightly compared to when the number of LVs is determined from the full set of models. Hence, when the number of LVs producing the lowest RMSEP for a model is high, the same is likely true for the overall performance of the specific system.

13.3. Comparison with sequential calibration

In this section, the novel random mixture approach is compared with the traditional sequential approach for gas sensor calibration and characterization. The comparison is done for the AS-MLV sensor as an example. This sensor type is believed to make a good model system as it has a good performance for many, but not all of the tested gases, and has been used in many other measurements at LMT. Figure 13.4 shows the sensor system's performance for all gases with different evaluation approaches for the sequential and random mixture calibration scheme. They will be discussed in that order in the following paragraphs. All error bars are 68 % confidence intervals computed from the fold-variance of 6-fold testing.

The "easiest" task for a model is quantifying one and only one gas without any interference from other gases ("sequential (others ignored)"). This means that only exposures where the respective gas was present at a non-zero concentration are used for the model training – all other exposures are ignored. The only exception is, here, water because each gas concentration was measured at three different humidity levels in the sequential calibration scheme. The resulting performances suggest exceptional sensitivity (but not selectivity) to benzene, as well as very good sensitivity to acetone and carbon monoxide, and acceptable sensitivity to toluene, formaldehyde, and water. Note that water is a special case since no exposures with water alone were defined, i. e., water will, in all cases, have all other gases as interferents. As this does not change with the evaluation strategy, the performance values for all three strategies based on the sequential calibration scheme are the same.

The next evaluation strategy ("sequential (others 0)"), which also takes selectivity into account, is to include all exposures in the training. Six individual gases were measured at four concentrations and three humidity

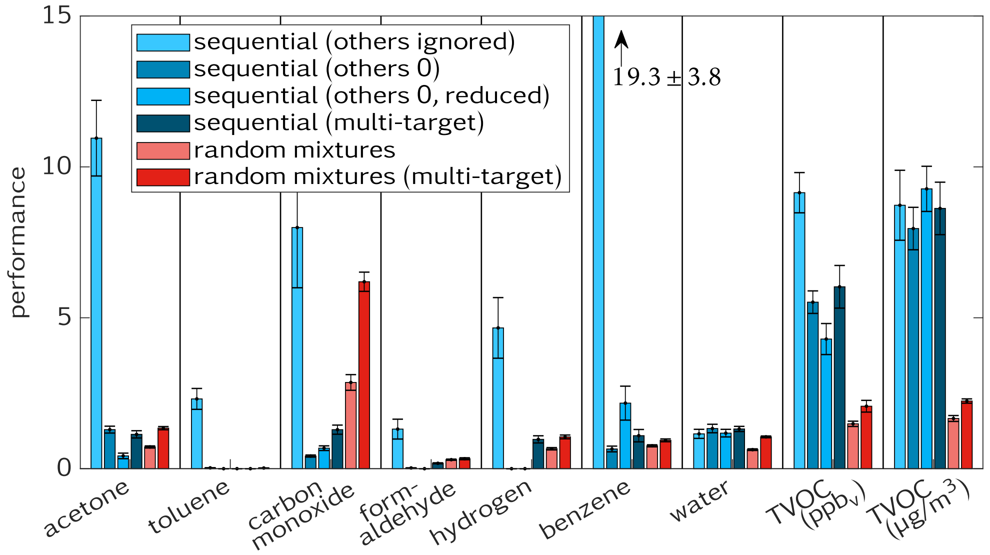

Figure 13.4.: Performance of the AS-MLV for sequential (blue) and random-mixture (red) calibration using different evaluation strategies.

levels, resulting in 72 exposures. Twelve of these exposures contain non-zero concentrations of a target gas, whereas the remaining 60 count as zero. This is a fundamental problem with the sequential approach which becomes only worse for more gases. Training a model with all exposures, giving 0 as the target value for all exposures not containing the target gas, will lead to a model which focuses on “getting the zero right”, i. e., it is trained to predict any non-target gas as zero. The few non-zero concentrations have little influence on the training, leading to large quantification errors in many cases. The RMSEP, being dominated by the zero-class, is over-optimistic in these cases and does not reflect the model degradation well. The correlation coefficient between predicted and target values is a better measure. While the RMSEP for toluene and formaldehyde increases only slightly between *others ignored* and *others 0* in Figure 13.5a, the correlation coefficient (Figure 13.5b) drops from 1, i. e., perfect correlation, to a value below 0.4 and 0.7, respectively, indicating a serious degradation. Note that the performance reflects both types of degradation well.

In Figure 13.5a, the theoretical accuracy and repeatability of the gasmixer are shown as gray lines left and right from each bar group. The two lines on the left of the bar group show the 10 to 90-percentile of the concentration range used in the sequential calibration. The two lines on the right show the same for the concentration range during the random-mixtures calibration. The inner line stands for the smaller repeatability, the outer

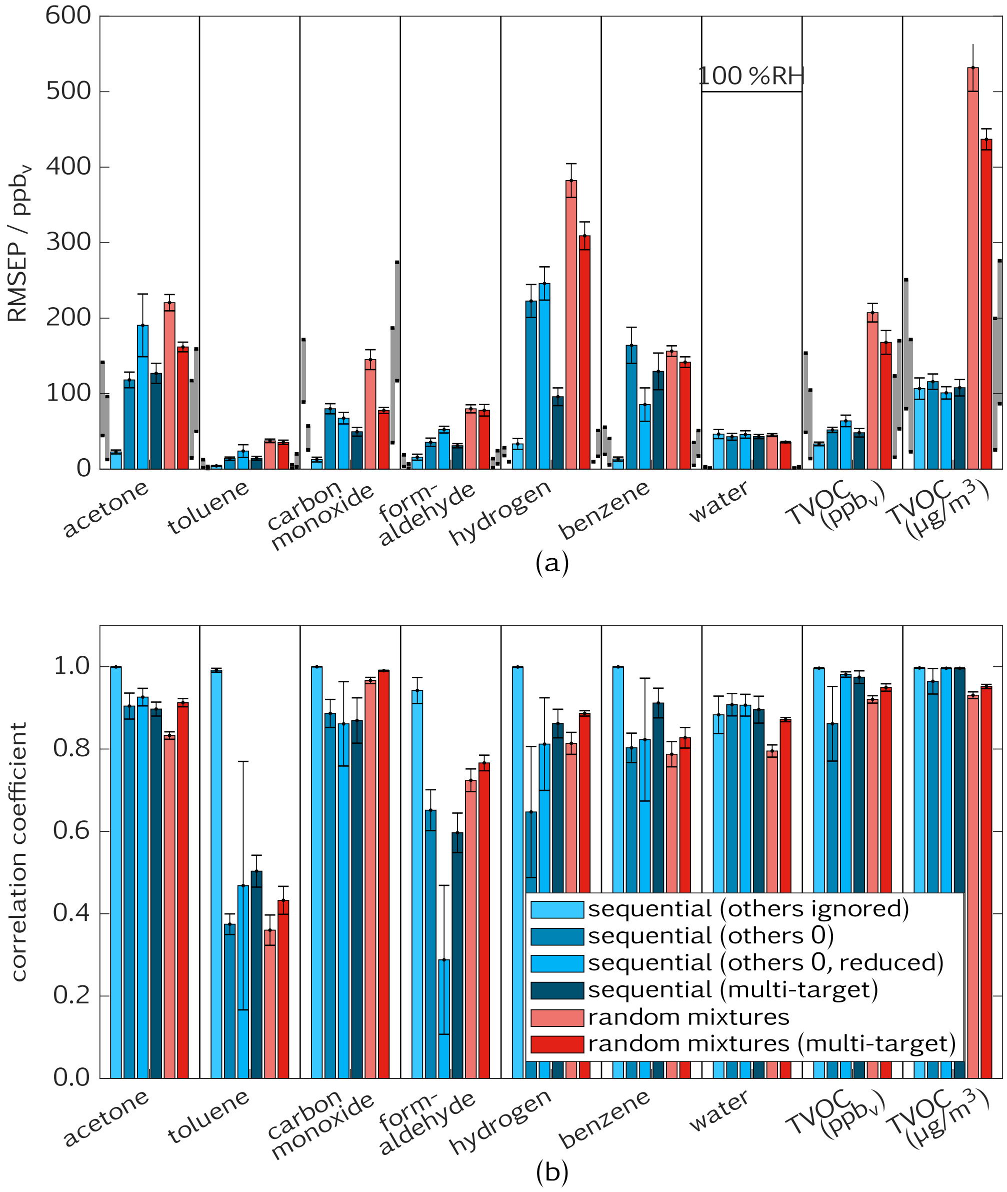

(a)

(b)

Figure 13.5.: (a) RMSEP and (b) correlation coefficient of models for the AS-MLV for sequential (blue) and random-mixture (red) calibration using different evaluation strategies.

line for the larger accuracy. Both uncertainties were calculated according to Equation 10.7 for hydrogen and water and to Equation 10.10 for all other gases. The uncertainty for TVOC was computed as the geometric mean of the uncertainties of acetone, toluene, formaldehyde, and benzene. Within this measurement, the repeatability is the important value since everything was recorded with the same gasmixer and gas supplies. When comparing the data to another measurement repeated with a different gasmixer or different gas supplies, the accuracy would have to be regarded instead. The sequential calibration evaluated with *others ignored* is, as mentioned above, the easiest problem and, therefore, the most likely to be restricted by the uncertainty of the measurement setup. Indeed, its RMSEP lies within or very close to the theoretical repeatability for all gases, suggesting that the sensor performance can be limited by the uncertainty of the calibration equipment.

The issue of large classes dominating the model training has been mentioned in section 3.9.1, along with a suggested counter-measure: reduction of all classes to equal size. This does, indeed, remove the dominance of the zero-class (“sequential (others 0, reduced)”). However, due to the large ratio between target to non-target gas exposures (12 to 60), removing observations from the zero-class randomly introduces a large portion of variance, i. e., chance, in the model’s performance. This variance is not captured in validation or testing since the data reduction is, for consistency, only done once before a complete training run. This could be changed in the implementation which would, however, not change the fact that the performance of the finally trained model greatly depends on the observations removed in this particular training run.

PLSR can handle multiple targets at once, finding the best possible set of models to predict all concentrations simultaneously. The interaction between the models can improve the overall model performance. Applied here to the *others 0* approach, carbon monoxide and hydrogen prediction benefit significantly (“sequential (multi-target)”).

In a nutshell, however, all four evaluation strategies presented for the sequential calibration scheme have drawbacks seriously limiting the applicability of any resulting model. These drawbacks arise from the data structure imposed by the calibration scheme. Other issues, like the lack of gas interactions or varying TVOC mixtures in the training data, must also be addressed.

The structure of the random-mixtures calibration scheme solves all of the issues mentioned above. By incorporating all gases in each exposure with varying concentrations, the focus is shifted from levels or classes to concentrations and, thus, from a classification to a quantification problem. Exposures where one or more gases are zero are still included and important, but the ratio between zero and non-zero exposures is roughly equal, or can be tuned to be. All in all, the resulting models and their performances are expected to be much closer to the true performance achieved in an application. Looking at Figure 13.4 and the results for “random mixtures”, the ability to quantify a specific gas changes strongly with the type of calibration and evaluation, so that both should match the later real-world conditions as closely as possible to facilitate the calibration transfer between laboratory and field.

Application of multi-target PLSR improves the performance for all gases (“random mixtures (multi-target)”), except toluene, consistently and significantly, i. e., it is more effective compared to its use in the sequential calibration. Interestingly, the resulting performance of both calibration strategies is almost equal for all gases with multi-target PLSR. So far, however, only different evaluation methods and their issues have been compared and not the calibration strategies themselves. This will be done in the following.

The comparison is made between models trained with data from the sequential and random-mixtures calibration, respectively. Both are evaluated with multi-target PLSR. This kind of evaluation has resulted in almost equal, and also the best of the more realistic approaches (i. e., excluding *others ignored*), performances for both calibration schemes before. While the sequential calibration produced 72 exposures, the random mixture calibration produced over 350, i. e., five times the amount of training data. In order to make a fair comparison, the random-mixtures model is trained with only 70 randomly chosen exposures in 6 iterations. With around 70 exposures of 20 min each, the total duration for both schemes is equal and less than 24 h.

The sequential and random-mixtures model are tested for their ability to predict random-mixtures data. Validation of both models is done, exposure-based, 6-fold, and testing with data from the random-mixtures calibration scheme. This data is obviously more challenging and more realistic and, potentially, allows for a more efficient training since each exposure contains an unique data point for each gas. For a fair comparison, all exposures with any gas concentration not included in the sequential calibration (cf. Table 13.1) are removed before the prediction with the sequential model, leaving 462 cycles from 29 unique exposures. The random-mixtures model is trained with 70 exposures from the random-mixtures calibration and all the remaining 280 exposures are predicted. This is done in 6 iterations. The features are averaged before training, validation, and testing, so that each observation represents one exposure.

The resulting performances in Figure 13.6 show that training with the random mixtures data is consistently superior and basically includes the sequentially trained model, i. e., there is no benefit of using the sequential

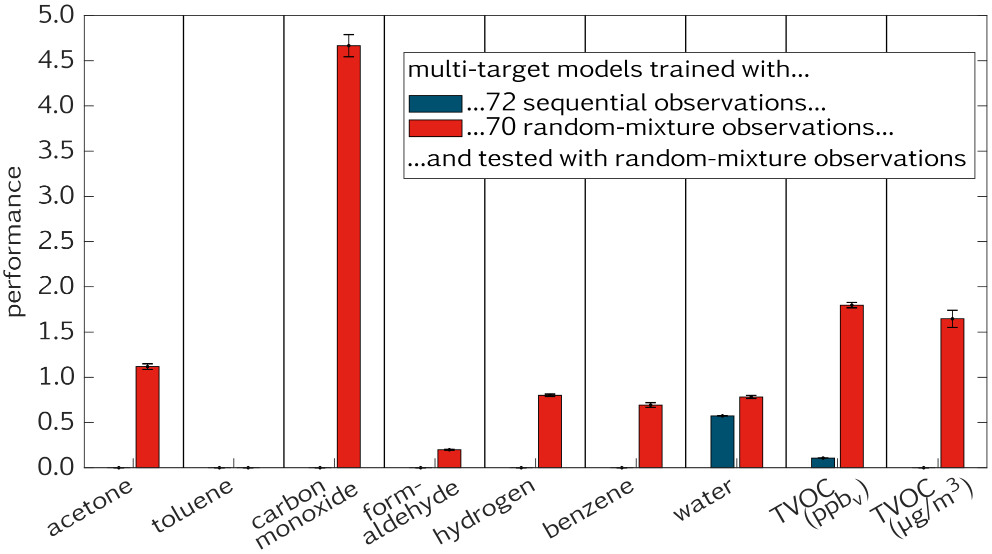

Figure 13.6.: Comparison between random-mixture and sequential calibration for models trained with the same number of exposures.

approach. Water is the only exception with an almost equal performance in both schemes. This is explained by the fact that water was the only gas in the sequential calibration trained with all other gases as interferents because there were no dedicated water exposures. Comparison of the performance of random-mixtures trained with 280 (cf. Figure 13.4) and 70 exposures, i. e., 75 % less training data, shows a decrease in performance of only 25 %. These results clearly show that the random-mixtures calibration scheme is more efficient and leads to better generalizing models. In the same amount of time, it produces a significantly better model than the sequential calibration scheme which can, if so desired, be gradually improved with more training data.

Part IV.

Conclusion and outlook

14. Conclusion

This thesis gave an overview over current gas sensor technologies and the multitude of prospective applications. Many of these applications, ranging from safety (fire detection) over comfort (odor detection) to health (on-line air quality monitoring and non-invasive detection of diseases), depend on precise quantification of specific gas components in a complex mixture. Much effort has been spent over the last decades to the development of cheap, yet accurate and precise gas sensor systems capable of this task. The fact that, despite all these works, gas sensor systems are not yet in widespread use but only employed in niche applications gives an idea of the many challenges to overcome. Modern sensor systems implement a complex measurement chain with many items, all of which must be attended to in order to improve the system's overall performance. With application in mind, this thesis has focused on three important aspects of contemporary gas sensing: data evaluation and validation of data-driven models, physical modelling of sensors and optimization of their operating mode, as well as test gas generation and calibration strategies in general.

In regard to data evaluation and data-driven models, a MATLAB-based toolbox called DAV^{3}E (Data Analysis and Verification/Visualization/Validation Environment) has been developed over the course of this PhD project. It focuses on cyclic sensor data as they are common not only with temperature-cycled virtual multisensors, but also industrial condition monitoring, or time-resolved spectral methods. The underlying assumption of a repeating cycle enables cycle-based preprocessing and interactive visualization methods mostly missing from current software tools within the same scope. The graphical feature extraction, not found in any other tool to the best of the author's knowledge, allows in-depth exploration of complex datasets and the addition of expert or model-based knowledge during the feature extraction process. DAV^{3}E further implements a collection of common methods in machine learning and pattern recognition for dimensionality reduction, classification, quantification, validation, and testing.

The guidance that DAV^{3}E as a framework provides is especially important with regard to model validation and testing which can quickly lead to wrong, over-optimistic performance estimates when applied incautiously. This thesis has introduced testing as a separate step of the model-building process in the first place and has pointed out the danger of “polluting” datasets through improper experimental design, e. g., through recording many observations in identical experimental conditions. Countermeasures, namely exposure-based and concentration-based validation and testing, as well as data reduction algorithms, have been developed, implemented, and shown to lead to significantly better, i. e., more realistic, model selection.

Data fusion, both in parallel, i. e., from many systems, and in series, i. e., from many measurements, is an important feature to facilitate the evaluation of large real-world datasets. A simple *track* system has been conceived to define the position of data streams relative to each other, allowing for automatic data fusion when the start time and sampling rates of all data streams are known. It was made sure that data is never resampled at any point to avoid unnecessary computational load. The performance of three simple data fusion algorithms for unequal cycle lengths, conceived during this PhD project, was evaluated with 100 000 simulated and one similar, real dataset. While the specific results obviously differ greatly with the data, some general properties and recommendations could be derived for each method. Based on these results, one of these algorithms, unweighted mean, which fuses features from longer cycles with average features from multiple shorter cycles, was implemented in DAV^{3}E. Hence, this toolbox implements all necessary methods to arrive from raw sensor data to a validated and tested model which can predict, i. e., classify or quantify, new observations. It can be used as a command-line tool for complex or batch evaluation tasks, but, also, provides a graphical user interface (GUI) to guide the user through the process.

DAV^{3}E replaces and supersedes the previous accumulation of four custom-written software tools at the Lab for Measurement Technology (LMT), comprising separate tools for feature extraction, regression, dimensionality reduction and classification, and support vector machine (SVM) classification. As one consistent, self-contained software, it significantly accelerates data evaluation which often is an iterative process with data-driven models, and, at the same time, avoids many user errors by providing a clear structure and a rigorous framework. This has led to quick adaption in both research and teaching: DAV^{3}E has been actively used as the main data evaluation tool at LMT for several years now and has recently gained recognition from international research groups of diverse fields. It has been used to teach the basics of data-driven modeling to students in a hands-on way both at LMT and international workshops. To ensure transparency and continued development, it has been made publicly available under the GNU AGPL open-source license [166].

For data-driven models to succeed, a sensor must produce data which reflect all interesting quantities as well as possible. Gas sensor arrays and virtual multisensors, mostly with temperature-cycled operation (TCO), are the *de facto* standard to increase sensitivity and, especially, selectivity of MOS gas sensors. Recent advances in physical sensor modeling have given rise to highly optimized temperature cycles for MOS gas sensors [58], [163], yet similar studies regarding dynamic effects for gas-sensitive field-effect transistors (GasFETs) are rare in literature. The benefits of TCO with GasFETs have been demonstrated by Bur [200], but similarly comprehensive studies are missing for other sensor parameters, namely gate bias and light influx, motivating the investigations in this thesis.

A new software was written to be able to cycle all sensor parameters independently. Further, signal compensation through temperature and gate bias is implemented, allowing for an operating mode where the sensor signal is kept constant by varying the gate bias. A comparison between this mode and measurements at fixed drain-source voltage found negligible differences in performance. However, the curvature of the logarithmic sensor response characteristics changed significantly more over the applied temperature cycle during the compensated mode. A model has been proposed to explain the observed, dynamic effects based on the assumption that fringing electric fields can move charges, oxygen anions in particular, between metal and oxide regions of the sensor surface. This model was validated through measurements at different oxygen concentrations (0 % to 20 %), gate biases (±2 V), and temperatures (150 °C to 300 °C), showing a significantly lower response at the negative gate bias. The observed decrease of the difference between positive and negative gate bias with increasing temperature is consistent with a broadening of the distribution of oxygen on the surface.

A combined TCO/GBCO cycle with sharp gate bias steps instead of steady ramps as in [314] was designed and tested. Both the static and dynamic effects of GBCO were shown to be gas-dependent and features could be extracted to discriminate gas types and quantify each gas, with the best results for ammonia (17 $\mathrm{ppm_v}$ to 50 $\mathrm{ppm_v}$) and nitrogen dioxide (0.2 $\mathrm{ppm_v}$ to 1 $\mathrm{ppm_v}$). Moreover, a combined TCO/GBCO cycle applied to a silicon-carbide-based field-effect transistor (SiC-FET) with dense palladium gate was able to produce selective features for humidity and hydrogen, respectively, significantly increasing the selectivity to both. Most notably, positive gate biases suppressed the hydrogen response entirely.

Preliminary investigations on the influence of soft UV light (λ >370 nm) revealed additional dynamic effects after a gate bias step which cannot be explained entirely with changes in the device's electrical properties. There is evidence that the UV increases the mobility of charges on the surface. Features extracted from the dynamic parts of the sensor response were able to successfully classify several gas types.

In addition to these novel parameter variations, tungsten trioxide (WO_3) was deposited as the top-most oxide layer on the gate of a SiC-FET in an attempt to improve its sensitivity and selectivity to volatile organic compounds (VOCs)[1]. A test with naphthalene (0 ppb_v to 40 ppb_v) in much higher levels of ethanol (0 ppm_v to 5 ppm_v) gave strong evidence for different sensing mechanisms on WO_3 as compared to SiO_2. Different arithmetic signs of the response to naphthalene and ethanol, respectively, as well as an almost binary ethanol response suggest improved selectivity for WO_3. Indeed, the best regression model for WO_3 can predict naphthalene concentrations up to 10 ppb_v with an uncertainty of 2.9 ppb_v, decreasing to below 0.4 ppb_v at 0 ppb_v, independent of the widely varying ethanol concentration. The model for SiO_2 achieves a constant uncertainty around 6 ppb_v.

The final part of this thesis was concerned with calibration strategies for gas sensors. It gave a brief overview about possible sources of unknown variables, like systematic errors in the calibration equipment or insufficient complexity of the calibration profile, and presented an interlaboratory study, a field test, and a novel calibration strategy based on random gas mixtures.

The interlaboratory study between LMT and Bundesanstalt für Materialforschung und -prüfung (BAM) trained a sensor system with an exhaustive training dataset recorded at LMT and investigated the performance of the resulting models for the data recorded with an independent system at BAM. The relatively large initial error, especially for TVOC, could be reduced greatly by updating the trained model with three or fewer observations from the validation measurement. Taking all variations, i. e., the varying background of up to ten different VOCs and the dissimilar calibration systems, into account, prediction errors of 48 ppb_v and 92 $\mu g/m^3$ for formaldehyde and TVOC, respectively, are a promising result and strengthen the confidence in the sensor system, both calibration systems, and the evaluation chain, especially because the BAM gas exposure concentrations were analytically determined. Moreover, a large bias initially observed for the prediction was explained by environmental hydrogen or carbon monoxide not being removed by the activated carbon filter in the BAM system. While this is irrelevant for analytical methods, it has a great impact on the less selective gas sensors and is a prime example for the importance of interlaboratory studies in the gas sensor field.

Of similar importance are field tests which hold many challenges. A field-

---

[1] Due to the many different definitions of what is considered a VOC, the working definition in this thesis was that a VOC is any organic gas, except for methane, which can be generated in the ppb_v range at room temperature and atmospheric pressure.

test system prototype for GasFETs was designed and built at LiU during this PhD project, featuring automatic temperature calibration, a touchscreen for basic input/output operations, and an actively pumped measurement chamber. The predecessor of this system, with a SiC-FET with WO_3 as gate oxide, was deployed in a Swedish school for several weeks together with reference instruments for temperature, relative humidity, carbon dioxide and formaldehyde. The measured formaldehyde concentrations were low ($<30\,\mathrm{ppb_v}$) over 9 days. They showed a strong negative correlation with the level of ventilation, causing a strong positive correlation with carbon dioxide as an indicator of human presence. Good correlation between the sensor signal and higher formaldehyde concentrations was observed with comparatively low reaction to carbon dioxide and other gases associated with human presence. The exact determination of cross-sensitivity effects, however, would require more analytical equipment to determine the atmospheric composition, or a suitable calibration profile to simulate the main influences in the laboratory.

A strategy to create such a profile has been proposed in this thesis. It is based on unique gas exposures whose composition is randomly determined from pre-defined concentration distributions for each component. This strategy was evaluated by calibrating ten gas sensor systems with 750 random exposures, resulting in one of the most extensive datasets of its kind to date. Evaluation of ten systems trained with 350 random exposures revealed striking differences between the sensor systems' performances. Models trained with the same number of exposures for both the novel random-mixtures method and the classic sequential method, i. e., one gas per exposure, achieved a consistently better prediction error for the random-mixtures approach, showing its superior efficiency. A correlation of up to 90 % was found between the average number of selected latent variables (LVs) for the regression models of a given sensor system with its performance. 80 % correlation could still be achieved between the system performance and the number of LVs selected for a hydrogen regression model, presenting an attractive shortcut for the screening of sensor system performances with random-mixtures calibration.

These results were facilitated through a new gas mixer control software developed in cooperation between LMT and 3S GmbH which is flexible enough to be adapted to other calibration equipment, facilitating interlaboratory studies in the future.

15. Outlook

All in all, this work has achieved important scientific and technological advances for many items of a modern gas sensor system's measurement chain. DAV^{3}E has grown to be a stable platform for data evaluation of cyclically operated sensors. It contains a basic set of tools to solve the majority of tasks. On the other hand, future challenges could require new algorithms and modules to be implemented, which the existing plugin system should facilitate. One area of pattern recognition still missing is clustering and novelty detection which, as unsupervised methods, would enable the discovery of structures and anomalies in large, unlabeled datasets. Systems able to recognize an unknown input can improve safety and security, and can learn more efficiently by requesting labels for specific unknown observations from human operators. A module to generate secondary features, e. g., the product or quotient of two features, would be a welcome addition to DAV^{3}E since feature interactions like these can reveal new, previously invisible relations. This kind of data processing is currently not possible in the GUI, and, therefore, not easily accessible. More future work includes optimization for large datasets by finishing the interface for hard disk memory mapping to avoid loading all data into memory, support for genuinely unknown target values, and on-line capability to test and possibly train models on-the-fly.

Cyclic operation is a relatively novel approach to increase the sensitivity and selectivity of GasFETs. The recently presented results with TCO and experimental GBCO [200] have been extended with a basic model explaining the processes during gate bias cycling in this thesis. The model is consistent in air, but cannot explain all signal variations with test gas present. The same goes for UV light irradiation, indicating the need to extend the model, e. g., with experimental data about the oxygen distribution on the surface at different gate bias levels. Robert Falkowski is currently investigating the effect of light intensity and wavelength on MOS sensors in his Bachelor thesis at LMT. Also, a SiC-FET with dense palladium gate, showing strong changes in response to hydrogen and humidity with the gate bias, could be an interesting model system to develop the model further. WO_3 as gate oxide is interesting because of the evidently different reactions to naphthalene and ethanol which is not seen for SiO_2. The explanations given for these observations should be checked with other gases but, most importantly, more

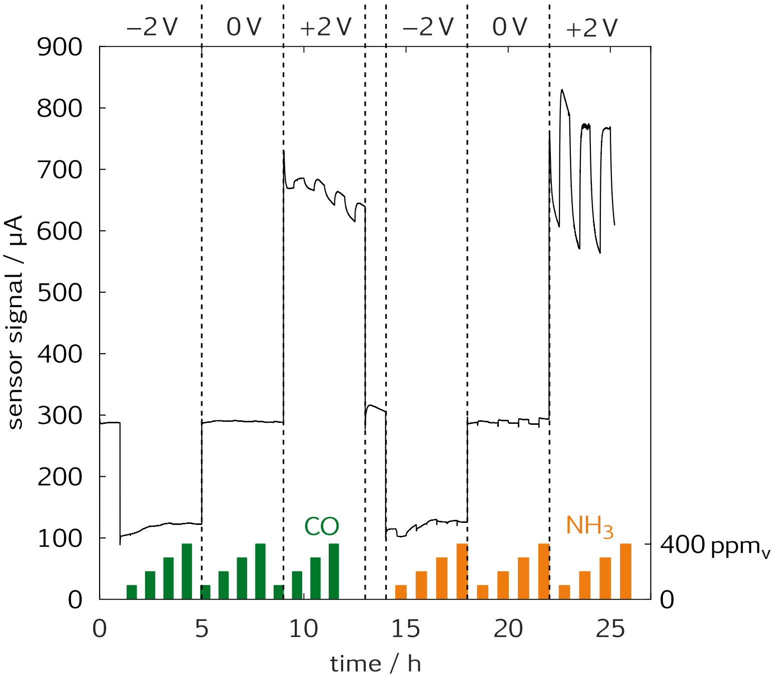

Figure 15.1.: A thin YSZ oxide layer improves the sensor response at positive gate biases dramatically.

research must be done regarding the stability of the Ir/WO_3 gate to achieve more reliable results for this kind of sensor.

Different gate oxides can, in general, be an interesting subject to study in combination with dynamic operation, and GBCO in particular. First results[1] show a dramatic increase in response at positive gate biases for devices with a thin yttria-stabilized zirconia (YSZ) layer, an oxygen ion conductor, as top-most oxide (Figure 15.1). The influence of the oxide on surface reactions could be leveraged by increasing its surface. One way to achieve this are nanoparticles deposited on the gate, which was shown to be feasible in this PhD project with TiO_2 (Figure 15.2). Orientation measurements showed no obvious differences, e. g., concerning the influence of humidity, but more systematic measurements to confirm or deny this finding should be done.

The importance of gas sensor calibration and the interaction between experimental design and data evaluation is often underestimated in sensor science. In the past and even today, many publications deal with classification of single gases, neglecting the reality of changing gas mixtures. The

---

[1] Achieved by Claudia Daut during a short-term scientific mission, funded by *PortASAP* (COST Action CA 16215), at the group of Dr. Krisjanis Smits at the University of Latvia, in cooperation with LiU.

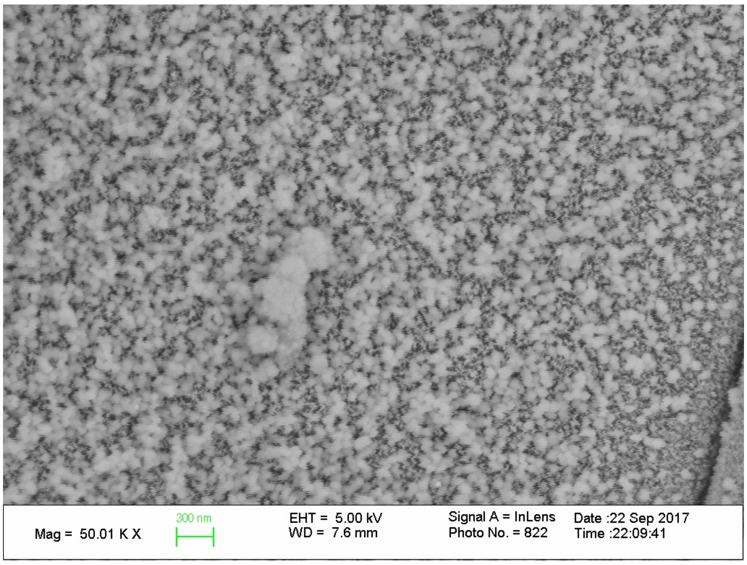

Figure 15.2.: TiO_2 nanoparticles on the porous gate electrode of a SiC-FET. Thanks to Rickard Gunnarsson (LiU) for his help with the deposition.

importance of interlaboratory studies and field tests, in order to discover previously unknown complications and account for them in the system design, has been pointed out in this work. In the future, the gas sensor community should put greater emphasis on interlaboratory studies to increase the confidence in the usually custom-built calibration equipment. To this end, the newly developed gas mixer control software can act as a common base to define and share calibration profiles. Regarding the design of these profiles, the random-mixtures method produces promising results and should be developed further, possibly using tailored concentration distributions for specific problems and more rigorous statistical methods to, eventually, arrive at a standardized testing method with reliable confidence intervals just like they exist today for physical sensors.

Bibliography

[1] W. Göpel, J. Hesse, J. N. Zemel, T. Grandke, and W. H. Ko, Eds., *Vol. 1: Fundamentals and General Aspects*, Sensors - A Comprehensive Survey 1, Wiley, 1989, ISBN: 978-3-527-62012-8. DOI: `10.1002/9783527620128`.

[2] J. Fraden, *Handbook of Modern Sensors: Physics, Designs, and Applications*, 2nd ed. Cham: Springer, 1996, ISBN: 978-3-319-19302-1. DOI: `10.1007/978-3-319-19303-8`.

[3] R. Pallás-Areny and J. G. Webster, *Sensors and Signal Conditioning*. 2012, ISBN: 978-1-118-58593-1.

[4] F. Bernhard, Ed., *Handbuch der technischen Temperaturmessung*, 2nd ed., VDI-Buch, Berlin Heidelberg: Springer Vieweg, 2014, 1619 pp., ISBN: 978-3-642-24505-3. DOI: `10.1007/978-3-642-24506-0`.

[5] A. D'Amico, C. Di Natale, and P. M. Sarro, "Ingredients for sensors science", *Sensors and Actuators B: Chemical*, vol. 207, pp. 1060–1068, Part B 2015. DOI: `10.1016/j.snb.2014.07.065`.

[6] Nobel Media AB. (2004). The Nobel Prize in Physiology or Medicine 2004, [Online]. Available: `https://www.nobelprize.org/prizes/medicine/2004/press-release/` (visited on 02/18/2019).

[7] L. B. Buck, "Unraveling the Sense of Smell (Nobel Lecture)", *Angewandte Chemie International Edition*, vol. 44, no. 38, pp. 6128–6140, 2005. DOI: `10.1002/anie.200501120`.

[8] S. Zozulya, F. Echeverri, and T. Nguyen, "The human olfactory receptor repertoire", *Genome Biology*, vol. 2, no. 6, RESEARCH0018, 2001.

[9] C. Bushdid, M. O. Magnasco, L. B. Vosshall, and A. Keller, "Humans can discriminate more than 1 trillion olfactory stimuli.", *Science*, vol. 343, no. 6177, pp. 1370–2, 2014. DOI: `10.1126/science.1249168`.

[10] U. Stockhorst and R. Pietrowsky, "Olfactory perception, communication, and the nose-to-brain pathway", *Physiology & Behavior*, vol. 83, no. 1, pp. 3–11, 2004. DOI: `10.1016/j.physbeh.2004.07.018`.

[11] J. E. Schwob, "Neural regeneration and the peripheral olfactory system", *The Anatomical Record*, vol. 269, no. 1, pp. 33–49, 2002. DOI: 10.1002/ar.10047.

[12] E. Comini, G. Faglia, and G. Sberveglieri, *Solid State Gas Sensing*. US: Springer, 2009, ISBN: 978-0-387-09664-3. DOI: 10.1007/978-0-387-09665-0.

[13] W. Göpel and K.-D. Schierbaum, "Definitions and Typical Examples", in *Sensors*, W. Göpel, J. Hesse, and J. N. Zemel, Eds., Wiley, 2008, pp. 1–27, ISBN: 978-3-527-62013-5. DOI: 10.1002/9783527620135.ch1.

[14] H.-R. Tränkler and L. Reindl, Eds., *Sensortechnik: Handbuch für Praxis und Wissenschaft*, VDI-Buch, Berlin Heidelberg: Springer Vieweg, 1998, 1584 pp., ISBN: 978-3-642-29941-4. DOI: 10.1007/978-3-642-29942-1.

[15] N. Yamazoe and K. Shimanoe, "Theory of power laws for semiconductor gas sensors", *Sensors and Actuators B: Chemical*, vol. 128, no. 2, pp. 566–573, 2008. DOI: 10.1016/j.snb.2007.07.036.

[16] S. K. Jha and R. D. S. Yadava, "Power Scaling of Chemiresistive Sensor Array Data for Odor Classification", *Journal of Pattern Recognition Research*, vol. 6, no. 1, pp. 65–74, 2011. DOI: 10.13176/11.247.

[17] M. Eriksson, I. Lundström, and L.-G. Ekedahl, "A model of the Temkin isotherm behavior for hydrogen adsorption at Pd–SiO_2 interfaces", *Journal of Applied Physics*, vol. 82, no. 6, pp. 3143–3146, 1997. DOI: 10.1063/1.366158.

[18] J. Vessman, "Selectivity or specificity? Validation of analytical methods from the perspective of an analytical chemist in the pharmaceutical industry", *Journal of Pharmaceutical and Biomedical Analysis*, vol. 14, no. 8-10, pp. 867–869, 1996. DOI: 10.1016/0731-7085(95)01679-1.

[19] J. Vessman, R. I. Stefan, J. F. V. Staden, K. Danzer, W. Lindner, D. T. Burns, A. Fajgelj, and H. Müller, "Selectivity in Analytical Chemistry (IUPAC Recommendations 2001)", *Pure and Applied Chemistry*, vol. 73, no. 8, pp. 1381–1386, 2001. DOI: 10.1351/pac200173081381.

[20] G. Tournier and C. Pijolat, "Selective filter for SnO-based gas sensor: Application to hydrogen trace detection", *Sensors and Actuators B: Chemical*, vol. 106, no. 2, pp. 553–562, 2005. DOI: 10.1016/j.snb.2004.06.037.

[21] A. Hulanicki, S. Glab, and F. Ingman, "Chemical sensors: Definitions and classification", *Pure and Applied Chemistry*, vol. 63, no. 9, pp. 1247–1250, 1991. DOI: 10.1351/pac199163091247.

[22] C.-D. Kohl and T. Wagner, Eds., *Gas Sensing Fundamentals*, red. by G. Urban, vol. 15, Springer Series on Chemical Sensors and Biosensors, Berlin Heidelberg: Springer, 2014, ISBN: 978-3-642-54518-4.

[23] O. W. Johnson, "Gas detection apparatus", Patent no. US2,786,350, 1957.

[24] A. R. Baker, "Apparatus for detecting combustible gases having an electrically conductive member enveloped in a refractory material", Patent no. US3,092,799A, 1963.

[25] S. Amrehn, X. Wu, and T. Wagner, "Tungsten Oxide Photonic Crystals as Optical Transducer for Gas Sensing", *ACS Sensors*, vol. 3, no. 1, pp. 191–199, 2018. DOI: 10.1021/acssensors.7b00845.

[26] C.-H. Hsu, C.-C. Chang, C.-M. Tseng, C.-C. Chan, W.-H. Chao, Y.-R. Wu, M.-H. Wen, Y.-T. Hsieh, Y.-C. Wang, C.-L. Chen, M. J. Wang, and M.-K. Wu, "An ultra-fast response gasochromic device for hydrogen gas detection", *Sensors and Actuators B: Chemical*, vol. 186, pp. 193–198, 2013. DOI: 10.1016/j.snb.2013.06.004.

[27] T. Nash, "The colorimetric estimation of formaldehyde by means of the Hantzsch reaction", *The Biochemical Journal*, vol. 55, no. 3, pp. 416–421, 1953.

[28] M. J. Madou and S. R. Morrison, *Chemical Sensing with Solid State Devices*. San Diego: Academic Press, 1989, ISBN: 0-12-464965-3.

[29] G. Neri, "First Fifty Years of Chemoresistive Gas Sensors", *Chemosensors*, vol. 3, no. 1, pp. 1–20, 2015. DOI: 10.3390/chemosensors3010001.

[30] G. H. Jain, "MOS gas sensors: What determines our choice?", in *2011 Fifth International Conference on Sensing Technology*, Palmerston North, New Zealand: IEEE, 2011, pp. 66–72. DOI: 10.1109/ICSensT.2011.6137067.

[31] M. Andersson, R. Pearce, and A. Lloyd Spetz, "New generation SiC based field effect transistor gas sensors", *Sensors and Actuators B: Chemical*, vol. 179, pp. 95–106, 2013. DOI: 10.1016/j.snb.2012.12.059.

[32] E. Ivers-Tiffée, K. H. Härdtl, W. Menesklou, and J. Riegel, "Principles of solid state oxygen sensors for lean combustion gas control", *Electrochimica Acta*, vol. 47, no. 5, pp. 807–814, 2001. doi: 10.1016/S0013-4686(01)00761-7.

[33] Z. Darmastuti, R. Pearce, A. Lloyd Spetz, and M. Andersson, "The influence of gate bias and structure on the CO sensing performance of SiC based field effect sensors", in *2011 IEEE SENSORS Proceedings*, IEEE, 2011, pp. 133–136, isbn: 978-1-4244-9289-3. doi: 10.1109/ICSENS.2011.6127261.

[34] C. Xu, J. Tamaki, N. Miura, and N. Yamazoe, "Grain size effects on gas sensitivity of porous SnO_2-based elements", *Sensors and Actuators B: Chemical*, vol. 3, no. 2, pp. 147–155, 1991. doi: 10.1016/0925-4005(91)80207-Z.

[35] M. Ulrich, C. D. Kohl, and A. Bunde, "Percolation model of a nanocrystalline gas sensitive layer", *Thin Solid Films*, vol. 391, pp. 299–302, 2001. doi: 10.1016/S0040-6090(01)00999-3.

[36] J. Newman, L. Tigwell, P. Warner, and A. Turner, "Biosensors: Boldly going into the new millennium", *Sensor Review*, vol. 21, no. 4, pp. 268–271, 2001. doi: 10.1108/EUM0000000005999.

[37] I. Lundström, M. S. Shivaraman, and C. M. Svensson, "A hydrogen-sensitive Pd-gate MOS transistor", *Journal of Applied Physics*, vol. 46, no. 9, pp. 3876–3881, 1975. doi: 10.1063/1.322185.

[38] G. Tournier, C. Pijolat, R. Lalauze, and B. Patissier, "Selective detection of CO and CH_4 with gas sensors using SnO_2 doped with palladium", *Sensors and Actuators B: Chemical*, vol. 26, no. 1-3, pp. 24–28, 1995. doi: 10.1016/0925-4005(94)01549-W.

[39] K. Everaert, "Catalytic combustion of volatile organic compounds", *Journal of Hazardous Materials*, vol. 109, no. 1-3, pp. 113–139, 2004. doi: 10.1016/j.jhazmat.2004.03.019.

[40] C. Park, S. Akbar, and J. Hwang, "Selective gas detection with catalytic filter", *Materials Chemistry and Physics*, vol. 75, no. 1-3, pp. 56–60, 2002. doi: 10.1016/S0254-0584(02)00030-5.

[41] C. H. Kwon, D. H. Yun, H.-K. Hong, S.-R. Kim, K. Lee, H. Y. Lim, and K. H. Yoon, "Multi-layered thick-film gas sensor array for selective sensing by catalytic filtering technology", *Sensors and Actuators B: Chemical*, vol. 65, no. 1-3, pp. 327–330, 2000. doi: 10.1016/S0925-4005(99)00426-8.

[42] J. Viricelle, A. Pauly, L. Mazet, J. Brunet, M. Bouvet, C. Varenne, and C. Pijolat, "Selectivity improvement of semi-conducting gas sensors by selective filter for atmospheric pollutants detection", *Materials Science and Engineering: C*, vol. 26, no. 2-3, pp. 186–195, 2006. DOI: 10.1016/j.msec.2005.10.062.

[43] S. M. Cho, Y. J. Kim, G. S. Heo, and S.-M. Shin, "Two-step preconcentration for analysis of exhaled gas of human breath with electronic nose", *Sensors and Actuators B: Chemical*, vol. 117, no. 1, pp. 50–57, 2006. DOI: 10.1016/j.snb.2005.10.050.

[44] M. Leidinger, M. Rieger, T. Sauerwald, C. Alépée, and A. Schütze, "Integrated pre-concentrator gas sensor microsystem for ppb level benzene detection", *Sensors and Actuators B: Chemical*, 2016. DOI: 10.1016/j.snb.2016.04.064.

[45] P. Reimann and A. Schütze, "Sensor Arrays, Virtual Multisensors, Data Fusion, and Gas Sensor Data Evaluation", in *Gas Sensing Fundamentals*, ser. Springer Series on Chemical Sensors and Biosensors, C.-D. Kohl and T. Wagner, Eds., vol. 15, Berlin, Heidelberg: Springer Berlin Heidelberg, 2014, pp. 67–107, ISBN: 978-3-642-54518-4. DOI: 10.1007/5346_2013_52.

[46] D. Kohl, J. Kelleter, and H. Petig, "Detection of Fires by Gas Sensors", *Sensors Update*, vol. 9, no. 1, pp. 161–223, 2001. DOI: 10.1002/1616-8984(200105)9:1<161::AID-SEUP161>3.0.CO;2-A.

[47] J. Fonollosa, A. Solórzano, J. Jiménez-Soto, S. Oller-Moreno, and S. Marco, "Gas Sensor Array for Reliable Fire Detection", *Procedia Engineering*, vol. 168, pp. 444–447, 2016. DOI: 10.1016/j.proeng.2016.11.540.

[48] T. Maekawa, K. Suzuki, and T. Takada, "Odor identification using a SnO_2- based sensor array", *Sensors and Actuators B: Chemical*, vol. 80, no. 1, pp. 51–58, 2001. DOI: 10.1016/S0925-4005(01)00885-1.

[49] D. L. A. Fernandes and M. T. S. R. Gomes, "Development of an electronic nose to identify and quantify volatile hazardous compounds", *Talanta*, vol. 77, no. 1, pp. 77–83, 2008. DOI: 10.1016/j.talanta.2008.05.042.

[50] S. Zampolli, I. Elmi, F. Ahmed, M. Passini, G. C. Cardinali, S. Nicoletti, and L. Dori, "An electronic nose based on solid state sensor arrays for low-cost indoor air quality monitoring applications", *Sensors and Actuators B: Chemical*, vol. 101, no. 1-2, pp. 39–46, 2004. DOI: 10.1016/j.snb.2004.02.024.

[51] J. W. Gardner and P. N. Bartlett, "A brief history of electronic noses", *Sensors and Actuators B: Chemical*, vol. 18, no. 1-3, pp. 210–211, 1994. DOI: `10.1016/0925-4005(94)87085-3`.

[52] A. Shaposhnik, P. Moskalev, A. Zviagin, K. Chegereva, S. Ryabtsev, A. Vasiliev, and P. Shaposhnik, "Selective Gas Detection by a Single MOX-Sensor", *Proceedings*, vol. 1, no. 4, pp. 594–594, 2017. DOI: `10.3390/proceedings1040594`.

[53] J. Fonollosa, A. Vergara, and R. Huerta, "Algorithmic mitigation of sensor failure: Is sensor replacement really necessary?", *Sensors and Actuators B: Chemical*, vol. 183, pp. 211–221, 2013. DOI: `10.1016/j.snb.2013.03.034`.

[54] A. Vergara, S. Vembu, T. Ayhan, M. A. Ryan, M. L. Homer, and R. Huerta, "Chemical gas sensor drift compensation using classifier ensembles", *Sensors and Actuators B: Chemical*, vol. 166-167, pp. 320–329, 2012. DOI: `10.1016/j.snb.2012.01.074`.

[55] A. Ziyatdinov, S. Marco, A. Chaudry, K. Persaud, P. Caminal, and A. Perera, "Drift compensation of gas sensor array data by common principal component analysis", *Sensors and Actuators B: Chemical*, vol. 146, no. 2, pp. 460–465, 2010. DOI: `10.1016/j.snb.2009.11.034`.

[56] A. Schütze, A. Gramm, and T. Rühl, "Identification of organic solvents by a virtual multisensor system with hierarchical classification", *IEEE Sensors Journal*, vol. 4, no. 6, pp. 857–863, 2004. DOI: `10.1109/JSEN.2004.833514`.

[57] A. P. Lee and B. J. Reedy, "Temperature modulation in semiconductor gas sensing", *Sensors and Actuators B: Chemical*, vol. 60, no. 1, pp. 35–42, 1999. DOI: `10.1016/S0925-4005(99)00241-5`.

[58] C. Schultealbert, T. Baur, A. Schütze, and T. Sauerwald, "Facile Quantification and Identification Techniques for Reducing Gases over a Wide Concentration Range Using a MOS Sensor in Temperature-Cycled Operation", *Sensors*, vol. 18, no. 3, 2018. DOI: `10.3390/s18030744`.

[59] T. Baur, A. Schütze, and T. Sauerwald, "Detection of short gas pulses for trace gas analysis", *tm - Technisches Messen*, vol. 84, no. s1, pp. 88–92, 2017. DOI: `10.1515/teme-2017-0035`.

[60] H. Eicker, "Method and apparatus for determining the concentration of one gaseous component in a mixture of gases", Patent no. US4,012,692A, 1977.

[61] M. Engel, M. Baumbach, T. Kammerer, and A. Schütze, "Preparation of microstructured pellistors and their application for fast fuel vapor discrimination", in *17th IEEE International Conference on Micro Electro Mechanical Systems. Maastricht MEMS 2004 Technical Digest*, Maastricht, Netherlands: IEEE, 2004, pp. 268–271, ISBN: 978-0-7803-8265-7. DOI: `10.1109/MEMS.2004.1290574`.

[62] C. Bur, M. Bastuck, D. Puglisi, A. Schütze, A. Lloyd Spetz, and M. Andersson, "Discrimination and quantification of volatile organic compounds in the ppb-range with gas sensitive SiC-FETs using multivariate statistics", *Sensors and Actuators B: Chemical*, vol. 214, pp. 1–9, 2015. DOI: `10.1016/j.snb.2015.03.016`.

[63] C. Bur, M. Bastuck, A. Lloyd Spetz, M. Andersson, and A. Schütze, "Selectivity enhancement of SiC-FET gas sensors by combining temperature and gate bias cycled operation using multivariate statistics", *Sensors and Actuators B: Chemical*, vol. 193, 2014. DOI: `10.1016/j.snb.2013.12.030`.

[64] M. Bastuck, A. Schütze, and T. Sauerwald, "A new approach to self-monitoring of amperometric oxygen sensors", *Sensors and Actuators B: Chemical*, vol. 214, pp. 218–224, 2015. DOI: `10.1016/j.snb.2015.02.116`.

[65] F. Xu and H.-P. Ho, "Light-Activated Metal Oxide Gas Sensors: A Review", *Micromachines*, vol. 8, no. 11, p. 333, 2017. DOI: `10.3390/mi8110333`.

[66] N. Markiewicz, O. Casals, C. Fabrega, H. S. Wasisto, A. Waag, and J. D. Prades, "An LED Platform for Micropower Gas Sensors", *Proceedings*, vol. 2, no. 13, p. 971, 2018. DOI: `10.3390/proceedings2130971`.

[67] O. Gonzalez, T. Welearegay, E. Llobet, and X. Vilanova, "Pulsed UV Light Activated Gas Sensing in Tungsten Oxide Nanowires", *Procedia Engineering*, vol. 168, pp. 351–354, 2016. DOI: `10.1016/j.proeng.2016.11.118`.

[68] S. Capone, A. Forleo, L. Francioso, R. Rella, P. Siciliano, J. Spadavecchia, D. S. Presicce, and A. M. Taurino, "Solid State Gas Sensors: State of the Art and Future Activities", *ChemInform*, vol. 35, no. 29, 2004. DOI: `10.1002/chin.200429283`.

[69] N. Taguchi, "Gas detecting element and method of making it", Patent no. US3,644,795A, 1972.

[70] T. Seiyama and N. Yamazoe, “Recent Advances in Gas Sensors in Japan”, in *Fundamentals and Applications of Chemical Sensors*, D. Schuetzle and R. Hammerle, Eds., vol. 309, Washington, DC: American Chemical Society, 1986, pp. 39–55, ISBN: 978-0-8412-0973-2. DOI: `10.1021/bk-1986-0309.ch002`.

[71] A. Kumar, T. M. G. Kingson, R. P. Verma, A. Kumar, R. Mandal, S. Dutta, S. K. Chaulya, and G. M. Prasad, “Application of Gas Monitoring Sensors in Underground Coal Mines and Hazardous Areas”, vol. 3, no. 3, p. 15, 2013.

[72] W. Nellißen, “Vorrichtung zum wiederholten Anzeigen Schlagwettern”, Patent no. DE449502, 1927.

[73] D. Kohl, “Function and applications of gas sensors”, *Journal of Physics D: Applied Physics*, vol. 34, no. 19, R125–R149, 2001. DOI: `10.1088/0022-3727/34/19/201`.

[74] M. T. Soo, K. Y. Cheong, and A. F. M. Noor, “Advances of SiC-based MOS capacitor hydrogen sensors for harsh environment applications”, *Sensors and Actuators B: Chemical*, vol. 151, no. 1, pp. 39–55, 2010. DOI: `10.1016/j.snb.2010.09.059`.

[75] B. Sharma, A. Sharma, and J.-S. Kim, “Recent advances on H_2 sensor technologies based on MOX and FET devices: A review”, *Sensors and Actuators B: Chemical*, vol. 262, pp. 758–770, 2018. DOI: `10.1016/j.snb.2018.01.212`.

[76] P. Reimann and A. Schütze, “Fire detection in coal mines based on semiconductor gas sensors”, *Sensor Review*, vol. 32, no. 1, pp. 47–58, 2012. DOI: `10.1108/02602281211197143`.

[77] M. Nilsson and P. van Hees, “Advantages and challenges with using hypoxic air venting as fire protection”, *Fire and Materials*, vol. 38, no. 5, pp. 559–575, 2014. DOI: `10.1002/fam.2197`.

[78] R. Ramamoorthy, P. K. Dutta, and S. A. Akbar, “Oxygen sensors: Materials, methods, designs”, *Journal of Materials Science*, vol. 38, no. 21, pp. 4271–4282, 2003. DOI: `10.1023/A:1026370729205`.

[79] S. S. Yoon, “Deaths From Unintentional Carbon Monoxide Poisoning and Potential for Prevention With Carbon Monoxide Detectors”, *JAMA*, vol. 279, no. 9, p. 685, 1998. DOI: `10.1001/jama.279.9.685`.

[80] T. Nandy, R. Coutu, and C. Ababei, “Carbon Monoxide Sensing Technologies for Next-Generation Cyber-Physical Systems”, *Sensors*, vol. 18, no. 10, p. 3443, 2018. DOI: `10.3390/s18103443`.

[81] N. Yamazoe, "Toward innovations of gas sensor technology", *Sensors and Actuators B: Chemical*, vol. 108, no. 1-2, pp. 2–14, 2005. DOI: `10.1016/j.snb.2004.12.075`.

[82] C. Yu, Q. Hao, S. Saha, L. Shi, X. Kong, and Z. L. Wang, "Integration of metal oxide nanobelts with microsystems for nerve agent detection", *Applied Physics Letters*, vol. 86, no. 6, p. 063 101, 2005. DOI: `10.1063/1.1861133`.

[83] A. A. Tomchenko, G. P. Harmer, and B. T. Marquis, "Detection of chemical warfare agents using nanostructured metal oxide sensors", *Sensors and Actuators B: Chemical*, vol. 108, no. 1-2, pp. 41–55, 2005. DOI: `10.1016/j.snb.2004.11.059`.

[84] J. W. Schwank and M. DiBattista, "Oxygen Sensors: Materials and Applications", *MRS Bulletin*, vol. 24, no. 6, pp. 44–48, 1999. DOI: `10.1557/S0883769400052507`.

[85] M. Koebel, M. Elsener, and T. Marti, "NOx -Reduction in Diesel Exhaust Gas with Urea and Selective Catalytic Reduction", *Combustion Science and Technology*, vol. 121, no. 1-6, pp. 85–102, 1996. DOI: `10.1080/00102209608935588`.

[86] M. Koebel, M. Elsener, and M. Kleemann, "Urea-SCR: A promising technique to reduce NO_x emissions from automotive diesel engines", *Catalysis Today*, vol. 59, no. 3-4, pp. 335–345, 2000. DOI: `10.1016/S0920-5861(00)00299-6`.

[87] P. Forzatti, L. Lietti, I. Nova, and E. Tronconi, "Diesel NOx aftertreatment catalytic technologies: Analogies in LNT and SCR catalytic chemistry", *Catalysis Today*, vol. 151, no. 3-4, pp. 202–211, 2010. DOI: `10.1016/j.cattod.2010.02.025`.

[88] L. Uneus, T. Artursson, M. Mattsson, P. Ljung, R. Wigren, P. Martensson, M. Holmberg, I. Lundstrom, and A. Lloyd Spetz, "Evaluation of on-line flue gas measurements by MISiCFET and metal-oxide sensors in boilers", *IEEE Sensors Journal*, vol. 5, no. 1, pp. 75–81, 2005. DOI: `10.1109/JSEN.2004.839132`.

[89] Z. Darmastuti, C. Bur, P. Möller, R. Rahlin, N. Lindqvist, M. Andersson, A. Schütze, and A. Lloyd Spetz, "SiC-FET based SO_2 sensor for power plant emission applications", *Sensors and Actuators B: Chemical*, vol. 194, pp. 511–520, 2014. DOI: `10.1016/j.snb.2013.11.089`.

[90] R. Menzel and J. Goschnick, "Gradient gas sensor microarrays for on-line process control — a new dynamic classification model for fast and reliable air quality assessment", *Sensors and Actuators B: Chemical*, vol. 68, no. 1-3, pp. 115–122, 2000. DOI: 10.1016/S0925-4005(00)00470-6.

[91] M. Marth, D. Maier, J. Honerkamp, M. Rupprecht, and J. Goschnick, "Early transition detection-A dynamic extension to common classification methods", *Chemometrics and Intelligent Laboratory Systems*, vol. 43, no. 1-2, pp. 123–133, 1998. DOI: 10.1016/S0169-7439(98)00081-1.

[92] N. E. Klepeis, W. C. Nelson, W. R. Ott, J. P. Robinson, A. M. Tsang, P. Switzer, J. V. Behar, S. C. Hern, and W. H. Engelmann, "The National Human Activity Pattern Survey (NHAPS): A resource for assessing exposure to environmental pollutants.", *Journal of Exposure Analysis and Environmental Epidemiology*, vol. 11, no. 3, pp. 231–252, 2001. DOI: 10.1038/sj.jea.7500165.

[93] World Health Organization, Regional Office for Europe, *Air Quality Guidelines for Europe*, 2nd ed, ser. WHO Regional Publications 91. Copenhagen, 2000, 273 pp., ISBN: 978-92-890-1358-1.

[94] WHO Regional Office for Europe, *WHO Guidelines for Indoor Air Quality*. Geneva, 2010, vol. 9, 454 pp., ISBN: 978 92 890 0213 4. DOI: 10.1186/2041-1480-2-S2-I1.

[95] S. Sillman, "The relation between ozone, NO_x and hydrocarbons in urban and polluted rural environments", *Atmospheric Environment*, vol. 33, no. 12, pp. 1821–1845, 1999. DOI: 10.1016/S1352-2310(98)00345-8.

[96] D. J. Jacob, E. G. Heikes, S.-M. Fan, J. A. Logan, D. L. Mauzerall, J. D. Bradshaw, H. B. Singh, G. L. Gregory, R. W. Talbot, D. R. Blake, and G. W. Sachse, "Origin of ozone and NO_x in the tropical troposphere: A photochemical analysis of aircraft observations over the South Atlantic basin", *Journal of Geophysical Research: Atmospheres*, vol. 101, no. D19, pp. 24 235–24 250, 1996. DOI: 10.1029/96JD00336.

[97] World Health Organization, Ed., *Nitrogen Oxides*, 2nd ed., Environmental Health Criteria 188, Geneva, 1997, 550 pp., ISBN: 978-92-4-157188-3.

[98] L. Mølhave, "Volatile organic compounds, indoor air quality and health", *Indoor Air*, vol. 1, no. 4, pp. 357–376, 1991. DOI: 10.1111/j.1600-0668.1991.00001.x.

[99] IARC Working Group on the Evaluation of Carcinogenic Risk to Humans, "Formaldehyde, 2-Butoxyethanol and 1-tert-Butoxypropan-2-ol", *IARC Monographs on the Evaluation of Carcinogenic Risks to Humans*, vol. 88, I. A. for Research on Cancer, Ed., 2006.

[100] B. Clarisse, A. M. Laurent, N. Seta, Y. Le Moullec, A. El Hasnaoui, and I. Momas, "Indoor aldehydes: Measurement of contamination levels and identification of their determinants in Paris dwellings", *Environmental Research*, vol. 92, no. 3, pp. 245–253, 2003. DOI: `10.1016/S0013-9351(03)00039-2`.

[101] H. Neumann, M. Buxtrup, S. Benitez, and J. Hahn, "VOC- und Aldehydkonzentrationen in beschwerdefreien Klassenräumen unter unterschiedlichen Nutzungs- und Lüftungsbedingungen", vol. 74, no. 3, pp. 85–94, 2014.

[102] H. Schleibinger, U. Hott, D. Marchl, P. Braun, P. Plieninger, and H. Rüden, "VOC-concentrations in Berlin indoor environments between 1988 and 1999", *Gefahrstoffe - Reinhaltung der Luft*, no. 1/2, pp. 26–26, 2001.

[103] K. Koistinen, D. Kotzias, S. Kephalopoulos, C. Schlitt, P. Carrer, M. Jantunen, S. Kirchner, J. McLaughlin, L. Mølhave, E. O. Fernandes, and B. Seifert, "The INDEX project: Executive summary of a European Union project on indoor air pollutants", *Allergy: European Journal of Allergy and Clinical Immunology*, vol. 63, no. 7, pp. 810–819, 2008. DOI: `10.1111/j.1398-9995.2008.01740.x`.

[104] US Environmental Protection Agency, "Sick building syndrome.", 4, 1993.

[105] P. Wolkoff, P. A. Clausen, B. Jensen, G. D. Nielsen, and C. K. Wilkins, "Are We Measuring the Relevant Indoor Pollutants?", *Indoor Air*, vol. 7, no. 2, pp. 92–106, 1997. DOI: `10.1111/j.1600-0668.1997.t01-2-00003.x`.

[106] X. Chen, F. Li, C. Liu, J. Yang, J. Zhang, and C. Peng, "Monitoring, Human Health Risk Assessment and Optimized Management for Typical Pollutants in Indoor Air from Random Families of University Staff, Wuhan City, China", *Sustainability*, vol. 9, no. 7, p. 1115, 2017. DOI: `10.3390/su9071115`.

[107] WHO Regional Office for Europe, "Indoor air quality: Organic pollutants", Copenhagen, 1989.

[108] The European Parliament and the Council of the European Union, “Directive 2004/42/CE of the European Parliament and of the Council of 21 April 2004 on the limitation of emissions of volatile organic compounds due to the use of organic solvents in certain paints and varnishes and vehicle refinishing products and amending Directive 1999/13/EC”, *Official Journal of the European Union*, vol. L143, no. 47, pp. 87–96, 2004.

[109] The Council of the European Union, “Council Directive 1999/13/EC of 11 March 1999 on the limitation of emissions of volatile organic compounds due to the use of organic solvents in certain activities and installations”, *Official Journal of the European Communities*, vol. L85, no. 42, pp. 1–22, 1999.

[110] Australian Government/Department of the Environment, Water, Heritage and the Arts, *NPI Volatile Organic Compound definition and information*, 2009.

[111] US Environmental Protection Agency, *40 CFR Part 51, Subpart F - Procedural Requirements*, 2018.

[112] B. Seifert, “Richtwerte für die Innenraumluft: Die Beurteilung der Innenraumlufqualität mit Hilfe der Summe der flüchtigen organischen Verbindungen (TVOC-Wert)”, *Bundesgesundheitsblatt - Gesundheitsforschung - Gesundheitsschutz*, vol. 42, no. 3, pp. 270–278, 1999.

[113] L. Mølhave, B. Bach, and O. F. Pedersen, “Human reactions to low concentrations of volatile organic compounds”, *Environment International*, vol. 12, no. 1-4, pp. 167–175, 1986. DOI: 10.1016/0160-4120(86)90027-9.

[114] L. Mølhave and G. D. Nielsen, “Interpretation and limitations of the concept “Total volatile organic compounds”(TVOC) as an indicator of human responses to exposures of volatile organic compounds (VOC) in indoor air”, *Indoor Air*, vol. 2, no. 2, pp. 65–77, 1992.

[115] B. Berglund, G. Clausen, J. de Ceaurriz, A. Kettrup, T. Lindvall, M. Maroni, L. Mølhave, A. C. Pickering, U. Risse, H. Rothweiler, B. Seifert, and M. Younes, *Total Volatile Organic Compounds (TVOC) in Indoor Air Quality Investigations*, ser. European Collaborative Action Indoor Air Quality & Its Impact on Man EUR 17675. Luxembourg: Office for Official Publications of the European Communities, 1997, vol. 19, 46 pp., ISBN: 978-92-828-1078-1.

[116] International Organization for Standardization, Ed., *Indoor Air - Part 6: Determination of volatile organic compounds in indoor and test chamber air by active sampling Tenax TA(R) sorbent, thermal desorption and gas chromatography using MS/FID (ISO 16000-6.2011)*, 2011.

[117] M. Jin, N. Bekiaris-Liberis, K. Weekly, C. J. Spanos, and A. M. Bayen, "Occupancy Detection via Environmental Sensing", *IEEE Transactions on Automation Science and Engineering*, vol. 15, no. 2, pp. 443–455, 2018. DOI: `10.1109/TASE.2016.2619720`.

[118] S. Herberger and H. Ulmer, "New IAQ sensor for demand controlled ventilation", *REHVA Journal*, 2012.

[119] T. M. Hellman and F. H. Small, "Characterization of the Odor Properties of 101 Petrochemicals Using Sensory Methods", *Journal of the Air Pollution Control Association*, vol. 24, no. 10, pp. 979–982, 1974. DOI: `10.1080/00022470.1974.10470005`.

[120] R. Lebrero, L. Bouchy, R. Stuetz, and R. Muñoz, "Odor Assessment and Management in Wastewater Treatment Plants: A Review", *Critical Reviews in Environmental Science and Technology*, vol. 41, no. 10, pp. 915–950, 2011. DOI: `10.1080/10643380903300000`.

[121] J.-J. Fang, N. Yang, D.-Y. Cen, L.-M. Shao, and P.-J. He, "Odor compounds from different sources of landfill: Characterization and source identification", *Waste Management*, vol. 32, no. 7, pp. 1401–1410, 2012. DOI: `10.1016/j.wasman.2012.02.013`.

[122] R. W. Melse and N. W. M. Ogink, "Air scrubbing techniques for ammonia and odor reduction at livestock operations: Review of on-farm research in the Netherlands", *Transactions of the ASAE*, vol. 48, no. 6, pp. 2303–2313, 2005. DOI: `10.13031/2013.20094`.

[123] J. H. Ruth, "Odor thresholds and irritation levels of several chemical substances: A review.", *American Industrial Hygiene Association Journal*, vol. 47, no. 3, A142–A151, 1986. DOI: `10.1080/15298668691389595`.

[124] "Air quality - Determination of odour concentration by dynamic olfactometry", European Committee for Standardization, EN 13725:2003, 2003.

[125] "Ambient air - Determination of odour in ambient air by using field inspection - Part 1: Grid method", European Committee for Standardization, EN 16841-1:2016, 2016.

[126] "Ambient air - Determination of odour in ambient air by using field inspection - Part 2: Plume method", European Committee for Standardization, EN 16841-2:2016, 2016.

[127] K. Suzuki and T. Takada, "Highly sensitive odour sensors using various SnO_2 thick films", *Sensors and Actuators B: Chemical*, vol. 25, no. 1-3, pp. 773–776, 1995. DOI: `10.1016/0925-4005(95)85171-2`.

[128] H. Ulmer, J. Mitrovics, G. Noetzel, U. Weimar, and W. Göpel, "Odours and flavours identified with hybrid modular sensor systems", *Sensors and Actuators B: Chemical*, vol. 43, no. 1-3, pp. 24–33, 1997. DOI: `10.1016/S0925-4005(97)00161-5`.

[129] H. V. Shurmer and J. W. Gardner, "Odour discrimination with an electronic nose", *Sensors and Actuators B: Chemical*, vol. 8, no. 1, pp. 1–11, 1992. DOI: `10.1016/0925-4005(92)85001-D`.

[130] J. Gardner, H. Shurmer, and T. Tan, "Application of an electronic nose to the discrimination of coffees", *Sensors and Actuators B: Chemical*, vol. 6, no. 1-3, pp. 71–75, 1992. DOI: `10.1016/0925-4005(92)80033-T`.

[131] R. Gutierrez-Osuna and H. T. Nagle, "A method for evaluating data-preprocessing techniques for odor classification with an array of gas sensors", *IEEE Transactions on Systems, Man, and Cybernetics, Part B: Cybernetics*, vol. 29, no. 5, pp. 626–632, 1999. DOI: `10.1109/3477.790446`.

[132] B. Buszewski, J. Rudnicka, T. Ligor, M. Walczak, T. Jezierski, and A. Amann, "Analytical and unconventional methods of cancer detection using odor", *TrAC Trends in Analytical Chemistry*, vol. 38, pp. 1–12, 2012. DOI: `10.1016/j.trac.2012.03.019`.

[133] E. Boedeker, G. Friedel, and T. Walles, "Sniffer dogs as part of a bimodal bionic research approach to develop a lung cancer screening", *Interactive CardioVascular and Thoracic Surgery*, vol. 14, no. 5, pp. 511–515, 2012. DOI: `10.1093/icvts/ivr070`.

[134] M. Leja, H. Liu, and H. Haick, "Breath testing: The future for digestive cancer detection", *Expert Review of Gastroenterology & Hepatology*, vol. 7, no. 5, pp. 389–391, 2013. DOI: `10.1586/17474124.2013.811033`.

[135] J.-N. Cornu, G. Cancel-Tassin, V. Ondet, C. Girardet, and O. Cussenot, "Olfactory Detection of Prostate Cancer by Dogs Sniffing Urine: A Step Forward in Early Diagnosis", *European Urology*, vol. 59, no. 2, pp. 197–201, 2011. DOI: `10.1016/j.eururo.2010.10.006`.

[136] C. M. Willis, S. M. Church, C. M. Guest, W. A. Cook, N. McCarthy, A. J. Bransbury, M. R. T. Church, and J. C. T. Church, “Olfactory detection of human bladder cancer by dogs: Proof of principle study”, *BMJ*, vol. 329, no. 7468, p. 712, 2004. DOI: 10.1136/bmj.329.7468.712.

[137] A. Catala, M. Grandgeorge, J.-L. Schaff, H. Cousillas, M. Hausberger, and J. Cattet, “Dogs demonstrate the existence of an epileptic seizure odour in humans”, *Scientific Reports*, vol. 9, no. 1, 2019. DOI: 10.1038/s41598-019-40721-4.

[138] Z. Wang and C. Wang, “Is breath acetone a biomarker of diabetes? A historical review on breath acetone measurements”, *Journal of Breath Research*, vol. 7, no. 3, p. 037 109, 2013. DOI: 10.1088/1752-7155/7/3/037109.

[139] M. Righettoni, A. Tricoli, and S. E. Pratsinis, “Thermally stable, silica-doped epsilon-WO_3 for sensing of acetone in the human breath”, *Chemistry of Materials*, vol. 22, no. 10, pp. 3152–3157, 2010. DOI: 10.1021/cm1001576.

[140] C. Di Natale, R. Paolesse, E. Martinelli, and R. Capuano, “Solid-state gas sensors for breath analysis: A review”, *Analytica Chimica Acta*, vol. 824, pp. 1–17, 2014. DOI: 10.1016/j.aca.2014.03.014.

[141] K. Kalantar-Zadeh, K. J. Berean, N. Ha, A. F. Chrimes, K. Xu, D. Grando, J. Z. Ou, N. Pillai, J. L. Campbell, R. Brkljača, K. M. Taylor, R. E. Burgell, C. K. Yao, S. A. Ward, C. S. McSweeney, J. G. Muir, and P. R. Gibson, “A human pilot trial of ingestible electronic capsules capable of sensing different gases in the gut”, *Nature Electronics*, vol. 1, no. 1, pp. 79–79, 2018. DOI: 10.1038/s41928-017-0004-x.

[142] R. Gutierrez-Osuna, “Pattern analysis for machine olfaction: A review”, *IEEE Sensors Journal*, vol. 2, no. 3, pp. 189–202, 2002. DOI: 10.1109/JSEN.2002.800688.

[143] S. Marco and A. Gutierrez-Galvez, “Signal and data processing for machine olfaction and chemical sensing: A review”, *IEEE Sensors Journal*, vol. 12, no. 11, pp. 3189–3214, 2012. DOI: 10.1109/JSEN.2012.2192920.

[144] T. Hastie, R. Tibshirani, and J. Friedman, *The Elements of Statistical Learning*, ser. Springer Series in Statistics. New York: Springer, 2009, vol. 1, 337 pp., ISBN: 978-0-387-84857-0. DOI: 10.1007/978-0-387-84858-7.

[145] A. Gramm and A. Schütze, "High performance solvent vapor identification with a two sensor array using temperature cycling and pattern classification", *Sensors and Actuators B: Chemical*, vol. 95, no. 1-3, pp. 58–65, 2003. doi: `10.1016/S0925-4005(03)00404-0`.

[146] C. Böhm, S. Berchtold, and D. Keim, "Searching in high-dimensional spaces: Index structures for improving the performance of multimedia databases", *ACM Computing Surveys*, vol. 33, no. 3, pp. 322–373, 2001. doi: `10.1145/502807.502809`.

[147] R. T. Olszewski, "Generalized Feature Extraction for Structural Pattern Recognition in Time-Series Data", Dissertation, School of Computer Science, Pittsburgh, USA, 2001.

[148] T. Schneider, N. Helwig, and A. Schütze, "Industrial condition monitoring with smart sensors using automated feature extraction and selection", *Measurement Science and Technology*, vol. 29, no. 9, p. 094 002, 2018. doi: `10.1088/1361-6501/aad1d4`.

[149] N. Helwig, E. Pignanelli, and A. Schütze, "Condition monitoring of a complex hydraulic system using multivariate statistics", in *2015 IEEE International Instrumentation and Measurement Technology Conference (I2MTC) Proceedings*, IEEE, 2015, pp. 210–215, isbn: 978-1-4799-6114-6. doi: `10.1109/I2MTC.2015.7151267`.

[150] S. Gomri, T. Contaret, and J.-L. Seguin, "A New Gases Identifying Method With MOX Gas Sensors Using Noise Spectroscopy", *IEEE Sensors Journal*, vol. 18, no. 16, pp. 6489–6496, 2018. doi: `10.1109/JSEN.2018.2850817`.

[151] H. Sanz, C. Valim, E. Vegas, J. M. Oller, and F. Reverter, "SVM-RFE: Selection and visualization of the most relevant features through non-linear kernels", *BMC Bioinformatics*, vol. 19, no. 1, 2018. doi: `10.1186/s12859-018-2451-4`.

[152] I. Kononenko, E. Šimec, and M. Robnik-Šikonja, "Overcoming the Myopia of Inductive Learning Algorithms with RELIEFF", *Applied Intelligence*, vol. 7, no. 1, pp. 39–55, 1997. doi: `10.1023/A:1008280620621`.

[153] R. Fisher, "The Use of Multiple Measurements in Taxonomic Problems", *Annals of Eugenics*, vol. 7, pp. 179–188, 1936. doi: `10.1111/j.1469-1809.1936.tb02137.x`.

[154] M. A. Pimentel, D. A. Clifton, L. Clifton, and L. Tarassenko, "A review of novelty detection", *Signal Processing*, vol. 99, pp. 215–249, 2014. doi: `10.1016/j.sigpro.2013.12.026`.

[155] Xing Su, Hanghang Tong, and Ping Ji, "Activity recognition with smartphone sensors", *Tsinghua Science and Technology*, vol. 19, no. 3, pp. 235–249, 2014. DOI: 10.1109/TST.2014.6838194.

[156] J. D. Olden and D. A. Jackson, "Illuminating the "black box": A randomization approach for understanding variable contributions in artificial neural networks", *Ecological Modelling*, vol. 154, no. 1-2, pp. 135–150, 2002. DOI: 10.1016/S0304-3800(02)00064-9.

[157] S. Wold, M. Sjöström, and L. Eriksson, "PLS-regression: A basic tool of chemometrics", *Chemometrics and Intelligent Laboratory Systems*, vol. 58, no. 2, pp. 109–130, 2001. DOI: 10.1016/S0169-7439(01)00155-1.

[158] H. Zou and T. Hastie, "Regularization and variable selection via the elastic net", *Journal of the Royal Statistical Society. Series B: Statistical Methodology*, vol. 67, no. 2, pp. 301–320, 2005. DOI: 10.1111/j.1467-9868.2005.00503.x.

[159] R. Tibshirani, "Regression Selection and Shrinkage via the Lasso", *Journal of the Royal Statistical Society B*, vol. 58, no. 1, pp. 267–288, 1994. DOI: 10.2307/2346178.

[160] A. E. Hoerl and R. W. Kennard, "Ridge Regression: Biased Estimation for Nonorthogonal Problems", *Technometrics*, vol. 42, no. 1, pp. 80–86, 2000. DOI: 10.1080/00401706.1970.10488634.

[161] R. Kohavi, "A Study of Cross-Validation and Bootstrap for Accuracy Estimation and Model Selection", *International Joint Conference on Artificial Intelligence*, vol. 14, pp. 1137–1143, 1995. DOI: 10.1067/mod.2000.109031.

[162] G. Vanwinckelen and H. Blockeel, "On Estimating Model Accuracy with Repeated Cross-Validation", in *BeneLearn 2012: Proceedings of the 21st Belgian-Dutch Conference on Machine Learning*, 2012, pp. 39–44.

[163] T. Baur, A. Schütze, and T. Sauerwald, "Optimierung des temperaturzyklischen Betriebs von Halbleitergassensoren", *tm - Technisches Messen*, vol. 82, no. 4, pp. 187–195, 2015. DOI: 10.1515/teme-2014-0007.

[164] C. Schultealbert, T. Baur, A. Schütze, S. Böttcher, and T. Sauerwald, "A novel approach towards calibrated measurement of trace gases using metal oxide semiconductor sensors", *Sensors and Actuators B: Chemical*, vol. 239, pp. 390–396, 2017. DOI: 10.1016/j.snb.2016.08.002.

[165] S. Lapuschkin, S. Wäldchen, A. Binder, G. Montavon, W. Samek, and K.-R. Müller, “Unmasking Clever Hans predictors and assessing what machines really learn”, *Nature Communications*, vol. 10, no. 1, p. 1096, 2019. DOI: `10.1038/s41467-019-08987-4`.

[166] M. Bastuck, *DAV^{3}E*, version 1902, Zenodo, 2019. DOI: `10.5281/zenodo.2634024`.

[167] M. Bastuck, T. Baur, and A. Schütze, “DAV^{3}E – a MATLAB toolbox for multivariate sensor data evaluation”, *Journal of Sensors and Sensor Systems*, vol. 7, no. 2, pp. 489–506, 2018. DOI: `10.5194/jsss-7-489-2018`.

[168] T. Schneider, N. Helwig, and A. Schütze, “Automatic feature extraction and selection for condition monitoring and related datasets”, in *2018 IEEE International Instrumentation and Measurement Technology Conference (I2MTC)*, Houston, TX, USA: IEEE, 2018, pp. 1–6, ISBN: 978-1-5386-2222-3. DOI: `10.1109/I2MTC.2018.8409763`.

[169] P. Boilot, E. L. Hines, M. A. Gongora, and R. S. Folland, “Electronic noses inter-comparison, data fusion and sensor selection in discrimination of standard fruit solutions”, *Sensors and Actuators B: Chemical*, vol. 88, no. 1, pp. 80–88, 2003. DOI: `10.1016/S0925-4005(02)00313-1`.

[170] L. Armesto, S. Chroust, M. Vincze, and J. Tornero, “Multi-rate fusion with vision and inertial sensors”, *IEEE International Conference on Robotics and Automation, 2004. Proceedings. ICRA ’04. 2004*, vol. 1, pp. 193–199, 2004. DOI: `10.1109/ROBOT.2004.1307150`.

[171] L. P. Yan, B. S. Liu, and D. H. Zhou, “The modeling and estimation of asynchronous multirate multisensor dynamic systems”, *Aerospace Science and Technology*, vol. 10, no. 1, pp. 63–71, 2006. DOI: `10.1016/j.ast.2005.09.001`.

[172] S. Haykin, Ed., *Kalman Filtering and Neural Networks*, Wiley, 2001, ISBN: 978-0-471-22154-8. DOI: `10.1002/0471221546`.

[173] M. Bastuck, T. Baur, and A. Schütze, “Fusing cyclic sensor data with different cycle length”, in *IEEE International Conference on Multisensor Fusion and Integration for Intelligent Systems*, 2017, ISBN: 978-1-4673-9708-7. DOI: `10.1109/MFI.2016.7849469`.

[174] R. a van den Berg, H. C. J. Hoefsloot, J. a Westerhuis, A. K. Smilde, and M. J. van der Werf, “Centering, scaling, and transformations: Improving the biological information content of metabolomics data.”, *BMC genomics*, vol. 7, pp. 142–142, 2006. doi: `10.1186/1471-2164-7-142`.

[175] S. Wold, K. Esbensen, and P. Geladi, “Principal component analysis”, *Chemometrics and Intelligent Laboratory Systems*, vol. 2, no. 1-3, pp. 37–52, 1987. doi: `10.1016/0169-7439(87)80084-9`.

[176] J. Bergstra and Y. Bengio, “Random Search for Hyper-Parameter Optimization”, *Journal of Machine Learning Research*, vol. 13, pp. 281–305, 2012, ACMID: 2188395.

[177] H. Delgado, X. Anguera, C. Fredouille, and J. Serrano, “Novel Clustering Selection Criterion for Fast Binary Key Speaker Diarization”, 2015. doi: `10.13140/rg.2.1.3073.2886`.

[178] H. Abdi, “Partial least squares regression and projection on latent structure regression”, *Wiley Interdisciplinary Reviews: Computational Statistics*, vol. 2, no. 1, pp. 97–106, 2010. doi: `10.1002/wics.051`.

[179] G. W. Milligan and M. C. Cooper, “An examination of procedures for determining the number of clusters in a data set”, *Psychometrika*, vol. 50, no. 2, pp. 159–179, 1985. doi: `10.1007/BF02294245`.

[180] M. Pardo, G. Sberveglieri, S. Gardini, and E. Dalcanale, “A hierarchical classification scheme for an Electronic Nose”, *Sensors and Actuators B: Chemical*, vol. 69, no. 3, pp. 359–365, 2000. doi: `10.1016/S0925-4005(00)00486-X`.

[181] Z. Darmastuti, C. Bur, N. Lindqvist, M. Andersson, A. Schütze, and A. Lloyd Spetz, “Chemical Hierarchical methods to improve the performance of the SiC-FET as SO_2 sensors in flue gas desulphurization systems”, *Sensors & Actuators: B. Chemical*, vol. 206, pp. 609–616, 2015. doi: `10.1016/j.snb.2014.09.113`.

[182] R. Boiger, S. Defregger, A. Kock, M. Mucke, R. Wimmer-Teubenbacher, and G. Toschkoff, “Temperature Modulated Operation of SnO_2-Based Gas Sensor Arrays”, in *2018 12th International Conference on Advanced Semiconductor Devices and Microsystems (ASDAM)*, Smolenice: IEEE, 2018, isbn: 978-1-5386-7490-1. doi: `10.1109/ASDAM.2018.8544491`.

[183] D. A. Neamen, *Semiconductor Physics and Devices: Basic Principles*, 3rd ed. Boston: McGraw-Hill, 2003, 746 pp., isbn: 978-0-07-232107-4.

[184] T. Tille and D. Schmitt-Landsiedel, "Feldeffekttransistoren", in *Mikroelektronik: Halbleiterbauelemente Und Deren Anwendung in Elektronischen Schaltungen*, Springer, 2004, pp. 105–145, ISBN: 978-3-540-20422-0. DOI: 10.1007/3-540-26730-1_4.

[185] H. Bentarzi, "The MOS Structure", in *Transport in Metal-Oxide-Semiconductor Structures*. Berlin, Heidelberg: Springer, 2011, pp. 5–16, ISBN: 978-3-642-16303-6. DOI: 10.1007/978-3-642-16304-3_2.

[186] L.-G. Petersson, H. Dannetun, and I. Lundström, "The water-forming reaction on palladium", *Surface Science*, vol. 161, no. 1, pp. 77–100, 1985. DOI: 10.1016/0039-6028(85)90729-0.

[187] M. Eriksson and L.-G. Ekedahl, "Hydrogen adsorption states at the Pd/SiO_2 interface and simulation of the response of a Pd metal-oxide-semiconductor hydrogen sensor", *Journal of Applied Physics*, vol. 83, no. 8, pp. 3947–3951, 1998. DOI: 10.1063/1.367150.

[188] J. Fogelberg, M. Eriksson, H. Dannetun, and L. G. Petersson, "Kinetic modeling of hydrogen adsorption/absorption in thin films on hydrogen-sensitive field-effect devices: Observation of large hydrogen-induced dipoles at the Pd-SiO_2 interface", *Journal of Applied Physics*, vol. 78, no. 2, pp. 988–996, 1995. DOI: 10.1063/1.360293.

[189] T. C. Leung, C. L. Kao, W. S. Su, Y. J. Feng, and C. T. Chan, "Relationship between surface dipole, work function and charge transfer: Some exceptions to an established rule", *Physical Review B*, vol. 68, no. 19, 2003. DOI: 10.1103/PhysRevB.68.195408.

[190] L.-G. Ekedahl and I. Lundström, "Hydrogen Sensing Mechanisms of Metal-Insulator Interfaces", *Accounts of Chemical Research*, vol. 4842, no. 97, pp. 249–256, 1998. DOI: 10.1021/ar970068s.

[191] I. Lundström, H. Sundgren, F. Winquist, M. Eriksson, C. Krantz-Rülcker, and A. Lloyd Spetz, "Twenty-five years of field effect gas sensor research in Linköping", *Sensors and Actuators B: Chemical*, vol. 121, no. 1, pp. 247–262, 2007. DOI: 10.1016/j.snb.2006.09.046.

[192] I. Lundström, M. Armgarth, and L.-G. Petersson, "Physics with catalytic metal gate chemical sensors", *Critical Reviews in Solid State and Materials Sciences*, vol. 15, no. 3, pp. 201–278, 1989. DOI: 10.1080/10408438908243446.

[193] J. Harris, B. Kasemo, and E. Törnqvist, "The water reaction on platinum: An example of a precursor mechanism?", *Surface Science Letters*, vol. 105, no. 2-3, pp. L288–L296, 1981. doi: `10.1016/0167-2584(81)90069-4`.

[194] C. Senft, P. Iskra, and I. Eisele, "Theory and Application of Suspended Gate FET Gas Sensors", in *Solid State Gas Sensors - Industrial Application*, M. Fleischer and M. Lehmann, Eds., vol. 11, Berlin, Heidelberg: Springer Berlin Heidelberg, 2012, pp. 79–112, isbn: 978-3-642-28093-1. doi: `10.1007/5346_2011_12`.

[195] M. Löfdahl, *Spatially Resolved Gas Sensing*, ser. Linköping Studies in Science and Technology Dissertations 696. Linköping: Univ., Dep. of Physics and Measurement Techn., Div. of Applied Physics, 2001, 142 pp., isbn: 978-91-7373-040-2.

[196] J. Fogelberg, I. Lundström, and L. G. Petersson, "Ammonia Dissociation on Oxygen Covered Palladium Studied with a Hydrogen Sensitive Pd-MOS Device", *Physica Scripta*, vol. 35, no. 5, pp. 702–705, 1987. doi: `10.1088/0031-8949/35/5/017`.

[197] J. Schalwig, P. Kreisl, S. Ahlers, and G. Müller, "Response mechanism of SiC-based MOS field-effect gas sensors", *IEEE Sensors Journal*, vol. 2, no. 5, pp. 394–402, 2002. doi: `10.1109/JSEN.2002.806214`.

[198] A. Lloyd Spetz, A. Baranzahi, P. Tobias, and I. Lundström, "High Temperature Sensors Based on Metal–Insulator–Silicon Carbide Devices", *Physica Status Solidi (a)*, vol. 162, no. 493, pp. 493–511, 1997. doi: `10.1002/1521-396X(199707)162:1<493::AID-PSSA493>3.0.CO;2-C`.

[199] Y. Omura, "Proposal of High-Temperature-Operation Tolerant SOI MOSFET and Preliminary Study on Device Performance Evaluation", *Active and Passive Electronic Components*, vol. 2011, p. 850 481, 2011. doi: `10.1155/2011/850481`.

[200] C. Bur, "Selectivity Enhancement of Gas Sensitive Field Effect Transistors by Dynamic Operation", Linköping University Electronic Press / Shaker Verlag, 2015, isbn: 978-91-7519-119-5. doi: `10.3384/diss.diva-114670`.

[201] D. Puglisi, J. Eriksson, C. Bur, A. Schütze, A. Lloyd Spetz, and M. Andersson, "Catalytic metal-gate field effect transistors based on SiC for indoor air quality control", *Journal of Sensors and Sensor Systems*, vol. 4, no. 1, pp. 1–8, 2015. doi: `10.5194/jsss-4-1-2015`.

[202] D. Briand, H. Sundgren, B. van der Schoot, I. Lundström, and N. de Rooij, “Thermally isolated MOSFET for gas sensing application”, *IEEE Electron Device Letters*, vol. 22, no. 1, pp. 11–13, 2001. DOI: `10.1109/55.892428`.

[203] M. Bastuck, *FETcontrol*, version 0.1, Zenodo, 2018. DOI: `10.5281/zenodo.2634015`.

[204] J. Teigelkötter, *Energieeffiziente elektrische Antriebe: Grundlagen, Leistungselektronik, Betriebsverhalten und Regelung von Drehstrommotoren*. Wiesbaden: Vieweg+Teubner, 2013, 185 pp., ISBN: 978-3-8348-1938-3. DOI: `10.1007/978-3-8348-2330-4`.

[205] M. Eriksson, A. Salomonsson, I. Lundström, D. Briand, and A. E. Åbom, “The influence of the insulator surface properties on the hydrogen response of field-effect gas sensors”, *Journal of Applied Physics*, vol. 98, no. 3, p. 034 903, 2005. DOI: `10.1063/1.1994941`.

[206] HDF5 Group. (2019). HDF5, [Online]. Available: `https://www.hdfgroup.org/HDF5/` (visited on 01/17/2019).

[207] M. Armgarth and C. Nylander, “A stable hydrogen-sensitive Pd gate metal-oxide semiconductor capacitor”, *Applied Physics Letters*, vol. 39, no. 1, pp. 91–92, 1981. DOI: `10.1063/1.92528`.

[208] O. Weidemann, M. Hermann, G. Steinhoff, H. Wingbrant, A. Lloyd Spetz, M. Stutzmann, and M. Eickhoff, “Influence of surface oxides on hydrogen-sensitive Pd:GaN Schottky diodes”, *Applied Physics Letters*, vol. 83, no. 4, pp. 773–775, 2003. DOI: `10.1063/1.1593794`.

[209] C. Nylander, M. Armgarth, and C. Svensson, “Hydrogen-Sodium Interactions in Pd-MOS Devices”, in *Insulating Films on Semiconductors*, ser. Springer Series in Electronics and Photonics 7, M. J. Schulz and G. Pensl, Eds., Berlin, Heidelberg: Springer, 1981, pp. 195–198, ISBN: 978-3-642-68249-0. DOI: `10.1007/978-3-642-68247-6_30`.

[210] K. Dobos, M. Armgarth, G. Zimmer, and I. Lundström, “The influence of different insulators on palladium-gate metal-insulator-semiconductor hydrogen sensors”, *IEEE Transactions on Electron Devices*, vol. 31, no. 4, pp. 508–510, 1984. DOI: `10.1109/T-ED.1984.21558`.

[211] S. Nakagomi, K. Okuda, and Y. Kokubun, “Electrical properties dependent on H_2 gas for new structure diode of Pt–thin WO_3–SiC”, *Sensors and Actuators B: Chemical*, vol. 96, no. 1-2, pp. 364–371, 2003. DOI: `10.1016/S0925-4005(03)00570-7`.

[212] S. Kandasamy, A. Trinchi, W. Wlodarski, E. Comini, and G. Sberveglieri, “Study of Pt/TiO_2/SiC schottky diode based gas sensor”, in *Proceedings of IEEE Sensors, 2004.*, Vienna, Austria: IEEE, 2004, pp. 738–741, ISBN: 978-0-7803-8692-1. DOI: `10.1109/ICSENS.2004.1426273`.

[213] A. Trinchi, Y. X. Li, W. Wlodarski, S. Kaciulis, L. Pandolfi, and S. Viticoli, “Investigation of Pt/Ga_2O_3-ZnO/SiC Schottky-diode-based hydrocarbon gas sensors”, presented at the SPIE’s International Symposium on Smart Materials, Nano-, and Micro- Smart Systems, D. K. Sood, A. P. Malshe, and R. Maeda, Eds., Melbourne, Australia, 2002, p. 327. DOI: `10.1117/12.469674`.

[214] S. Jacobsén, U. Helmersson, L.-G. Ekedahl, I. Lundström, P. Mårtensson, and A. Lloyd Spetz, “Pt/CeO_2/SiC Schottky diodes with high response to hydrogen and hydrocarbons”, in *Transducers ’01 Eurosensors XV*, E. Obermeier, Ed., Berlin, Heidelberg: Springer, 2001, pp. 832–836, ISBN: 978-3-540-42150-4. DOI: `10.1007/978-3-642-59497-7`.

[215] B.-J. Kim and J.-S. Kim, “Highly sensitive dual-FET hydrogen gas sensors with a surface modified gate electrode”, *International Journal of Hydrogen Energy*, vol. 40, no. 35, pp. 11 756–11 761, 2015. DOI: `10.1016/j.ijhydene.2015.02.126`.

[216] M. Löfdahl, M. Eriksson, M. Johansson, and I. Lundström, “Difference in hydrogen sensitivity between Pt and Pd field-effect devices”, *Journal of Applied Physics*, vol. 91, no. 7, pp. 4275–4280, 2002. DOI: `10.1063/1.1448874`.

[217] A. Staerz, S. Somacescu, M. Epifani, T. Russ, U. Weimar, and N. Barsan, “WO_3 Based Gas Sensors”, *Proceedings*, vol. 2, no. 13, p. 826, 2019. DOI: `10.3390/proceedings2130826`.

[218] M. Penza, G. Cassano, and F. Tortorella, “Gas recognition by activated WO_3 thin-film sensors array”, *Sensors and Actuators B: Chemical*, vol. 81, no. 1, pp. 115–121, 2001. DOI: `10.1016/S0925-4005(01)00941-8`.

[219] S. Nakata, K. Shimanoe, N. Miura, and N. Yamazoe, “NO_2 sensing properties of WO_3 gate-fitted FET device”, *Electrochemistry*, vol. 71, no. 6, pp. 503–507, 2003.

[220] M. Penza, C. Martucci, and G. Cassano, “NOx gas sensing characteristics of WO_3 thin films activated by noble metals (Pd, Pt, Au) layers”, *Sensors and Actuators B: Chemical*, vol. 50, no. 1, pp. 52–59, 1998. DOI: `10.1016/S0925-4005(98)00156-7`.

[221] H.-T. Sun, C. Cantalini, L. Lozzi, M. Passacantando, S. Santucci, and M. Pelino, “Microstructural effect on NO_2 sensitivity of WO_3 thin film gas sensors Part 1. Thin film devices, sensors and actuators”, *Thin Solid Films*, vol. 287, no. 1-2, pp. 258–265, 1996. DOI: `10.1016/S0040-6090(96)08745-7`.

[222] A. K. Nayak, R. Ghosh, S. Santra, P. K. Guha, and D. Pradhan, “Hierarchical nanostructured WO_3–SnO_2 for selective sensing of volatile organic compounds”, *Nanoscale*, vol. 7, no. 29, pp. 12 460–12 473, 2015. DOI: `10.1039/C5NR02571K`.

[223] M. Ahmad, J. Kang, A. Sadek, A. Moafi, G. Sberveglieri, and W. Wlodarski, “Synthesis of WO_3 Nanorod based Thin Films for Ethanol and H_2 Sensing”, *Procedia Engineering*, vol. 47, pp. 358–361, 2012. DOI: `10.1016/j.proeng.2012.09.157`.

[224] A. Staerz, U. Weimar, and N. Barsan, “Understanding the Potential of WO_3 Based Sensors for Breath Analysis”, *Sensors*, vol. 16, no. 11, p. 1815, 2016. DOI: `10.3390/s16111815`.

[225] J. Zhang, X. Liu, M. Xu, X. Guo, S. Wu, S. Zhang, and S. Wang, “Pt clusters supported on WO_3 for ethanol detection”, *Sensors and Actuators B: Chemical*, vol. 147, no. 1, pp. 185–190, 2010. DOI: `10.1016/j.snb.2010.03.017`.

[226] M. Leidinger, J. Huotari, T. Sauerwald, J. Lappalainen, and A. Schütze, “Selective detection of naphthalene with nanostructured WO_3 gas sensors prepared by pulsed laser deposition”, *Journal of Sensors and Sensor Systems*, vol. 5, no. 1, pp. 147–156, 2016. DOI: `10.5194/jsss-5-147-2016`.

[227] A. Staerz, C. Berthold, T. Russ, S. Wicker, U. Weimar, and N. Barsan, “The oxidizing effect of humidity on WO_3 based sensors”, *Sensors and Actuators B: Chemical*, vol. 237, pp. 54–58, 2016. DOI: `10.1016/j.snb.2016.06.072`.

[228] M. Bastuck, D. Puglisi, J. Huotari, T. Sauerwald, J. Lappalainen, A. Lloyd Spetz, M. Andersson, and A. Schütze, “Exploring the selectivity of WO_3 with iridium catalyst in an ethanol/naphthalene mixture using multivariate statistics”, *Thin Solid Films*, vol. 618, pp. 263–270, 2016. DOI: `10.1016/j.tsf.2016.08.002`.

[229] H. Hofmann and P. Plieninger, “Bereitstellung einer Datenbank zum Vorkommen von flüchtigen organischen Verbindungen in der Raumluft”, Umweltbundesamt, UBA-FB 001131, 2008.

[230] P. Boffetta, N. Jourenkova, and P. Gustavsson, "Cancer risk from occupational and environmental exposure to polycyclic aromatic hydrocarbons", *Cancer Causes and Control*, vol. 8, no. 3, pp. 444–472, 1997. doi: `10.1023/A:1018465507029`.

[231] S.-C. Chen and C.-M. Liao, "Health risk assessment on human exposed to environmental polycyclic aromatic hydrocarbons pollution sources", *Science of The Total Environment*, vol. 366, no. 1, pp. 112–123, 2006. doi: `10.1016/j.scitotenv.2005.08.047`.

[232] M. Andersson, M. Bastuck, J. Huotari, A. Lloyd Spetz, J. Lappalainen, A. Schütze, and D. Puglisi, "SiC-FET Sensors for Selective and Quantitative Detection of VOCs Down to ppb Level", in *Procedia Engineering*, vol. 168, Budapest, Hungary, 2016, pp. 216–220. doi: `10.1016/j.proeng.2016.11.165`.

[233] J. M. Campbell, S. Seimanides, and C. T. Campbell, "Probing ensemble effects in surface reactions. 2. Benzene adsorption on clean and bismuth-covered platinum(111)", *The Journal of Physical Chemistry*, vol. 93, no. 2, pp. 815–826, 1989. doi: `10.1021/j100339a057`.

[234] W. Gao, W. T. Zheng, and Q. Jiang, "Dehydrogenation of benzene on Pt(111) surface", *The Journal of Chemical Physics*, vol. 129, no. 16, p. 164 705, 2008. doi: `10.1063/1.3001610`.

[235] D. Sellick, D. Morgan, and S. Taylor, "Silica Supported Platinum Catalysts for Total Oxidation of the Polyaromatic Hydrocarbon Naphthalene: An Investigation of Metal Loading and Calcination Temperature", *Catalysts*, vol. 5, no. 2, pp. 690–702, 2015. doi: `10.3390/catal5020690`.

[236] T. Sauerwald, "Investigation of surface processes affecting a multi signal generation of tin oxide and tungsten oxide gas sensors", Dissertation, Justus-Liebig-Universität Gießen, Gießen, 2007.

[237] R. Amrollahi, K. Wenderich, and G. Mul, "Room Temperature Oxidation of Ethanol to Acetaldehyde over Pt/WO_3", *Advanced Materials Interfaces*, vol. 3, no. 18, p. 1 600 266, 2016. doi: `10.1002/admi.201600266`.

[238] H.-F. Wang and Z.-P. Liu, "Comprehensive Mechanism and Structure-Sensitivity of Ethanol Oxidation on Platinum: New Transition-State Searching Method for Resolving the Complex Reaction Network", *Journal of the American Chemical Society*, vol. 130, no. 33, pp. 10 996–11 004, 2008. doi: `10.1021/ja801648h`.

[239] J. Ob-eye, P. Praserthdam, and B. Jongsomjit, "Dehydrogenation of Ethanol to Acetaldehyde over Different Metals Supported on Carbon Catalysts", *Catalysts*, vol. 9, no. 1, p. 66, 2019. DOI: `10.3390/catal9010066`.

[240] DDBST Dortmund Data Bank Software & Separation Technology GmbH. (2019). Saturated Vapor Pressure, [Online]. Available: `http://ddbonline.ddbst.de/AntoineCalculation/AntoineCalculationCGI.exe` (visited on 03/23/2019).

[241] L. E. Heim, S. Vallazza, D. van der Waals, and M. H. G. Prechtl, "Water decontamination with hydrogen production using microwave-formed minute-made ruthenium catalysts", *Green Chemistry*, vol. 18, no. 6, pp. 1469–1474, 2016. DOI: `10.1039/C5GC01798J`.

[242] M. Trincado, V. Sinha, R. E. Rodriguez-Lugo, B. Pribanic, B. de Bruin, and H. Grützmacher, "Homogeneously catalysed conversion of aqueous formaldehyde to H_2 and carbonate", *Nature Communications*, vol. 8, p. 14 990, 2017. DOI: `10.1038/ncomms14990`.

[243] H. Zheng, J. Z. Ou, M. S. Strano, R. B. Kaner, A. Mitchell, and K. Kalantar-zadeh, "Nanostructured Tungsten Oxide - Properties, Synthesis, and Applications", *Advanced Functional Materials*, vol. 21, no. 12, pp. 2175–2196, 2011. DOI: `10.1002/adfm.201002477`.

[244] C. Daut, "Signalkompensation mittels Gate-Bias bei gassensitiven SiC-Feldeffekttransistoren", Bachelor thesis, Lab for Measurement Technology, Saarland University, Saarbrücken, 2017.

[245] M. Bastuck, C. Daut, and A. Schütze, "Signalkompensation mittels Gate-Potential bei gassensitiven Feldeffekttransistoren", in *13. Dresdner Sensor-Symposium*, 2017, pp. 277–282. DOI: `10.5162/13dss2017/P4.03`.

[246] S. Nakagomi, A. Fukumura, Y. Kokubun, S. Savage, H. Wingbrant, M. Andersson, I. Lundström, M. Löfdahl, and A. Lloyd Spetz, "Influence of gate bias of MISiC-FET gas sensor device on the sensing properties", *Sensors and Actuators B: Chemical*, vol. 108, no. 1-2, pp. 501–507, 2005. DOI: `10.1016/j.snb.2004.11.057`.

[247] P. Kreisl, A. Helwig, G. Müller, E. Obermeier, and S. Sotier, "Detection of hydrocarbon species using silicon MOS field-effect transistors operated in a non-stationary temperature-pulse mode", *Sensors and Actuators B: Chemical*, vol. 106, no. 1, pp. 442–449, 2005. DOI: `10.1016/j.snb.2004.09.004`.

[248] P. Kreisl, A. Helwig, A. Friedberger, G. Muller, E. Obermeier, and S. Sotier, "Detection of hydrocarbon species using silicon MOS capacitors operated in a non-stationary temperature pulse mode", *Sensors and Actuators B: Chemical*, vol. 106, no. 2, pp. 489–497, 2005. doi: `10.1016/j.snb.2004.07.030`.

[249] R. Pohle, O. Von Sicard, M. Fleischer, H. P. Frerichs, C. Wilbertz, and I. Freund, "Gate pulsed readout of floating gate FET gas sensors", *Procedia Engineering*, vol. 5, pp. 13–16, 2010. doi: `10.1016/j.proeng.2010.09.036`.

[250] M. Bastuck, D. Puglisi, A. Lloyd Spetz, A. Schütze, and M. Andersson, "Characterizing the influence of gate bias on electrical and catalytical properties of a porous platinum gate on field effect gas sensors", in *Proceedings of IEEE Sensors*, 2017, isbn: 978-1-4799-8287-5. doi: `10.1109/ICSENS.2016.7808458`.

[251] C. G. Vayenas, S. Bebelis, and S. Neophytides, "Non-Faradaic electrochemical modification of catalytic activity", *The Journal of Physical Chemistry*, vol. 92, no. 18, pp. 5083–5085, 1988. doi: `10.1021/j100329a007`.

[252] A. Katsaounis, "Recent developments and trends in the electrochemical promotion of catalysis (EPOC)", *Journal of Applied Electrochemistry*, vol. 40, no. 5, pp. 885–902, 2010. doi: `10.1007/s10800-009-9938-7`.

[253] E. Espid and F. Taghipour, "UV-LED Photo-activated Chemical Gas Sensors: A Review", *Critical Reviews in Solid State and Materials Sciences*, vol. 42, no. 5, pp. 416–432, 2017. doi: `10.1080/10408436.2016.1226161`.

[254] ams AG. (2015). AS-MLV-P2 datasheet, [Online]. Available: `https://ams.com/documents/20143/36005/AS-MLV-P2_DS000359_1-00.pdf/43d38978-7af6-ed5c-f1dd-46950855abca` (visited on 09/04/2019).

[255] Sensirion AG. (2018). SGP30 datasheet, [Online]. Available: `https://www.sensirion.com/fileadmin/user_upload/customers/sensirion/Dokumente/0_Datasheets/Gas/Sensirion_Gas_Sensors_SGP30_Datasheet.pdf` (visited on 09/04/2019).

[256] M. F. Khan, M. W. Iqbal, M. Z. Iqbal, M. A. Shehzad, Y. Seo, and J. Eom, "Photocurrent Response of MoS_2 Field-Effect Transistor by Deep Ultraviolet Light in Atmospheric and N_2 Gas Environments", *ACS Applied Materials & Interfaces*, vol. 6, no. 23, pp. 21 645–21 651, 2014. doi: `10.1021/am506716a`.

[257] N. Huo, S. Yang, Z. Wei, S.-S. Li, J.-B. Xia, and J. Li, "Photoresponsive and Gas Sensing Field-Effect Transistors based on Multilayer WS_2 Nanoflakes", *Scientific Reports*, vol. 4, no. 1, 2015. DOI: 10.1038/srep05209.

[258] R. Y. Khosa, E. B. Thorsteinsson, M. Winters, N. Rorsman, R. Karhu, J. Hassan, and E. Ö. Sveinbjörnsson, "Electrical characterization of amorphous Al_2O_3 dielectric films on n-type 4H-SiC", *AIP Advances*, vol. 8, no. 2, p. 025 304, 2018. DOI: 10.1063/1.5021411.

[259] A. Stokłosa, S. S. Kurek, and B. Laskowska, "Binding Energy and the Heat of Chemisorption on Metallic Catalysts — A Thermodynamic Aspect", *Adsorption Science & Technology*, vol. 23, no. 2, pp. 161–172, 2005. DOI: 10.1260/0263617054037790.

[260] M. Bastuck, D. Puglisi, A. Lloyd Spetz, A. Schütze, T. Sauerwald, and M. Andersson, "UV-Assisted Gate Bias Cycling in Gas-Sensitive Field-Effect Transistors", in *Proceedings*, vol. 2, Graz, Austria: MDPI, 2018, p. 999. DOI: 10.3390/proceedings2130999.

[261] M. Roschke and F. Schwierz, "Electron mobility models for 4H, 6H, and 3C SiC", *IEEE Transactions on Electron Devices*, vol. 48, no. 7, pp. 1442–1447, 2001. DOI: 10.1109/16.930664.

[262] C. Di Natale, S. Marco, F. Davide, and A. D'Amico, "Sensor-array calibration time reduction by dynamic modelling", *Sensors and Actuators B: Chemical*, vol. 25, no. 1-3, pp. 578–583, 1995. DOI: 10.1016/0925-4005(95)85126-7.

[263] W. Tsujita, H. Ishida, and T. Moriizumi, "Dynamic gas sensor network for air pollution monitoring and its auto-calibration", in *Proceedings of IEEE Sensors, 2004.*, Vienna, Austria: IEEE, 2004, pp. 56–59, ISBN: 978-0-7803-8692-1. DOI: 10.1109/ICSENS.2004.1426098.

[264] D. Hasenfratz, O. Saukh, and L. Thiele, "On-the-Fly Calibration of Low-Cost Gas Sensors", in *Wireless Sensor Networks*, G. P. Picco and W. Heinzelman, Eds., vol. 7158, Berlin, Heidelberg: Springer, 2012, pp. 228–244, ISBN: 978-3-642-28168-6. DOI: 10.1007/978-3-642-28169-3_15.

[265] G. W. Oehlert, *A First Course in Design and Analysis of Experiments*. New York: W.H. Freeman, 2000, 659 pp., ISBN: 978-0-7167-3510-6.

[266] D. C. Montgomery, *Introduction to Statistical Quality Control*, 7th ed. Wiley, 2013, 754 pp., ISBN: 978-1-118-14681-1.

[267] M. Down, *Measurement System Analysis: Reference Manual*. Southfield, Michigan: Automotive Industry Action Group, 2010, ISBN: 978-1-60534-211-5.

[268] International Organization for Standardization, Ed., *Standard Practice for Conducting an Interlaboratory Study to Determine the Precision of a Test Method (ASTM E691-05)*, 2005.

[269] International Organization for Standardization, Ed., *Accuracy (trueness and precision) of measurement methods and results – Part 2: Basic method for the determination of repeatability and reproducibility of a standard measurement method (ISO 5725-2:1994)*, 1994.

[270] M. Bastuck, T. Baur, M. Richter, B. Mull, A. Schütze, and T. Sauerwald, "Comparison of ppb-level gas measurements with a metal-oxide semiconductor gas sensor in two independent laboratories", *Sensors and Actuators B: Chemical*, vol. 273, 2018. DOI: `10.1016/j.snb.2018.06.097`.

[271] T. Sauerwald, T. Baur, M. Leidinger, W. Reimringer, L. Spinelle, M. Gerboles, G. Kok, and A. Schütze, "Highly sensitive benzene detection with metal oxide semiconductor gas sensors – an inter-laboratory comparison", *Journal of Sensors and Sensor Systems*, vol. 7, no. 1, pp. 235–243, 2018. DOI: `10.5194/jsss-7-235-2018`.

[272] L. Spinelle, M. Gerboles, G. Kok, S. Persijn, and T. Sauerwald, "Performance Evaluation of Low-Cost BTEX Sensors and Devices within the EURAMET Key-VOCs Project", *Proceedings*, vol. 1, no. 4, p. 425, 2017. DOI: `10.3390/proceedings1040425`.

[273] W. Buttner, R. Burgess, C. Rivkin, M. Post, L. Boon-Brett, G. Black, F. Harskamp, and P. Moretto, "Inter-laboratory assessment of hydrogen safety sensors performance under anaerobic conditions", *International Journal of Hydrogen Energy*, vol. 37, no. 22, pp. 17 540–17 548, 2012. DOI: `10.1016/j.ijhydene.2012.03.165`.

[274] N. Helwig, M. Schüler, C. Bur, A. Schütze, and T. Sauerwald, "Gas mixing apparatus for automated gas sensor characterization", *Measurement Science and Technology*, vol. 25, no. 5, p. 055 903, 2014. DOI: `10.1088/0957-0233/25/5/055903`.

[275] M. Leidinger, C. Schultealbert, J. Neu, A. Schütze, and T. Sauerwald, "Characterization and calibration of gas sensor systems at ppb level—a versatile test gas generation system", *Measurement Science and Technology*, vol. 29, 2018. DOI: `10.1088/1361-6501/aa91da`.

[276] T. Baur, A. Schütze, and T. Sauerwald, "A4.2 - Detection of short trace gas pulses", 2017. DOI: `10.5162/sensor2017/a4.2`.

[277] VICI AG International. (2019). GT Plus 1500 Ultra-Zero Air Generator, [Online]. Available: `https://www.vici-dbs.com/collections/gt-plus-ultra-zero-air/products/gt-plus-1500-ultra-zero-air-generator` (visited on 10/04/2019).

[278] T. Aalto, M. Lallo, J. Hatakka, and T. Laurila, "Atmospheric hydrogen variations and traffic emissions at an urban site in Finland", *Atmospheric Chemistry and Physics Discussions*, vol. 9, no. 3, pp. 13 917–13 942, 2009. DOI: `10.5194/acpd-9-13917-2009`.

[279] H. Price, L. Jaeglé, A. Rice, P. Quay, P. C. Novelli, and R. Gammon, "Global budget of molecular hydrogen and its deuterium content: Constraints from ground station, cruise, and aircraft observations", *Journal of Geophysical Research*, vol. 112, no. D22, 2007. DOI: `10.1029/2006JD008152`.

[280] P. Pochanart, "Regional background ozone and carbon monoxide variations in remote Siberia/East Asia", *Journal of Geophysical Research*, vol. 108, no. D1, p. 4028, 2003. DOI: `10.1029/2001JD001412`.

[281] S. V. Jagovkina, I. L. Karol, V. A. Zubov, V. E. Lagun, A. I. Reshetnikov, and E. V. Rozanov, "Model Study of Distribution and Intensity of Methane Fluxes in West Siberia and Russian Arctic", in *Air Pollution Modelling and Simulation*, B. Sportisse, Ed., Berlin, Heidelberg: Springer, 2002, pp. 169–176, ISBN: 978-3-540-42515-1. DOI: `10.1007/978-3-662-04956-3_18`.

[282] J. Pichlmaier, "Befeuchtung von Prüfgas für die Kalibrierung von Gas- und Feuchtesensoren / Humidification of test gas for the calibration of gas sensors and humidity sensors", *tm - Technisches Messen*, vol. 58, pp. 471–477, JG 1991. DOI: `10.1524/teme.1991.58.jg.471`.

[283] T. Kammerer, "Entwurf und Realisierung von Messplattformen zur effizienten Entwicklung intelligenter Gasmesssysteme", Dissertation, Saarland University, Saarbrücken, 2005.

[284] M. Richter, *Entwicklung , Validierung Und Anwendung Eines Verfahrens Zur Erzeugung Langzeitstabiler VOC-Gasgemische*. 2010, ISBN: 978-3-9813550-9-3.

[285] M. Richter, O. Jann, W. Horn, L. Pyza, and O. Wilke, "System to generate stable long-term VOC gas mixtures of concentrations in the ppb range for test and calibration purposes", *Gefahrstoffe Reinhaltung der Luft*, vol. 73, pp. 103–106, 2013.

[286] VICI AG International. (2019). VICI Metronics Dynacalibrator® Model 150 Instruction Manual, [Online]. Available: `https://www.vici.com/support/manuals/dyna150.pdf` (visited on 09/04/2019).

[287] The SciPy community. (2019). SciPy v1.2.1. reference guide, [Online]. Available: `https://docs.scipy.org/doc/scipy/reference/generated/scipy.optimize.minimize.html#id35` (visited on 10/04/2019).

[288] D. Kraft, "A software package for sequential quadratic programming", *Forschungsbericht- Deutsche Forschungs- und Versuchsanstalt fur Luft- und Raumfahrt*, 1988.

[289] MKS Instruments, Inc. (2018). MF1-MFC datasheet, [Online]. Available: `https://www.mksinst.com/mam/celum/celum_assets/resources/MF1-DS.pdf` (visited on 12/04/2019).

[290] International Organization for Standardization, Ed., *Indoor Air - Part 3: Determination of formaldehyde and other carbonyl compounds - Active sampling method (ISO 16000-3.2011)*, 2011.

[291] T. Baur, C. Schultealbert, A. Schütze, and T. Sauerwald, "Device for the detection of short trace gas pulses", *tm - Technisches Messen*, vol. 85, no. 7-8, pp. 496–503, 2018. DOI: `10.1515/teme-2017-0137`.

[292] Senseair. (2019). Senseair tSENSE Display Manual, [Online]. Available: `https://senseair.com/products/tsense/tsense-display/` (visited on 08/04/2019).

[293] Hammond Manufacturing Company Limited. (2019). 1590LB Enclosure datasheet, [Online]. Available: `http://www.hammondmfg.com/pdf/1590LB.pdf` (visited on 05/14/2019).

[294] M. Bastuck, D. Puglisi, P. Möller, W. Reimringer, A. Schütze, A. Lloyd Spetz, and M. Andersson, "Low-cost chemical gas sensors for selective formaldehyde quantification at ppb-level in the field", in *Proceedings Sensor 2017*, Nuremberg, Germany, 2017, pp. 702–707, ISBN: 978-3-9816876-4-4. DOI: `10.5162/sensor2017/p5.4`.

[295] Graywolf Sensing Solutions. (2019). Graywolf FM-801 Datasheet, [Online]. Available: `https://www.wolfsense.com/pdf/GrayWolf-Formaldehyde_Monitor_brochure-1011.pdf` (visited on 01/17/2019).

[296] T. Salthammer, S. Mentese, and R. Marutzky, "Formaldehyde in the indoor environment", *Chemical Reviews*, vol. 110, no. 4, pp. 2536–2572, 2010. DOI: `10.1021/cr800399g`.

[297] A. Blondel and H. Plaisance, “Screening of formaldehyde indoor sources and quantification of their emission using a passive sampler”, *Building and Environment*, vol. 46, no. 6, pp. 1284–1291, 2011. doi: `10.1016/j.buildenv.2010.12.011`.

[298] J. Kwak, B. A. Geier, M. Fan, S. A. Gogate, S. A. Rinehardt, B. S. Watts, C. C. Grigsby, and D. K. Ott, “Detection of volatile organic compounds indicative of human presence in the air”, *Journal of Separation Science*, vol. 38, no. 14, pp. 2463–2469, 2015. doi: `10.1002/jssc.201500261`.

[299] P. R. Veres, P. Faber, F. Drewnick, J. Lelieveld, and J. Williams, “Anthropogenic sources of VOC in a football stadium: Assessing human emissions in the atmosphere”, *Atmospheric Environment*, vol. 77, pp. 1052–1059, 2013. doi: `10.1016/j.atmosenv.2013.05.076`.

[300] W. Ding, R. Hayashi, J. Suehiro, G. Zhou, K. Imasaka, and M. Hara, “Calibration methods of carbon nanotube gas sensor for partial discharge detection in SF_6”, *IEEE Transactions on Dielectrics and Electrical Insulation*, vol. 13, no. 2, pp. 353–361, 2006. doi: `10.1109/TDEI.2006.1624280`.

[301] E. J. Wolfrum, R. M. Meglen, D. Peterson, and J. Sluiter, “Calibration transfer among sensor arrays designed for monitoring volatile organic compounds in indoor air quality”, *IEEE Sensors Journal*, vol. 6, no. 6, pp. 1638–1643, 2006. doi: `10.1109/JSEN.2006.884558`.

[302] A. Jordan and B. Steinberg, “Calibration of atmospheric hydrogen measurements”, *Atmospheric Measurement Techniques*, vol. 4, no. 3, pp. 509–521, 2011. doi: `10.5194/amt-4-509-2011`.

[303] I. Rodriguez-Lujan, J. Fonollosa, A. Vergara, M. Homer, and R. Huerta, “On the calibration of sensor arrays for pattern recognition using the minimal number of experiments”, *Chemometrics and Intelligent Laboratory Systems*, vol. 130, pp. 123–134, 2014. doi: `10.1016/j.chemolab.2013.10.012`.

[304] L. Fernandez, S. Guney, A. Gutierrez-Galvez, and S. Marco, “Calibration transfer in temperature modulated gas sensor arrays”, *Sensors and Actuators B: Chemical*, vol. 231, pp. 276–284, 2016. doi: `10.1016/j.snb.2016.02.131`.

[305] J. Fonollosa, I. Rodríguez-Luján, and R. Huerta, “Chemical gas sensor array dataset”, *Data in Brief*, vol. 3, pp. 85–89, 2015. doi: `10.1016/j.dib.2015.01.003`.

[306] J. Fonollosa, I. Rodríguez-Luján, M. Trincavelli, and R. Huerta, "Dataset from chemical gas sensor array in turbulent wind tunnel", *Data in Brief*, vol. 3, pp. 169–174, 2015. DOI: `10.1016/j.dib.2015.02.014`.

[307] J. Fonollosa. (2016). Twin gas sensor arrays Data Set, [Online]. Available: `https://archive.ics.uci.edu/ml/datasets/Twin+gas+sensor+arrays` (visited on 06/04/2019).

[308] M. Bastuck and T. Fricke, *Temperature-Modulated Gas Sensor Signal*, 2018. DOI: `10.5281/zenodo.1411209`.

[309] J. Fonollosa. (2015). Gas sensor array under dynamic gas mixtures Data Set, [Online]. Available: `http://archive.ics.uci.edu/ml/datasets/gas+sensor+array+under+dynamic+gas+mixtures` (visited on 06/04/2019).

[310] H. Sundgren, F. Winquist, I. Lukkari, and I. Lundstrom, "Artificial neural networks and gas sensor arrays: Quantification of individual components in a gas mixture", *Measurement Science and Technology*, vol. 2, no. 5, pp. 464–469, 1991. DOI: `10.1088/0957-0233/2/5/008`.

[311] R. Johnson. (2018). Product distribution of two uniform distribution, what about 3 or more, [Online]. Available: `https://math.stackexchange.com/questions/659254/product-distribution-of-two-uniform-distribution-what-about-3-or-more` (visited on 05/04/2019).

[312] J. Kelleter, *Künstliche Nase für gasförmige Emissionen aus unvollständiger Verbrennung: Aufbau und Erprobung eines Multi-Gassensor-Systems*, ser. Berichte aus der Physik. Aachen: Shaker, 1997, ISBN: 978-3-8265-2072-3.

[313] N. R. Drapper and H. Smith, *Applied Regression Analysis*, ser. Wiley Series in Probability and Mathematical Statistics. Wiley, 1998, ISBN: 978-0-471-17082-2.

[314] C. Bur, M. Bastuck, A. Schütze, A. Lloyd Spetz, and M. Andersson, "Combination of temperature cycled and gate bias cycled operation to enhance the selectivity of SiC-FET gas sensors", in *TRANSDUCERS & EUROSENSORS XXVII*, 2013, pp. 2041–2044, ISBN: 978-1-4673-5981-8. DOI: `10.1109/Transducers.2013.6627199`.

Own publications

1. Peer-reviewed journal papers

J1. M. Rodner, **M. Bastuck**, A. Schütze, M. Andersson, J. Huotari, J. Puustinen, J. Lappalainen, and T. Sauerwald, "Lithium doped tungsten oxide films for gas sensing", *Journal of Sensors and Sensor Systems*, vol. 8, pp. 261–267, 2019. DOI: `10.5194/jsss-8-261-2019`

> MR, under the supervision of TS, conceived and performed all experiments, evaluated and interpreted the data, and wrote the manuscript. MB was involved in all of the above and contributed, like all authors, with substantial revisions.

J2. H. Lensch, **M. Bastuck**, T. Baur, A. Schütze, and T. Sauerwald, "Impedance model for a high-temperature ceramic humidity sensor", *Journal of Sensors and Sensor Systems*, vol. 8, no. 1, pp. 161–169, 2019. DOI: `10.5194/jsss-8-161-2019`

> HL conceived and performed the experiments. MB was involved in evaluation and interpretation of the data and, like all authors, contributed with substantial revisions.

J3. **M. Bastuck**, T. Baur, and A. Schütze, "DAV^{3}E – a MATLAB toolbox for multivariate sensor data evaluation", *Journal of Sensors and Sensor Systems*, vol. 7, no. 2, pp. 489–506, 2018. DOI: `10.5194/jsss-7-489-2018`

> **open access.** MB developed and implemented the prototype DAV^{3}E is based on. MB and TB improved upon this prototype with new ideas, concepts, and implementations. MB wrote the manuscript, and TB and AS contributed with substantial revisions.

J4. **M. Bastuck**, T. Baur, M. Richter, B. Mull, A. Schütze, and T. Sauerwald, "Comparison of ppb-level gas measurements with a metal-oxide semiconductor gas sensor in two independent laboratories", *Sensors and Actuators B: Chemical*, vol. 273, 2018. DOI: `10.1016/j.snb.2018.06.097`

> MB together with TB planned and executed the gas sensor measurements. MB wrote the manuscript. MR and BM set up the measurement and performed the analytic analysis at BAM and, as all authors, contributed with interpretations and substantial revisions.

J5. **M. Bastuck**, D. Puglisi, J. Huotari, T. Sauerwald, J. Lappalainen, A. Lloyd Spetz, M. Andersson, and A. Schütze, "Exploring the selectivity of WO_3 with iridium catalyst in an ethanol/naphthalene mixture using multivariate statistics", *Thin Solid Films*, vol. 618, pp. 263–270, 2016. DOI: `10.1016/j.tsf.2016.08.002`

MB conceived and performed all measurements, evaluated and interpreted the data, and wrote the manuscript. JH did the layer deposition and characterization. All authors contributed with interpretations and substantial revisions.

J6. **M. Bastuck**, A. Schütze, and T. Sauerwald, "A new approach to self-monitoring of amperometric oxygen sensors", *Sensors and Actuators B: Chemical*, vol. 214, pp. 218–224, 2015. DOI: `10.1016/j.snb.2015.02.116`

MB conceived the experiments together with TS. MB performed the measurements, interpreted the data together with TS, and wrote the manuscript. AS contributed with interpretations and substantial revisions.

J7. C. Bur, **M. Bastuck**, D. Puglisi, A. Schütze, A. Lloyd Spetz, and M. Andersson, "Discrimination and quantification of volatile organic compounds in the ppb-range with gas sensitive SiC-FETs using multivariate statistics", *Sensors and Actuators B: Chemical*, vol. 214, pp. 1–9, 2015. DOI: `10.1016/j.snb.2015.03.016`

CB conceived and performed the experiments, evaluated and interpreted the data, and wrote the manuscript. MB was involved in the planning of all the above, and contributed, like all authors, with substantial revisions.

J8. **M. Bastuck**, C. Bur, A. Lloyd Spetz, M. Andersson, A. Schütze, A. L. Spetz, M. Andersson, and A. Schütze, "Gas identification based on bias induced hysteresis of a gas-sensitive SiC field effect transistor", *Journal of Sensors and Sensor Systems*, vol. 3, no. 1, pp. 9–19, 2014. DOI: `10.5194/jsss-3-9-2014`

open access. MB, under the supervision of CB, conceived and performed the experiments, evaluated and interpreted the data, and wrote the manuscript. All authors contributed with interpretations and substantial revisions.

J9. C. Bur, **M. Bastuck**, A. Schütze, J. Juuti, A. Lloyd Spetz, and M. Andersson, "Characterization of ash particles with a microheater and gas-sensitive SiC field-effect transistors", *Journal of Sensors and Sensor Systems*, vol. 3, no. 2, pp. 305–313, 2014. DOI: `10.5194/jsss-3-305-2014`

open access. CB conceived and performed the experiments, evaluated and interpreted the data, and wrote the manuscript. MB was involved in the planning of the experiments and the evaluation and contributed, like all authors, with substantial revisions.

J10. C. Bur, **M. Bastuck**, A. Lloyd Spetz, M. Andersson, and A. Schütze, "Selectivity enhancement of SiC-FET gas sensors by combining temperature and gate bias cycled operation using multivariate statistics", *Sensors and Actuators B: Chemical*, vol. 193, 2014. DOI: `10.1016/j.snb.2013.12.030`

> CB conceived and performed the experiments, evaluated and interpreted the data, and wrote the manuscript. MB was involved in evaluation and planning of experiments and contributed, like all authors, with substantial revisions.

2. Peer-reviewed conference contributions

C1. **M. Bastuck**, D. Puglisi, A. Lloyd Spetz, A. Schütze, T. Sauerwald, and M. Andersson, "UV-Assisted Gate Bias Cycling in Gas-Sensitive Field-Effect Transistors", in *Proceedings*, vol. 2, Graz, Austria: MDPI, 2018, p. 999. DOI: `10.3390/proceedings2130999`

> **open access, poster presentation, best poster award.** MB conceived and performed all experiments, evaluated and interpreted the data, wrote the manuscript and designed and presented the poster. All other authors contributed with interpretations and substantial revisions.

C2. **M. Bastuck**, D. Puglisi, P. Möller, W. Reimringer, A. Schütze, A. Lloyd Spetz, and M. Andersson, "Low-cost chemical gas sensors for selective formaldehyde quantification at ppb-level in the field", in *Proceedings Sensor 2017*, Nuremberg, Germany, 2017, pp. 702–707, ISBN: 978-3-9816876-4-4. DOI: `10.5162/sensor2017/p5.4`

> **open access, poster presentation.** MB defined the sensor operating mode and evaluated and interpreted the data, wrote the manuscript and presented the poster. PM and WR developed the hardware and, like all other authors, contributed with interpretations and substantial revisions.

C3. **M. Bastuck**, C. Daut, and A. Schütze, "Signalkompensation mittels Gate-Potential bei gassensitiven Feldeffekttransistoren", in *13. Dresdner Sensor-Symposium*, 2017, pp. 277–282. DOI: `10.5162/13dss2017/P4.03`

> **open access, poster presentation, best poster award.** MB supervised the Bachelor thesis of CD in which the experiments, evaluation, and interpretation were performed, wrote the manuscript, and was involved in the poster design. CD presented the poster and, like AS, contributed with substantial revisions.

C4. **M. Bastuck**, T. Baur, and A. Schütze, "Fusing cyclic sensor data with different cycle length", in *IEEE International Conference on Multisensor*

Fusion and Integration for Intelligent Systems, 2017, ISBN: 978-1-4673-9708-7. DOI: `10.1109/MFI.2016.7849469`

> **oral presentation.** MB conceived the fusion methods, wrote the code, performed the simulations, interpreted the data, and wrote the manuscript. TB and AS contributed with substantial revisions.

C5. **M. Bastuck**, D. Puglisi, A. Lloyd Spetz, A. Schütze, and M. Andersson, "Characterizing the influence of gate bias on electrical and catalytical properties of a porous platinum gate on field effect gas sensors", in *Proceedings of IEEE Sensors*, 2017, ISBN: 978-1-4799-8287-5. DOI: `10.1109/ICSENS.2016.7808458`

> **poster presentation.** MB conceived and performed the experiments, evaluated and interpreted the data, wrote the manuscript, and designed and presented the poster. All authors contributed with interpretations and substantial revisions.

C6. **M. Bastuck**, T. Baur, T. Schneider, and A. Schütze, "DAV^{3}E – a comprehensive toolbox for multisensor data fusion not only for gas sensors", in *Sixth Scientific Meeting EuNetAir*, 2016, pp. 50–53. DOI: `10.5162/6EuNetAir2016/13`

> **poster presentation.** MB developed and implemented the prototype DAV^{3}E is based on. MB and TB improved upon this prototype with new ideas, concepts, and implementations. MB wrote the manuscript and designed the poster. AS presented the poster. All authors contributed with substantial revisions.

C7. **M. Bastuck**, W. Reimringer, T. Conrad, and A. Schütze, "Dynamic Multi-sensor Operation and Read-out for Highly Selective Gas Sensor Systems", in *Procedia Engineering*, vol. 168, 2016. DOI: `10.1016/j.proeng.2016.11.490`

> **oral and poster presentation.** MB defined the sensor cycles, recorded and evaluated the data, designed and presented the poster and gave the oral presentation. WR developed and implemented the hardware. All authors contributed with substantial revisions.

C8. D. Puglisi, **M. Bastuck**, M. Andersson, J. Huotari, J. Lappalainen, A. Schütze, and A. Lloyd Spetz, "Gas sensitive SiC-FET sensors for indoor air quality control", in *Proceedings Indoor Air 2016*, Ghent, Belgium, 2016, ISBN: 978-0-9846855-5-4

> **poster presentation.** DP wrote the abstract. MB, like all authors, contributed with substantial revisions.

C9. D. Puglisi, J. Eriksson, M. Andersson, J. Huotari, **M. Bastuck**, C. Bur, J. Lappalainen, A. Schütze, and A. Lloyd Spetz, "Exploring the Gas Sensing Performance of Catalytic Metal/Metal Oxide 4H-SiC Field

Effect Transistors", *Materials Science Forum*, vol. 858, 2016. doi: `10.4028/www.scientific.net/MSF.858.997`

poster presentation. DP wrote the abstract. MB, like all authors, contributed with substantial revisions.

C10. M. Andersson, **M. Bastuck**, J. Huotari, A. Lloyd Spetz, J. Lappalainen, A. Schütze, and D. Puglisi, "SiC-FET Sensors for Selective and Quantitative Detection of VOCs Down to ppb Level", in *Procedia Engineering*, vol. 168, Budapest, Hungary, 2016, pp. 216–220. doi: `10.1016/j.proeng.2016.11.165`

oral presentation. MA wrote the abstract. MB, like all authors, contributed with substantial revisions.

C11. **M. Bastuck**, C. Bur, T. Sauerwald, A. Schütze, A. Lloyd Spetz, and M. Andersson, "Quantification of Volatile Organic Compounds in the ppb-range using Partial Least Squares Regression", in *Proceedings SENSOR 2015*, Nuremberg, Germany, 2015, pp. 584–589, isbn: 978-3-9813484-8-4. doi: `10.5162/sensor2015/d5.1`

oral presentation. MB, under the supervision of CB, conceived and performed the experiments, evaluated and interpreted the data, wrote the manuscript, and gave the oral presentation. All authors contributed with substantial revisions.

C12. **M. Bastuck**, M. Leidinger, T. Sauerwald, and A. Schütze, "Improved quantification of naphthalene using non-linear Partial Least Squares Regression", 2015

poster presentation. MB implemented the methods, evaluated and interpreted the data, wrote the manuscript and designed the poster. ML recorded the data. AS presented the poster. All authors contributed with substantial revisions.

C13. **M. Bastuck**, A. Schütze, and T. Sauerwald, "A new Approach to the Surveillance of Amperometric Oxygen Sensors", presented at the Eurosensors 2014, Brescia, Italy, 2014

poster presentation. MB together with TS conceived the experiments, performed the measurements, interpreted the data, wrote the abstract, and designed the poster. TS presented the poster. AS contributed with interpretations and substantial revisions.

C14. C. Bur, **M. Bastuck**, M. Andersson, A. LLoyd Spetz, and A. Schütze, "Increasing the selectivity of gas sensitive field effect transistors by dynamic operation", in *E-MRS Spring Meeting 2014, Lille, France*, 2014

oral presentation, student award. CB conceived and performed the experiments, evaluated and interpreted the data, and wrote the abstract. MB was involved in all the above and gave the oral presentation. All authors contributed with substantial revisions.

C15. C. Bur, **M. Bastuck**, D. Puglisi, A. Schütze, A. Lloyd Spetz, and M. Andersson, "Discrimination and quantification of volatile organic compounds in the ppb-range with gas sensitive SiC-Field effect transistors", in *Procedia Engineering*, vol. 87, 2014, pp. 604–607. DOI: `10.1016/j.proeng.2014.11.561`

> **poster presentation.** CB conceived and performed the experiments, evaluated and interpreted the data, and wrote the abstract. MB was involved in the experiments and the evaluation. All authors contributed with substantial revisions.

C16. **M. Bastuck**, A. Schütze, and T. Sauerwald, "A new approach to self-monitoring of amperometric oxygen sensors", in *Procedia Engineering*, vol. 87, 2014, pp. 1007–1010. DOI: `10.1016/j.proeng.2014.11.330`

> **extended abstract.** MB together with TS conceived the experiments, performed the measurements, interpreted the data, and wrote the manuscript. AS contributed with interpretations and substantial revisions.

C17. **M. Bastuck**, C. Bur, A. Lloyd Spetz, M. Andersson, and A. Schütze, "Identification of ammonia and carbon monoxide based on the hysteresis of a gas-sensitive SiC field effect transistor", in *TRANSDUCERS & EUROSENSORS XXVII*, IEEE, 2013, pp. 250–253, ISBN: 978-1-4673-5983-2. DOI: `10.1109/Transducers.2013.6626749`

> **poster presentation.** MB (supervised by CB), conceived and performed the experiments, evaluated and interpreted the data, and wrote the manuscript. All authors contributed with interpretations and substantial revisions.

C18. C. Bur, **M. Bastuck**, A. Schütze, A. Lloyd Spetz, and M. Andersson, "Combination of temperature cycled and gate bias cycled operation to enhance the selectivity of SiC-FET gas sensors", in *TRANSDUCERS & EUROSENSORS XXVII*, 2013, pp. 2041–2044, ISBN: 978-1-4673-5981-8. DOI: `10.1109/Transducers.2013.6627199`

> **poster presentation.** CB conceived and performed the experiments, evaluated and interpreted the data, and wrote the abstract. MB was involved in all the above and, like all authors, contributed with substantial revisions.

C19. C. Bur, **M. Bastuck**, M. Andersson, A. Schütze, and A. Lloyd Spetz, "Influence of a Changing Gate Bias on the Sensing Properties of SiC Field Effect Gas Sensors", in *Proc. IMCS 2012: The 14th International Meeting on Chemical Sensors*, Nuremberg, Germany, 2012, pp. 140–143, ISBN: 978-3-9813484-2-2. DOI: `10.5162/IMCS2012/1.5.4`

> **poster presentation.** MB (supervised by CB), conceived and performed the experiments, evaluated and interpreted the data, and wrote the manuscript. All authors contributed with interpretations and substantial revisions.

3. Other publications

O1. **M. Bastuck**, T. Baur, and A. Schütze, "DAV³E - a versatile Data Analysis and Verification/Visualization/Validation Environment for MATLAB", presented at the Sino-German Symposium on Intelligent Gas Sensors: Principles and Applications, Huazhong University of Science and Technology, Wuhan, China, 2018

> **invited poster presentation, best poster award.** MB developed and implemented the prototype DAV^{3}E is based on. MB and TB improved upon this prototype with new ideas, concepts, and implementations. MB and AS wrote the abstract. MB designed and presented the poster. All authors contributed with substantial revisions.

O2. **M. Bastuck** and T. Fricke, *Temperature-Modulated Gas Sensor Signal*, 2018. DOI: `10.5281/zenodo.1411209`

> **dataset.** MB curated the dataset, TF recorded it.

O3. D. Puglisi, **M. Bastuck**, Y. Hasegawa, H.-Y. Chen, Schütze, Andreas, A. Lloyd Spetz, and M. Andersson, "Field Effect Based Sensors for Highly Sensitive and Selective Detection of Hydrocarbons", presented at the Convegno Nazionale Sensori (CNS), Catania, Italy, –Feb. 23, 2018

> **oral presentation.** DP wrote the abstract. MB, like all authors, contributed with substantial revisions.

O4. **M. Bastuck**, T. Baur, and A. Schütze, "DAV³E : Data Analysis and Verification / Visualization / Validation Environment für die Multisensor-Datenfusion", in *18. GMA/ITG-Fachtagung Sensoren Und Messsysteme 2016*, 2016, pp. 729–734. DOI: `10.5162/sensoren2016/P7.3`

> **poster presentation.** MB developed and implemented the prototype DAV^{3}E is based on. MB and TB improved upon this prototype with new ideas, concepts, and implementations. MB wrote the manuscript and designed the poster with TB. TB presented the poster. All authors contributed with substantial revisions.

O5. **M. Bastuck**, D. Puglisi, A. Lloyd Spetz, and M. Andersson, "Operating Modes and Signal Processing", *SENSIndoor Newsletter*, no. 2, 2016

> **newsletter article.** MB wrote the article, all other authors contributed with substantial revisions.

O6. A. Schütze and **M. Bastuck**, "Signalverarbeitung als Schlüssel für moderne Mess- und Sensortechnik", *Jahresmagazin Mess- und Sensortechnik 2016/2017, Institut für wissenschaftliche Veröffentlichungen (IWV)*, pp. 26–34, 2016

> **invited article.** AS wrote the article, MB contributed with substantial revisions especially in the section about DAV^{3}E.

O7. D. Puglisi, J. Eriksson, **M. Bastuck**, M. Andersson, A. Lloyd Spetz, and A. Schütze, "Gas Sensors for Indoor Air Quality", in *Sixth Scientific Meeting EuNetAir*, 2016. doi: `10.5162/6eunetair2016/06`

> **poster presentation.** DP wrote the abstract. MB, like all authors, contributed with substantial revisions.

O8. D. Puglisi, J. Eriksson, J. Huotari, **M. Bastuck**, M. Andersson, and A. Lloyd Spetz, "Exploring the gas sensing performance of catalytic metal/metal oxides on gas sensitive SiC-FETs", presented at the 1st International Workshop on Functional Oxide (FOX) Materials, Linköping, Sweden, 2015

> **oral presentation.** DP wrote the abstract. MB, like all authors, contributed with substantial revisions.

O9. A. Lloyd Spetz, D. Puglisi, **M. Bastuck**, and M. Andersson, "Smart solutions for better indoor air quality using silicon carbide field effect transistors", *SENSIndoor Newsletter*, no. 1, 2015

> **newsletter article.** ALS wrote the article. MB, like all authors, contributed with substantial revisions.

O10. D. Puglisi, C. Bur, **M. Bastuck**, A. Schütze, M. Andersson, R. Yakimova, A. Lloyd Spetz, and J. Eriksson, "Mastering VOC detection for better indoor air quality", presented at the Third Scientific Meeting EuNetAir, Istanbul, Turkey, 2014

> **oral presentation.** DP wrote the abstract. MB, like all authors, contributed with substantial revisions.

O11. C. Bur, **M. Bastuck**, A. Schütze, M. Andersson, and A. Lloyd Spetz, "Characterization of Dust and Ash Particles with a Micro-heater and Gas Sensitive SiC Field Effect Transistors", presented at the Third Scientific Meeting EuNetAir, Istanbul, Turkey, 2014

> **poster presentation.** CB wrote the abstract. MB, like all authors, contributed with substantial revisions.

Acronyms

3S	sensitivity, selectivity, and stability
3S GmbH	3S GmbH - Sensors, Signal Processing, Systems, Saarbrücken, Germany
AC	alternating current
ADC	analog-digital converter
AFM	atomic force microscope
AGPL	Affero General Public License
ALA	adaptive linear approximation
ANN	artificial neural network
API	application programming interface
ASTM	American Society for Testing and Materials
BAM	Bundesanstalt für Materialforschung und -prüfung
BBB	BeagleBone Black
CAS	Chemical Abstracts Service
CDA	canonical discriminant analysis
CMOS	complementary metal-oxide-semiconductor
CSV	comma-separated values
DAV^{3}E	Data Analysis and Verification/Visualization/Validation Environment
DC	direct current
DF	discriminant function
DIP	dual in-line package
DSR	differential surface reduction
D-SUB	D-subminiature
EDX	energy dispersive X-ray spectroscopy
EPOC	electrochemical promotion of catalysis
FET	field-effect transistor
FID	flame ionization detector
FTDI	Future Technology Devices International

GasFET	gas-sensitive field-effect transistor
GBCO	gate bias-cycled operation
GCF	gas correction factor
GC-MS	gas chromatograph with mass spectrometer
GMA	gas mixing apparatus
GPIO	general purpose input/output
GPS	Global Positioning System
GUI	graphical user interface
HDF5	Hierarchical Data Format 5
HMDSO	hexamethyldisiloxane
HPLC	high-performance liquid chromatography
HPLC-DAD	high performance liquid chomatography with a diode array detector
IAQ	indoor air quality
ISO	International Organization for Standardization
JPEG	Joint Photographic Experts Group
JSON	JavaScript object notation
knn	k nearest neighbors
LASSO	least absolute shrinkage and selection operator
LDA	linear discriminant analysis
LED	light-emitting diode
LiU	Linköping University
LMT	Lab for Measurement Technology
LR	logistic regression
LV	latent variable
MFC	mass flow controller
MFM	mass flow meter
MIS	metal-insulator-oxide
MISFET	metal-oxide-semiconductor field-effect transistor
MLR	multiple linear regression
MOF	metal-organic framework
MOS	metal-oxide semiconductor
MSE	mean square error
NDIR	non-dispersive infrared
NEMCA	non-Faradaic electrochemical modification of catalytic activity

OOP	object-oriented programming
ou	odor unit
PAH	polycyclic aromatic hydrocarbons
PC	principal component
PCA	principal component analysis
PCB	printed circuit board
PFA	perfluoroalkoxy alkane
PI	proportional–integral
PID	proportional–integral–derivative
PLD	pulsed laser deposition
PLS	partial least squares (or) projection to latent structures
PLSR	partial least squares regression
$\mathbf{ppb_v}$	parts per billion
$\mathbf{ppm_v}$	parts per million
$\mathbf{ppt_v}$	parts per trillion
PVD	physical vapor deposition
QCM	quartz crystal microbalance
RFESVM	recursive feature elimination support vector machine
RH	relative humidity
RJ45	Registered Jack 45
RMSE	root mean square error
RMSEC	root mean square error of calibration
RMSEP	root mean square error of prediction
RMSEV	root mean square error of validation
ROI	range of interest
S(N)CR	selective (non-)catalytic reduction
SEM	scanning electron microscope
SiC-FET	silicon-carbide-based field-effect transistor
SLSQP	Sequential Least Squares Programming
SS	sum of squares
std	standard deviation
SVM	support vector machine
SVN	Apache Subversion
TCO	temperature-cycled operation
TO-8	transistor outline 8
TVOC	total volatile organic compounds
USB	Universal Serial Bus

UV	ultraviolet
VOC	volatile organic compound
WHO	World Health Organization
XML	Extensible Markup Language
XPS	X-ray photo electron spectroscopy
YSZ	yttria-stabilized zirconia

List of Figures

List of Tables

List of Listings

Acknowledgments

The present dissertation is a compilation of scientific results of four years' worth of work in Saarbrücken and Linköping. Scientific writing is, however, less suited to reflect all associated difficulties and, much more importantly, all the help and support I have experienced from friends and colleagues during all this time. This chapter shall, therefore, acknowledge all these people and their contributions to the success of this doctorate.

I highly appreciate the support and guidance from my supervisors, Prof. Andreas Schütze and Dr. Mike Andersson. Especially their constant availability for discussions as well as their commitment to make this joint PhD project work cannot at all be taken for granted.

At least as important as excellent supervisors is an enjoyable working atmosphere for which I would like to thank my colleagues and friends at LMT. First and foremost Caroline Schultealbert, Tobias Baur, and Henrik Lensch for years of outstanding teamwork, discussions in- and outside of work, and for listening to my complaints about poor customer support. Tilman Sauerwald for many helpful pieces of advice and fruitful discussions; Julian Joppich, who agreed to take over teaching as well as DAV^{3}E; my former and current "office mates" – Bastian Schmitt, Martin Leidinger, and Sebastian Höfner – as well as all other former and current colleagues: Christian Bur, Eliseo Pignanelli, Harald Nagel, Marco Schott, Marco Schüler, Nikolai Helwig, Nicolas Michaelis, Steffen Klein, Tanja Dorst, Thomas Fricke, and Tizian Schneider.

I would also like to include all student assistants and thesis workers in these acknowledgments. They bring life to the lab and help a lot with getting things done. In particular, I thank all student assistants I supervised in teaching or the lab for the good collaboration - please excuse the missing list of names; it would become quite lengthy and I would not want to forget anyone. I further appreciate the interesting discussions and results during the theses of Bhanu Prakash Medichalam, Srikanth Bommaraveni, and Claudia Daut, as well as Claudia's great help with all kinds of things GasFET-related.

But, as mentioned several times before, I was lucky enough to have had two workplaces, the other one being in Linköping, Sweden. In this relation, I would like to point out the important role of my former supervisor/colleague Christian Bur who not only first established the connection between both

groups, but also sparked my interest in Sweden. Many of the results on GasFETs in this dissertation are based on his previous work. Another "link" between Saarbrücken and Linköping is Marius Rodner, who I have known since school and who, after his Master's thesis at LMT, moved to the Applied Sensor Science group in Linköping for his doctorate. It is always great fun to discuss all kinds of things, about sensors or otherwise. And: having a "proxy" in Linköping is invaluable.

Naturally, organization tends to become a bit complex from time to time with two workplaces in two countries with different regulations. Hence, huge thanks to Christiana Dabove and Anette Andersson for staying on top of things and for always being ready and able to help.

I felt always more than welcome in Linköping during my visits, and for that, I would like to thank my great Swedish[1] colleagues and friends: Donatella Puglisi, Jens Eriksson, Marius Rodner, Lida Khajavizadeh, Francesca Santangelo, Peter Möller, Anita Lloyd Spetz, and her husband Tomas.

A huge thank you to Marianne Nilsson, my fabulous host during all my visits to Linköping, for the interesting talks (giving me the opportunity to practice my Swedish) and common dinners. Incidentally, I would like to extend these thanks to my next-(guest)room neighbors in Marianne's house, Lisa Laurence from France and Joni Kilpijärvi from Finland for their good company.

Besides France and Finland (and Sweden, obviously), I had the opportunity to visit and talk to many people from all over the world which has been a great experience. It is nice to see how easily common interests can bring people from all nations and cultures together. I would like to especially point out the hospitality I have experienced in China and India, two cultures very different from the European one so that a little support from locals was very welcome. As representatives for a lot of great people I have met in both countries, I would like to thank Hua-Yao Li and Zhixiang Hu from China, and Karabi Biswas and Moupali Chakraborty from India.

But also the "local" events were always a lot of fun, be it the yearly garden party organized by Andreas and Annette, or barbecues, dinners and sports in Sweden. Also the monthly *VDE-Stammtisch* with regular attendees including, besides (German) colleagues, Susanne Brandl and Christopher Uhl, was, and hopefully continues to be, a nice tradition.

In addition, I would like to thank Achim Koch, Alexej Gaidoukov, Chantal Sinnwell, Julian Lenhof, Kristina Brix, Michaela Braun, Nadja Klippel, Sarah Fischer, and many more, for their long-standing friendship. Moreover, the

---

[1] Actually, while they happen to live in Sweden, they come from all parts of the world, including Italy, Iran, and Germany.

weekly rehearsals with my fellow musicians in the *Musikverein Reisbach* are a great compensation for the daily work with gas sensors.

I would, further, like to acknowledge the proofreading of different parts of this thesis by Sarah, Caroline, Tobias, and Marius, and their many helpful comments.

Last, and most important, I thank my family for their constant and unconditional support, no matter what the situation. I would like to especially mention my sister Isabelle, my aunt Gabriele, and my parents Melitta and Albert, without whom none of this would have been possible.

Part V.

Appendix

Listings

1. Synthetic data generation for fusion algorithms

Listing 1.: Synthetic data generation for fusion algorithms (MATLAB).

```
function [dist,featRatio,cycleRatio,nTotalFeat,cv,nObs,s] =
↪ makeData(weight)

nObs = randi(9000) + 1000;
nGroups = 3;
conc = zeros(nObs,nGroups);
switchGroups = round(nObs/nGroups)*(1:nGroups-1) +
↪ randi(round(0.2*nObs),1,nGroups-1) - round(0.1*nObs);
switchGroups = [0 switchGroups nObs];
for i = 1:nGroups
    region = switchGroups(i)+1:switchGroups(i+1);
    conc(region,i) = 1 + randn(numel(region),1)*0.1;
end

nSens = 2;
nFeatVec = [6 + randi(10), 2 + randi(4)];

sensorCorr = cell(nSens,1);
for i = 1:nSens
    nFeat = nFeatVec(i);
    corr = zeros(nGroups,nFeat);
    for j = 1:nGroups
        corr(j,:) = 2*(rand(1,nFeat)-0.5);%*sens(j);
    end
    sensorCorr{i} = corr;
    noise{i} = rand(1,nFeat)*2;
end

s = createSimData(sensorCorr,conc,noise);

% simulate several short cycles in a long cycle
cycleRatio = randi(6);

maxNCycles = floor(nObs/cycleRatio)*cycleRatio;
```

```
s.cycleRatio = cycleRatio;

s.conc = s.conc(1:maxNCycles,:);
s.group = s.group(1:maxNCycles,:);
s.features{1} = s.features{1}(1:maxNCycles,:);
s.features{2} = s.features{2}(1:maxNCycles,:);

% long cycle covers more than one observations, hence the first part of its
 ↪  features comes from the first observation, the second part from the
 ↪  second observation, and so on...
nFeatS1 = size(s.features{1},2);
evenDivisionStep = floor(nFeatS1/cycleRatio);
start = 1:evenDivisionStep:evenDivisionStep*cycleRatio;
if isempty(start)
    start = 1;
end
stop = [start(2:end)-1 nFeatS1];
for i = 2:cycleRatio
    s.features{1}(1:cycleRatio:end,start(i):stop(i)) = ...
    s.features{1}(i:cycleRatio:end,start(i):stop(i));
end
s.features{1} = s.features{1}(1:cycleRatio:end,:);

g = s.group;
s.group = cell(2,1);
s.group{1} = g(1:cycleRatio:end,:);
s.group{2} = g;

if ~exist('weight','var')
    weight = 1 / s.cycleRatio;
end

s = applyFeatureCombinations(s,weight);

nComb = numel(s.comb);
dist = zeros(1,nComb);
for i = 1:nComb
    try
        coeff = ...
        pca(s.comb(i).features,...
        'VariableWeights',s.comb(i).varWeights,...
        'Weights',s.comb(i).obsWeights,...
        'NumComponents',2);
    catch
        dist = run();
        return;
    end

    coeff = diag(sqrt(s.comb(i).varWeights))*coeff;
```

```
    d = [s.comb(i).features*coeff(:,1) s.comb(i).features*coeff(:,2)];
    nTotalFeat(i) = size(s.comb(i).features,2);
    cv(i) =
     ↪  performCV(s.comb(i).features,s.comb(i).group,s.comb(i).varWeights);
end

featRatio = nFeatVec(1) / nFeatVec(2);
end


function [correct,stddev] = performCV(feat,groups,varWeights)
    p = cvpartition(groups,'KFold',10);
    correct = nan(10,1);
    for i = 1:10
        f = feat(p.training(i),:);
        g = groups(p.training(i));
        coeff = pca(f,'VariableWeights',varWeights);
        coeff = diag(sqrt(varWeights))*coeff;
        d = [f*coeff(:,1) f*coeff(:,2)];

        dProj = [feat(p.test(i),:)*coeff(:,1)
         ↪  feat(p.test(i),:)*coeff(:,2)];
        dist = [mahal(dProj,d(g==1,:)) mahal(dProj,d(g==2,:))
         ↪  mahal(dProj,d(g==3,:))];
        [~,gProj] = min(dist,[],2);
        tempCorrect = sum(gProj==groups(p.test(i))) / numel(gProj);
        correct(i) = tempCorrect;
    end
    stddev = std(correct);
    correct = sum(correct)/10;
end
```

Listing 2.: Apply fusion algorithms (MATLAB).

```
function s = applyFeatureCombinations(s,weight)
nlc = s.littleCyclesInBigCycle;

s.comb = [];
clr = [...
    0         0.4470    0.7410;...
    0.8500    0.3250    0.0980;...
    0.9290    0.6940    0.1250;...
    0.4940    0.1840    0.5560];

% only long cycle
c = numel(s.comb) + 1;
s.comb(c).caption = 'long cycle';
s.comb(c).lineStyle = '-';
s.comb(c).marker = 's';
s.comb(c).color = clr(1,:);
s.comb(c).features = s.features{1};
s.comb(c).group = s.group{1};
s.comb(c).varWeights = ones(1,size(s.comb(c).features,2));
s.comb(c).obsWeights = ones(1,size(s.comb(c).features,1));

% only short cycle
c = numel(s.comb) + 1;
s.comb(c).caption = 'short cycle';
s.comb(c).lineStyle = '-.';
s.comb(c).marker = 's';
s.comb(c).color = clr(1,:);
s.comb(c).features = s.features{2};
s.comb(c).group = s.group{2};
s.comb(c).varWeights = ones(1,size(s.comb(c).features,2));
s.comb(c).obsWeights = ones(1,size(s.comb(c).features,1));

% only short cycle, smoothed
c = numel(s.comb) + 1;
s.comb(c).caption = 'short cycle (mv)';
s.comb(c).lineStyle = '-.';
s.comb(c).marker = 's';
s.comb(c).color = clr(1,:);

s.comb(c).features = zeros(size(s.features{2}));
for i = 1:size(s.features{2},2)
    s.comb(c).features(:,i) = smooth(s.features{2}(:,i),nlc);
end
s.comb(c).group = s.group{2};
s.comb(c).varWeights = ones(1,size(s.comb(c).features,2));
s.comb(c).obsWeights = ones(1,size(s.comb(c).features,1));
```

```

% only short cycle, smoothed
c = numel(s.comb) + 1;
s.comb(c).caption = 'short cycle (lowess)';
s.comb(c).lineStyle = '-.';
s.comb(c).marker = 's';
s.comb(c).color = clr(1,:);

s.comb(c).features = zeros(size(s.features{2}));
for i = 1:size(s.features{2},2)
    s.comb(c).features(:,i) =
     ↪  smooth(s.features{2}(:,i),nlc/size(s.features{2},1),'lowess');
end
s.comb(c).group = s.group{2};
s.comb(c).varWeights = ones(1,size(s.comb(c).features,2));
s.comb(c).obsWeights = ones(1,size(s.comb(c).features,1));

% copy latest complete long cycle
c = numel(s.comb) + 1;
s.comb(c).caption = 'hold latest long cycle (mv)';
s.comb(c).lineStyle = '-';
s.comb(c).marker = 'o';
s.comb(c).color = clr(2,:);
[t1, t2] = [...
    repelem(s.features{1}(1:end-1,:),nlc,1),...
    s.comb(3).features(nlc:end-1,:)];
s.comb(c).features = [t1 t2];
s.comb(c).group = s.group{2}(nlc+1:end);
s.comb(c).varWeights = ones(1,size(s.comb(c).features,2));
s.comb(c).obsWeights = ones(1,size(s.comb(c).features,1));

% combine mean of n short cycles with one long cycle (weighted with 1/nlc)
c = numel(s.comb) + 1;
s.comb(c) = s.comb(c-1);
s.comb(c).caption = 'hold... (weighted)';
s.comb(c).lineStyle = '--';
s.comb(c).marker = 'o';
s.comb(c).varWeights(1:size(s.features{1},2)) = weight;

% combine mean of n short cycles with one long cycle
c = numel(s.comb) + 1;
s.comb(c).caption = 'hold latest long cycle (mv)';
s.comb(c).lineStyle = '-';
s.comb(c).marker = 'o';
s.comb(c).color = clr(2,:);
[t1, t2] = [...
    repelem(s.features{1}(1:end-1,:),nlc,1),...
    s.comb(4).features(nlc:end-1,:)];
s.comb(c).features = [t1 t2];
```

```
s.comb(c).group = s.group{2}(nlc+1:end);
s.comb(c).varWeights = ones(1,size(s.comb(c).features,2));
s.comb(c).obsWeights = ones(1,size(s.comb(c).features,1));

% combine mean of n short cycles with one long cycle (weighted with 1/nlc)
c = numel(s.comb) + 1;
s.comb(c) = s.comb(c-1);
s.comb(c).caption = 'hold... (weighted)';
s.comb(c).lineStyle = '--';
s.comb(c).marker = 'o';
s.comb(c).varWeights(1:size(s.features{1},2)) = weight;

end
```

2. Randomized gas exposure generation

Listing 3.: Generation of gas exposures with random gas concentrations (Python).

```python
import numpy as np
from tabulate import tabulate
import h5py

from grupy.gasconfig.gas import get_registry
from grupy.gasconfig.concentration_units import *
from grupy.gasconfig.gasmixer import Gasmixer
from grupy.statesequence.statesequence import StateSequence
from grupy.hardware.hwconfig import HardwareConfigParser
from grupy.gasconfig.assembly import DeviceParameterRegistry

H2 = get_registry().get_substance('H2')
CO = get_registry().get_substance('CO')
humidity = get_registry().get_substance('water')
acetone = get_registry().get_substance('acetone')
formaldehyde = get_registry().get_substance('formaldehyde')
benzene = get_registry().get_substance('benzene')
toluene = get_registry().get_substance('toluene')

### USER-DEFINED PARAMETERS ###
# min/max concentrations
conc_range = {
    'H2': (300, 2500),            # ppb
    'CO': (100, 2000),            # ppb
    'humidity': (25, 75),         # %relsat
    'formaldehyde': (12.4, 248),  # ug/m3 (in ppb: (10, 200)), factor 1.240
    'benzene': (0.3225, 161.25),  # ug/m3 (in ppb: (0.1, 50)), factor 3.225
    'TVOC': (100, 5000)           # ug/m3
}

runin_time = 7200     # run-in time in s
exposure_time = 1200  # length of gas exposure in s
tflow = 400           # total flow in ml/min

temp = 22             # °C
pressure = 101325     # Pa

n_rows = 100          # number gas exposures
prob_zero = 0.1       # probability of any VOC being 0 (independent)

output_file = 'gas_profile.h5'
### ###

# determine random concentrations for each gas component
```

```
H2_concs = np.around(np.interp(np.random.rand(n_rows, 1), (0, 1), conc_range['H2']))
CO_concs = np.around(np.interp(np.random.rand(n_rows, 1), (0, 1), conc_range['CO']))
humidity_concs = np.around(np.interp(np.random.rand(n_rows, 1), (0, 1), conc_range['humidity']))
tvoc_concs = np.around(np.interp(np.random.rand(n_rows, 1), (0, 1), conc_range['TVOC']))

# random ratios: target/background gases in TVOC, and target ratio and background ratio
# example: with a TVOC of 1000 ug/m3 and a target/background ratio of 0.3, 300 ug/m3 will be made up of target gases
#          a target gas ratio of 0.6 means that 120 ug/m3 will be benzene, and 180 ug/m3 formaldehyde
#          similar for the background gases
ratios_target_background = np.interp(np.around(np.random.rand(n_rows, 1), 3), (0, 1), (0, 0.2))  # the last tuple defines the range
ratios_targets = np.interp(np.around(np.random.rand(n_rows, 1), 3), (0, 1), (0, 1))
ratios_backgrounds = np.interp(np.around(np.random.rand(n_rows, 1), 3), (0, 1), (0, 1))

cum_target_concs = tvoc_concs * ratios_target_background
cum_background_concs = tvoc_concs * (1 - ratios_target_background)

benzene_conc = cum_target_concs * ratios_targets
formaldehyde_conc = cum_target_concs * (1 - ratios_targets)
acetone_conc = cum_background_concs * ratios_backgrounds
toluene_conc = cum_background_concs * (1 - ratios_backgrounds)

# set some concentrations randomly to zero
benzene_conc *= np.random.rand(n_rows, 1) > prob_zero
formaldehyde_conc *= np.random.rand(n_rows, 1) > prob_zero
acetone_conc *= np.random.rand(n_rows, 1) > prob_zero
toluene_conc *= np.random.rand(n_rows, 1) > prob_zero

mat = np.concatenate((ug_per_m3(benzene_conc, benzene, temperature=temp) * 1000,
                      ug_per_m3(formaldehyde_conc, formaldehyde, temperature=temp) * 1000,
                      ug_per_m3(acetone_conc, acetone, temperature=temp) * 1000,
                      ug_per_m3(toluene_conc, toluene, temperature=temp) * 1000,
                      H2_concs,
                      CO_concs,
                      humidity_concs), axis=1)

```

```
header = ['benzene', 'formaldehyde', 'acetone', 'toluene', 'H2', 'CO',
↪   'humidity']

print(tabulate(mat, headers=header))
print('\nmedian')
print(tabulate([np.median(mat, axis=0)], headers=header))

dtype = [('time', np.uint64), ('state', np.uint64),
         ('.'.join(('Gasmixer', str(benzene))), np.float64),
         ↪   ('.'.join(('Gasmixer', str(formaldehyde))), np.float64),
         ('.'.join(('Gasmixer', str(acetone))), np.float64),
         ↪   ('.'.join(('Gasmixer', str(toluene))), np.float64),
         ('.'.join(('Gasmixer', str(H2))), np.float64),
         ↪   ('.'.join(('Gasmixer', str(CO))), np.float64),
         ('.'.join(('Gasmixer', str(humidity))), np.float64),
         ↪   ('.'.join(('Gasmixer', 'total_flow')), np.float64)]

first_row = np.array([(0, 0, 0, 0, 0, 0, 500, 150, 50, tflow)],
↪   dtype=dtype)

statenr = np.asarray(range(mat.shape[0])).reshape(-1, 1)
times = statenr * exposure_time + runin_time
statenr += 1

mat = np.concatenate((statenr, times, mat, np.ones((mat.shape[0],
↪   1))*tflow), axis=1)
totmat = np.empty((mat.shape[0], 1), dtype=dtype)
for i, column in enumerate(mat.T):
    totmat[dtype[i][0]] = column.reshape(-1, 1)
totmat = np.append(first_row, totmat)  # np.concatenate((first_row,
↪   totmat), axis=0)

totmat = np.resize(totmat, (-1, 1))

with h5py.File(output_file, 'w') as file:
    file.create_dataset('statesequence', data=totmat)
    file.flush()
```

PCBs and schematics

1. 3S GasFET electronics extension board

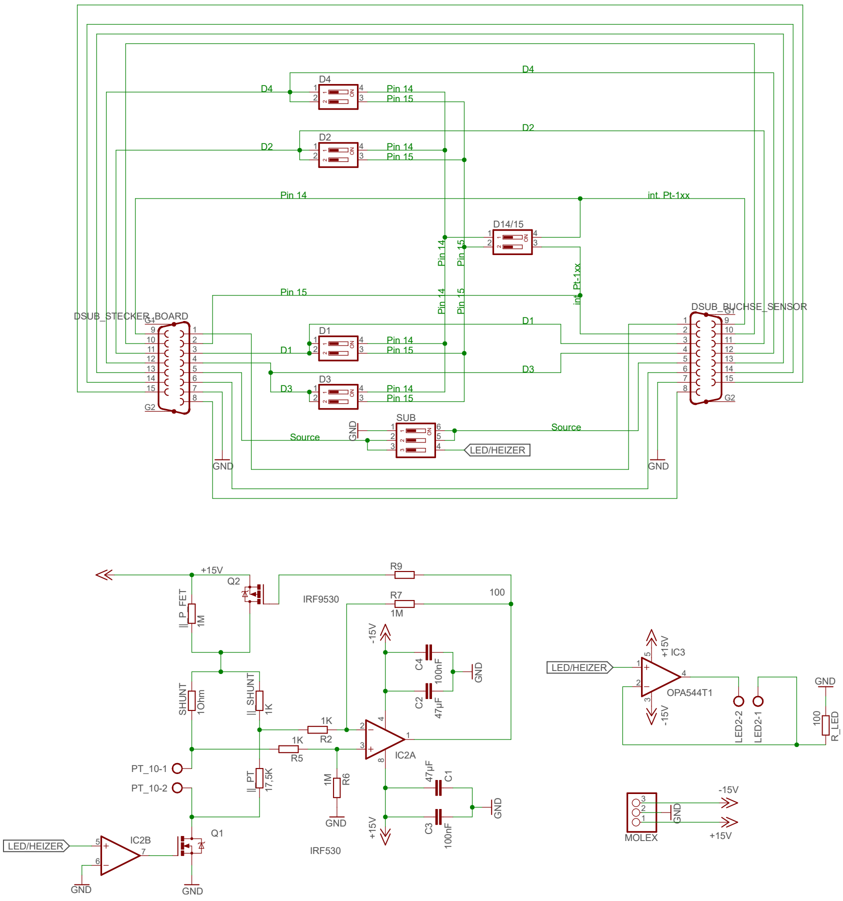

Figure 1.: Extension board schematics for the 3S GasFET electronics.

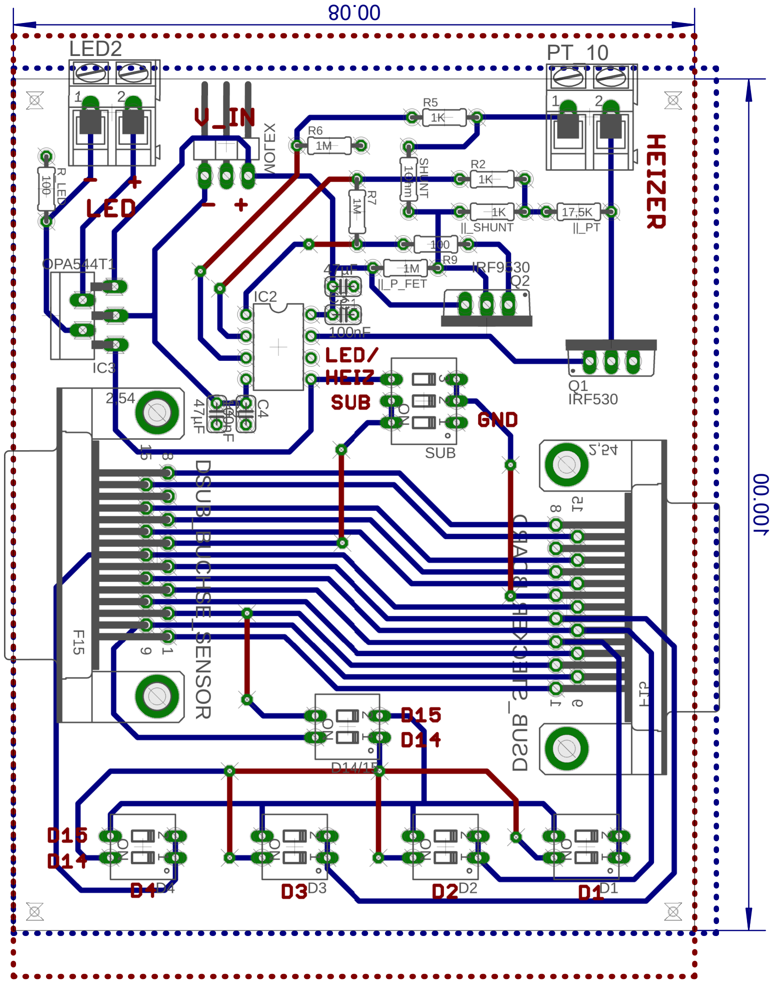

Figure 2.: Extension board layout for the 3S GasFET electronics (copper pouring left out for clarity, routed by Claudia Daut).

2. TO-8 header adapter board

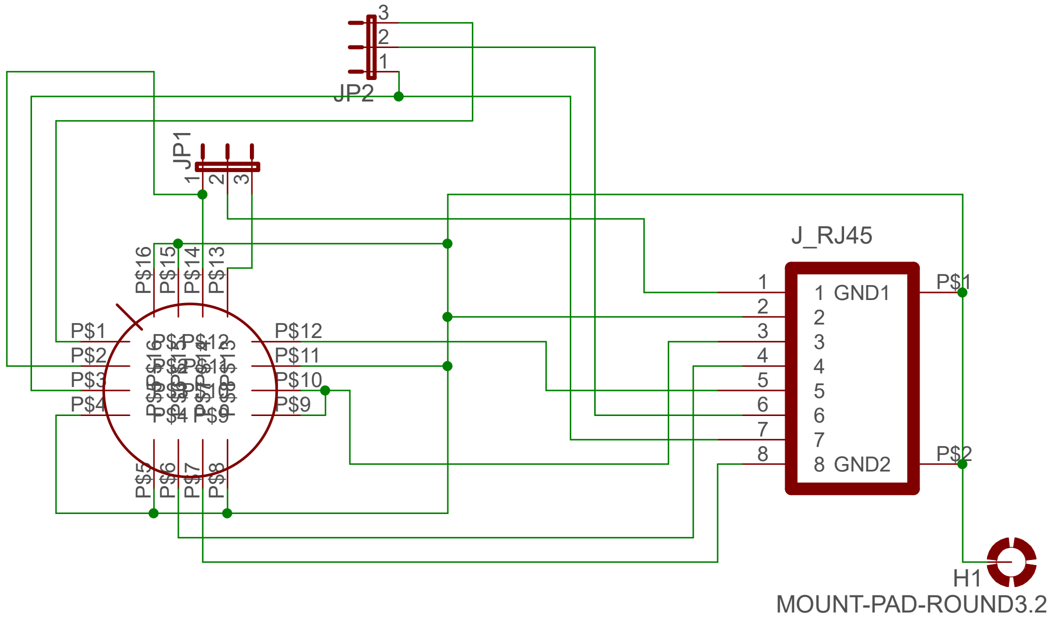

Figure 3.: Adapter board schematics for TO-8 to RJ45.

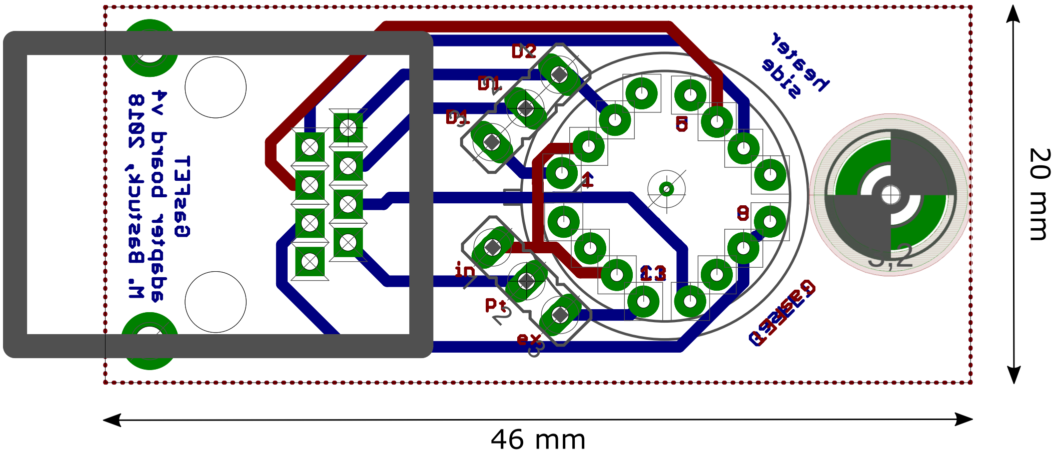

Figure 4.: Adapter board layout for TO-8 to RJ45 (copper pouring left out for clarity).